TRIBOLOGICAL INVESTIGATION OF ELECTRICAL CONTACTS

A Dissertation
Presented to
The Academic Faculty

By

Dinesh Bansal

In Partial Fulfillment
Of the Requirements for the Degree
Doctor of Philosophy in Mechanical Engineering

Georgia Institute of Technology
December, 2009

TRIBOLOGICAL INVESTIGATION OF ELECTRICAL CONTACTS

Approved by:

Dr. Jeffrey Streator, Advisor
School of Mechanical Engineering
Georgia Institute of Technology

Dr. Steven Danyluk
School of Mechanical Engineering
Georgia Institute of Technology

Dr. Thierry Blanchet
Department of Mechanical, Aerospace & Nuclear Engineering
Rensselaer Polytechnic Institute

Dr. Richard Neu
School of Mechanical Engineering
Georgia Institute of Technology

Dr. Richard Cowan
Manufacturing Research Center
Georgia Institute of Technology

Dr. Naresh Thadhani
School of Materials Science and Engineering
Georgia Institute of Technology

Date Approved: July 27, 2009

I dedicate this dissertation to my parents.

ACKNOWLEDGEMENTS

My journey of obtaining the Ph.D. degree would not have been possible without the support that I received from my family, friends and colleagues. I take this opportunity to thank those who supported me and encouraged me during this journey.

To begin with I thank my parents for their unconditional love and encouragement during the course of this journey. I cannot thank them enough for putting up with my excuses for not visiting them often. I only hope that my achievements make them proud parents.

I would always be thankful to my advisor Prof. Jeffrey Streator for all the intellectually stimulating discussions that we have had over last several years. The freedom that he gave me to pursue my research ideas has resulted in this dissertation. I would also like to thank my thesis reading committee members, especially Professors Richard Neu and Naresh Thadhani for their suggestions regarding the interpretation of voltage saturation results. The suggestions given by Prof. Blanchet during the proposal and defense process have helped in highlighting some of the contributions of my work, and I thank him for those. I would also like to thank Dr. Richard Cowan who also has been a mentor in addition to serving on the thesis reading committee.

My achievements would not have been possible without the help that I received from Steven Sheffield, Kyle French, John Graham and the support staff of Electronics laboratory and Machine shop.

My friends and colleagues with whom I have shared last several years have been instrumental for providing the much needed moral support during the times of despair,

and I am thankful to them. I will always cherish the time that I spent with Narasimhan Swaminathan, Arnab Choudhury, Kyle French, Amar Atre, Azam Thatte, Vivek Gupta, Ramesh Singh, Sathyan Subbiah, Sriram Subramanian, and Mukund Kumar.

TABLE OF CONTENTS

LIST OF TABLES

LIST OF FIGURES

NOMENCLATURE

A	Real area of contact
A_o	Nominal or apparent area of contact
A_{pq}	Regression coeffcients
$\overline{A}$	Area of contact of an asperity
$\overline{A}_{AF}$	Area of contact obtained from AF model
$\overline{A}_c$	Area of contact at the point of critical interference
$\overline{A}_{JG}$	Area of contact obtained from JG model
$\overline{A}_{JGH}$	Area of contact obtained from JHG model
$\overline{A}_{ZMC}$	Area of contact obtained from ZMC model
a	Contact half width (radius) in the direction of sliding (along major axis)
α	Thermal diffusivity
α	Temperature coefficient of electrical resistivity
B	Material dependent exponent
b	Contact half width in the transverse direction (along minor axis)
β	Temperature coefficient of thermal conductivity
β_c	Non-dimensional factor accounting for Coulomb heating
β_j	Non-dimensional factor accounting for Joule heating
c	Ellipticity ratio
Δ	Signal amplitude

$\Delta\Theta^*$	Error in temperature matching
E	Modulus of elasticity
E_2	Least squares error
E^*	Normalized least squares error
ε	Error in the estimation of heat partition
F	Contact load
$\bar{F}_c$	Contact force at the point of critical interference
f	Frequency
ζ	Radius of curvature
H	Hardness
H_G	Hardness geometric limit
η	Non-dimensional distance along Y-axis
η	Area density of asperities
Θ	Non-dimensional temperature
I	Electrical current
K	Thermal conductivity
k_o	Thermal conductivity at room temperature
λ	Wavelength
μ	Coefficient of friction
N	Number of asperities in contact
ν	Poisson's ratio
ξ	Non-dimensional distance along X-axis
Pe	Peclet number

$\overline{p}$, p_m	Mean pressure in the interface
$\tilde{Q}$	Non-dimensional heat flow due to bulk temperature difference
q_f	Frictional heat generated at the interface
q_j	Joule heat generated at the interface
q_1 , q_2	Heat flux flow into Body 1 and Body 2
σ	Heat partition fraction
R	Radial distance measured from the center of the circle
R_c	Contact resistance
ρ	Electrical resistivity
ρ_o	Electrical resistivity at room temperature
T	Temperature
T_i	Initial bulk temperature
T_m	Melting temperautre
τ	Shear strength of the material
Ψ	Non-dimensional initial bulk temperature
U	Sliding velocity
V	Voltage
Z_{pq}	DFT coefficients
z	Asperity height measured from the mean plane of asperity heights
ω	Interference
ω_c	Critical interference
ECR	Electrical contact resistance

FFT	Fast Fourier transform
DFT	Discrete Fourier transform

SUMMARY

The temperature rise at the interface of two sliding bodies has significant bearing on the friction and wear characteristics of the bodies. The friction heat generated at the interface can be viewed as "loss of exergy" of the system, which also leads to accelerated wear in the form of oxidation, corrosion, and scuffing. This has a direct impact on the performance of the components or the machinery. If the sliding interface is also conducting electric current then the physics at the interface becomes complicated. The presence of electrical current leads to Joule heat generation at the interface along with other effects like electromotive, electroplasticity, stress relaxation and creep.

The interface of an electrical contact, either stationary or dynamic, is a complex environment as several different physical phenomena can occur simultaneously at different scales of observations. The main motivation for this work stems from the need to provide means for accurate determination or prediction of the critical contact parameters viz., temperature and contact resistance. Understanding the behavior of electrical contacts both static and dynamic under various operating conditions can provide new insights into the behavior of the interface. This dissertation covers three major topics: (1) temperature rise at the interface of sliding bodies, (2) study on static electrical contacts, and (3) study of factors influencing behavior of sliding electrical contacts under high current densities.

A model for determining the steady-state temperature distribution at the interface of two sliding bodies, with arbitrary initial temperatures and subjected to Coulomb and/or Joule heating, is developed. The model applies the technique of least squares regression to apply the condition of temperature continuity at every point in the domain. The results

of the analysis are presented as a function of non-dimensional parameters of Peclet number, thermal conductivity ratio and ellipticity ratio. This model is first of its kind and enables the prediction of full temperature field. The analysis can be applied to a macro-scale contact, ignoring surface roughness, between two bodies and also to contact between two asperities. This analysis also yields an analytical expression for determining the heat partition between two bodies, if the Jaeger's hypothesis of equating average temperatures of both the bodies is being implemented.

In general for design purposes one is interested in either the maximum or the average temperature rise at the interface of two sliding bodies. Jaeger had presented simple equations, based on matching the average temperatures of both bodies, for square and band shaped contact geometries. Engineers since then have been using those equations for determining the interface temperature for circular and elliptical shaped contact geometries. Curve fit equations for determining the maximum and the average interface temperature for circular and elliptical contact with semi-ellipsoidal form of heat distribution are presented. These curve fit equations are also applicable for the case when both the bodies have dissimilar initial bulk temperatures. The equations are presented in terms of non-dimensional parameters and hence can easily be applied to any practical scenario.

The knowledge of electrical contact resistance between two bodies is important in ascertaining the Joule heat generation at the interface. The prediction of the contact resistance thus becomes important in predicting the performance of the contact or the machinery where the contact exists. The existing models for predicting ECR suffer from the drawback of ambiguity of the definition of input parameters as they depend on the

sampling resolution of the measuring device. A multi-scale ECR model which decomposes the surface into its component frequencies, thus capturing the multi scale nature of rough surfaces, is developed to predict the electrical contact resistance. This model, based on the JS multi-scale contact model, overcomes the sensitivity to sampling resolution inherent in many asperity based models in the literature. The multi-scale ECR model also offers orders of magnitude of savings in computation time when compared to deterministic contact models. The model predictions are compared with the experimental observations over a wide range of loads and surface roughness of the specimens, and it is observed that the model predictions are within 50% of the experimental observations.

The effect of current cycling through static electrical contact is presented. It is observed that, the voltage drop across the contact initially increases with current until a certain critical voltage is increased. Beyond this critical point any increase in the current causes essentially no increase in steady-state contact voltage. This critical voltage is referred to as "saturation voltage." The saturation voltage for Al 6061 interface is found to be in the range of 160 – 190 mV and that for Cu 110 interface is in the range of 100 – 130 mV. The effect of load and surface roughness on voltage saturation is also demonstrated experimentally. An explanation based on the softening of the interface, due to temperature rise, is proposed rather than more widely referred hypothesis of recrystallization.

The phenomenon of voltage saturation is also demonstrated in sliding electrical contacts. The behavior of sliding interfaces of aluminum–copper (Al–Cu) and aluminum–aluminum (Al–Al) are analyzed under high current densities. Experimental results are presented that demonstrate the influence of load, speed, current and surface roughness on

coefficient of friction, contact voltage, contact resistance, interface temperature and wear rate. The experimental results reveal that thermal softening of the interface is the primary reason for accelerated wear under the test conditions. The results from the experiments presents an opportunity to form constitutive equations which could be used to predict the performance of the contact based on input parameters.

The fusion of the findings of this dissertation provide methodologies along with experimental tools and findings to model, study and interpret the behavior of electrical contacts.

CHAPTER 1. INTRODUCTION

1.1 Motivation

The study of wear and friction at the interface of two sliding bodies has been a topic of great interest for many years. One can find the work on understanding of friction and wear dating back to the days of Leonardo da Vinci (1452–1519). Guillaume Amontons (1663–1705) later on independently verified the findings of Leonardo da Vinci [1]. With great advances made in the arena of experimental techniques, data acquisition and diagnostic tools (microscope, profilometer, SEM, XRD, spectrometer etc.) the understanding of friction and wear has also improved. The knowledge of tribology finds application in many fields ranging from machining, automobiles, bio-implants, space applications, power generating devices, weapon systems and many more. In many of these fields several old hypotheses and paradigms are still used to design and evaluate the performance of the components therein.

The interface of an electrical contact, either stationary or dynamic, is a complex environment as several different physical phenomena can occur simultaneously at different scales of observations. The area of contact in such a scenario keeps changing due to wear and/or thermal induced softening. Direct *in-situ* determination of the contact area is impossible and only the *in-situ* force, voltage and current measurements and the results from the post-mortem analysis of the specimens are used to hypothesize about the phenomena at the interface. On the micro scale the roughness on the surfaces of the contact bodies contribute to the electrical and thermal contact resistance. The asperities which make the contact are responsible for conducting the current and heat across the

interface. The locations in the interface which do not make contact could be sites of micro-arcing and cause melting of non contacting asperities.

The main motivation for this work stems from the need to provide means for accurate determination or prediction of the critical contact parameters viz., temperature and contact resistance of a sliding interface through which electrical current is flowing. Understanding the behavior of electrical contacts both static and dynamic under various operating conditions can provide new insights into the behavior of the interface. The results of this study may then be applied in various applications like design of electronic contacts, designing interfaces for high current density applications– e.g., power generating devices, electro-magnetic launchers, machining and other processes.

1.2 Research gaps

1.2.1 Heat partition and temperature rise in sliding contacts

The friction-induced temperature rise at the interface of two sliding bodies can cause a number of effects, including yield strength reduction, accelerated oxidation wear and thermoelastic instability, all of which may lead to degradation of performance or even the failure of the associated components. It is of interest, therefore, to accurately determine the temperature field resulting from sliding contact. After the pioneering work of Blok [2, 3] and Jaeger [4], researchers have implemented various schemes to determine interfacial temperatures in sliding contacts. However, several have faced obstacles with the singular kernel [5-8], and/or were not able to account properly for the case of one body sliding against a stationary body [6, 9]. Some researchers solved only 1D sliding contact problem [10]. Review of the literature suggests that there is a need for

a methodology to compute interface temperature, due to Coulomb and/or Joule heating, based on point wise temperature matching throughout the interface for bodies with arbitrary initial temperatures.

In many engineering scenarios designers need values of either maximum or average interface temperature. In most cases they resort to much simpler equations put forth by Jaeger [4]. Jaeger provided approximate equations for average temperature rise for square and band shaped contact regions for very low Peclet numbers (< 0.1) or for very high Peclet numbers (> 10). Jaeger's equations are not applicable to Hertzian contact configuration. Kuhlmann-Wilsdorf [11-13] modified the equation for maximum temperature rise put forth by Blok [3] to include the shape factor for elliptical contacts and used it to compute flash temperature due to friction and Joule heating. However the accuracy of these relations has not been verified by other models and the author herself admitted several shortcomings of those relations. Hence it can be said that there exist no accurate formulae available to aid designers for predicting interface temperature in sliding Hertzian contacts.

1.2.2 Predicting electrical contact resistance

The prediction of electrical contact resistance between two real surfaces is of great importance for several electronics and electrical applications. Several models, as discussed later in Chapter 5, have been developed for the same. However, some of the models are overly simple and few have been compared with experimental results.

1.2.3 Voltage limits in static contacts

In order to better understand the behavior of the interface of sliding electrical contacts it is helpful to first study the static interface. The effect of load on contact resistance has been studied extensively but the effect of cycling current through the interface has not been given due attention. It has been suggested that for each material pair there is a "softening" and "melting" voltage at which the interface begins to soften and melt respectively [14]. However, the explanation provided for achieving those conditions ignores the most important aspect of dependence of material properties on temperature.

1.2.4 Sliding electrical contact at high current density

The performance of an electrical contact under high contact pressures and current densities is important for several applications like those in power generators, motors, electro-magnetic launchers (EML) etc. With keeping the focus on EML, understanding behavior of copper and aluminum under the operating contact pressures and current densities of an EML is important. Conducting experimental studies on a full size EML has limitations and hence some studies have been conducted on pin-on-disk type of test apparatus [15] while others have been conducted on test rigs with linear sliding motion but under small currents (~10 amps) and very short sliding distances (i.e., a few microns) [16]. None of these apparatus replicate the wear process occurring at the sliding interface of armature and rail of linear sliding with macro-scale contact under high current densities over representative linear distances. Hence there is a need for a precision bench top tribo-simulator which would replicate the wear mechanisms occurring in an EML of a

macro-scale interface sliding under comparable current densities over representatives distances of an EML. The test results of materials under high current densities and contact pressures can provide more relevant parameters for modeling the multi-physics nature of the interface.

1.3 Objective

The main objective of the thesis is to analyze the tribological effects of static and dynamic electrical contacts under wide range of conditions.

This objective is accomplished through the following tasks:

1. Develop a model to evaluate heat partition and temperature rise in sliding electrical contacts
2. Develop simple curve fit relations to compute the maximum and average temperature rise in sliding Hertzian contacts
3. Develop a model to predict the electrical contact resistance based on the topographical parameters and material properties of the surfaces in contact
4. Study the effect of cycling of load and current on static electrical contacts
5. Study the behavior of sliding copper and aluminum interfaces under high contact pressures and current densities

1.4 Organization of the dissertation

This dissertation covers three major topics: (1) temperature rise at the interface of sliding bodies, (2) study on static electrical contacts, and (3) study of factors influencing behavior of sliding electrical contacts under high current densities. Chapters 2–4 are

concerned with the first topic, chapters 5–6 with the second topic, and chapters 7–8 with the third topic, as detailed below. Each of these chapters begins with an introduction followed by the relevant literature review. Figure 1.1 presents an outline of the organization of the thesis.

Chapters 2–4: Heat partition and temperature rise in sliding bodies

Chapter 2 provides an extensive literature review on different hypotheses and models put forth to evaluate the heat partition and temperature rise at the interface of two sliding bodies. A methodology is then presented to evaluate the heat partition and the temperature distribution at the interface by applying the condition of "temperature continuity" at every point in the interface. This model is then extended to evaluate the scenario when the two bodies have dissimilar initial temperatures and when the two bodies are moving with respect to the interface.

Since Hertzian type contacts find wide applications, curve fit relations are presented in Chapter 3 to compute temperature rise over wide range of Peclet numbers, thermal conductivity ratios and ellipticity ratios. The heat partition or the temperature rise model is then extended to evaluate the interface temperature for sliding electrical contacts. Although a uniform distribution of Joule heating is assumed the results of the analysis provide qualitative trends on the influence of Peclet number, and proportional magnitudes of Coulomb heat and Joule heat on the interface temperature rise.

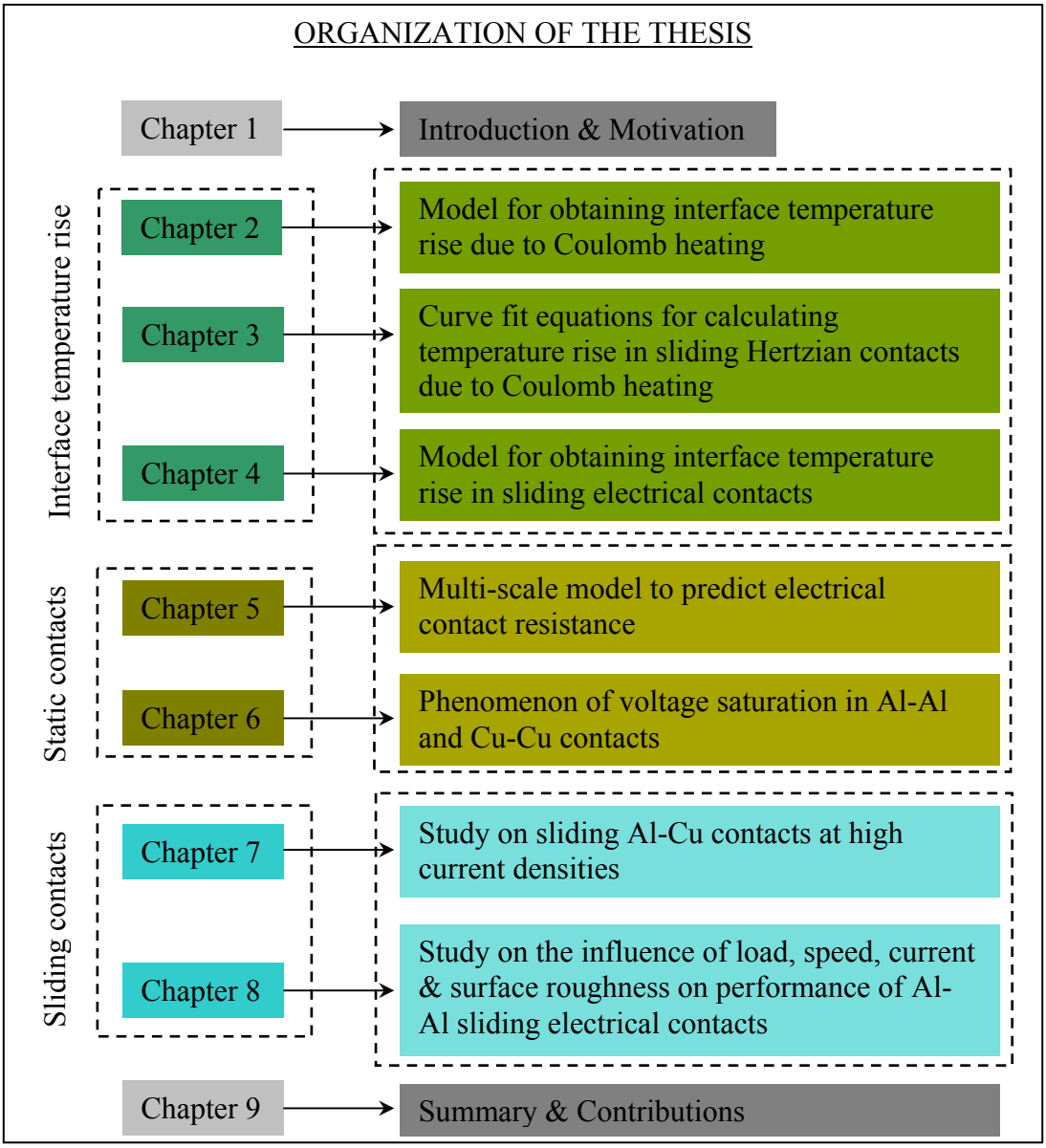

Figure 1.1 Organization of the thesis

Chapters 5–6: Study on static electrical contacts

In Chapter 5, a multi-scale model is presented to predict the electrical contact resistance based on the topographical information and material properties of the contacting surfaces. The model predictions are then compared with the experimental results.

In Chapter 6, experimental results with stationary Al–Al and Cu–Cu contacts are presented showing that voltage increases with current until a certain threshold voltage; termed here the "saturation voltage" is reached. Once the saturation voltage is reached any increase in current causes no increase in voltage and the interface undergoes morphological changes.

Chapters 7–8: Study on sliding electrical contacts at high current densities

In this section of the thesis, several sliding electrical contacts are analyzed. The interface of aluminum–copper (Al–Cu) in flat–on–flat and sphere–on–flat contact configurations is analyzed at high current densities in Chapter 7. Diagnostic tools like optical microscopy, scanning electron microscopy and X-ray diffraction analysis are used to analyze the wear of the pins.

In Chapter 8, the influence of load, speed, current and surface roughness on the performance of Al–Al in sphere–on–flat contact configuration is presented. The behavior of coefficient of friction, contact resistance, contact voltage, temperature rise and pin wear will be discussed in the light of the operating conditions.

Chapter 9: Conclusions and contributions

The last chapter presents the major conclusions and summarizes the significant intellectual contributions.

CHAPTER 2. METHODOLOGY FOR OBTAINING INTERFACE TEMPERATURE RISE DUE TO COULOMB HEATING

2.1 Introduction

Determining the temperature distribution at the interface of two sliding bodies has long been a topic of great interest in the field of tribology. Accurate knowledge of the temperature rise is critical for performing thermal stress analysis between two sliding bodies [17-22], or thermal wear modeling [23, 24] both of which are relevant to many applications, such as machine tools [25-27], brake pads [28, 29], gear teeth [30, 31], and wheel-rail contacts [32]. When one body slides over another body, heat is generated at the interface due to friction and this heat is partitioned between the two bodies. The partitioning of heat is a function of the thermal properties of the bodies, the contact geometry and the sliding speed.

In this chapter a methodology of obtaining the temperature rise at the interface of two sliding semi-infinite bodies by partitioning the heat between them in such a way that the temperature at every grid point in the interface is same for both the bodies. A polynomial form is assumed for the unknown heat partition function and then a linear regression is performed to find the coefficients that optimize the temperature matching at the interface.

2.2 Literature review

One of the first models for estimating the temperature rise at the interface of two sliding surfaces was due to Blok [2, 3]. Blok approximated the condition of continuity of

temperature at the interface by equating the steady-state maximum temperature rise at the interfaces of two sliding bodies in order to find the heat partition factor. That is, a total interfacial heating rate, attributed to frictional dissipation, is partitioned between the stationary and moving bodies so that the associated maximum temperature rises—as per the respective stationary and moving heat source models—is the same for each body. Blok assumed that at low Peclet numbers the maximum temperature is independent of the speed and thus used the expression for the maximum temperature due to a stationary heat source to calculate the temperature rise at the interface. For high Peclet numbers, Blok suggested that the heat flow in the direction transverse to the sliding direction will be negligible and the square heat source can thus be approximated as an infinitely long band source. For intermediate Peclet numbers, Blok curve fitted the results of numerical integration to approximate the maximum temperature rise in the contact. The notion that a good estimate for the maximum temperature rise can be found from Blok's approach to temperature matching will be hereon be referred to as "Blok's hypothesis."

Jaeger [4] performed a heat partitioning analysis similar to that of Blok, but his method was based on matching the average temperature rise rather than the maximum temperature rise. In order to find the temperature distribution at the interface due to moving heat sources, Jaeger integrated asymptotic approximations of the Bessel function valid either for very low Peclet numbers (< 0.1) or for very high Peclet numbers (> 10). For each case, he provided expressions for the average temperature rise and the maximum temperature rise within the heating zone. For intermediate Peclet numbers, Jaeger, like Blok, provided curve fit solutions for average and maximum temperature rise for both square and band shaped heat sources. In order to compute the heat partition at

the interface formed by one moving body sliding against a stationary body, Jaeger equated the average temperature rise of both the bodies, using the appropriate expression for each body based on its Peclet no. The notion that a good estimate for the temperature rise at the interface can be obtained from Jaeger's approach to equating temperatures is generally referred to as "Jaeger's hypotheses."

An approach similar to that of both Blok and that of Jaeger was presented by Archard [33], but based on the premise the interface temperature should be 1/2 of the harmonic mean of the hypothetical average temperatures that would result for the two bodies should all generated heat be applied to each body independently.

Ling [34] equated temperature rise at every point within the interface of a stationary band source on a moving semi-infinite body under steady state conditions and arrived at a Fredholm integral equation of the first kind for the heat partition function. The method of Ling, which applies to contact geometries that can be modeled as an infinite band, involves an analytical inversion of the uniform band heat source solution.

Cameron et al. [5], while studying the problem of temperature rise at gear teeth contacts, idealized the physics of the problem by considering each gear to be a moving semi-infinite body upon which was a uniform moving band source of heat. The condition of pointwise temperature matching was satisfied for both the cases of two bodies moving in the same and the opposite directions, and expressions for the temperature rise were provided. The solution obtained had a velocity term in the denominator and thus could not be applied to the case where one body was stationary while the other was moving. Symm [9] reformulated the problem analyzed by Cameron et al. [5] and arrived at a solution that could be applied to the case of one body sliding against a stationary body.

Symm used the asymptotic approximation to the solution kernel to arrive at an expression for the temperature rise for a stationary body. However, Symm's model yields the curious result that the stationary body receives no heat whatsoever.

Francis [35] derived an approximate analytical expression for steady-state temperature rise within a fast moving (Peclet no. > 5) circular contact with ellipsoidal heat distribution. In order to partition the heat between the stationary and the fast moving bodies, Francis used Archard's [33] half harmonic mean approach.

Kennedy [36] used finite element analysis (FEA) to study temperature rise at the interface of a sliding system under steady state conditions. Kennedy constructed a finite element model of two stationary bodies in contact and supplied heat to the contact elements on the interface that was equivalent to heat that would be generated due to friction if the two bodies were moving. Kennedy used the analysis put forth by Floquet et al. [37] in which the partitioning of heat is determined in the FEA model from the specified heat generation at the interface and from the enforcement of a temperature matching at the nodes between the two bodies. However, this kind of analysis, in principle, does not analyze the case of heat generation between two sliding bodies as both the bodies in the Kennedy model see a stationary heat source.

Gecim and Winer [38], analyzed the steady state temperature distribution on a rotating cylinder at large Peclet numbers in the presence of convective heat transfer, and partitioned the heat by employing Blok's hypothesis. In a subsequent study, Gecim and Winer [39], used Jaeger's hypothesis to find a single heat partition factor for a sliding circular contact.

Lai and Cheng [40] analyzed transient temperatures in a lubricated contact between a stationary elastic rough surface and a moving rigid smooth surface. In their analysis, the authors discretized the contact domain in several (discrete) sub-domains and partitioned the heat within each subdomain, essentially using the harmonic mean approach of Archard [33], but based on the hypothetical maximum temperature rises rather than the average temperature rises.

Yuen [6], while studying the temperature rise in strip rolling process, analyzed the system as a moving uniform band source with respect to both bodies, the coordinate system being fixed to the source. Yuen derived an asymptotic solution of the Fredholm integral equation valid only for large Peclet numbers (i.e., greater than about 10).

Tian and Kennedy [41], in their study on temperature rise of finite bodies when the contact area cyclically sweeps over the other body, suggested that small scale restriction to heat flow at the interface leads to temperature jump, which they termed as "non-linear temperature drop," across the interface. They defined the total contact temperature to be sum of local surface temperature, due to small scale heat flow restriction, nominal surface temperature, due to large scale heat flow restriction, and the background bulk temperature. The local surface temperature was obtained by considering a point source on a semi-infinite body while the nominal surface temperature was calculated by considering the convection from the surface and restriction to the heat flow due to the boundary conditions of the finite body. The heat flux entering each body, which was needed to calculate nominal surface temperature and the local surface temperature, was obtained using Blok's hypothesis. In a subsequent study, Tian and Kennedy [42] presented solutions of temperature rise in a semi-infinite body due to

uniform heat sources applied over circular and square regions and an ellipsoidal heat source applied over an elliptical region. In order to obtain the heat partition, they used Blok's approach of equating the maximum surface temperatures of both the bodies in the contact region.

Bos and Moes [7, 8], used a multi-grid solution technique with Jacoby relaxation scheme to equate temperature rise at all the points within the contact region. The authors also provided an asymptotic solution for the temperature rise for very high Peclet nos. (but without specifying the lower limit on Peclet number range) by neglecting the heat flow in the direction perpendicular to the sliding direction. They also analyzed cases with very low Peclet number by approximating them to be stationary contacts.

Qui and Cheng [43] employed an influence coefficient method to solve for the interfacial temperature distribution in for a mixed lubricated contact. Heat partitioning was done by attempting to match surface temperatures at each of the nodes on a 2D grid. However, the heat partition factor was forced to range from 0 and 1, which led to temperature mismatch at some nodes.

Komanduri and Hou analyzed the problems of temperature rise at the interface of a sleeve bearing and its housing [44] and also at the chip tool interface [45]. They modeled frictional heating in the interface by considering a band source on a semi-infinite body at steady state. For each of the two contact bodies, they assumed a particular functional form for the heat partition function, based on trial and error.

Recently, Kadiric et al. [10] applied an influence coefficient method to calculate the temperatures for a line contact (i.e., a 1D grid). Partition coefficients were defined at

each node and their values determined by solving the system of equations associated with matching the temperatures of the contacting surfaces at each grid point.

In summary, after the pioneering works of Blok and Jaeger, researchers have implemented various schemes to determine interfacial temperatures in sliding contacts. Several authors [5-8, 10, 34, 45] have attacked the problem of matching temperatures throughout the contact, considering either 1 or 2 independent spatial variables (i.e., x or x & y). However, several have faced obstacles with the singular kernel [5-8], and/or were not able to account properly for the case of one body sliding against a stationary body [5, 6, 9]. It seems only Kadiric et al. [10] have correctly solved the general 1D sliding contact problem—"correct" in that the accuracy of their results are limited only by the resolution of the grid, and "general" in the sense that the surface heat distribution can be of any shape.

2.3 Description of the heat partition model

The following assumptions are made in order to obtain the heat partition distribution and thus the temperature rise at the interface:

i. The temperature response of each body to surface heating is the same as that of a half-space (which is insulated outside of the contact region). In other words, the heat transfer to the surroundings due to convection and radiation are neglected.
ii. The area of contact does not change during sliding.
iii. The sliding time has been long enough for steady-state conditions to have been attained.

iv. A constant coefficient of kinetic friction exists that serves as the proportionality factor between interfacial shear stress and contact pressure.

v. The bodies have matching temperatures at every point within the contact zone.

vi. The heat partition distribution can be represented by a polynomial function.

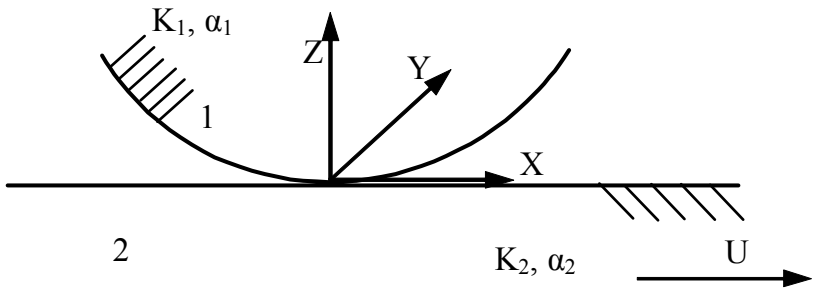

Figure 2.1 Schematic of the problem of interest

Consider two semi-infinite bodies sliding across each other, as indicated in Figure 2.1. For the sake of simplicity, we shall keep the upper body (Body 1) stationary and move the lower body (Body 2) with a velocity U to right. Let T_{1i} and T_{2i} be the initial temperatures of Body 1 and Body 2, respectively. Let K_1 and K_2 be the thermal conductivities and α_1 and α_2 be thermal diffusivities of Body 1 and Body 2, respectively. In general, the upper body (Body 1) has different radii of curvatures in the sliding and transverse directions within the sliding plane and this will give rise to an elliptical shaped contact. Consider a coordinate system that is attached to Body 1 with its origin placed at the center of the contact region (Figure 2.1). It is assumed that the radius of curvatures of both the bodies are large compared to the width of the contact region so that the both the bodies can be modeled as half-spaces. The heat generation rate per unit area q_f at the interface due to friction can be expressed as

$$\begin{aligned} q_f &= \mu p_m U && \text{for uniform contact pressure} \\ q_f &= \mu p_m U \frac{3}{2}\sqrt{1-\frac{x^2}{a^2}-\frac{y^2}{b^2}} && \text{for Hertzian contact pressure} \end{aligned} \tag{2.1}$$

where p_m is the average contact pressure over the contact area, U is the velocity of Body 2, a is the contact radius, and μ is the coefficient of friction. The first relation in Eq. (2.1) is quite simple, but might, nevertheless, be representative of a case where the interface has been run-in. The latter relation in Eq. (2.1) supposes that the contact is elastic in nature and that the presence of frictional shear stress has no impact on the normal contact stress distribution. Further, we ignore here any potential effects of thermal expansion. Let q_1 and q_2 be the heat flow rates per unit area into Bodies 1 and 2, respectively, and $q(x,y)$ be their sum such that:

$$q(x,y) = q_1(x,y) + q_2(x,y) \tag{2.2}$$

Additionally let q_{1f} and q_{2f} be the heat flow rates per unit area into Bodies 1 and 2, respectively, due to frictional heat generation, and q' be the heat flow rate per unit area from Body 1 into Body 2 due to an initial difference in bulk temperatures between the bodies. Then

$$\begin{aligned} q_1(x,y) &= q_{1f}(x,y) - q'(x,y) \\ q_2(x,y) &= q_{2f}(x,y) + q'(x,y) \end{aligned} \tag{2.3}$$

Note that $q' > 0$ when Body 1 is initially at a higher temperature than Body 2 (i.e., when $T_{1i} > T_{2i}$). Also note that $q_1 + q_2 = q_{1f} + q_{2f} = q_f = q$.

It is clear from Figure 2.1 that Body 1 sees a stationary heat source, while the Body 2 sees a moving heat source. The temperature distribution at the surfaces of both the bodies can then be expressed as [46]

$$T_1(x,y) = \frac{1}{2\pi K_1}\iint \frac{q_1(x',y')}{\sqrt{(x-x')^2+(y-y')^2}}dx'dy' + T_{1i} \tag{2.4}$$

$$T_2(x,y) = \frac{1}{2\pi K_2}\iint q_2(x',y')\frac{\exp\left\{-\frac{U}{2\alpha_2}\left(\sqrt{(x-x')^2+(y-y')^2}-(x-x')\right)\right\}}{\sqrt{(x-x')^2+(y-y')^2}}dx'dy' + T_{2i} \tag{2.5}$$

Now let the heat partition factor, $\sigma(x,y)$, between the two bodies be defined as the ratio of the heat transfer into the moving body (Body 2) at *(x,y)* to the total heat generated at *(x,y)*, i.e.

$$\sigma(x,y) = \frac{q_2(x,y)}{q(x,y)} \tag{2.6}$$

Now let

$$\begin{aligned} &q_o = \mu p_m U \\ &f(x',y') = 1 \qquad \text{for uniform pressure} \\ &f(x',y') = \frac{3}{2}\sqrt{1-\frac{x'^2}{a^2}-\frac{y'^2}{a^2}} \qquad \text{for Hertzian pressure} \end{aligned} \tag{2.7}$$

Then, using Eq. (2.7), Eq. (2.1) can be expressed as

$$q(x',y') = q_o f(x',y') \tag{2.8}$$

Expressing the above equations in terms of the heat partition function, we obtain

$$T_1(x,y) = \frac{q_o}{2\pi K_1}\iint \frac{\left(1-\sigma(x',y')\right)f(x',y')}{\sqrt{(x-x')^2+(y-y')^2}}dx'dy' + T_{1i} \tag{2.9}$$

$$T_2(x,y)=\frac{q_o}{2\pi K_2}\iint\sigma(x',y')f(x',y')\frac{\exp\left\{-\frac{U}{2\alpha_2}\left(\sqrt{(x-x')^2+(y-y')^2}-(x-x')\right)\right\}}{\sqrt{(x-x')^2+(y-y')^2}}dx'dy'+T_{2i} \tag{2.10}$$

We now introduce dimensionless variables according to

$$\begin{aligned}
&X=\frac{x}{a} \qquad Y=\frac{y}{a} \qquad \xi=\frac{x'}{a} \qquad \eta=\frac{y'}{a}\\
&\mathrm{Pe}=\frac{Ua}{2\alpha_2} \qquad K=\frac{K_2}{K_1}\\
&\Theta_1(X,Y)=T_1(x,y)\frac{2\pi K_2}{q_o a} \qquad \Theta_2(X,Y)=T_2(x,y)\frac{2\pi K_2}{q_o a}\\
&\Psi_1=T_{1i}\frac{2\pi K_2}{q_o a} \qquad \Psi_2=T_{2i}\frac{2\pi K_2}{q_o a}
\end{aligned} \tag{2.11}$$

Thus, the non-dimensional form of Eqs. (2.9) and (2.10) are

$$\Theta_1(X,Y)=K\iint\frac{(1-\sigma(\xi,\eta))f(\xi,\eta)}{\sqrt{(X-\xi)^2+(Y-\eta)^2}}d\xi d\eta+\Psi_1 \tag{2.12}$$

$$\Theta_2(X,Y)=\iint\sigma(\xi,\eta)f(\xi,\eta)\frac{\exp\left\{-\mathrm{Pe}\left(\sqrt{(X-\xi)^2+(Y-\eta)^2}-(X-\xi)\right)\right\}}{\sqrt{(X-\xi)^2+(Y-\eta)^2}}d\xi d\eta+\Psi_2 \tag{2.13}$$

Equations (2.12) and (2.13) have singularity of the first kind which can be removed by a change of Cartesian variables (ξ,η) to polar coordinates (s,ϕ), centered at (X,Y) (e.g., [47]). For convenience we also express (X, Y) in terms of polar coordinates (R, θ), whereby $X=R\cos\theta$, $Y=R\sin\theta$ and $R=\sqrt{X^2+Y^2}$. Figure 2.2 provides a

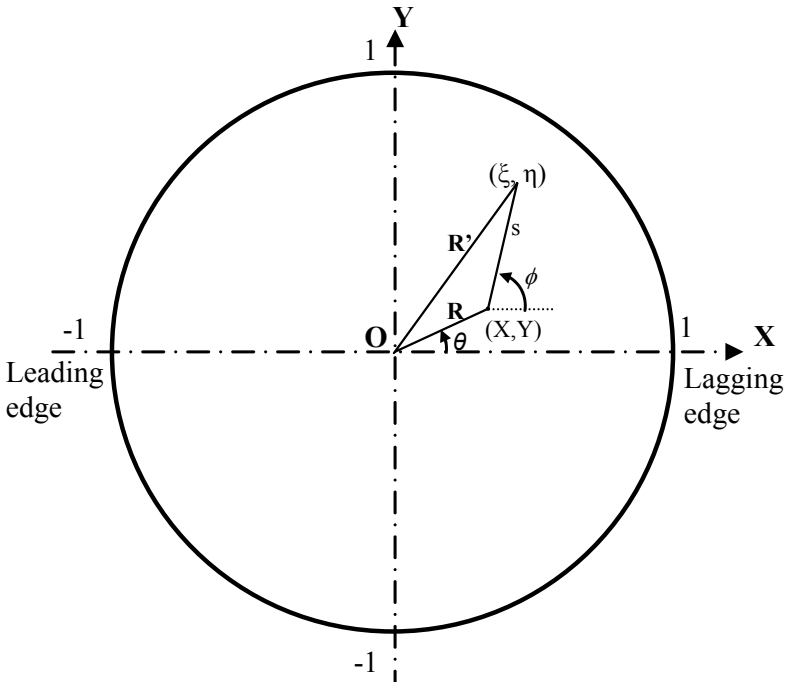

Figure 2.2 Graphical definition of new polar coordinate system variables (s, ϕ) in terms of coordinates (ξ, η) and (X, Y)

graphical representation of the new coordinate system. From Figure 2.2 we have the following relations:

$$\begin{aligned} s &= \sqrt{(X-\xi)^2 + (Y-\eta)^2} \\ s\cos\phi &= \xi - X \\ s\sin\phi &= \eta - Y \\ d\xi d\eta &= sdsd\phi \end{aligned} \tag{2.14}$$

Additionally, we can write

$$\begin{aligned} f(s,\phi) &= 1 && \text{for uniform contact pressure} \\ f(s,\phi) &= 1.5\sqrt{1-(R\cos\theta + s\cos\phi)^2 - (R\sin\theta + s\sin\phi)^2} && \text{for Hertzian contact pressure} \end{aligned} \tag{2.15}$$

The limits of integration are found by noting that, for a fixed ϕ, s varies from 0 to a value corresponding to reaching the edge of the unit circle, at which point R'=1. Letting s_b denote the boundary value of s for the given ϕ, we have from the Law of Cosines,

$$s_b^2 + R^2 + 2Rs_b \cos(\phi - \theta) = 1 \tag{2.16}$$

This gives,

$$s_b = -R\cos(\phi - \theta) + \sqrt{1 - R^2 \sin^2(\phi - \theta)} \tag{2.17}$$

Note that only the positive root is admissible because s_b must be positive, as it represents a radial distance. Now ϕ ranges from 0 to 2π for all the interior points *(X,Y)*. In the special case of R=1 (i.e., when *(X,Y)* is on the boundary of the circle), then ϕ ranges from $\theta + \pi/2$ to $\theta + 3\pi/2$ and Eq. (2.17) simplifies to

$$s_b = -2\cos(\phi - \theta) \tag{2.18}$$

After making the change of variables, Eqs. (2.12) and (2.13) can be rewritten as:

$$\Theta_1(R,\theta) = K \int_{\phi=0}^{2\pi} \int_{s=0}^{s_b(R,\theta,\phi)} \left(1 - \sigma(s,\phi)\right) f(s,\phi)\, ds d\phi + \Psi_1 \tag{2.19}$$

$$\Theta_2(R,\theta) = \int_{\phi=0}^{2\pi} \int_{s=0}^{s_b(R,\theta,\phi)} \sigma(s,\phi) f(s,\phi) \exp\left\{-\mathrm{Pe}\, s\left(1 + \cos\phi\right)\right\} ds d\phi + \Psi_2 \tag{2.20}$$

with aforementioned modifications necessary in the limits on ϕ for points on the boundary.

Applying the condition of continuity of temperature across the interface at each point within the contact region, we set $\Theta_1(R,\theta) = \Theta_2(R,\theta)$, which, after rearrangement, leads to

$$\Psi_1 - \Psi_2 + K\int_{\phi=0}^{2\pi}\int_{s=0}^{s_b(R,\theta,\phi)} f(s,\phi)\,ds d\phi = \int_{\phi=0}^{2\pi}\int_{s=0}^{s_b(R,\theta,\phi)} f(s,\phi)\sigma(s,\phi)\left[K + \exp\left\{-\mathrm{Pe}\, s\left(1+\cos\phi\right)\right\}\right] ds d\phi$$

(2.21)

The above equation is difficult to solve as the unknown heat partition function appears inside the integral on the RHS and depends on the variables of integration. Here we employ a regression technique to provide an estimate of the true heat partition function. In that regard, the actual heat partition function can be expressed as

$$\sigma(\xi,\eta) = \sigma_e(\xi,\eta) + \sigma_\varepsilon(\xi,\eta) \tag{2.22}$$

where σ_e is the estimated heat partition function and σ_ε is the error in the estimation. We represent the estimated heat partition function as a polynomial expansion (in the untransformed coordinates) according to the following relation

$$\sigma_e(\xi,\eta) = \sum_{p=0}^{N}\sum_{q=0}^{p} A_{pq}\xi^{p-q}\eta^q \tag{2.23}$$

where q and $p-q$ are exponents and A_{pq} are coefficients to be determined, corresponding to the given values of p and q, and N is the order of the expansion (i.e., the largest sum of the exponents of ξ and η for any term in the expansion). Since the relative velocity is along the X-axis (or ξ-axis) only, the heat partition function will be symmetric about this axis and hence odd powers of η can be ignored; i.e., $A_{pq} = 0$ for odd q. With respect to the transformed coordinates, the estimated heat partition function can be represented as

$$\sigma_e(s,\phi) = \sum_{p=0}^{N}\sum_{q=0}^{p} A_{pq}\left(R\cos\theta + s\cos\phi\right)^{p-q}\left(R\sin\theta + s\sin\phi\right)^q \tag{2.24}$$

Substituting Eq. (2.24) in Eq. (2.22), we get

$$\sigma(\xi,\eta)=\sum_{p=0}^{N}\sum_{q=0}^{p}A_{pq}\left(R\cos\theta+s\cos\phi\right)^{p-q}\left(R\sin\theta+s\sin\phi\right)^{q}+\sigma_{\varepsilon}(\xi,\eta) \qquad (2.25)$$

This form of the heat partition function, when substituted in Eq. (2.21), gives

$$\begin{aligned}&\Delta\Psi+K\int_{\phi=0}^{2\pi}\int_{s=0}^{s_b(R,\theta,\phi)}f(s,\phi)\,ds\,d\phi=\\&\sum_{p=0}^{N}\sum_{q=0}^{p}A_{pq}\int_{\phi=0}^{2\pi}\int_{s=0}^{s_b(R,\theta,\phi)}f(s,\phi)\left(R\cos\theta+s\cos\phi\right)^{p-q}\left(R\sin\theta+s\sin\phi\right)^{q}\left[K+\exp\left\{-\mathrm{Pe}\,s\left(1+\cos\phi\right)\right\}\right]ds\,d\phi\\&+\int_{\phi=0}^{2\pi}\int_{s=0}^{s_b(R,\theta,\phi)}\sigma_{\varepsilon}(s,\phi)\,f(s,\phi)\left[K+\exp\left\{-\mathrm{Pe}\,s\left(1+\cos\phi\right)\right\}\right]ds\,d\phi\end{aligned} \qquad (2.26)$$

where $\Delta\Psi=\Psi_1-\Psi_2$

The above equation can be expressed compactly as

$$F_{ij}=\sum_{p=0}^{N}\sum_{q=0}^{p}A_{pq}G_{ijpq}+\varepsilon_{ij} \qquad (2.27)$$

where

$$\begin{aligned}F_{ij}&\equiv\Delta\Psi+K\int_{\phi=0}^{2\pi}\int_{s=0}^{s_b(R_i,\theta_j,\phi)}f(s,\phi)\,ds\,d\phi\\G_{ijpq}&\equiv\int_{\phi=0}^{2\pi}\int_{s=0}^{s_b(R_i,\theta_j,\phi)}f(s,\phi)\left(R_i\cos\theta_j+s\cos\phi\right)^{p-q}\left(R_i\sin\theta_j+s\sin\phi\right)^{q}\left[K+\exp\left\{-\mathrm{Pe}\,s\left(1+\cos\phi\right)\right\}\right]ds\,d\phi\\\varepsilon_{ij}&\equiv\int_{\phi=0}^{2\pi}\int_{s=0}^{s_b(R_i,\theta_j,\phi)}\sigma_{\varepsilon}(s,\phi)\,f(s,\phi)\left[K+\exp\left\{-\mathrm{Pe}\,s\left(1+\cos\phi\right)\right\}\right]ds\,d\phi\end{aligned} \qquad (2.28)$$

and where the subscripts *i*, *j* represent the grid point location defined by *(R, θ)*. In the above equation, the elements G_{ijpq} are computed directly by numerical integration, while the coefficients A_{pq} are obtained via a regression process; i.e., they are chosen to minimize, in the least squares sense, the error term ε_{ij}. To formulate the regression problem, we first rearrange Eq. (26) according to

$$\varepsilon_{ij} = F_{ij} - \sum_{p=0}^{N}\sum_{q=0}^{p} A_{pq} G_{ijpq} \tag{2.29}$$

Then we re-label the nodal indices (*i, j*) based on the following relations:

$$k = (i-1) j_{\max} + j \qquad 1 \le i \le i_{\max},\ \ 1 \le j \le j_{\max} \tag{2.30}$$

where $j_{\max}$ is the number of nodal points in the coordinate θ and $i_{\max}$ is the number of nodal points in the coordinate R. In terms of the new indices, we have

$$\varepsilon_k = F_k - \sum_{p=0}^{N}\sum_{q=0}^{p} A_{pq} G_{kpq} \tag{2.31}$$

The total number of terms (n) in the polynomial expansion of the heat partition function can be found from the expression $n = \frac{1}{2}(N+1)(N+2)$. (Note that, due to y-axis symmetry, some of these n terms have coefficients equaling zero). For simplicity, we shall replace the double subscripts pq of the regression coefficients by single subscript v, where $v = \frac{1}{2} p(p+1) + q + 1$. Further simplification can be done by introducing the following definition

$$\hat{F}_k \equiv \sum_{v=1}^{n} A_v G_{kv} \tag{2.32}$$

so that

$$\varepsilon_k = F_k - \hat{F}_k \tag{2.33}$$

The quantity $\hat{F}_k$ can be thought of as the estimate of F_k. Then the task of regression is to find the coefficients A_{pq} to minimize the sum-square error E_2 defined by

$$E_2 = \sum_{k=1}^{k_{\max}} (\varepsilon_k)^2 = \sum_{k=1}^{k_{\max}} \left(F_k - \hat{F}_k\right)^2 = \sum_{k=1}^{k_{\max}} \left(F_k - \sum_{v=1}^{v_{\max}} A_v G_{kv}\right)^2 \tag{2.34}$$

where $k_{\max}$ is the total number grid points. By differentiating the error E_2 with respect to an arbitrary coefficient A_s and setting the result to zero, we obtain

$$0 = (-2)\left[\sum_{k=1}^{k_{\max}} F_k G_{ks} - \sum_{k=1}^{k_{\max}}\sum_{\nu=1}^{\nu_{\max}} G_{ks} G_{k\nu} A_\nu\right] \tag{2.35}$$

which can be simplified to

$$\sum_{k=1}^{k_{\max}}\sum_{\nu=1}^{\nu_{\max}} G_{ks} G_{k\nu} A_\nu = \sum_{k=1}^{k_{\max}} F_k G_{ks} \tag{2.36}$$

In direct (matrix) notation, we can express Eq. (2.35) succinctly as

$$\mathbf{G^T G A = G^T F} \tag{2.37}$$

where the definitions of **G**, **A** and **F** are clear through inspection of Eq. (2.35). Then the coefficient matrix, **A** can be solved for by matrix inversion, giving

$$\mathbf{A} = \left(\mathbf{G^T G}\right)^{-1} \mathbf{G^T F} \tag{2.38}$$

We can measure the overall fit of the regression by a normalized least square error E^*, defined as

$$E^* \equiv \sqrt{\frac{E_2}{\mathbf{F^T F}}} = \sqrt{\frac{\boldsymbol{\varepsilon^T \varepsilon}}{\mathbf{F^T F}}} \tag{2.39}$$

The regression coefficients obtained from Eq. (2.38), may be substituted into Eq. (2.23), to give the estimate of the heat partition function.

To illustrate the calculation of temperature, we first partition the matrix **G**. In subscript notation, with reference to Eq. (2.27) we write $G_{ijpq} = G_{1ijpq} + G_{2ijpq}$, where

$$G_{1ijpq} \equiv K \int_{\phi=0}^{2\pi} \int_{s=0}^{s_b(R_i,\theta_j,\phi)} f(s,\phi)\left(R_i\cos\theta_j + s\cos\phi\right)^{p-q}\left(R_i\sin\theta_j + s\sin\phi\right)^{q} ds d\phi$$

$$G_{2ijpq} \equiv \int_{\phi=0}^{2\pi} \int_{s=0}^{s_b(R_i,\theta_j,\phi)} f(s,\phi)\left(R_i\cos\theta_j + s\cos\phi\right)^{p-q}\left(R_i\sin\theta_j + s\sin\phi\right)^{q} \exp\left\{-\mathrm{Pe}\, s\left(1+\cos\phi\right)\right\} ds d\phi$$

(2.40)

In matrix notation, the partition is expressed as $\mathbf{G} = \mathbf{G_1} + \mathbf{G_2}$. Now from inspection of Eqs. (2.19) and (2.20) along with the definitions in Eqs. (2.27) and (2.38) we can write the regression-based estimates for the temperature as

$$\begin{aligned} \boldsymbol{\Theta}_\mathbf{1} &= \mathbf{F} - \mathbf{G_1 A} + \Psi_2 \\ \boldsymbol{\Theta}_\mathbf{2} &= \mathbf{G_2 A} + \Psi_2 \end{aligned} \tag{2.41}$$

where $\boldsymbol{\Theta}_\mathbf{1}$ and $\boldsymbol{\Theta}_\mathbf{2}$ are vectors whose elements are the calculated nodal temperatures for Bodies 1 and 2, respectively. Ideally, $\boldsymbol{\Theta}_\mathbf{1} = \boldsymbol{\Theta}_\mathbf{2}$ but, in practice, there will be some finite temperature mismatch. In order to assess the degree of temperature matching in the interface resulting from the regression process, we introduce a parameter we call the "local temperature matching error," which is defined as the absolute value of the difference in nodal temperatures between the two bodies, normalized by the mean of the global average interfacial temperature rises of both bodies relative to Ψ_2. Mathematically, this definition is expressed as

$$\Delta\Theta^*\left(R_i,\theta_j\right) = \frac{\left|\Theta_1\left(R_i,\theta_j\right) - \Theta_2\left(R_i,\theta_j\right)\right|}{1/2\left|\left(\bar{\Theta}_1 + \bar{\Theta}_2 - 2\Psi_2\right)\right|} \tag{2.42}$$

where

$$\bar{\Theta}_1 = \frac{1}{i_{\max} j_{\max}} \sum_{i=1}^{i_{\max}} \sum_{j=1}^{j_{\max}} \Theta_1\left(R_i,\theta_j\right) \qquad \bar{\Theta}_2 = \frac{1}{i_{\max} j_{\max}} \sum_{i=1}^{i_{\max}} \sum_{j=1}^{j_{\max}} \Theta_2\left(R_i,\theta_j\right) \tag{2.43}$$

In results to be presented below, the local temperature matching error $\Delta\Theta^*$ has been averaged over three sets of nodes: (1) the set of all nodes within the contact region, (2) the set of all nodes in the interior, and (3) the set of all nodes along the boundary of the contact region. These averages are given the symbols to $\Delta\overline{\Theta}^*_{all}$, $\Delta\overline{\Theta}^*_{interior}$, and $\Delta\overline{\Theta}^*_{boundary}$, respectively, and each is referred to as the "temperature matching error" for the appropriate set of nodes.

The computational analysis is performed on a circular domain that is discretized using 1887 nodes: 51 equally-spaced points along the radial axis and 37 equally-spaced points along the meridian axis (i.e., circumferential direction). In regards to the calculation of vectors **F** and **G**, as suggested by Eq. (2.28), the integration along the *s*-axis, where the limits of the integration depend on the value of ϕ, was carried out using a Romberg integration scheme using 8^{th}-level extrapolation and a convergence criterion set at 10^{-10}. Romberg integration provides faster convergence with smaller truncation error when compared to Simpson's 1/3 rule [48, 49]. The estimated error in the computed value of the integrals is 25%, 2% and 0.5%, respectively, when the convergence criterion is 10^{-5}, 10^{-7} and 10^{-8}, based on comparison with results for when the convergence criterion set at 10^{-10}. The integration along the meridian axis (ϕ-axis) was performed using Simpson's 1/3 rule using 301 and 451 integration points for the cases of uniform pressure and Hertzian pressure distribution respectively, yielding estimated convergence errors of less than 0.05%. The stringent convergence criterion used for the integrals ensures that the error in the computed values of temperature rise is dominated by that due to the regression process.

In looking at Eq. (2.28), it is observed that except for the scaling factor K, the expression for **F** depends only on the shape of the frictional heating distribution (e.g., uniform or hemispherical). Additionally, only part of the expression for **G** (i.e., $\mathbf{G_2}$) is seen to depend on the Peclet no., and the role of K in the other part (i.e., $\mathbf{G_1}$) is that of a simple scaling factor. Thus when varying the Peclet no. and thermal conductivity ratio (K), one need only repeat the integral calculations associated with $\mathbf{G_2}$. In this study, the computations were performed with MATLAB® R2007a, on an Intel Xeon 2.6 GHz processor with 2GB of RAM. The computation time for computing the integrals **F** and $\mathbf{G_1}$ was about 2.3 hours and 5.7 hours for the cases of uniform contact pressure and Hertzian contact pressure respectively. For each new Peclet no. considered, the computational time was about 2.6 hours for the case of uniform contact pressure, and about 5.5 hours for the case of Hertzian contact pressure. On the other hand, performing the matrix inversion required to obtain the regression coefficient matrix (**A**) via Eq. (2.38) involved, by comparison, almost negligible computational time. Once the regression coefficient matrix had been determined, the temperature estimates, $\mathbf{\Theta_1}$ and $\mathbf{\Theta_2}$ were found by simple matrix multiplication, in accordance with Eq. (2.41).

2.3.1 Scale of application of model

The Equation (2.1) assumes a constant coefficient of friction μ and thus applies to a macro-scale contact. If one were to apply the above presented methodology to a single asperity contact where the friction heat generation is of the form:

$$q_o = \tau U \tag{2.44}$$

where τ is the shear strength of the asperity contact and U is the sliding velocity. In this case the distribution of the frictional heat will take the form of distribution of shear stress over the asperity contact. In the simplest case the distribution can be assumed to be uniform and Eqs. (2.9) and (2.10) are still applicable with appropriate representation for $f(x',y')$.

2.4 Analysis results

In the first part of this section, we discuss the effect of polynomial order on the achievement of pointwise temperature matching, while, in the second part, some representative results are analyzed for the case when both the bodies have same initial temperatures. In the third part more general case of temperature rise at the interface of two sliding bodies at different initial temperatures is presented. For convenience, all results to be presented below correspond to cases for which the two bodies have the same thermal conductivity.

2.4.1 Effect of polynomial order

Figure 2.3 illustrates the effect of polynomial order on both the temperature matching error and the normalized least square error E^* for $K = 1$ and Pe = 5 in the case of a uniform contact pressure. As seen in Figure 2.3, the three temperature matching errors and the normalized least squares error decrease monotonically as the order of the polynomial is increased from 0 to 6. The temperature matching error considering all grid points ($\Delta\overline{\Theta}^*_{all}$) decreases from 18% for a 0^{th} order polynomial (i.e., a single heat partition value) to 1.2% for the 6^{th} order polynomial. The corresponding error for the interior

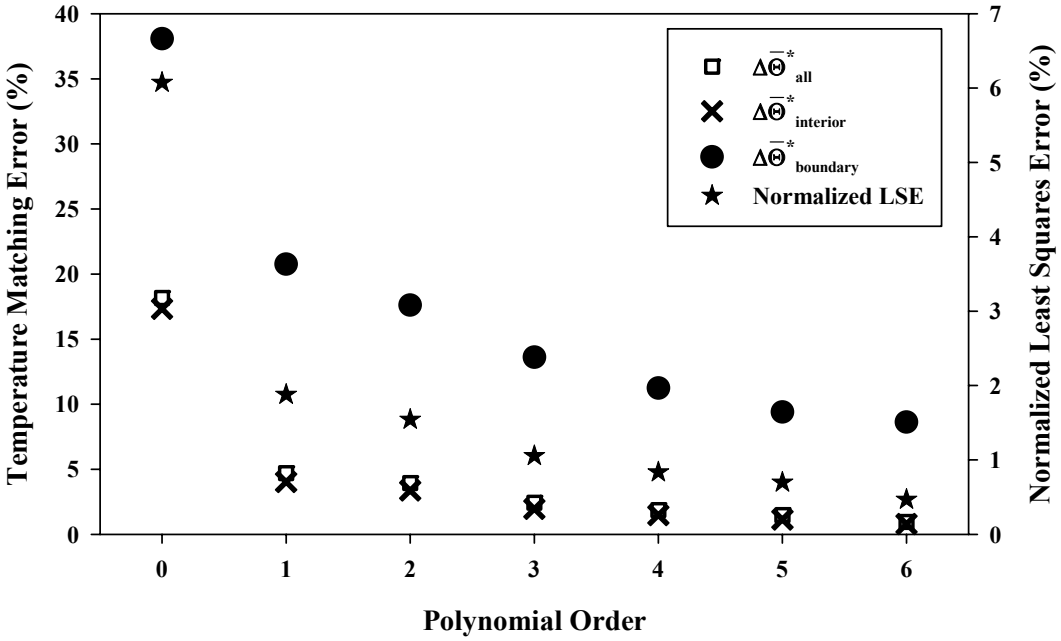

Figure 2.3 **Effect of polynomial order on the temperature matching errors and the normalized least squares error for the case of uniform contact pressure**

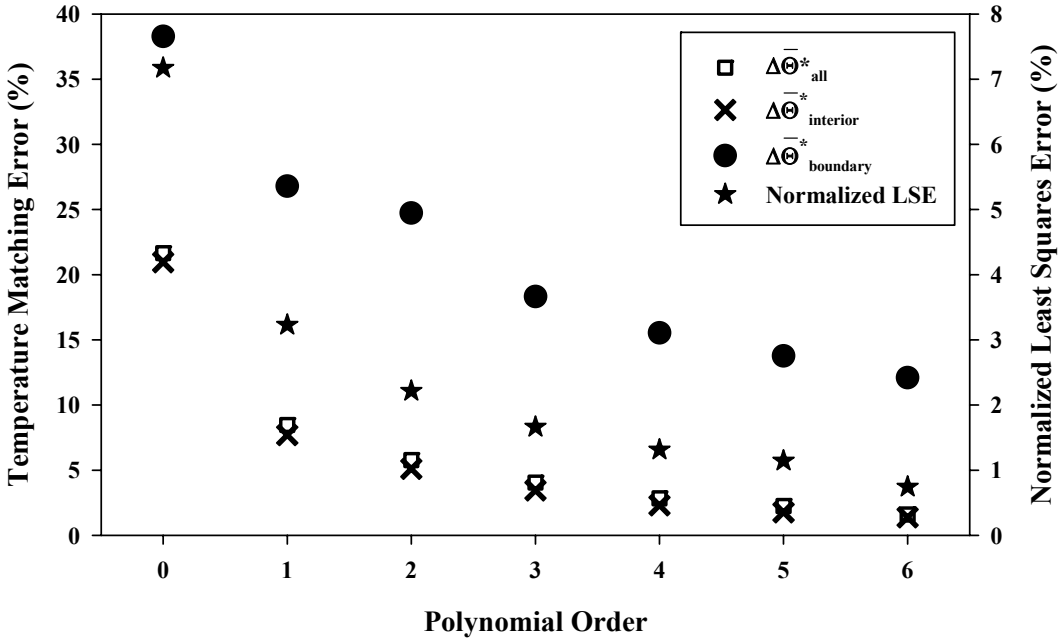

Figure 2.4 **Effect of polynomial order on the temperature matching errors and the normalized least squares error for the case of Hertzian contact pressure**

points only ($\Delta\bar{\Theta}^{*}_{interior}$) is found to be slightly lower than $\Delta\bar{\Theta}^{*}_{all}$ at all values of polynomial order. The temperature matching error calculated at the boundary of the contact ($\Delta\bar{\Theta}^{*}_{boundary}$) decreases from a value of 38%, for 0^{th} order polynomial, to less than 8% for 6^{th} order polynomial. It is not surprising that the largest errors occur at the boundary of contact, because it is here where the largest temperature gradients are expected. Figure 2.3 also shows that the normalized least squares error (Eq. (2.39)) decreases from 6.1 % to 0.5 % as the polynomial order is increased from 0 to 6. Figure 2.4, which corresponds to the case of Hertzian contact pressure, shows trends very similar to those of Figure 2.3, but with slightly higher error levels throughout.

The foregoing results indicate that the condition of temperature matching throughout the domain is satisfied with increasing accuracy as the order of the polynomial is increased. The 6^{th}-order polynomial fit for the heat partition function results in slightly greater mismatch for the case of Hertzian contact pressure as compared to the case of uniform contact pressure. Nevertheless, with the 6^{th}-order expansion, the temperature matching error in the case of Hertzian contact pressure (Figure 2.4) is less than 12% at the boundary of the contact region and only about 1.3% within the interior. Although a polynomial expansion of higher order than 6 would yield even greater accuracy, its implementation would also entail more computational cost.

2.4.2 Three dimensional heat partition and temperature distributions

Figure 2.5 shows the heat partition function in the interface for K = 1 and Pe = 0.5, for the case of uniform contact pressure and both bodies at the same initial bulk temperatures ($\Delta\Psi = 0$). As observed, the heat partition function decreases from a

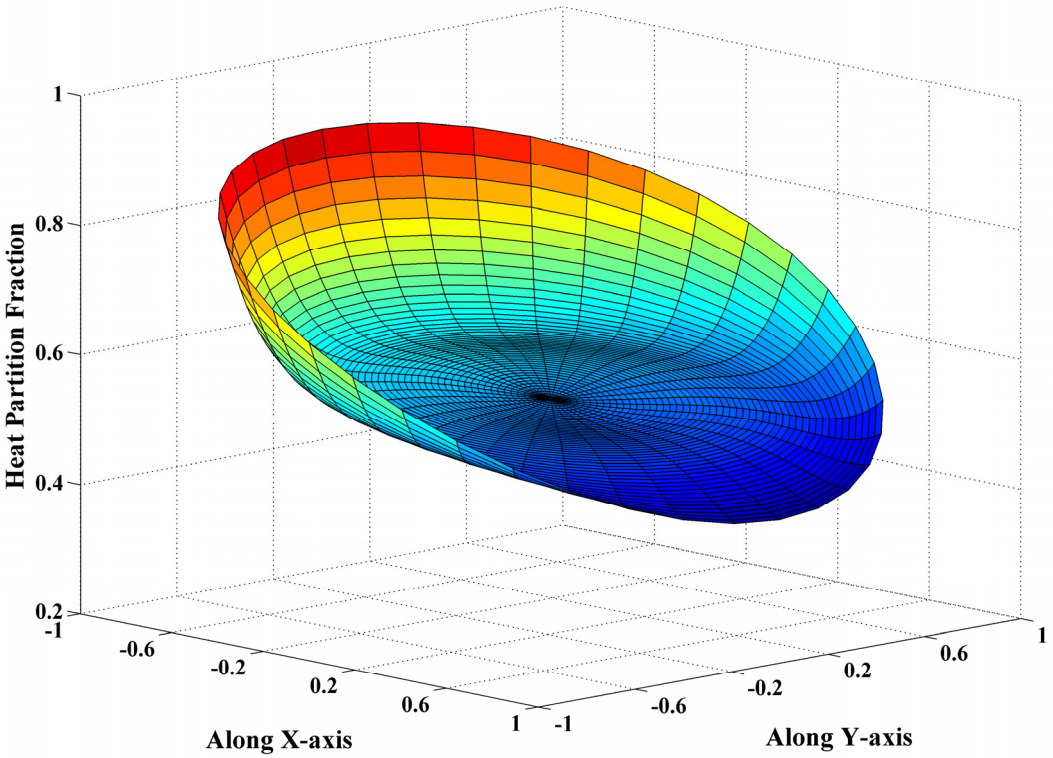

Figure 2.5 Heat partition function for the case of uniform contact pressure with K =1 and Pe = 0.5

maximum of 0.9 at the leading edge of contact to a minimum of 0.42 at the trailing edge of contact. Recalling the definition of heat partition as expressed in Eq. (2.6), a higher value of heat partition means that a greater proportion of heat flows into the stationary body. It is not surprising that the value of heat partition would be highest at the leading edge of contact because, at this location, relatively cool regions of the lower surface enter the contact zone and must be heated quickly to match the temperature of the upper surface, which is always in the heated zone.

Figure 2.6 show the temperature rises for the upper surface (a) and lower surface (b) within the contact zone for the contact conditions of Figure 2.5. As observed, the two

calculated temperature distributions are virtually indistinguishable and each has a nearly paraboloidal shape with a maximum temperature near the center of the contact region. Not surprisingly, the temperature at the trailing edge of the contact is higher than at the leading edge of the contact.

Figure 2.7 shows the heat partition distribution for the case of a Hertzian contact pressure for K = 1 and Pe = 0.5 and both bodies at the same initial bulk temperatures ($\Delta\Psi = 0$). Here the heat partition function is even more varied than in the case of uniform contact pressure. Perhaps, surprisingly, the value of the heat partition function exceeds unity at the leading edge of contact. This means that, not only does all of the locally dissipated heat go into the lower body, but that additional heat is drawn from the upper body into the lower body. The existence of a heat partition value greater than unity has important implications: Since heat must flow from higher temperature regions to lower temperature regions, it means that wherever $\sigma > 1$, heat is being conducted *into* the interface *from* the upper body. If for some Peclet number, the location of maximum interface temperature has a heat partition factor greater than unity, then the largest temperature rise would necessarily be in the interior of the body, rather than in the interface.

Figure 2.8 shows the temperature distributions corresponding to conditions of Figure 2.7 for the upper body (a) and the lower body (b). While the two temperature distributions are very close, some differences in shape can be seen near the leading edge of contact. The discrepancies between the two temperature distributions represent a limitation in the ability of a 6^{th}-order polynomial expansion to fully capture the variations in the heat partition function.

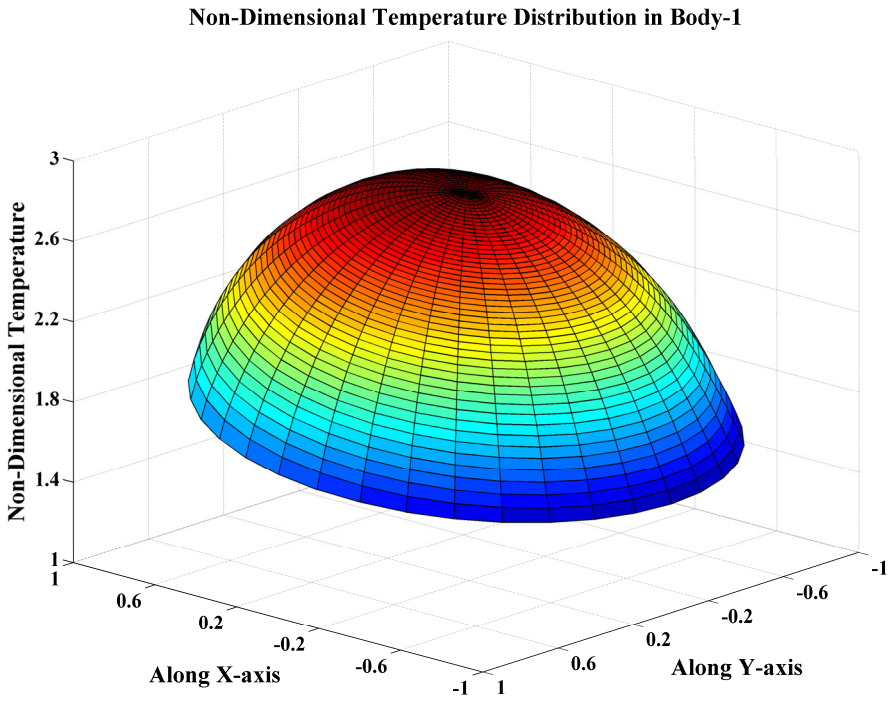

(a)

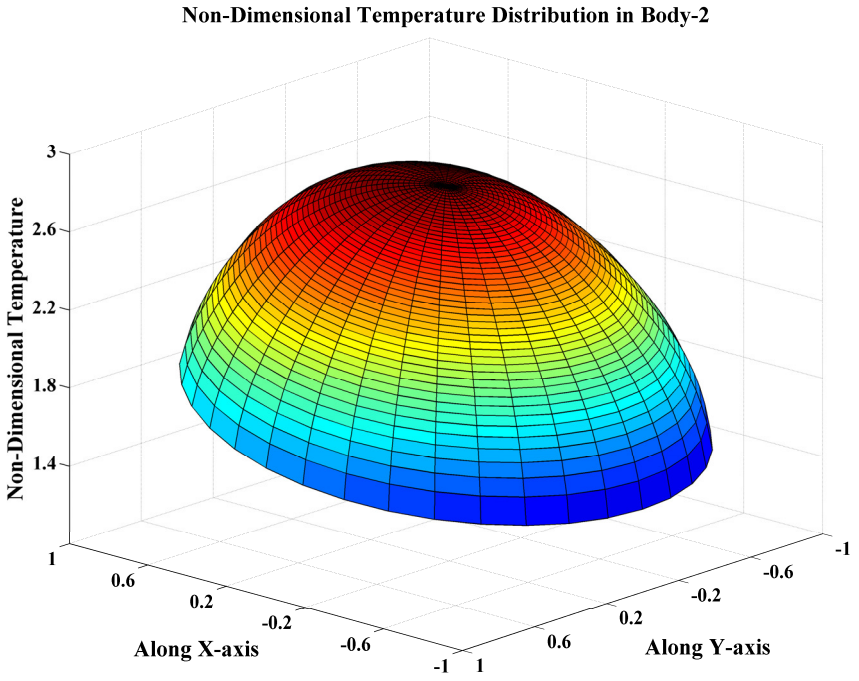

(b)

Figure 2.6 Dimensionless temperature for the case of uniform contact pressure with K =1 and Pe = 0.5: (a) stationary body (Body 1); (b) moving body (Body 2)

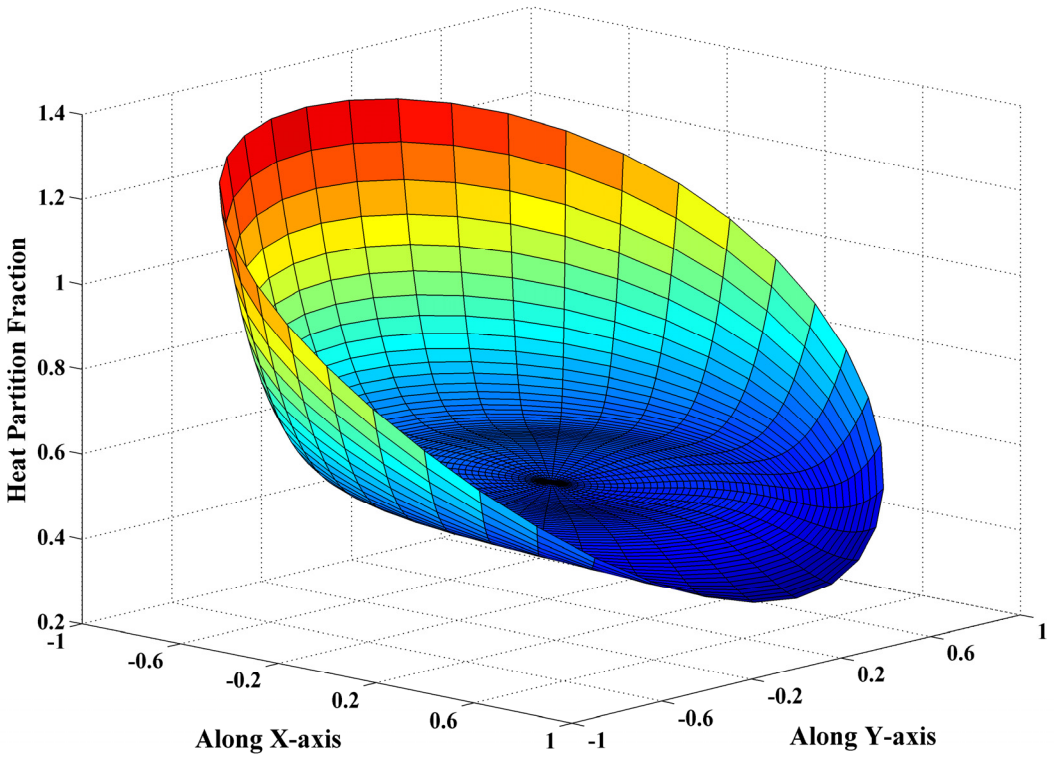

Figure 2.7 Heat partition function for the case of Hertzian contact pressure with K =1 and Pe = 0.5

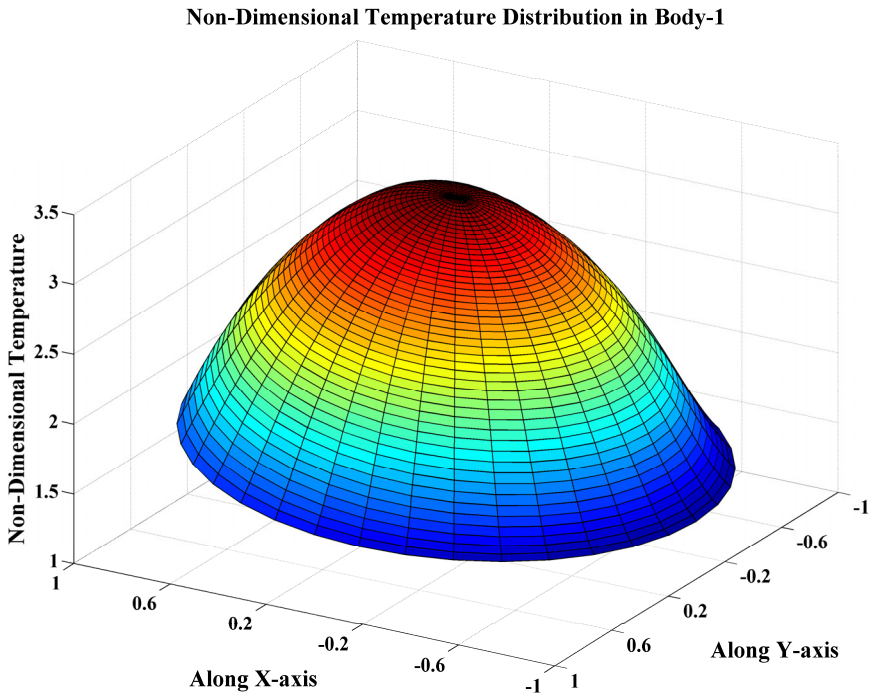

(a)

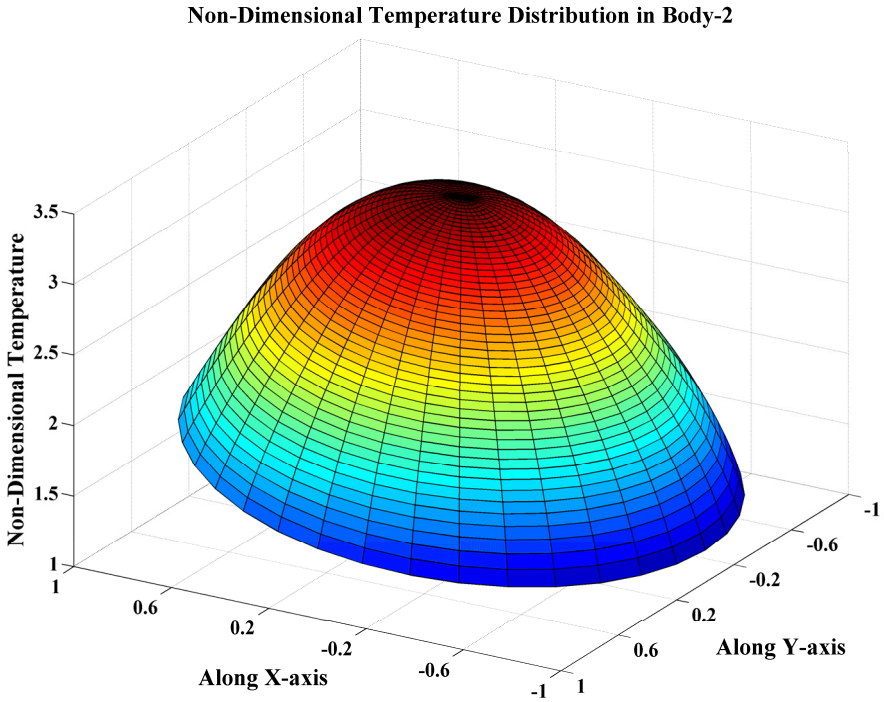

(b)

Figure 2.8 Dimensionless temperature for the case of Hertzian contact pressure with K =1 and Pe = 0.5: (a) stationary body (Body 1); (b) moving body (Body 2)

The role of Peclet no. for the case of uniform contact pressure is illustrated in Figure 2.9. Here the non-dimensional interfacial temperature rise is plotted along the centerline (in the sliding direction), for several values of Pe no., ranging from 0 to 100. For specificity, the interfacial temperature rise at any point is defined to be the average of the two calculated surface temperatures (which are nearly the same). Here the results for Peclet no. = 0 represents the solution at the lower limit of Peclet no., although no frictional heat would be generated at zero Peclet number. As the Peclet number increases, the position of the maximum temperature along the centerline moves towards the trailing edge of the contact. It should be noted that, since the temperature rise is normalized by the mean heating rate (i.e., $q_o = \mu p_m U$), the lower values of non-dimensional temperature rise at higher Peclet no. actually correspond to higher values of dimensional temperature rise.

Figure 2.10 shows results analogous to those of Figure 2.9 for the case of Hertzian contact pressure. As expected from the hemispherical shape of the pressure (and therefore the heating distribution), the peak temperatures in contact region are larger than in the case of uniform contact pressure. Over the full range of Peclet nos. considered, the peak temperature rise in the case of Hertzian contact pressure is 15-20% greater than in the case of uniform pressure.

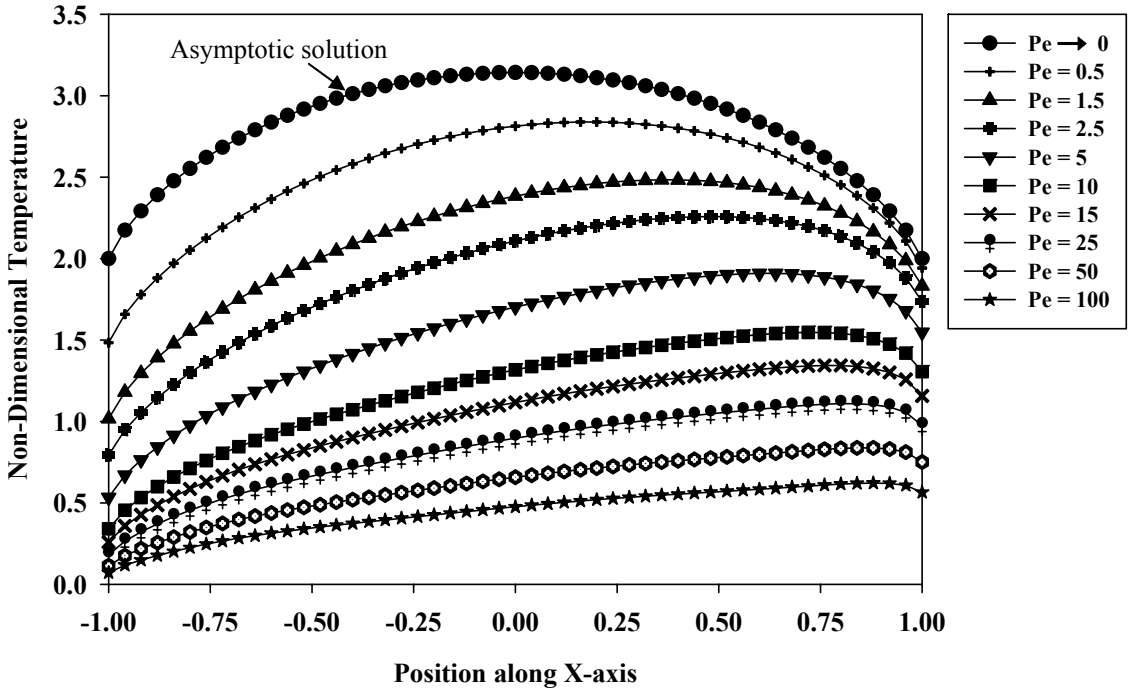

Figure 2.9 Dimensionless centerline temperature for the case of uniform contact pressure with $K = 1$

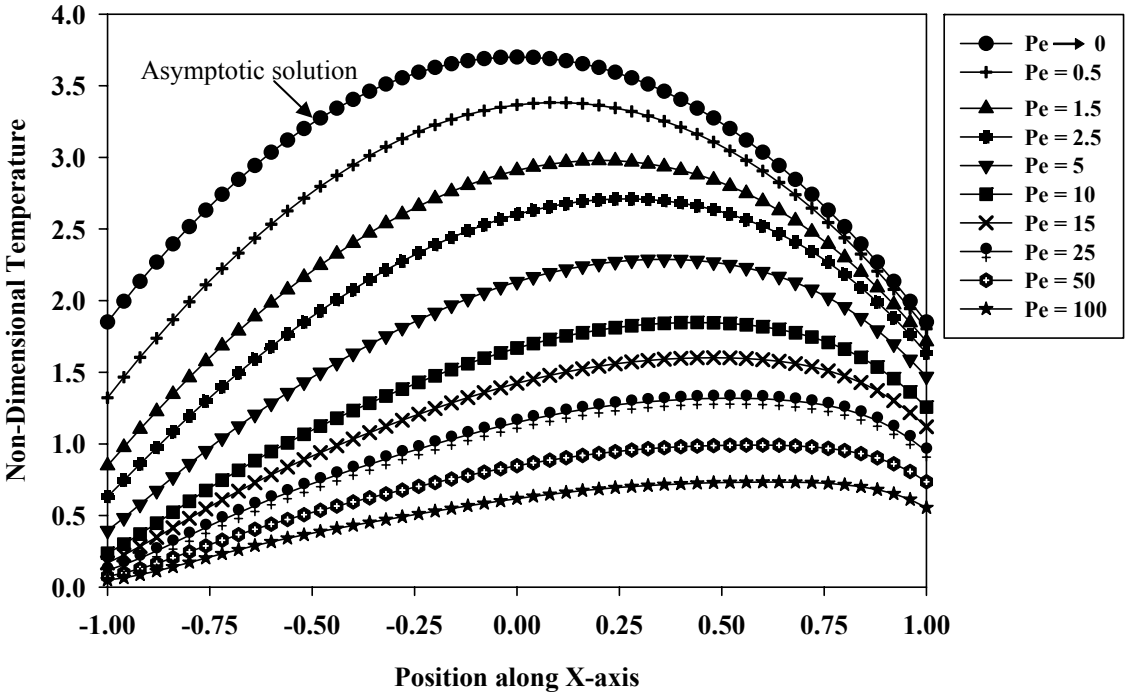

Figure 2.10 Dimensionless centerline temperature for the case of Hertzian pressure with $K = 1$

2.4.3 Global heat partition

The total heat conducted into the lower body (Body 2) normalized by the total heat generated at the interface gives the global heat partition (Σ). Figure 2.11 illustrates the variation in the percentage global heat partition against Peclet no. for both the cases of uniform and Hertzian contact pressure.

$$\Sigma = \frac{Q_2}{Q} = \frac{q_o \iint \sigma(x',y') f(x',y')\, dx'dy'}{q_o \iint f(x',y')\, dx'dy'} \tag{2.45}$$

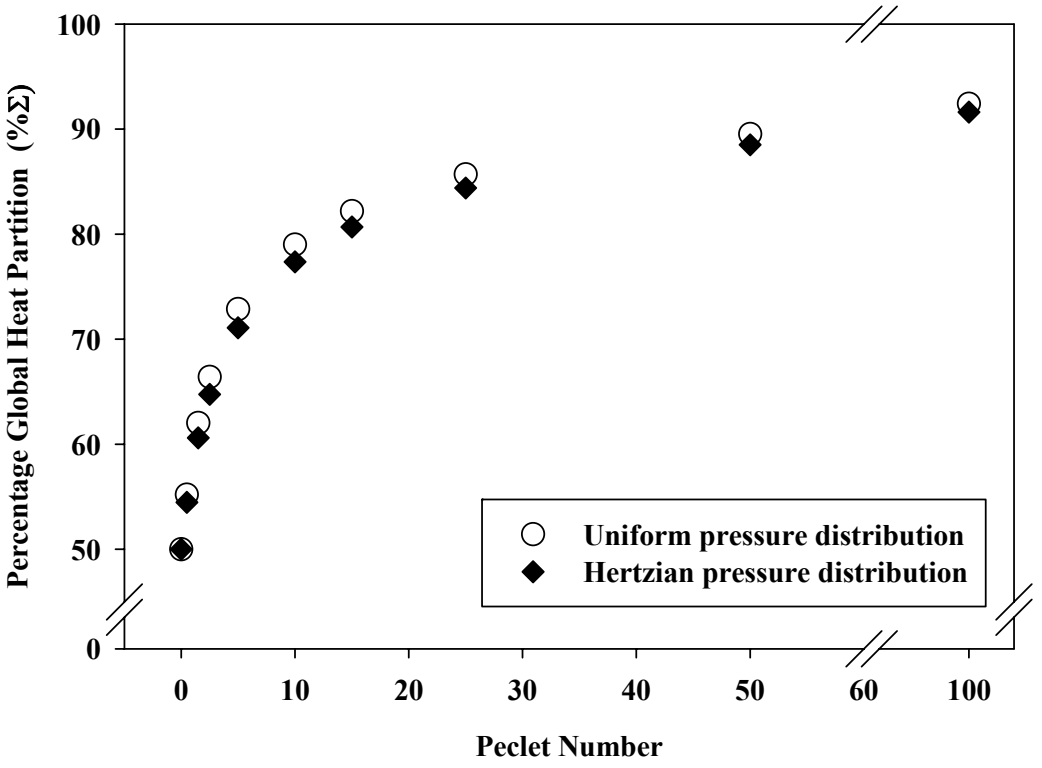

Figure 2.11 Variation in percentage global heat partition with Peclet no

As seen from the plot, for a given Peclet no., there is little difference in the global heat partition for the cases of uniform and Hertzian contact pressure. This suggests that heat partition is a function of sliding velocity, contact geometry and thermal properties of

the interface and is independent of the heat distribution. As the Peclet no. is increased a greater fraction of heat is conducted into Body 2. As the Peclet no. is increased (say via an increased sliding velocity), the contact patch on the Body 2 remains in contact with Body 1 for lesser and lesser time. Hence to maintain the condition of temperature continuity at the interface more and more heat is conducted into Body 2.

2.4.4 Comparison with Blok's and Jaeger's hypotheses

The maximum and the average temperature obtained from the current methodology are now compared with those obtained using Blok's and Jaeger's hypotheses. To apply the hypothesis of Blok, we first assume a constant heat partition value over the entire contact region and then integrate in Eqs. (2.19) and (2.20). For convenience, let us introduce the following definitions:

$$\begin{aligned} I_1(R,\theta) &\equiv \int_{\phi=0}^{2\pi} \int_{s=0}^{s_b(R,\theta,\phi)} f(s,\phi)\, ds d\phi \\ I_2(R,\theta) &\equiv \int_{\phi=0}^{2\pi} \int_{s=0}^{s_b(R,\theta,\phi)} f(s,\phi) \exp\{-\mathrm{Pe}\, s(1+\cos\phi)\} ds d\phi \end{aligned} \tag{2.46}$$

Thus, with the assumption of constant heat partition, estimates of the dimensionless temperature rises for each body can be written as

$$\begin{aligned} \Theta_1(R,\theta)\big|_{\sigma=\text{constant}} &= K(1-\sigma) I_1(R,\theta) \\ \Theta_2(R,\theta)\big|_{\sigma=\text{constant}} &= \sigma I_2(R,\theta) \end{aligned} \tag{2.47}$$

Now applying Blok's hypothesis that the maximum temperatures should match, and solving for the heat partition, we obtain:

$$\sigma_{\text{Block}} = \frac{K \max\left(I_1(R,\theta)\right)}{K \max\left(I_1(R,\theta)\right) + \max\left(I_2(R,\theta)\right)} \tag{2.48}$$

The corresponding temperature rise would then be given by

$$\left(\Theta_{\max}\right)_{\text{Blok}} = K(1-\sigma_{\text{Blok}})\max\left(I_1\left(R,\theta\right)\right) = \sigma_{\text{Blok}}\max\left(I_2\left(R,\theta\right)\right) \tag{2.49}$$

Similarly, applying Jaeger's hypothesis of equating the average temperature rises, one obtains analogous expressions:

$$\sigma_{\text{Jaeger}} = \frac{K\,\text{avg}\left(I_1(R,\theta)\right)}{K\,\text{avg}\left(I_1(R,\theta)\right)+\text{avg}\left(I_2(R,\theta)\right)} \tag{2.50}$$

$$\left(\Theta_{\text{avg}}\right)_{\text{Jaeger}} = K(1-\sigma_{\text{Jaeger}})\,\text{avg}\left(I_1\left(R,\theta\right)\right) = \sigma_{\text{Jaeger}}\,\text{avg}\left(I_2\left(R,\theta\right)\right) \tag{2.51}$$

Figure 2.12 presents the maximum interfacial temperature rise from both the current analysis and from the application of Blok's hypothesis (see Eq. (2.49)) as a function of Peclet no. for $K = 1$ for the cases of uniform contact pressure (a) and Hertzian contact pressure (b). For uniform contact pressure, it is observed that the application of Blok's hypothesis provides excellent agreement with the more rigorous analysis of the current work, the two predictions differing at most by a few percent. For the case with Hertzian contact pressure, on the other hand, Blok's method somewhat over-predicts the maximum interfacial temperature at the larger values of Peclet nos., being about 20% too high when Pe no. > 20.

Figure 2.13 compares predictions of the current analysis to those obtained using Jaeger's hypothesis (see Eq. (2.51)) for cases of uniform contact pressure (a) and Hertzian contact pressure (b). In all cases, the predictions from Jaeger's approach agree quite well with that of the current analysis.

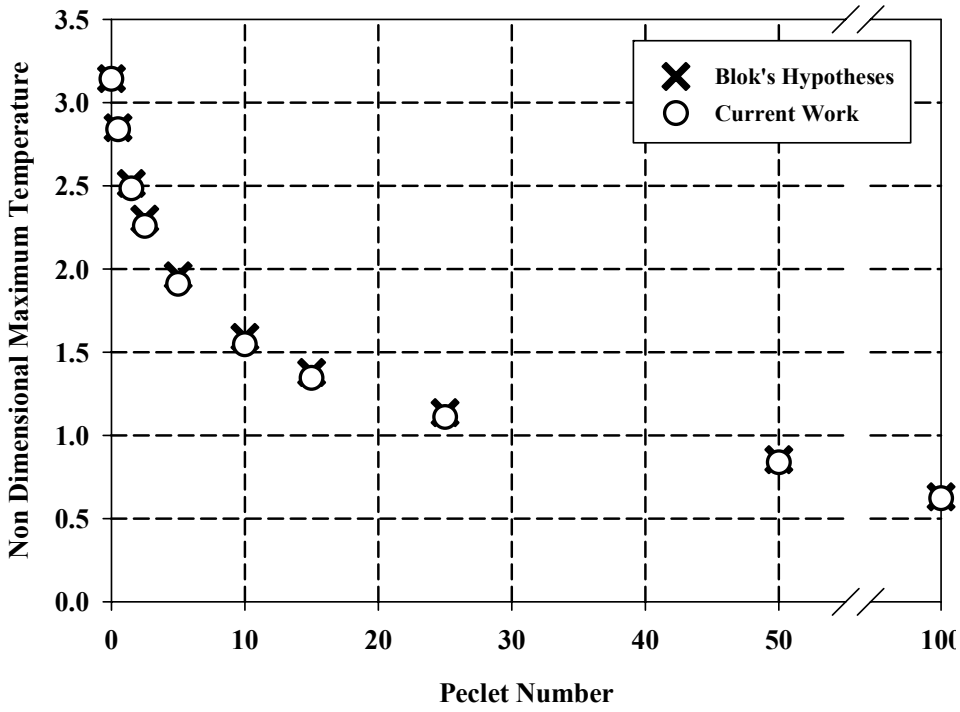

(a)

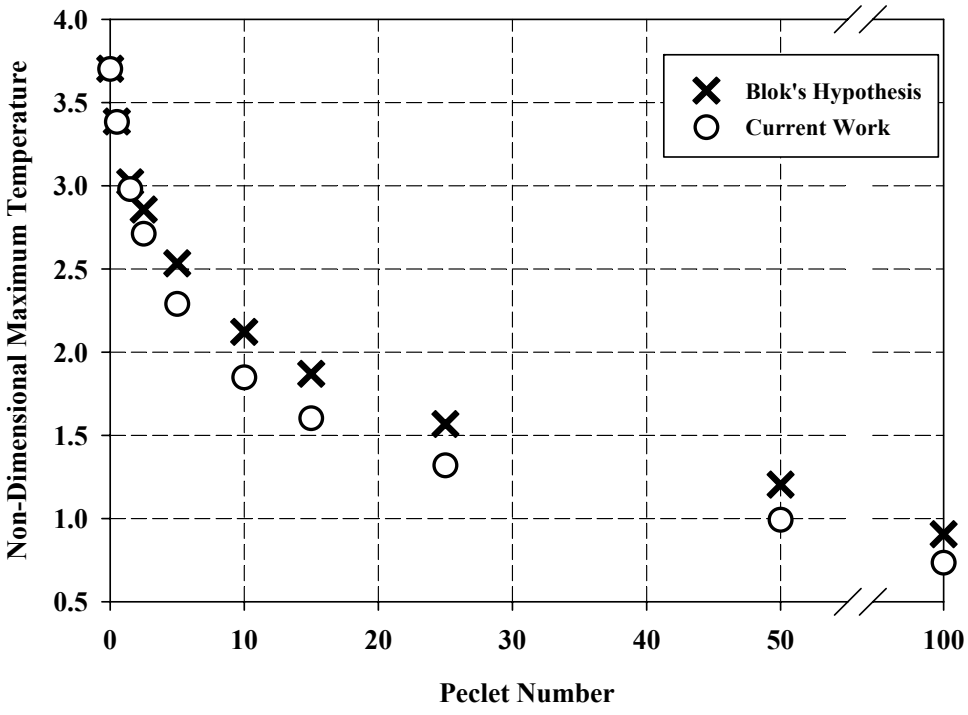

(b)

Figure 2.12 Dimensionless maximum temperature as a function of Peclet no. with $K = 1$: (a) uniform contact pressure; (b) Hertzian contact pressure

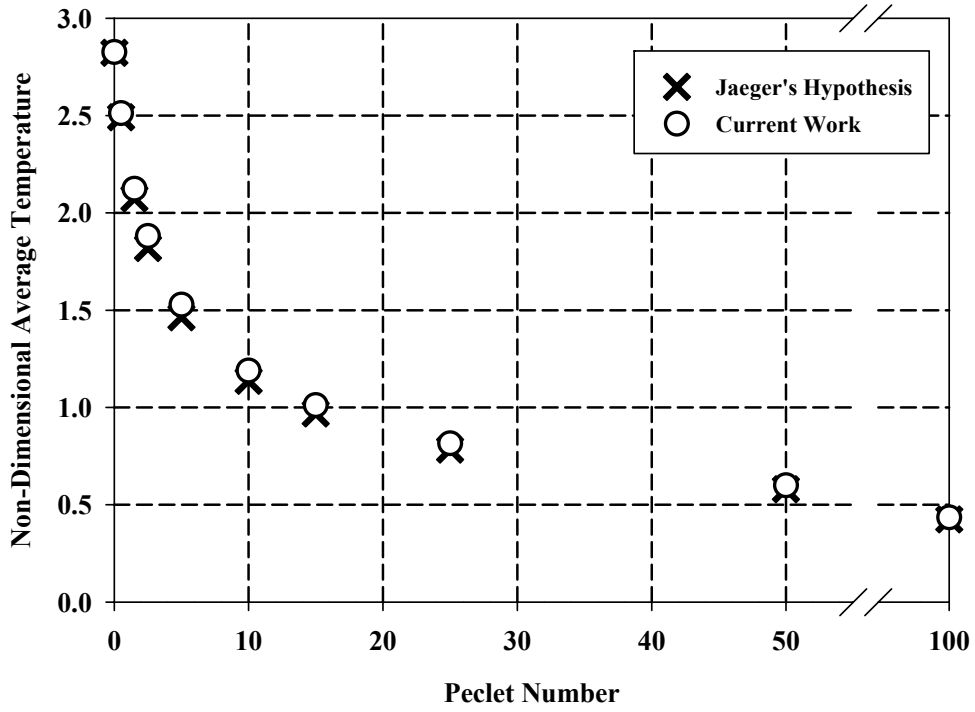

(a)

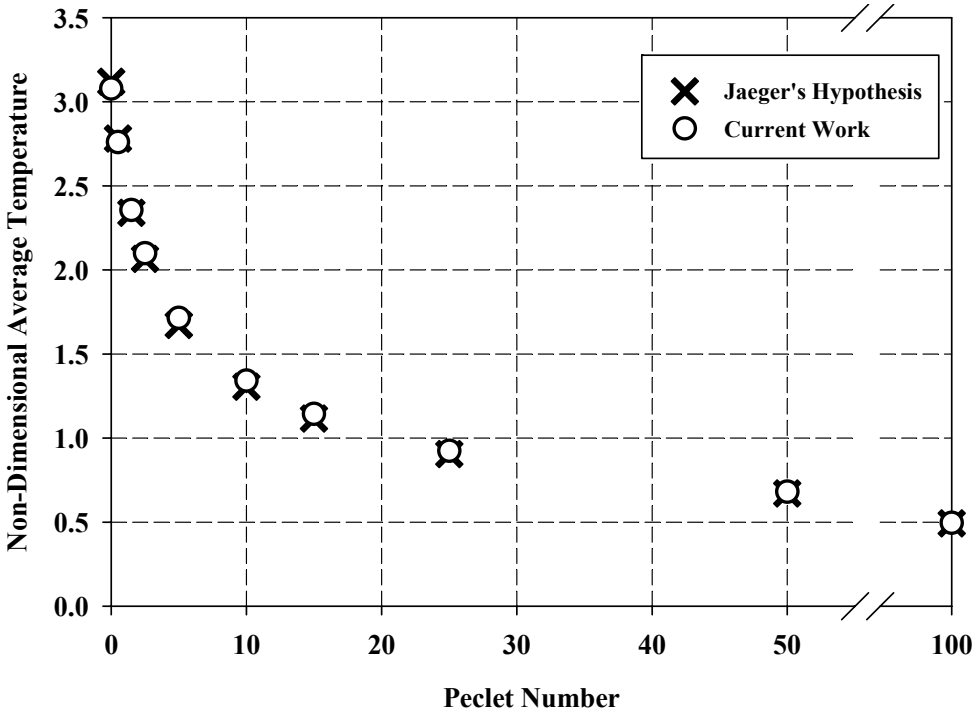

(b)

Figure 2.13 Dimensionless average temperature as a function of Peclet no. with K = 1: (a) uniform contact pressure; (b) Hertzian contact pressure

2.4.5 Bodies with different initial temperatures

In the section we discuss the results for the case when the two bodies are at different initial temperatures ($\Delta\Psi \neq 0$). Figure 2.14 shows the centerline temperature rise, for the case of uniform pressure distribution, at the interface for the Peclet numbers of 0.5 and 10 at different values of $\Delta\Psi$. The positive value of $\Delta\Psi$ indicates that the Body 1 is at higher initial temperature than the Body 2, while the negative value of $\Delta\Psi$ depicts the reverse scenario. For the case of low Peclet no. (Figure 2.14(a)), the presence of initial temperature difference essentially causes a shift, up or down, in the temperature profile, depending on sign of the temperature difference as compared to the case of no initial temperature difference. On the other hand, for the higher Peclet no. the initial temperature difference causes a greater change in the temperature rise at the trailing edge of contact than in the rest of the contact. In particular, for the $\Delta\Psi$ = 10 case, the temperature profile at the trailing edge has an increasing slope as compared to the decreasing slope seen at the trailing edge in the case of $\Delta\Psi$ = 0.

It is noted here that, as the magnitude of $\Delta\Psi$ is increased from 0, the error in temperature matching increases and this error also increases with increasing Peclet no. All cases considered above correspond to $\Delta\overline{\Theta}^{*}_{all}$ less than 4%. However, in the worst case of $\Delta\Psi$ = 10 and Pe = 10, $\Delta\overline{\Theta}^{*}_{boundary}$ is 35%. The analogous results for the Hertzian pressure case are shown in Figure 2.15. Trends similar to those of Figure 2.14 are found. At low Peclet nos., the initial temperature mismatch causes a shift in the profile, while at high Peclet nos., there is some skewing at the trailing edge.

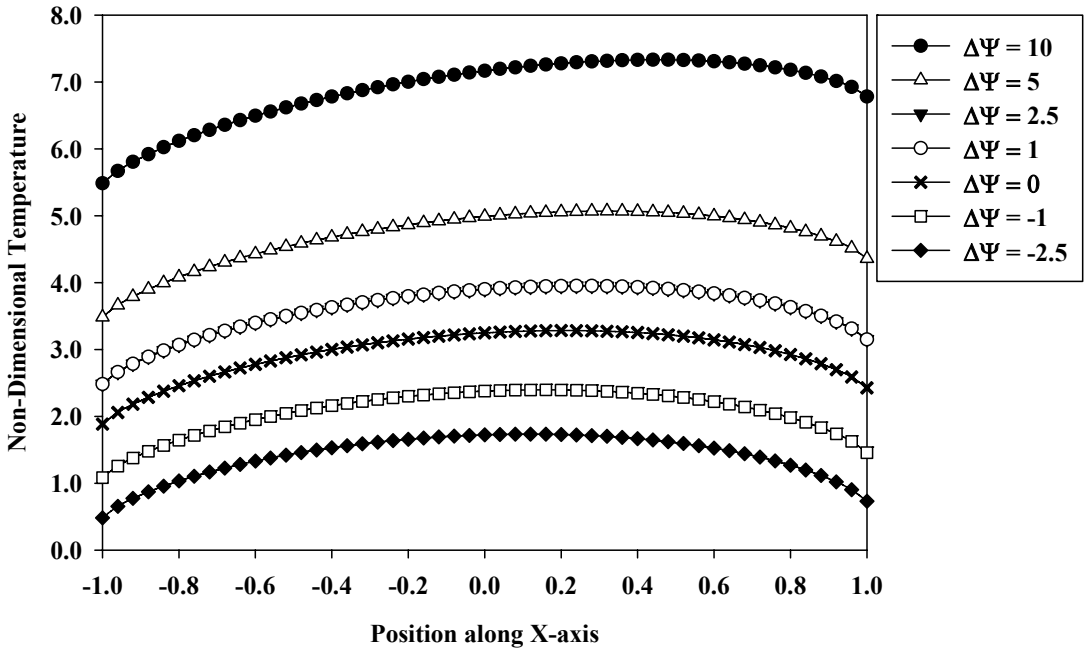

(a)

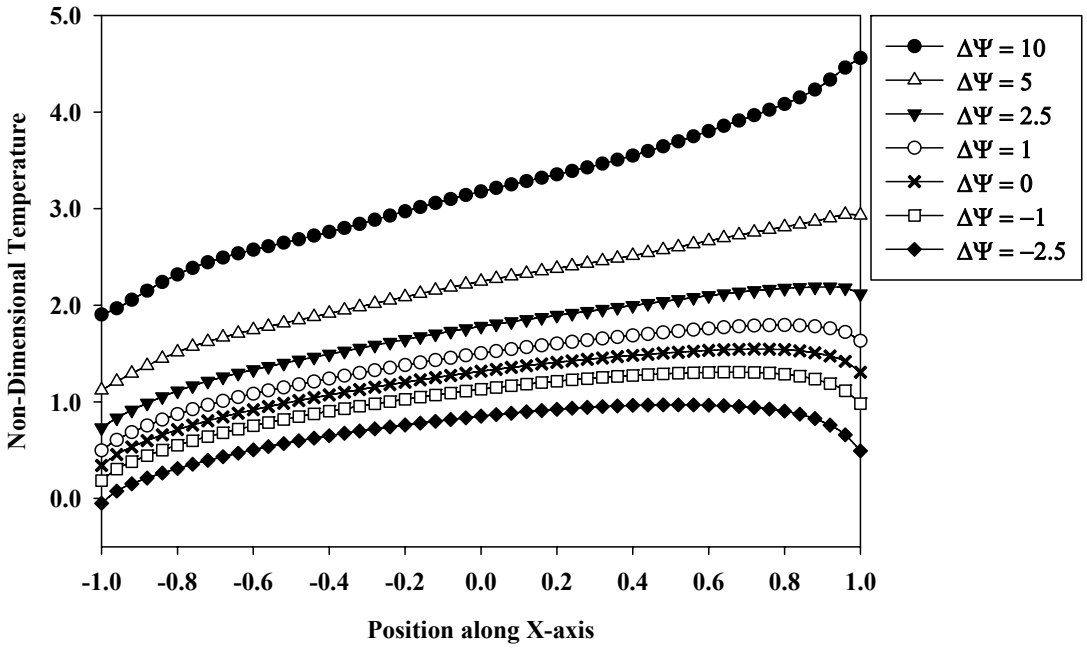

(b)

Figure 2.14 Dimensionless centerline temperature relative to Ψ_2 for uniform contact pressure at several $\Delta\Psi$'s with $K = 1$ and (a) Peclet no. = 0.5, and (b) Peclet no. = 10

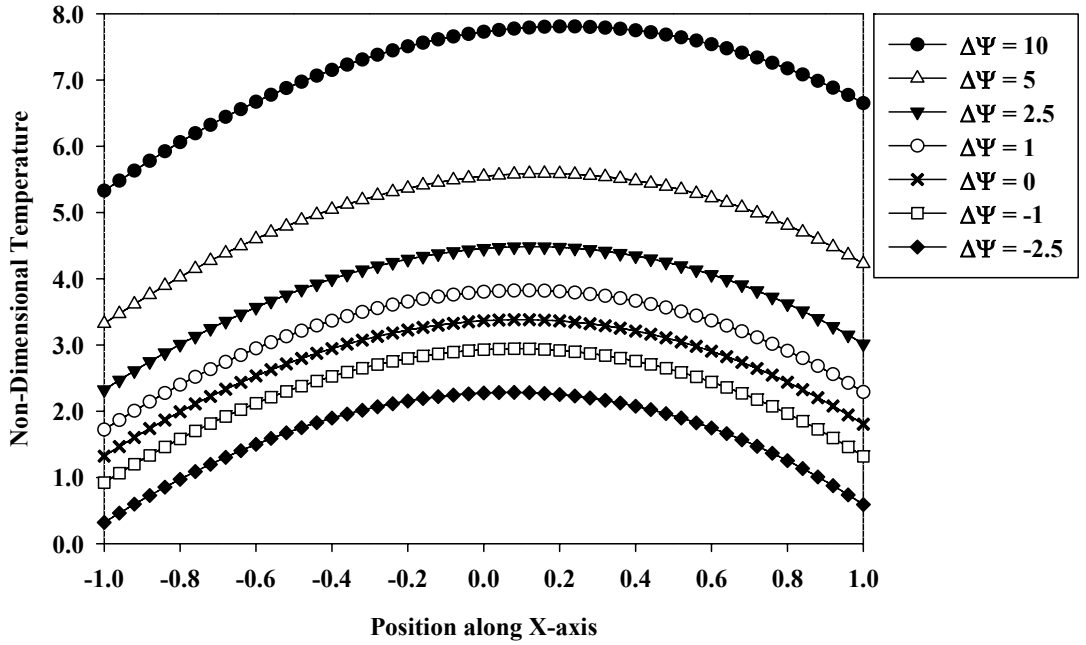

(a)

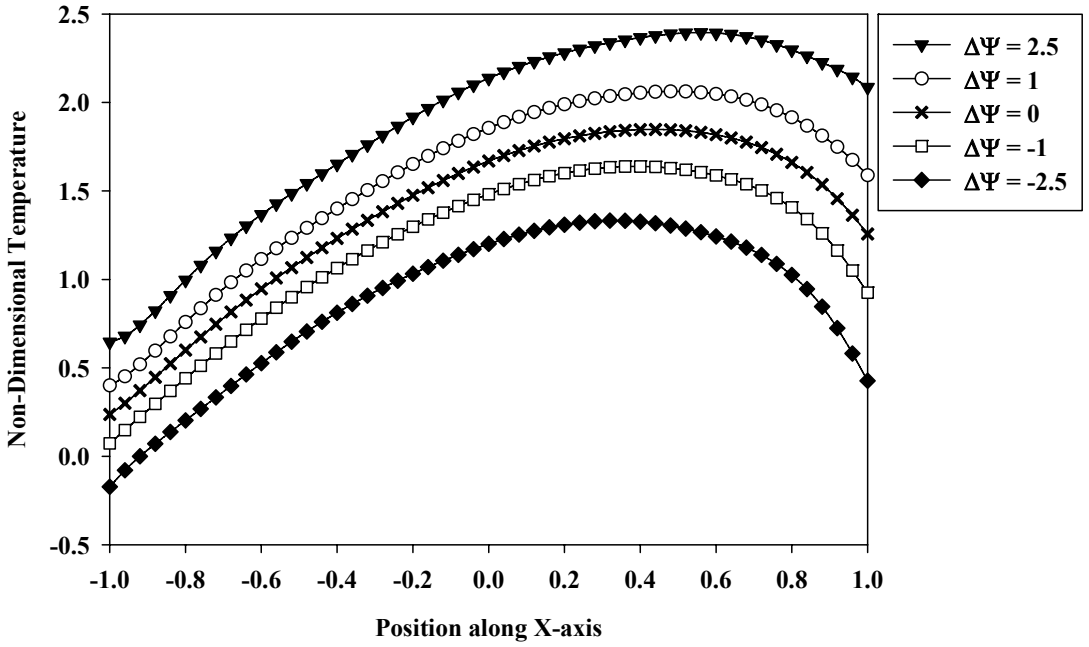

(b)

Figure 2.15 Dimensionless centerline temperature relative to Ψ_2 for Hertzian contact pressure at several $\Delta\Psi$'s with $K = 1$ and (a) Peclet no. = 0.5, and (b) Peclet no. = 10

2.5 Temperature rise at the interface of moving bodies

In this section the heat partition model is extended to evaluate the interface temperature rise when both the bodies are moving with respect to the contact region, as in a rolling contact. The coordinate axes are fixed to the interface and the Peclet numbers for both the bodies are calculated with reference to the interface. The non-dimensional temperature rise equations for evaluating the interface temperature, similar to Eqs. (2.19) and (2.20), are

$$\Theta_1\left(R,\theta\right) = K\int_{\phi=0}^{2\pi}\int_{s=0}^{s_b(R,\theta,\phi)}\left(1-\sigma\left(s,\phi\right)\right)f\left(s,\phi\right)\exp\left\{-\mathrm{Pe}_1\ s\left(1+\cos\phi\right)\right\}dsd\phi+\Psi_1 \quad (2.52)$$

$$\Theta_2\left(R,\theta\right) = \int_{\phi=0}^{2\pi}\int_{s=0}^{s_b(R,\theta,\phi)}\sigma\left(s,\phi\right)f\left(s,\phi\right)\exp\left\{-\mathrm{Pe}_2\ s\left(1+\cos\phi\right)\right\}dsd\phi+\Psi_2 \quad (2.53)$$

where,

$$\mathrm{Pe}_1 = \frac{U_1 a}{2\alpha_1}, \qquad \mathrm{Pe}_2 = \frac{U_2 a}{2\alpha_2} \quad (2.54)$$

here U_1 and U_2 are the surface velocities of Bodies 1 and 2 respectively relative to the contact region.

Applying the condition of continuity of temperature across the interface at each point within the contact region, we set $\Theta_1\left(R,\theta\right)=\Theta_2\left(R,\theta\right)$, which, after rearrangement, leads to

$$\Psi_1-\Psi_2+K\int_{\phi=0}^{2\pi}\int_{s=0}^{s_b(R,\theta,\phi)}f\left(s,\phi\right)\exp\left\{-\mathrm{Pe}_1\ s\left(1+\cos\phi\right)\right\}dsd\phi =$$
$$\int_{\phi=0}^{2\pi}\int_{s=0}^{s_b(R,\theta,\phi)}f\left(s,\phi\right)\sigma\left(s,\phi\right)\left[K\exp\left\{-\mathrm{Pe}_1\ s\left(1+\cos\phi\right)\right\}+\exp\left\{-\mathrm{Pe}_2\ s\left(1+\cos\phi\right)\right\}\right]dsd\phi \quad (2.55)$$

The heat partition fraction and the temperature rise can thus be evaluated as described in Section 2.3. However, it was observed that the temperature matching error $\Delta\bar{\Theta}^{*}_{all}$ exceeds 5% when Peclet no. of Body 1 exceeds 5 and 2.5 in the direction opposite to the direction of Body 2 for uniform contact pressure and Hertzian contact pressure respectively. In this section the results are presented for Hertzian pressure distribution at the interface for both the bodies with same initial temperature ($\Psi_1 = \Psi_2$). Figure 2.16 shows the interface temperature rise along the centerline of the interface for the case of two bodies having different Peclet nos. and $K = 1$.

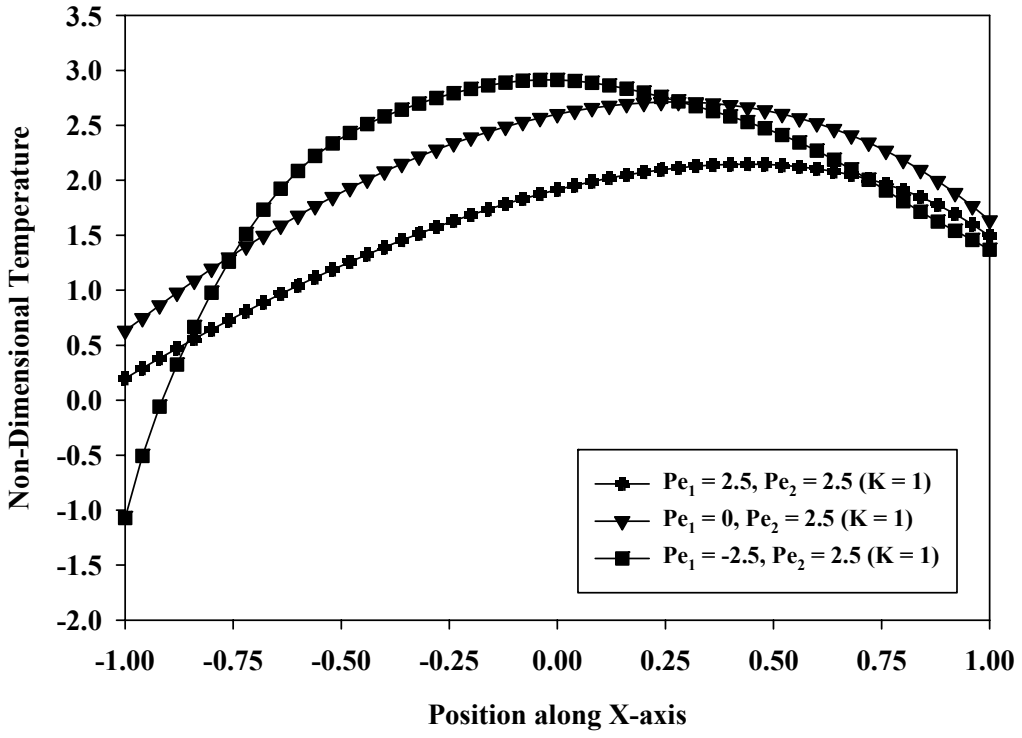

Figure 2.16 Interface temperature along the interface centerline for both bodies moving with different Peclet no., $K = 1$

It is seen that the dimensionless interface temperature is maximum when the bodies are moving in opposite directions and it is minimum when both the bodies are moving in the same direction. The position of the maximum interface temperature is near the center of the contact when the bodies move opposite directions, and this position moves towards the lagging edge of the contact when both the bodies move in the same direction.

2.6 Summary

A least squares regression-based methodology has been developed for obtaining the steady-state temperature distribution at the interface of two sliding bodies, whose initial uniform temperatures may be the same or different. The local frictional dissipation rate at the interface was assumed to be the product of the friction coefficient, the pressure and the sliding velocity. Both uniform and Hertzian contact pressure distributions were considered. Integral equations were developed, expressing the temperatures of each body in terms of an unknown heat partition function. By assuming a polynomial form for the heat partition function and optimizing the coefficients to obtain the least squares difference in temperature at the interface between the two bodies, an estimate for the heat partition function was obtained. Calculations were performed for various Peclet nos. ranging from 0 to 100, assuming that the two bodies had the same thermal conductivity. Results of the current analysis were compared to the more simple approaches of Blok and Jaeger who each assumed a single heat partition factor for the entire contact region. Based on the results, several conclusions can be made:

1) The regression approach provides an accurate means of determining the interfacial temperature distribution of sliding bodies.
2) The local value of heat partition function can exceed unity, which means that the temperature rises within one of the bodies just above (or below) this location is higher than the temperature at this point in the interface.
3) The approach of Jaeger, in which a single heat partition value is assumed and the resulting average temperatures of the two bodies are matched, provides a highly accurate prediction of the average interfacial temperature over a wide range of Peclet numbers.
4) The approach of Blok, in which a single heat partition value is assumed and the resulting maximum temperatures of the two bodies are matched, provides a good estimation of the maximum interfacial temperature at low Peclet nos., but tends to over-predict the maximum temperatures rise by about 20% for Peclet nos. greater than 20, in the case of Hertzian contact.
5) The current methodology can be applied to evaluate the steady-state temperature rise at the interface of two bodies with different initial temperatures and also to the case when both the bodies are moving with different Peclet nos.
6) The model can be applied to a macro-scale contact, ignoring surface roughness, between two bodies and also to contact between two asperities.

CHAPTER 3. DESIGN CURVES FOR TEMPERATURE RISE IN ELLIPTICAL CONTACTS

3.1 Introduction

The temperature rise due to frictional heat generation at the interface of two sliding components plays an important role in determining their performance and life. Accurate knowledge of the temperature rise is critical for performing thermal stress analysis between two sliding bodies [18-22], thermal wear modeling [23, 24, 50] both of which are relevant to many applications, such as machine tools [25-27], brake pads [28, 29], gear teeth [30, 31], and wheel-rail contacts [32]. As material strength can be significantly degraded at high temperatures, it is important to account for thermal effects due to sliding phenomenon. For example, the maximum temperature attained at tool-chip interface would have a direct bearing on the tool life. While the maximum surface temperature would generally be of greater interest, a prediction of the average interface temperature over the contact region can also be useful, as it is well correlated with the peak temperatures and may be easier to experimentally verify. In any case, a prediction of the maximum and/or average steady-state temperature rise at the interface of two sliding bodies can be valuable in designing against fatigue failure or other modes of system breakdown.

In this chapter the temperature rise at the interface of sliding Hertzian contacts is computed using the methodology presented in Chapter 2. In order to aid designers, curve fit equations are presented to calculate maximum temperature and average temperature

rise in non-dimensional form over a wide range of Peclet numbers, thermal conductivity ratios and ellipticity ratios.

3.2 Literature review

Jaeger [4] provided approximate equations for average temperature rise for square and band shaped contact regions for very low Peclet numbers (< 0.1) or for very high Peclet numbers (> 10). For intermediate Peclet numbers Jaeger, like Blok, provided curve fit solutions for average and maximum temperature rise. Although band shaped contacts may be good approximations of several engineering contact regions, such as in meshing gear teeth and in a tool-chip interface, elliptical and circular contacts are more commonly seen in engineering applications.

Kuhlmann-Wilsdorf [11, 12] modified the equation for maximum temperature rise put forth by Blok [2] to include the shape factor for elliptical contacts and used it to compute flash temperature due to friction and Joule heating. Kuhlmann-Wilsdorf used the Jaeger's solution to derive a curve fit equation representing the dependence of maximum temperature on sliding velocity, and used the same reasoning to form approximate expressions for shape factor relating ellipticity with sliding velocity. However, Kuhlmann-Wilsdorf mentioned that the shape factor relation could not be accurately applied to elliptical geometry and hence limited her discussion to circular shaped contacts. Later on Kuhlmann-Wilsdorf [12, 51] used those equations to determine flash temperatures in plastic contacts by accounting for changes in hardness due to flash temperatures. However, it is not clear how the partitioning of heat between the bodies

was handled in those studies. The results of average and maximum temperature rise from Kuhlmann-Wilsdorf's and the current work are compared.

Greenwood [52] put forth several interpolation formulae to calculate the maximum temperature rise in a body due to moving heat sources of circular, square and band shape, but did not address the issue of heat partition between the two bodies.

To summarize the literature review, there exist no published formula that would enable the direct calculation of maximum and average steady-state temperature rise within a sliding Hertzian contact derived from pointwise interfacial temperature matching. In the current study, a recently developed [53] regression-based technique is presented to determine the steady state temperature rise at the interface of two sliding semi-infinite bodies while applying the condition of no temperature jump across the interface. An elliptical contact geometry with semi-ellipsoidal (Hertzian) pressure distribution is considered. The computation is performed over a wide range of thermal conductivity ratios, Peclet numbers and ellipticity ratios. Based on the numerical results, curve fit equations for the average interface temperature and the maximum interface temperature are derived. This study is restricted to steady–state rather than transient–temperature rise because steady state conditions are generally achieved relatively quickly [54] and because the steady state values are typically of more practical interest. It is expected that the results of this study will provide designers a convenient tool to predict maximum and/or average temperature rise in sliding Hertzian contacts.

3.3 Heat partition

Following the methodology developed in Chapter 2 and [53], consider two semi-infinite bodies sliding across each other as shown in Figure 2.1. For the sake of simplicity, we shall keep the upper body (Body 1) stationary and move the lower body (Body 2) with a velocity U to right. Let T_{1i} and T_{2i} be the initial temperatures of Body 1 and Body 2, respectively. Let K_1 and K_2 be the thermal conductivities, and α_1 and α_2 be thermal diffusivities of Body 1 and Body 2, respectively. In general, the upper body (Body 1) has different radii of curvatures in the sliding and transverse directions within the sliding plane and this will give rise to an elliptical shaped contact. Consider a coordinate system that is attached to Body 1 with its origin placed at the center of the contact region (Figure 2.1). It is assumed that the radius of curvatures of both the bodies are large compared to the width of the contact region so that the both the bodies can be modeled as half-spaces. The heat generation rate per unit area q_f at the interface due to friction can be expressed as:

$$q_f(x,y) = \mu p(x,y)U = \frac{\mu FU}{\pi ab}\frac{3}{2}\sqrt{1-\frac{x^2}{a^2}-\frac{y^2}{b^2}} \tag{2.56}$$

where μ is the coefficient of friction, $p(x,y)$ is the Hertzian pressure distribution, U is the velocity of Body 2, F is the normal force, a is the semi-axis length in the sliding direction, and b is the semi-axis length the in the transverse direction. The relation in Eq. (2.1) supposes that the contact is elastic in nature and that the presence of frictional shear stress and thermal deformation have no impact on the normal contact stress distribution. It also assumes that one of the two principal directions of normal curvature of Body 1 is aligned with the sliding direction

Since Body 1 sees a stationary heat source, while the Body 2 sees a moving heat source, the non-dimensional temperature distributions at the surfaces of both the bodies can then be expressed as [46]

$$\Theta_1(X,Y) = K\iint \frac{\left(1-\sigma(\xi,\eta)\right) f(\xi,\eta)}{\sqrt{(X-\xi)^2+(Y-\eta)^2}} d\xi d\eta + \Psi_1 \tag{2.57}$$

$$\Theta_2(X,Y) = \iint \sigma(\xi,\eta) f(\xi,\eta) \frac{\exp\left\{-\mathrm{Pe}\left(\sqrt{(X-\xi)^2+(Y-\eta)^2}-(X-\xi)\right)\right\}}{\sqrt{(X-\xi)^2+(Y-\eta)^2}} d\xi d\eta + \Psi_2 \tag{2.58}$$

Equations (2.57) and (2.58) are similar to Eqs. (2.12) and (2.13) respectively, along with same definitions for the dimensionless variables as in Eq. (2.11). The term *f(x,y)* in the above equations represents the non-dimensional form of the heat distribution and is given as:

$$f(\xi,\eta) = \frac{3}{2}\sqrt{1-\xi^2-\frac{\eta^2}{c^2}} \tag{2.59}$$

where the ellipticity is given by $c = b/a$.

Equations (2.57) and (2.58) have singularity of the first kind which can be removed by a change of Cartesian variables (ξ,η) to polar coordinates (s,ϕ), centered at (*X,Y*) (e.g.,). Figure 3.1 provides a graphical representation of the new coordinate system. In the figure point *A(X, Y)* is the point of interest where temperature is being computed and is also the point of anchor of the new coordinate system. Now we can express *(X, Y)* in terms of polar coordinates (ρ,θ), whereby $X = \rho\cos\theta$, $Y = \rho\sin\theta$, $0 \le \rho \le \rho_b$ and $0 \le \theta \le 2\pi$. The length of *AC* determines the distance between the general integration point and our point where the temperature is being computed.

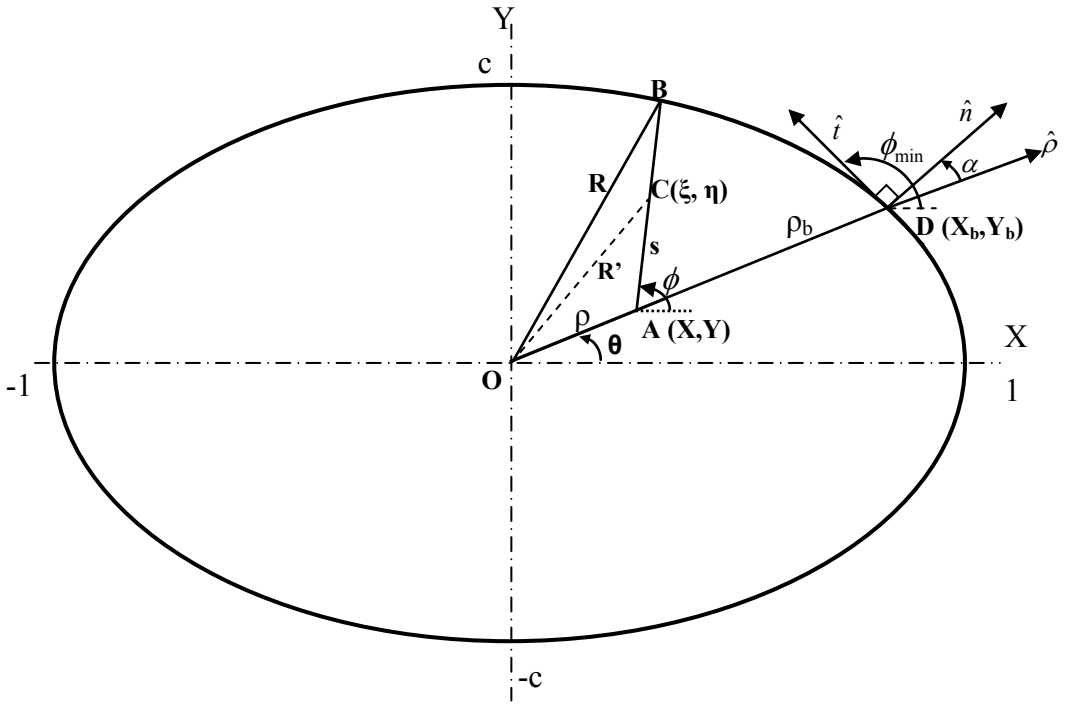

Figure 3.1 Illustration of coordinate transformation applied to an elliptical area

The equation of the ellipse in polar form is given as

$$\rho_b = \frac{ab}{\sqrt{a^2 \sin^2\theta + b^2 \cos^2\theta}} = \frac{a}{\sqrt{\cos^2\theta + \sin^2\theta / c^2}} \tag{2.60}$$

As shown in Figure 3.1, the non-dimensional length of the semi-axis in the sliding direction will be equal to 1, while the non-dimensional length of the transverse semi-axis will be equal to *c*. From Figure 3.1 we have the following relations:

$$\begin{aligned} s &= \sqrt{(X-\xi)^2 + (Y-\eta)^2} \\ s\cos\phi &= \xi - X \\ s\sin\phi &= \eta - Y \\ d\xi d\eta &= s\,ds\,d\phi \end{aligned} \tag{2.61}$$

Additionally, we can write

$$f(s,\phi) = 3/2\sqrt{1-(\rho\cos\theta + s\cos\phi)^2 - (\rho\sin\theta + s\sin\phi)^2 / c^2} \tag{2.62}$$

The limits of integration are found by noting that, for a fixed ϕ, s varies from 0 to a value corresponding to reaching the edge of the unit ellipse, at which point $R' = R$. Letting s_b (length of AB) denote the boundary value of s for the given ϕ, we have from the Law of Cosines,

$$s_b^2 + \rho^2 + 2\rho s_b \cos(\phi - \theta) = R^2 \tag{2.63}$$

At the boundary of the ellipse following relations are used to express R in terms of ξ and η

$$R^2 = \xi^2 + \eta^2 \qquad \text{and} \qquad 1 = \xi^2 + \eta^2 / c^2 \tag{2.64}$$

Hence,

$$R^2 = 1 + (\rho\sin\theta + s\sin\phi)^2 (1 - 1/c^2) \tag{2.65}$$

Substituting Eq. (2.65) in Eq. (2.63) and rearranging the terms,

$$\begin{aligned} &s_b^2 (1 - \sin^2\phi(1 - 1/c^2)) + 2s_b (\rho\cos(\theta - \phi) - \rho\sin\theta\sin\phi(1 - 1/c^2)) + \\ &\rho^2 - 1 - (\rho\sin\theta)^2 (1 - 1/c^2) = 0 \end{aligned} \tag{2.66}$$

The above quadratic equation can be solved to obtain the upper limit of integration on s. Note that only the positive root is admissible because s_b must be positive, as it represents a radial distance. Now ϕ ranges from 0 to 2π for all the interior points (X,Y). In the special case of $\rho = \rho_b$ (i.e., when (X,Y) is on the boundary of the circle), as illustrated in Figure 3.1, then ϕ ranges from $\alpha + \theta + \pi/2$ to $\alpha + \theta + 3\pi/2$, where α is the angle between the unit radial and the unit normal vectors at the boundary point (X_b, Y_b). Using vector calculus, the angle α is computed as

$$\alpha = \tan^{-1}\left(X_b Y_b \left(\frac{1}{c^2} - 1 \right) \right) \tag{2.67}$$

After making the change of variables, Eqs. (2.57) and (2.58) can be rewritten as:

$$\Theta_1(\rho,\theta) = K \int_{\phi=0}^{2\pi} \int_{s=0}^{s_b(\rho,\theta,\phi)} \left(1-\sigma(s,\phi)\right) f(s,\phi)\, ds d\phi + \Psi_1 \tag{2.68}$$

$$\Theta_2(\rho,\theta) = \int_{\phi=0}^{2\pi} \int_{s=0}^{s_b(\rho,\theta,\phi)} \sigma(s,\phi) f(s,\phi) \exp\left\{-\mathrm{Pe}\, s\left(1+\cos\phi\right)\right\} ds d\phi + \Psi_2 \tag{2.69}$$

Applying the condition of continuity of temperature across the interface at each point within the contact region, we set $\Theta_1(\rho,\theta) = \Theta_2(\rho,\theta)$, which, after rearrangement, leads to

$$\begin{aligned} \Psi_1 - \Psi_2 + K \int_{\phi=0}^{2\pi} \int_{s=0}^{s_b(\rho,\theta,\phi)} f(s,\phi)\, ds d\phi = \\ \int_{\phi=0}^{2\pi} \int_{s=0}^{s_b(\rho,\theta,\phi)} f(s,\phi)\sigma(s,\phi)\left[K + \exp\left\{-\mathrm{Pe}\, s\left(1+\cos\phi\right)\right\}\right] ds d\phi \end{aligned} \tag{2.70}$$

The implementation of the least squares regression methodology to obtain the heat partition and the interface temperature rise has been discussed in detail in Chapter 2.

3.4 Results

In the following sub-sections the effects of Peclet number, thermal conductivity ratio and ellipticity on the maximum and the average temperature rise are presented. These dependencies are then analyzed to arrive at simple analytical approximations. The computations are performed over a wide range of Peclet numbers (0 to 10,000), thermal conductivity ratios (0.25 to 10) and ellipticity ratios (2 to 0.25) in order to achieve broad applicability. It is to be noted that the results for Peclet no. = 0 represent the solution at

the lower limit of Peclet no., although no frictional heat would be generated at Pe = 0. In this section the discussion is limited to the special case of both the bodies starting off with same initial temperatures i.e., $\Delta\Psi = 0$.

3.4.1 Representative temperature distributions

Figure 3.2 illustrates typical temperature distribution calculations. Here we see the temperature distributions at the interface for the ellipticity ratios of 0.8 (Figure 3.2(a)) and 1.5 (Figure 3.2(b)) for K = 1.5 and Pe = 2. The temperature distributions for both the cases have a paraboloidal shape but the maximum temperature rise for the ellipticity ratio of 0.8 is slightly lower than that for the ellipticity of 1.5. From Eqs. (2.68)-(2.69), it can be seen that the temperature rise is a function of the shape of the contact region (or ellipticity), the Peclet number and thermal conductivity ratio.

3.4.2 Effect of thermal conductivity ratio

The ratio of the thermal conductivity of the bodies in contact has a marked effect on the heat partition between them and thus the interface temperature rise. Figure 3.3 illustrates the variation of the non-dimensional maximum temperature with the thermal conductivity ratio for certain values of Peclet numbers, for an ellipticity of 0.9. It is seen that, for a given ellipticity and Peclet no., the non-dimensional maximum temperature increases as the thermal conductivity ratio, K, is increased. At lower Peclet nos. (Pe < 5) the change with K is substantial while, at the higher Peclet nos. (Pe > 100) little increase is observed. Figure 3.4 shows the variation of non-dimensional average temperature with thermal conductivity ratio, K, for ellipticity ratio of 0.9. Trends similar to those of Figure 3.3 are

observed. It should be noted, however, that the *dimensional* temperature rise of Body 2 may follow a different trend with increasing K, depending specifically on whether changes in K_1 or K_2 or both are responsible for the increasing K (= K_2/K_1). If K is increased solely by decreasing K_1 then the trend of dimensional temperature would be identical to that of Figures. 3.3 and 3.4, as seen from Eq. (2.11). On the other hand, if K is increased solely by increasing K_2 the dimensional temperatures would be obtained from the results of Figure 3.3 and Figure 3.4 by decreasing the Peclet number (Eq. (2.11)) and then multiplying the resulting non-dimensional temperature values by a factor that has K_2 in the denominator, as per Eq. (1.11). Carrying out this process for a few cases of Figure 3.3 and Figure 3.4 indicates that the dimensional temperature would *decrease* with increasing K_2. This result is justified physically, as one would expect that a greater thermal conductivity of Body 2 would more effectively extract heat from the interface, thereby maintaining a lower temperature.

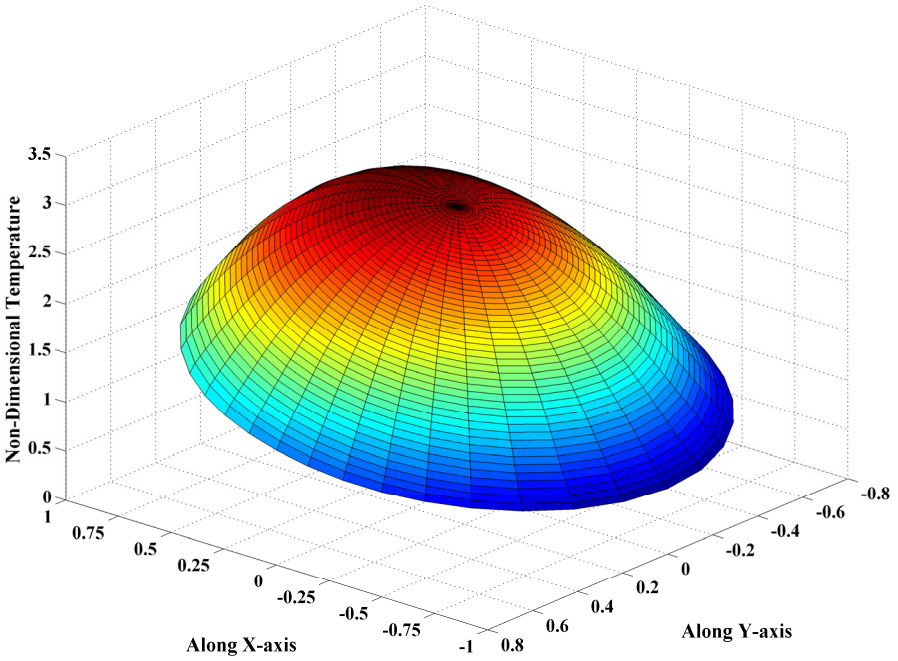

(a)

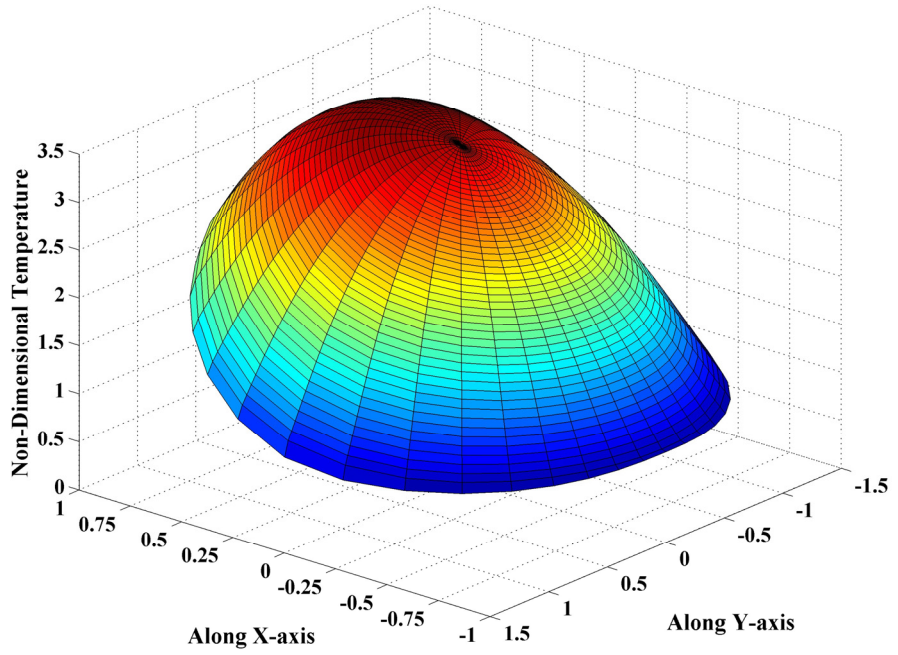

(b)

Figure 3.2 Non-dimensional temperature distribution at the interface for K = 1.5 and Pe = 2, for ellipticity ratios of (a) c = 0.8, and (b) c = 1.5

The effect of thermal conductivity ratio on the interface temperature can also be quantified via the *global heat partition*, Σ, which is defined as

$$\Sigma = \frac{Q_2}{Q} = \frac{q_o \iint \sigma(x',y') f(x',y')\, dx'dy'}{q_o \iint f(x',y')\, dx'dy'} \tag{2.71}$$

where Q_2 is the total heat flux into Body 2 and Q is the total rate of frictional dissipation. Figure 3.5 displays the global heat partition as a function of K for various Peclet nos. for an ellipticity of 0.9. It is seen that as K is increased for a given Peclet no., the global heat partition also increases. This increase is more noticeable at lower Peclet nos. than at higher Peclet nos. Another interesting observation is that at high values of K the effect of Peclet no. on global heat partition is mitigated as Σ approaches 100%.

3.4.3 Effect of Peclet number

Figures 3.3 – 3.5 also indicate the role of Peclet number. In Figure 3.3 and Figure 3.4, it is seen that increasing Pe decreases the non-dimensional temperature rise. Note, however, that since the decrease is much less than linear, when the results are converted to dimensional temperatures (i.e., via Eq. (2.11)), they show significantly increasing temperature with increasing Pe, if the sliding speed is the sole parameter that is being varied. For example, Figure 3.3 shows that for K = 10, an increase in Pe from 1 to 10 essentially halves the dimensionless temperature rise (i.e., from about 5 to about 2.5). However, in converting to the corresponding *dimensional* temperature one would scale the non-dimensional values by 10 to account for the ten-fold increase in velocity. Therefore, the dimensional temperature would be found to increase by a factor of 5.

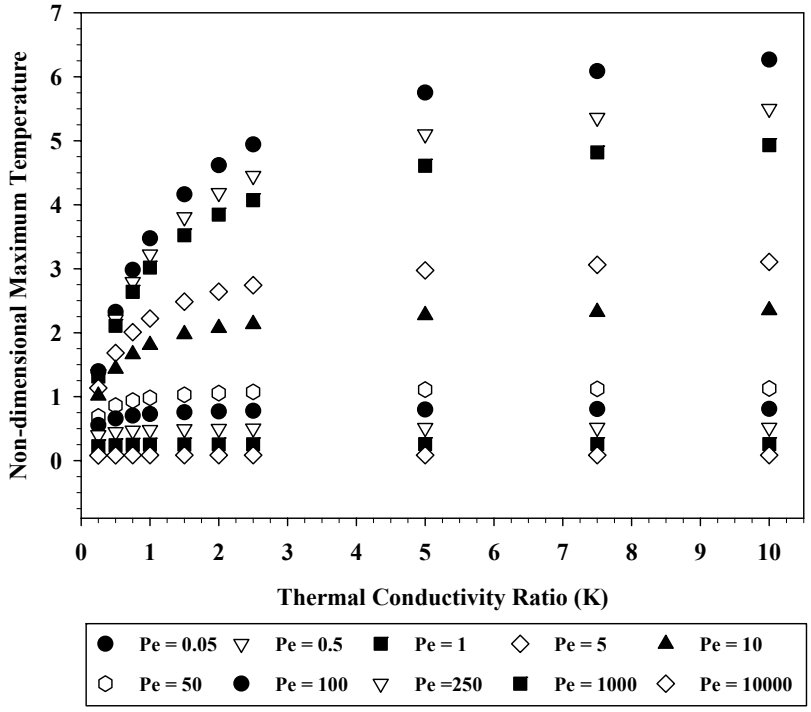

Figure 3.3 **Non-dimensional maximum temperature vs. thermal conductivity ratio for c = 0.9 at several values of Peclet number**

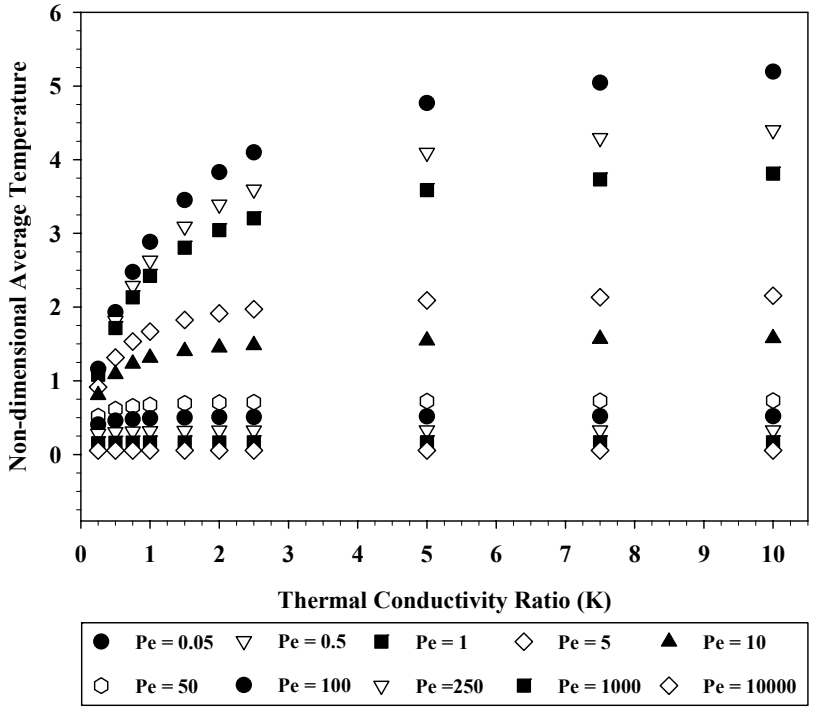

Figure 3.4 **Non-dimensional average temperature vs. thermal conductivity ratio for c = 0.9 at several values of Peclet number**

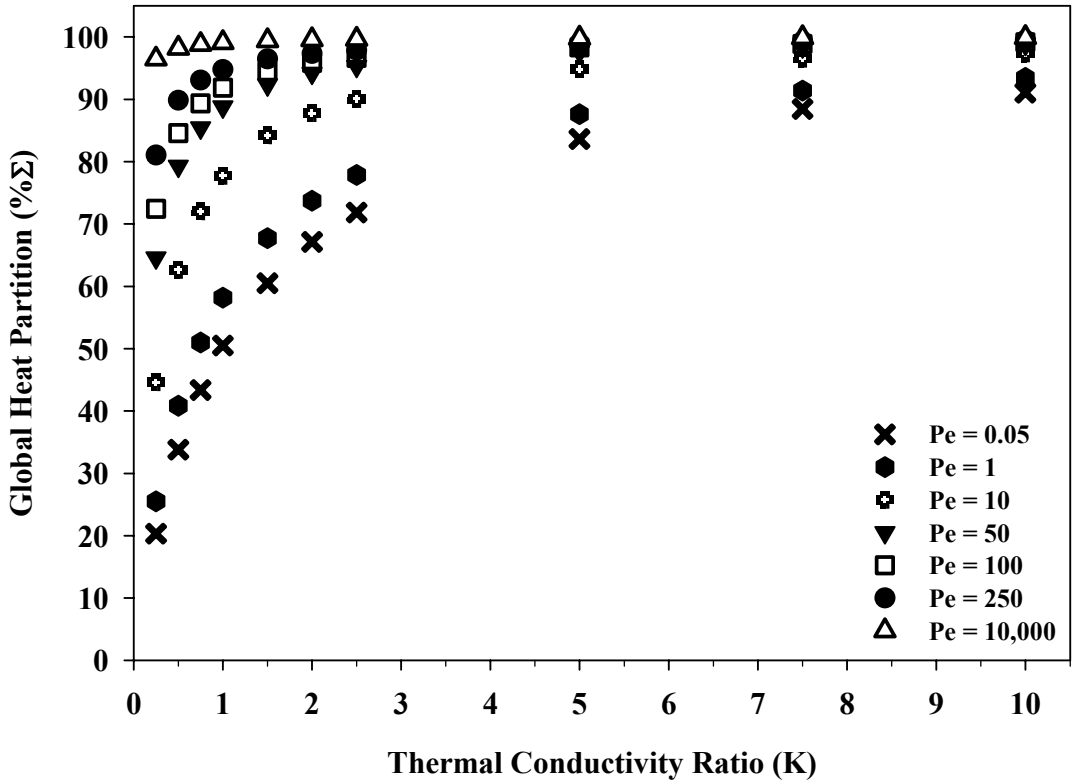

Figure 3.5 Global heat partition vs. thermal conductivity ratio for c = 0.9 at several values of Peclet number

Figure 3.5 illustrates the effect of Peclet no. on the global heat partition. As observed, the global heat partition increases with increasing Peclet no. for a given K. Now increasing the Peclet no. while holding K fixed can be accomplished by increasing the sliding speed, which results in Body 2 being more effective at removing heat from the interface [51, 53], similar to the effects of convective heat transfer. In the case of very high sliding speeds, therefore, almost all the heat generated at the interface would be conducted into the moving body.

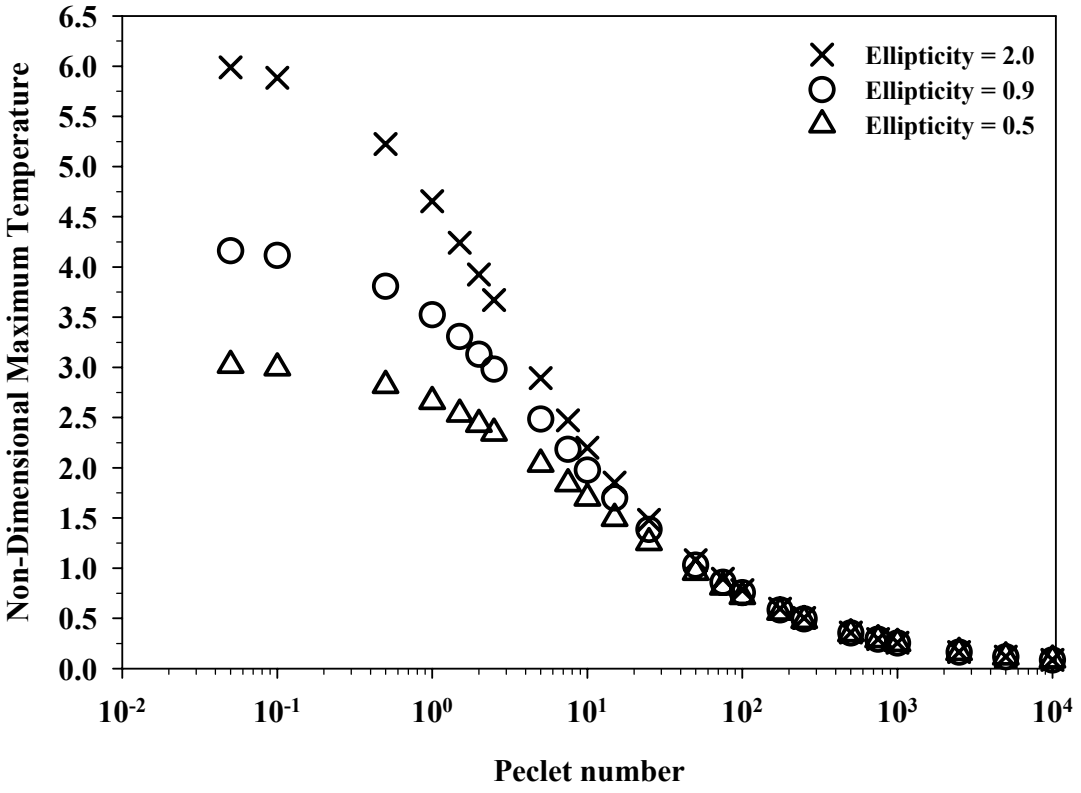

Figure 3.6 Non-dimensional maximum temperature vs. Peclet number for K = 1.5 and several ellipticity ratios

Figure 3.6 illustrates the variation of non-dimensional maximum temperature with Peclet no. for a thermal conductivity ratio of 1.5 and ellipticity ratios of 2, 0.9 and 0.5. It is seen that the non-dimensional maximum temperature decreases with increasing Peclet no. It is also observed that the non-dimensional maximum temperature rise increases with increasing ellipticity ratio. However, the influence of ellipticity is seen to diminish at large Peclet number.

3.4.4 Position of maximum temperature within the contact

Figure 3.7 illustrates the X-coordinate of maximum temperature rise within a circular contact as a function of Peclet no. for several values of thermal conductivity ratio *K*. (From symmetry considerations, the maximum temperature is known to occur somewhere on the X-axis.) It is observed in Figure 3.7 that for small Peclet nos. (Pe < 0.1) the maximum temperature occurs at or near to the center of the domain (i.e., the origin) while, for large Pe, the maximum temperature occurs near the trailing edge of the contact. It is also observed that increasing *K* moves the point of maximum temperature towards the trailing edge of the contact. Another interesting observation to be made is that asymptote, for the location of maximum temperature, is 0.74 and not 1.

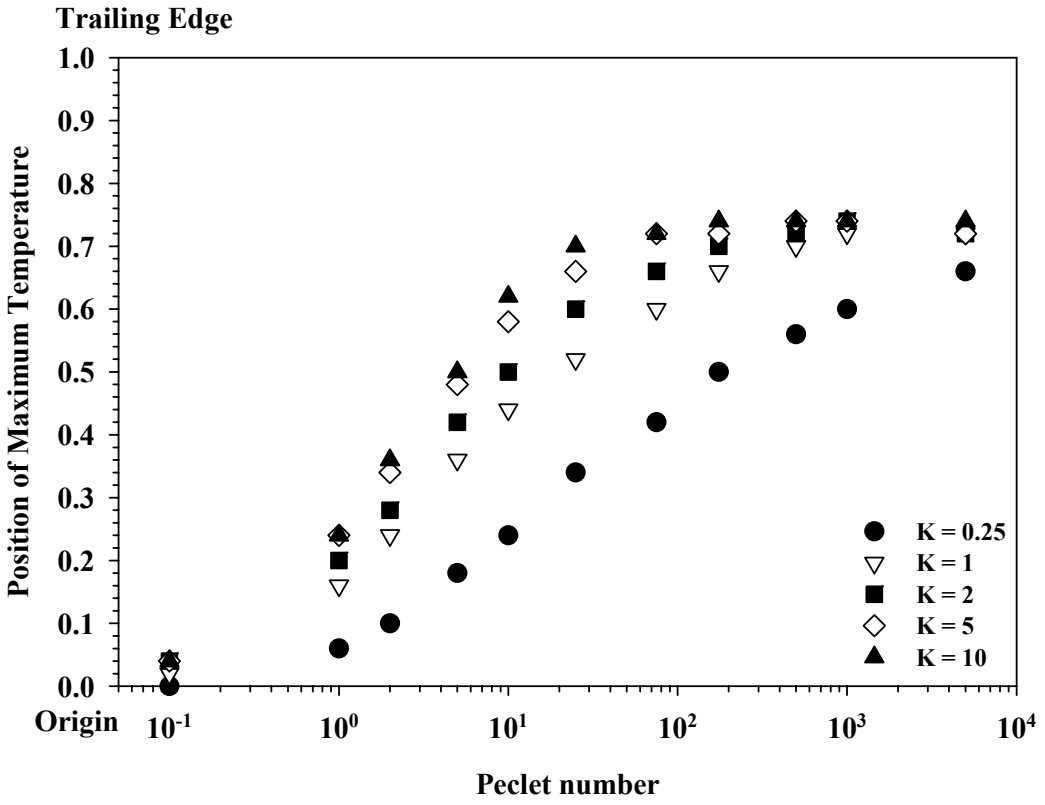

Figure 3.7 Position of maximum temperature for a circular contact vs. Peclet number at several thermal conductivity ratios

3.5 Curve Fit Equations for Interfacial Temperature

In this section, curve fit equations for computing the average and the maximum interfacial temperatures are presented for cases when the bodies have either the same or different initial temperatures. The curve fit equations were obtained after various trials with different forms of the equations. In each case the fit criterion was to minimize the least squares error. In order to obtain accurate curve fit equations, the Peclet no. range was split in three segments: $0 < \mathrm{Pe} \le 5$, $5 \le \mathrm{Pe} \le 100$, and $100 \le \mathrm{Pe} \le 10,000$.

3.5.1 Both bodies at same initial temperature ($\Delta\Psi = 0$)

In this section curve fit equations are presented for the special case of both the bodies having the same initial temperatures. Results of 2640 full numerical solutions were used to develop the curve fits.

3.5.1.1 *Peclet no. range $0 < Pe \le 5$*

For the range of $0 < \mathrm{Pe} \le 5$ the temperature variation with the thermal conductivity ratio, for a given ellipticity, can be accurately described by the following relation

$$\Theta\left(\mathrm{Pe}\right)\Big|_c = \frac{P\,K}{K+S} \tag{2.72}$$

where the coefficients *P*, and *S* are the functions of Peclet no. and ellipticity. For each value of ellipticity and Peclet no., the values of the coefficients were obtained by means of non-linear least squares regression technique with the criteria of keeping the least squares relative error less than 10^{-5}.

For a given ellipticity, once the values of the coefficients P, and S are obtained for all the values of Peclet nos., curve fit equations between the coefficients and Peclet no. are obtained. The values of the coefficients P, and S can be determined using following relations

$$P = \frac{p_1 \mathrm{Pe}^2 + p_2 \mathrm{Pe} + p_3}{\mathrm{Pe} + p_4}$$
$$S = \frac{s_1 \mathrm{Pe} + s_2}{\mathrm{Pe} + s_3} \tag{2.73}$$

Tables 3.1 and 3.2 list the values of the coefficients p_i, and s_i (i =1, 2 or 3), for different ellipticity ratios, for computing average and maximum temperature rise respectively.

Table 3.1 Coefficients for calculating average temperature for $0 < \mathrm{Pe} \leq 5$

$c = b/a$	$p_1 \times 10^3$	$p_2 \times 10$	$p_3 \times 10$	$p_4 \times 10$	$s_1 \times 10^3$	$s_2 \times 10$	$s_3 \times 10$
2.0	-15.382	11.106	99.733	11.678	74.428	12.006	11.978
1.5	-18.482	11.146	100.947	13.469	85.574	13.996	13.973
1.25	-21.180	11.311	100.507	14.625	94.291	15.371	15.351
1.0	-24.569	11.594	98.662	16.025	107.066	17.159	17.144
0.9	-26.045	11.740	97.289	16.668	114.064	18.042	18.030
0.8	-27.517	11.900	95.383	17.364	122.710	19.047	19.038
0.7	-28.885	12.065	92.768	18.114	133.634	20.200	20.196
0.6	-29.981	12.216	89.201	18.919	147.844	21.533	21.533
0.5	-30.523	12.315	84.331	19.773	167.000	23.081	23.087
0.4	-30.028	12.278	77.653	20.662	193.979	24.880	24.894
0.25	-25.535	11.551	62.471	22.011	261.898	28.061	28.085

Table 3.2 Coefficients for calculating maximum temperature for $0 < \mathrm{Pe} \le 5$

$c = b/a$	p_1 $\times 10^3$	p_2 $\times 10$	p_3	p_4 $\times 10$	s_1 $\times 10^2$	s_2 $\times 10$	s_3 $\times 10$
2.0	-61.124	20.848	14.282	13.638	14.116	15.818	15.870
1.5	-65.690	21.215	14.011	15.635	15.775	18.629	18.693
1.25	-69.937	21.768	13.791	16.739	17.278	20.465	20.540
1.0	-73.527	22.434	13.201	17.858	19.640	22.601	22.686
0.9	-74.590	22.713	12.801	18.266	20.945	23.553	23.642
0.8	-74.945	22.943	12.282	18.633	22.563	24.532	24.626
0.7	-73.726	23.009	11.646	18.977	24.573	25.507	25.605
0.6	-70.470	22.805	10.882	19.312	27.015	26.486	26.585
0.5	-64.684	22.191	9.987	19.675	29.947	27.489	27.587
0.4	-56.546	21.061	8.899	20.029	33.535	28.512	28.608
0.25	-38.920	17.773	6.797	20.611	40.874	29.818	29.904

3.5.1.2 ***Peclet no. range $5 \le Pe \le 100$***

In this range of Peclet no. an accurate variation of temperature with the thermal conductivity ratio, for a given ellipticity, can be described as

$$\Theta(\mathrm{Pe})\big|_c = A \log_{10} K + B\left(\log_{10} K\right)^2 + C\left(\log_{10} K\right)^3 + D \tag{2.74}$$

where the coefficients A, B, C and D are the functions of Peclet no. and ellipticity. For each value of ellipticity and Peclet no. the coefficients A, B, C and D were obtained by means of linear least squares regression technique. The values of the coefficients A, B, C and D are thus obtained using the following equations

$$\begin{aligned} A &= \frac{a_1 \log_{10} \mathrm{Pe} + a_2}{\left(\log_{10} Pe\right)^2 + a_3 \log_{10} Pe + a_4} \\ B &= b_1 \exp\left(-\left(\frac{\log_{10} \mathrm{Pe} - b_2}{b_3}\right)^2\right) \\ C &= c_1\left(\log_{10} \mathrm{Pe}\right)^3 + c_2\left(\log_{10} \mathrm{Pe}\right)^2 + c_3\left(\log_{10} \mathrm{Pe}\right) + c_4 \\ D &= \frac{d_1\left(\log_{10} \mathrm{Pe}\right)^3 + d_2}{\left(\log_{10} \mathrm{Pe}\right)^2 + d_3} \end{aligned} \tag{2.75}$$

where the values of the coefficients a_i, b_i, c_i and d_i (i =1, 2, 3 or 4) for several ellipticity ratios are listed in Tables 3.3 and 3.4, in order to compute average and maximum temperature rise, respectively.

3.5.1.3 ***Peclet no. range 100 ≤ Pe ≤ 10,000***

In this range of Peclet no. an accurate variation of temperature with the thermal conductivity ratio, for a given ellipticity, can be described as

$$\Theta\left(\mathrm{Pe}\right)\Big|_c = V \log_{10} K + W \left(\log_{10} K\right)^2 + Z \tag{2.76}$$

with values of the coefficients V, W and Z obtained using the following equations

$$\begin{aligned} V &= \frac{v_1 \log_{10} \mathrm{Pe} + v_2}{\left(\log_{10} \mathrm{Pe}\right)^4 + v_3} \\ W &= \frac{w_1 \log_{10} \mathrm{Pe} + w_2}{\left(\log_{10} \mathrm{Pe}\right)^4 + w_3} \\ Z &= \frac{z_1 \log_{10} \mathrm{Pe} + z_2}{\left(\log_{10} \mathrm{Pe}\right)^3 + z_3} \end{aligned} \tag{2.77}$$

and with the values of the coefficients v_i, w_i and z_i ,for several ellipticity ratios, listed in Tables 3.5 and 3.6 for computing average and maximum temperature rise, respectively.

Table 3.3 Coefficients for calculating average temperature for $5 \le \mathrm{Pe} \le 100$

$c = b/a$	a_1 $\times -10^2$	a_2 $\times 10^2$	a_3 $\times -10^2$	a_4 $\times 10^2$	b_1 $\times -10^2$	b_2 $\times 10^2$	b_3 $\times 10$	c_1 $\times 10^2$	c_2 $\times -10^2$	c_3 $\times 10$	c_4 $\times -10^2$	d_1 $\times -10^3$	d_2 $\times 10$	d_3 $\times 10$
2.0	29.271	76.127	59.879	54.958	94.254	-20.468	13.444	17.775	79.518	10.412	28.843	85.227	33.935	12.198
1.5	32.715	85.845	59.199	59.993	76.369	-1.510	13.018	18.808	87.065	12.148	41.503	87.332	34.059	13.161
1.25	35.018	92.385	59.201	64.080	67.084	10.232	12.744	18.970	89.670	12.954	48.414	89.190	34.218	13.941
1.0	38.067	101.046	59.567	70.319	57.542	24.058	12.422	18.527	89.971	13.533	55.204	92.028	34.526	15.125
0.9	39.644	105.502	59.867	73.864	53.608	30.389	12.277	18.045	88.870	13.630	57.664	93.570	34.725	15.793
0.8	41.532	110.824	60.264	78.361	49.602	37.236	12.127	17.282	86.588	13.583	59.725	95.403	34.985	16.631
0.7	43.867	117.388	60.752	84.256	45.506	44.668	11.975	16.138	82.656	13.324	61.112	97.582	35.329	17.712
0.6	46.874	125.828	61.331	92.330	41.280	52.818	11.829	14.472	76.406	12.756	61.410	100.160	35.791	19.156
0.5	50.959	137.286	61.989	104.079	36.857	61.881	11.702	12.106	66.928	11.734	59.975	103.149	36.425	21.173
0.4	56.918	154.070	62.663	122.742	32.119	72.195	11.626	8.860	53.165	10.073	55.875	106.354	37.306	24.176
0.25	73.906	202.969	63.319	186.252	23.910	91.718	11.786	2.451	23.616	6.025	42.169	108.650	39.251	32.792

Table 3.4 Coefficients for calculating maximum temperature for $5 \le \mathrm{Pe} \le 100$

$c = b/a$	a_1 $\times -10^2$	a_2 $\times 10^1$	a_3 $\times -10^2$	a_4 $\times 10^2$	b_1 $\times -10^2$	b_2 $\times 10^2$	b_3 $\times 10$	c_1 $\times 10^2$	c_2 $\times -10^2$	c_3 $\times 10$	c_4 $\times -10^2$	d_1 $\times -10^2$	d_2 $\times 10$	d_3 $\times 10$
2.0	67.003	18.303	47.839	74.652	84.908	13.736	13.412	23.714	117.31	18.201	79.190	12.513	51.440	14.470
1.5	72.811	20.076	50.000	82.729	71.420	31.975	12.910	22.943	117.56	19.140	90.757	12.993	52.229	15.764
1.25	76.982	21.370	51.962	89.737	63.955	42.983	12.631	21.341	112.62	19.011	95.173	13.406	52.932	16.857
1.0	82.573	23.168	54.638	100.86	56.039	55.125	12.367	18.369	101.44	18.023	96.537	14.008	54.031	18.574
0.9	85.059	24.002	56.428	107.03	52.601	60.770	12.246	16.471	93.809	17.198	95.491	14.339	54.647	19.558
0.8	87.792	24.940	58.871	114.88	48.984	66.889	12.125	13.900	83.077	15.926	92.584	14.737	55.418	20.815
0.7	91.629	26.231	61.132	125.46	45.223	73.137	12.037	10.886	70.020	14.272	87.863	15.179	56.366	22.452
0.6	96.732	27.970	63.186	140.11	41.233	79.804	11.973	7.622	55.339	12.304	81.457	15.653	57.541	24.652
0.5	103.33	30.279	65.165	161.15	36.943	87.054	11.936	4.042	38.609	9.932	72.779	16.097	58.969	27.715
0.4	112.37	33.488	67.237	193.79	32.202	95.446	11.947	0.406	20.602	7.195	61.595	16.374	60.636	32.188
0.25	152.52	45.847	68.928	323.48	23.687	111.94	12.530	-2.414	1.298	3.471	42.774	15.568	62.966	44.285

Table 3.5 Coefficients for calculating average temperature for $100 \le \mathrm{Pe} \le 10,000$

$c = b/a$	v_1 $\times$-10^2	v_2 $\times 10$	v_3 $\times 10$	w_1 $\times 10^2$	w_2 $\times$-10	w_3 $\times 10$	z_1 $\times$-10	z_2	z_3 $\times 10$
2.0	52.695	21.653	7.251	39.214	16.078	10.991	15.302	10.154	56.902
1.5	60.736	25.004	12.780	44.572	18.345	18.038	15.650	10.215	59.446
1.25	66.148	27.277	16.353	48.113	19.860	22.658	15.854	10.247	61.241
1.0	73.144	30.233	20.779	52.727	21.838	28.617	16.232	10.332	64.081
0.9	76.638	31.709	22.895	55.049	22.830	31.508	16.219	10.309	64.980
0.8	80.699	33.427	25.313	57.658	23.960	34.855	16.350	10.334	66.510
0.7	85.526	35.473	28.158	60.834	25.326	38.915	16.513	10.369	68.438
0.6	91.497	38.001	31.684	64.793	27.024	44.073	16.708	10.416	70.910
0.5	99.230	41.268	36.318	69.980	29.240	51.078	16.970	10.487	74.317
0.4	110.031	45.813	43.130	77.324	32.360	61.687	17.359	10.610	79.433
0.25	139.621	58.246	65.135	97.799	41.050	96.984	18.603	11.073	95.757

Table 3.6 Coefficients for calculating maximum temperature for $100 \le \mathrm{Pe} \le 10,000$

$c = b/a$	v_1 $\times$-10	v_2 $\times 10$	v_3 $\times 10$	w_1 $\times 10$	w_2 $\times$-10	w_3 $\times 10$	z_1 $\times$-10	z_2	z_3 $\times 10$
2.0	13.55	56.85	37.331	9.241	39.166	50.417	25.259	16.109	65.885
1.5	15.17	64.00	42.951	10.257	43.730	59.117	25.838	16.312	68.988
1.25	16.38	69.37	47.384	10.959	46.988	65.642	26.194	16.441	71.296
1.0	18.20	77.46	54.808	11.997	51.802	76.837	27.334	16.853	76.072
0.9	18.97	81.17	58.171	12.371	53.821	82.112	26.862	16.702	76.539
0.8	19.96	85.84	62.726	12.894	56.455	89.394	27.083	16.791	78.765
0.7	21.22	91.80	68.952	13.540	59.732	99.260	27.356	16.905	81.644
0.6	22.76	99.29	77.182	14.187	63.411	111.80	27.666	17.045	85.449
0.5	24.81	109.35	89.307	14.994	68.165	130.54	28.114	17.252	90.947
0.4	27.59	123.13	107.79	16.040	74.460	159.03	28.826	17.583	99.566
0.25	33.71	154.89	161.96	16.322	81.291	210.73	31.042	18.605	127.14

3.5.2 Comparing curve fits with numerical solution

The values of the average and the maximum temperatures from the curve fit equations are compared with those obtained from the full computational analysis in Figures 3.8–3.10. Figure 3.8 shows the values of average temperature rise at Peclet no. of 0.05 for different thermal conductivity and ellipticity ratios. It can be seen that the values obtained from the curve fit relations are in excellent agreement with those obtained from the computational analysis. For the range of $0 < \mathrm{Pe} \leq 5$ the percentage error between the temperature values computed from the curve fit Eqs. (2.72) and (2.73), and the values obtained from the full computational analysis was less than 0.08% over the entire range of thermal conductivity ratio (0.25 − 10) and ellipticity (0.25 − 2). Similar observations are made in Figure 3.9, which illustrates the values of maximum temperature at Pe = 75 for several different values of thermal conductivity and ellipticity ratio. The percentage error between the temperature values obtained from the curve fit Eqs. (2.74)and (2.75), and those obtained from the full computational analysis was less than 1% over the entire range of Peclet number ($5 \leq \mathrm{Pe} \leq 100$), thermal conductivity ratio (0.25−10) and ellipticity (0.25−2).

Figure 3.10 presents the comparison of maximum temperature rise obtained from the computation analysis and the curve fit Eqs. ((2.76) and (2.77)) for the Peclet number of 250 over a wide range of thermal conductivity and ellipticity ratios. Again, excellent agreement is observed. For the ranges of $100 \leq \mathrm{Pe} \leq 10,000$ the percentage error between the temperature values computed from the curve fit Eqs. (2.76) and (2.77) and the values obtained from the full computational analysis was less than 1.4% over the entire range of thermal conductivity ratios (0 − 10) and ellipticity (0.25 − 2).

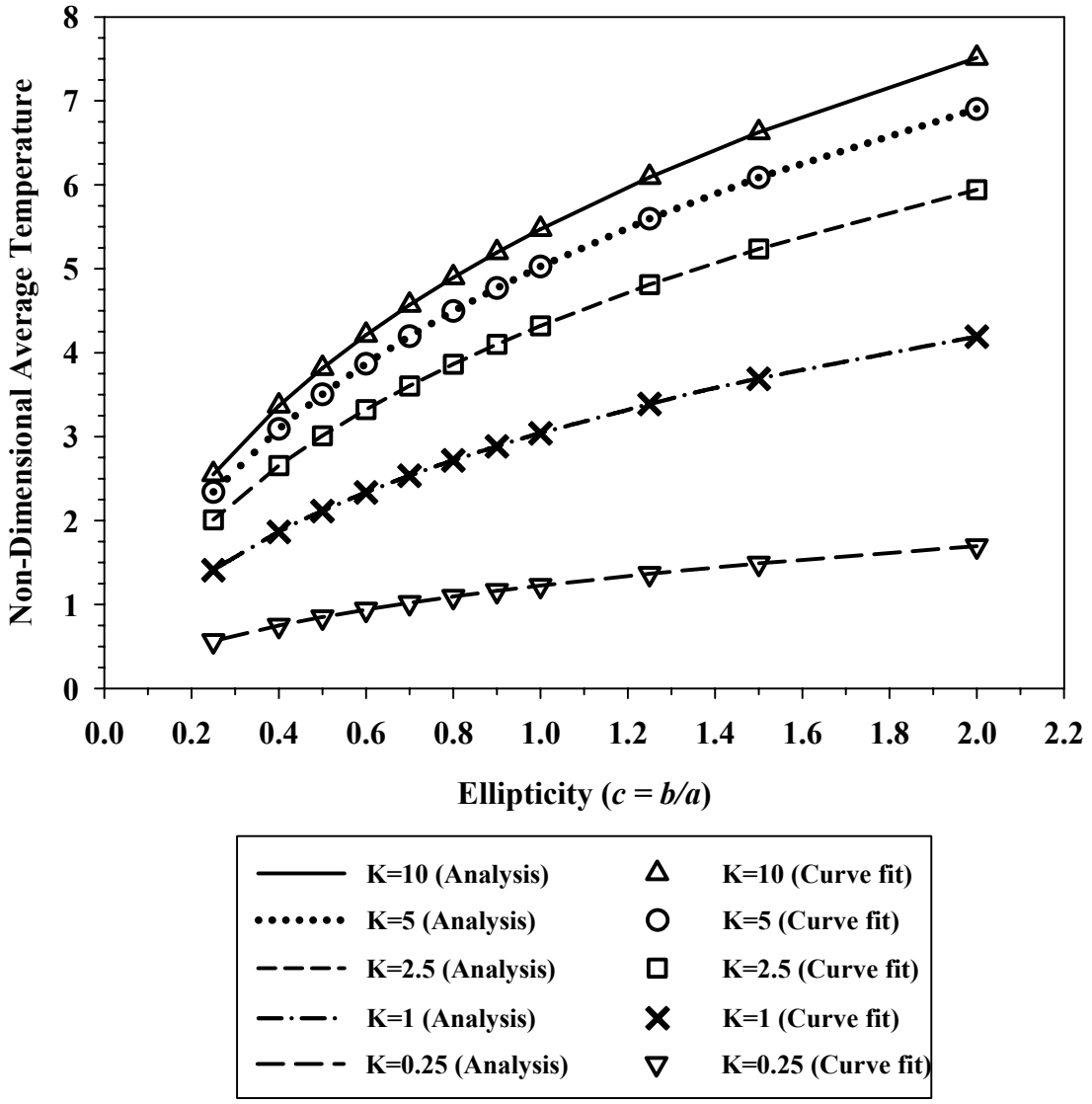

Figure 3.8 **Validation of curve fit relations for average temperature vs. ellipticity for Pe = 0.05 at several thermal conductivity ratios**

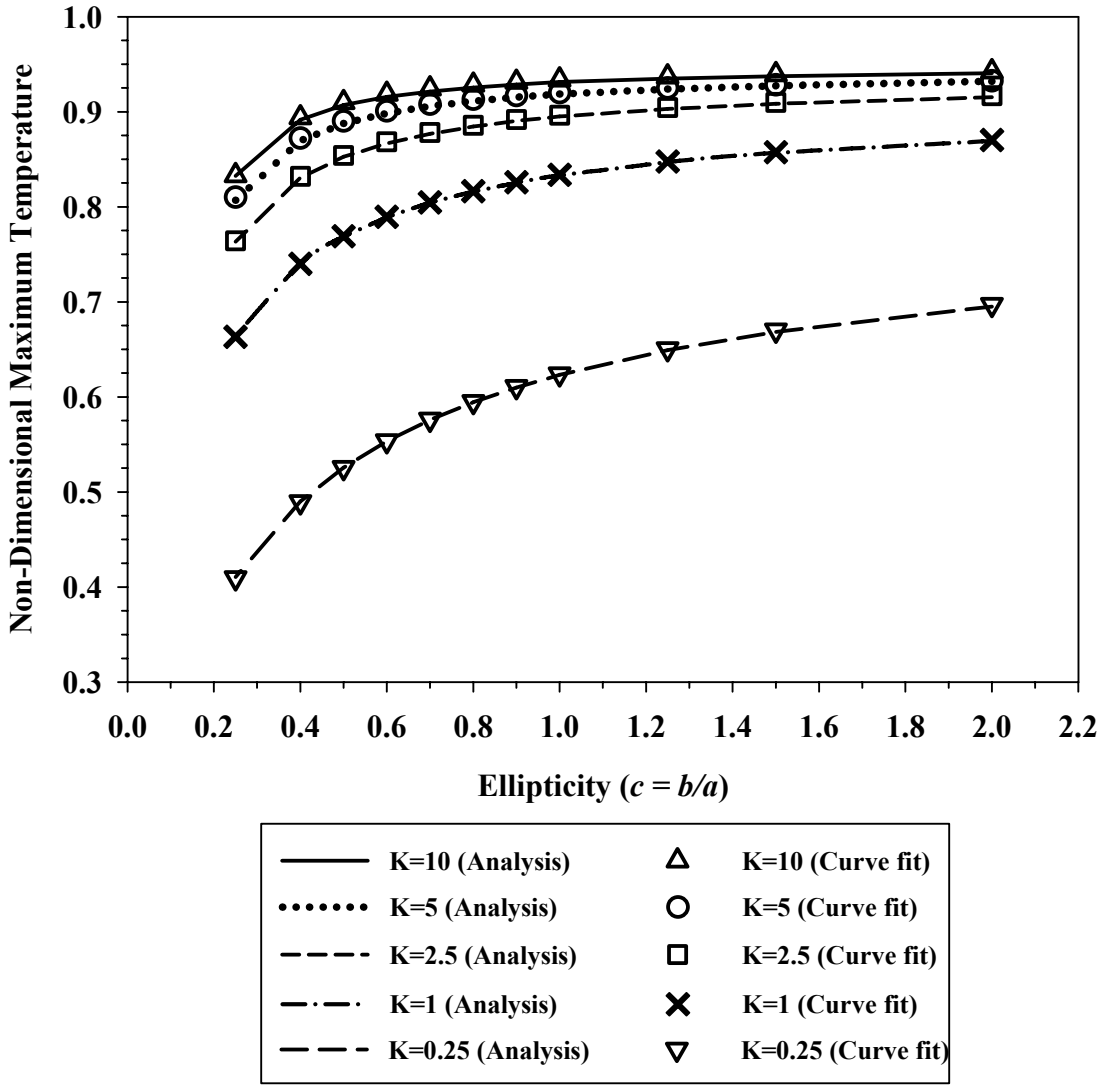

Figure 3.9 Validation of curve fit relations curve fit relations for maximum temperature vs. ellipticity for Pe = 75 at several thermal conductivity ratios

Figure 3.11 presents the comparison of non-dimensional maximum temperature as a function of Peclet no. for several values of thermal conductivity ratios and ellipticity ratio of c = 0.5. It is observed that the curve fit relations provide accurate predictions of the temperature rise over wide range of Peclet nos. and thermal conductivity ratios.

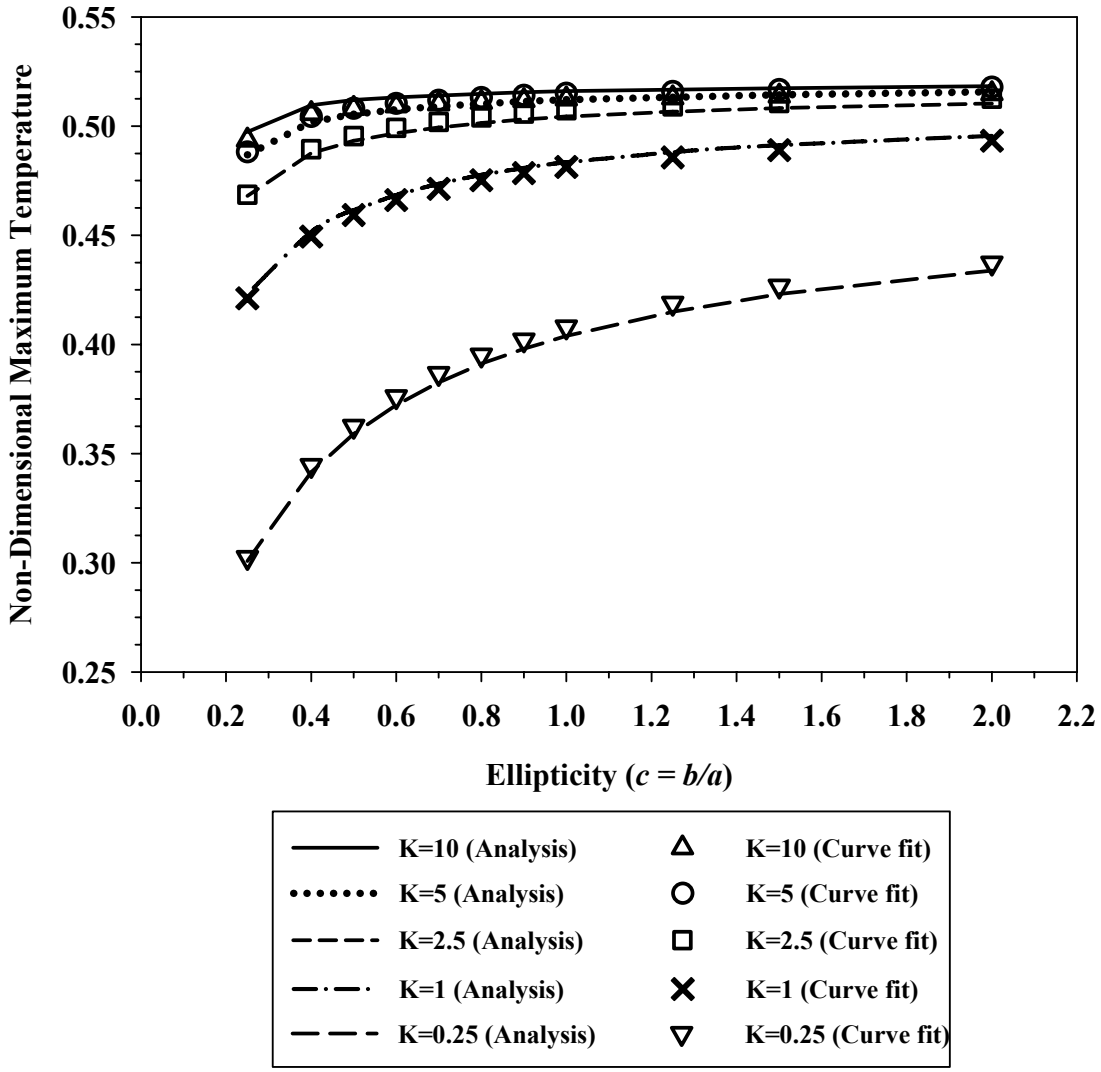

Figure 3.10 Validation of curve fit relations for maximum temperature at Pe = 250 for several thermal conductivity ratios

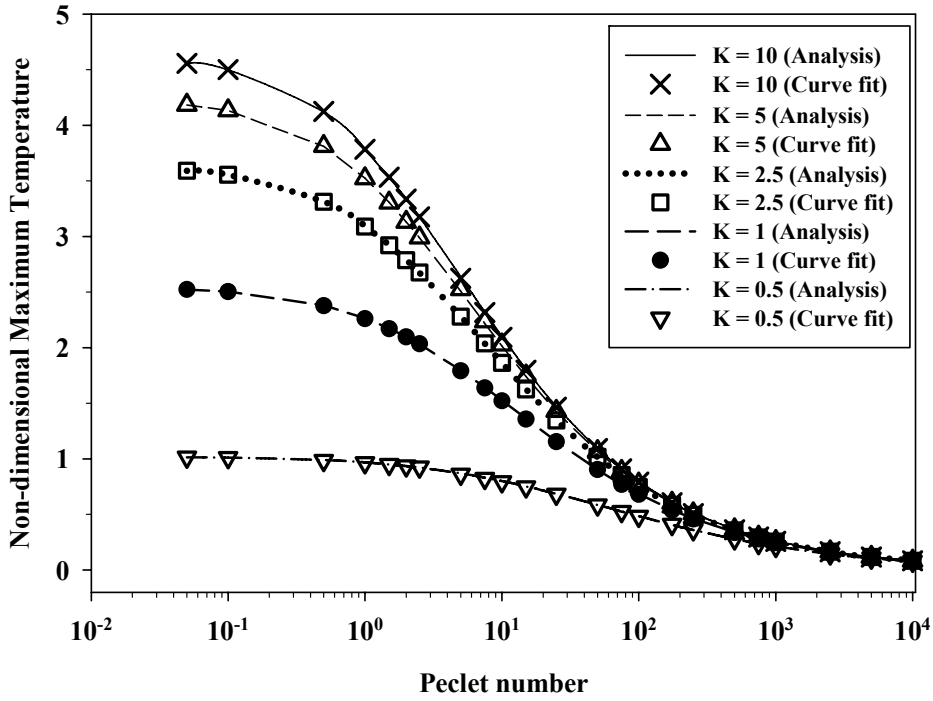

(a)

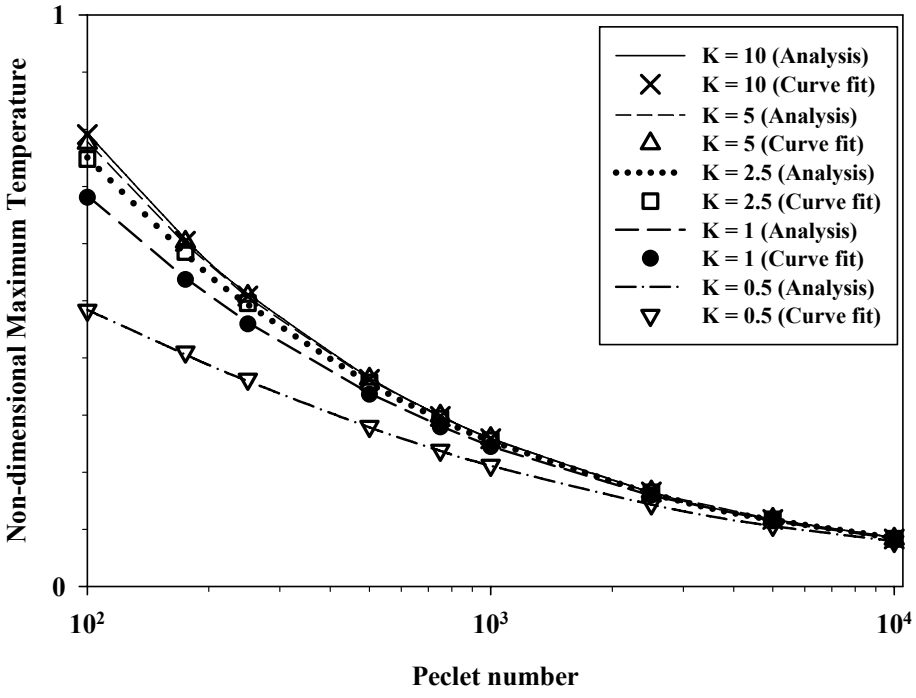

(b)

Figure 3.11 Validation of curve fit relations for maximum temperature for several thermal conductivity ratios and Pe nos., for $c = 0.5$

3.6 Bodies at different initial temperatures ($\Delta\Psi \neq 0$)

In this section the curve fit equations for computing the average and the maximum interface temperature are presented for the more general case of the two bodies having different initial temperatures. For the sake of clarity let us define a frictional heat partition variable λ which is the ratio of fraction of the frictional heat generated that is transferred into the Body 2, i.e.

$$\lambda(x,y) = \frac{q_{2f}(x,y)}{q_f(x,y)} = \frac{q_{2f}(x,y)}{q(x,y)} \tag{2.78}$$

Using Eqs. (2.3) and (2.6) the above equation can be expressed as

$$\sigma(x,y) = \lambda(x,y) + q^*(x,y) \tag{2.79}$$

where $q^*(x,y) = q'(x,y)/q(x,y)$

Now Eqs. (2.68) and (2.69) can be expressed as

$$\Theta_1(\rho,\theta) = K\int_{\phi=0}^{2\pi}\int_{s=0}^{s_b(\rho,\theta,\phi)}\left[\left(1-\lambda(s,\phi)\right)f(s,\phi) - Q^*(\rho,\theta,s,\phi)\right]dsd\phi + \Psi_1 \tag{2.80}$$

$$\Theta_2(\rho,\theta) = \int_{\phi=0}^{2\pi}\int_{s=0}^{s_b(\rho,\theta,\phi)}\left[\lambda(s,\phi)f(s,\phi) + Q^*(\rho,\theta,s,\phi)\right]\exp\left\{-\mathrm{Pe}\, s\left(1+\cos\phi\right)\right\}dsd\phi + \Psi_2 \tag{2.81}$$

where $Q^* = q^* f = q'/q_o$

Applying the condition of continuity of temperature across the interface at each point within the contact region, we set $\Theta_1(\rho,\theta) = \Theta_2(\rho,\theta) = \Theta(\rho,\theta)$, which, after rearrangement, leads to

$$\Delta\Psi + K\int_{\phi=0}^{2\pi}\int_{s=0}^{s_b(\rho,\theta,\phi)} f(s,\phi)\,ds\,d\phi = \int_{\phi=0}^{2\pi}\int_{s=0}^{s_b(\rho,\theta,\phi)} f(s,\phi)\lambda(s,\phi)\left[K+\exp\left\{-\mathrm{Pe}\,s\left(1+\cos\phi\right)\right\}\right]ds\,d\phi + \int_{\phi=0}^{2\pi}\int_{s=0}^{s_b(\rho,\theta,\phi)} Q^*(\rho,\theta,s,\phi)\left[K+\exp\left\{-\mathrm{Pe}\,s\left(1+\cos\phi\right)\right\}\right]ds\,d\phi \tag{2.82}$$

Since by definition Q^* is the heat flux associated with an initial bulk temperature difference between the bodies, it has no influence on λ, which is a frictional heat partition fraction. Thus λ and Q^* are independent of each other. Moreover, in the special case of no initial temperature difference both $\Delta\Psi$ and Q^* vanish, so we must have:

$$K\int_{\phi=0}^{2\pi}\int_{s=0}^{s_b(\rho,\theta,\phi)} f(s,\phi)\,ds\,d\phi = \int_{\phi=0}^{2\pi}\int_{s=0}^{s_b(\rho,\theta,\phi)} f(s,\phi)\lambda(s,\phi)\left[K+\exp\left\{-\mathrm{Pe}\,s\left(1+\cos\phi\right)\right\}\right]ds\,d\phi \tag{2.83}$$

Then using the above relation, which is valid for all $\Delta\Psi$, in Eq. (2.82), we obtain

$$\Delta\Psi = \int_{\phi=0}^{2\pi}\int_{s=0}^{s_b(\rho,\theta,\phi)} Q^*(\rho,\theta,s,\phi)\left[K+\exp\left\{-\mathrm{Pe}\,s\left(1+\cos\phi\right)\right\}\right]ds\,d\phi \tag{2.84}$$

Now Eq. (2.83) is of the same form as (2.21) when $\Delta\Psi = 0$ and the solution strategy for it remains the same as discussed in Chapter 2 and in [53]. The associated curve fit equations for computing the maximum and the average temperature rise in this homogenous case have been already discussed in Section 3.4.1.

In order to arrive at curve fit equations for the scenario of $\Delta\Psi \neq 0$ we proceed in the following manner. Let us define $\tilde{Q}$ such that

$$\tilde{Q}(\rho,\theta)=\frac{\int_{\phi=0}^{2\pi}\int_{s=0}^{s_b(\rho,\theta,\phi)} Q^*(\rho,\theta,s,\phi)\left[K+\exp\left\{-\mathrm{Pe}\, s\left(1+\cos\phi\right)\right\}\right]dsd\phi}{\int_{\phi=0}^{2\pi}\int_{s=0}^{s_b(\rho,\theta,\phi)}\left[K+\exp\left\{-\mathrm{Pe}\, s\left(1+\cos\phi\right)\right\}\right]dsd\phi} \tag{2.85}$$

Using the above equation, Eq. (2.84) can be expressed as

$$\Delta\Psi=\tilde{Q}\int_{\phi=0}^{2\pi}\int_{s=0}^{s_b(\rho,\theta,\phi)}\left[K+\exp\left\{-\mathrm{Pe}\, s\left(1+\cos\phi\right)\right\}\right]dsd\phi \tag{2.86}$$

Also using Eq. (2.85) one can write

$$\tilde{Q}=\frac{K\int_{\phi=0}^{2\pi}\int_{s=0}^{s_b(\rho,\theta,\phi)} Q^*dsd\phi}{\int_{\phi=0}^{2\pi}\int_{s=0}^{s_b(\rho,\theta,\phi)}\left[K+\exp\left\{-\mathrm{Pe}\, s\left(1+\cos\phi\right)\right\}\right]dsd\phi}+\frac{\int_{\phi=0}^{2\pi}\int_{s=0}^{s_b(\rho,\theta,\phi)} Q^*\exp\left\{-\mathrm{Pe}\, s\left(1+\cos\phi\right)\right\}dsd\phi}{\int_{\phi=0}^{2\pi}\int_{s=0}^{s_b(\rho,\theta,\phi)}\left[K+\exp\left\{-\mathrm{Pe}\, s\left(1+\cos\phi\right)\right\}\right]dsd\phi} \tag{2.87}$$

which in the simpler form can be expressed as

$$\tilde{Q}(\rho,\theta)=\tilde{Q}_1(\rho,\theta)+\tilde{Q}_2(\rho,\theta) \tag{2.88}$$

Substituting Eqs. (2.86), (2.87),and (2.88) in Eq. (2.81),we get

$$\Theta(\rho,\theta)=\int_{\phi=0}^{2\pi}\int_{s=0}^{s_b(\rho,\theta,\phi)}\lambda(s,\phi)\,f(s,\phi)\exp\left\{-\mathrm{Pe}\, s\left(1+\cos\phi\right)\right\}dsd\phi+Q_2(\rho,\theta)\frac{\Delta\Psi}{Q(\rho,\theta)}+\Psi_2$$

which can be written, more simply as

$$\Theta(\rho,\theta)-\Psi_2=\Theta_o(\rho,\theta)+\frac{\tilde{Q}_2(\rho,\theta)}{\tilde{Q}(\rho,\theta)}\Delta\Psi \tag{2.89}$$

where $\Theta_o(\rho,\theta)$ is the interfacial temperature *rise* when $\Delta\Psi=0$.

In the special case of two stationary bodies with dissimilar initial temperatures the ratio $\tilde{Q}_2/\tilde{Q}$ reduces to

$$\frac{\tilde{Q}_2}{\tilde{Q}} = \frac{\int_{\phi=0}^{2\pi} \int_{s=0}^{s_b(\rho,\theta,\phi)} Q^* ds d\phi}{(1+K)\int_{\phi=0}^{2\pi} \int_{s=0}^{s_b(\rho,\theta,\phi)} Q^* ds d\phi} = \frac{1}{1+K} \tag{2.90}$$

In order to arrive at the curve fit equations for computing the average and the maximum temperature rise for the case of bodies with dissimilar initial temperatures we have to find the curve fit equations for the ratio $\tilde{Q}_2 / \tilde{Q}$ as a function of Peclet number for different ellipticities. To do so, we rearrange Eq. (2.89) such that

$$\frac{\tilde{Q}_2(\rho,\theta)}{\tilde{Q}(\rho,\theta)} = \frac{\left(\Theta(\rho,\theta) - \Psi_2\right) - \Theta_o(\rho,\theta)}{\Delta\Psi} \tag{2.91}$$

The RHS of Eq. (2.91) is evaluated by solving Eq. (2.21) for both the given initial temperature difference, yielding $\Theta(\rho,\theta)$, as well as for the homogeneous case, yielding $\Theta_o(\rho,\theta)$.

Proceeding in this manner it was found that the average value of the ratio $\tilde{Q}_2 / \tilde{Q}$, for a given ellipticity ratio, can be expressed approximately as

$$\overline{\left(\frac{\tilde{Q}_2}{\tilde{Q}}\right)} = \frac{1}{1+K\left(\alpha Pe^{\beta} + \delta\right)} \tag{2.92}$$

where the values of α, β and δ are listed in the Table 3.7 for the three different ranges of Peclet numbers (similar to ones in Section 3.5.1) and different ellipticity ratios. Substituting Eq. (2.92) into Eq. (2.89) the average interface temperature relative to Ψ_2 is given as,

$$\bar{\Theta} - \Psi_2 = \bar{\Theta}_o + \frac{\Delta\Psi}{1+K\left(\alpha Pe^{\beta} + \delta\right)} \tag{2.93}$$

Figure 3.12 illustrates the comparison between the average interface temperature relative to Body 2 as calculated using the curve fit Eq. (2.93) and those obtained from regression analysis using Eq. (2.26) for the case of for $\Delta\Psi = 2$, K = 1 and several ellipticity ratios. The percentage error between the average temperature computed from the curve fit equations and those obtained using the regression analysis was less than 1%.

Figure 3.13 presents the comparison between the average interface temperature relative to Body 2 as calculated from the curve fit equations and computational analysis over a broad range of Peclet numbers for K = 1.5, ellipticity of 0.8 and different $\Delta\Psi$'s. It is seen that the curve fit equations accurately predict the interface temperature rise for the case of two bodies with different initial temperatures.

Table 3.7 Coefficients for calculating average temperature for $\Delta\Psi \neq 0$

c = b/a	$0 < \text{Pe} \leq 5$			$5 \leq \text{Pe} \leq 100$			$100 \leq \text{Pe} \leq 10,000$		
	α	β	δ	α	β	δ	α	β	δ
2.0	0.81	0.745	1	1.87	0.482	-0.32	5.2	0.345	-7.50
1.5	0.67	0.75	1	1.151	0.5	0.015	3.08	0.418	-6.00
1.25	0.61	0.76	1	1.375	0.505	0.02	2.73	0.424	-5.35
1.0	0.533	0.763	1	1.19	0.51	0.175	2.1	0.446	-4.00
0.9	0.496	0.761	1	1.1	0.512	0.28	2	0.444	-3.60
0.8	0.47	0.757	1	1	0.516	0.32	1.88	0.442	-3.30
0.7	0.445	0.75	1	0.925	0.518	0.35	1.75	0.44	-2.90
0.6	0.415	0.745	1	0.815	0.527	0.5	1.68	0.432	-2.60
0.5	0.373	0.733	1	0.71	0.53	0.55	1.52	0.435	-2.85
0.4	0.336	0.72	1	0.61	0.535	0.6	1.18	0.445	-1.40
0.25	0.27	0.69	1	0.418	0.54	0.84	0.72	0.47	-0.50

In order to develop a simple analytical approximation to the maximum interfacial temperature rise, a functional form identical to that of Eq. (2.92) was used. However accurate curve fits were obtainable only for the Peclet number range of $0 < Pe \leq 15$. The values of α, β and δ in Eq. (2.92) for computing maximum value of the ratio Q_2 / Q are listed in the Table 3.8 for different ellipticity ratios.

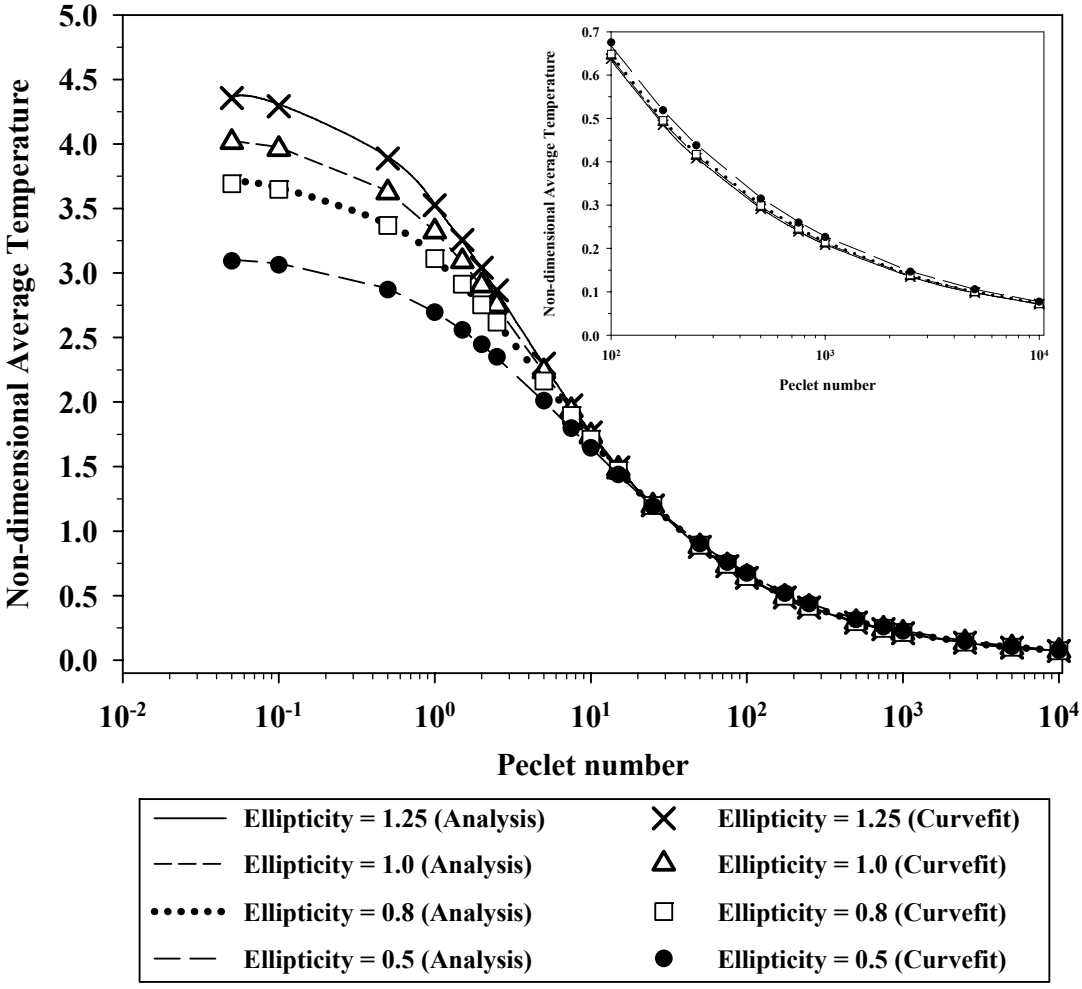

Figure 3.12 Validation of curve fit relations for average interface temperature relative to Ψ_2, for $\Delta\Psi = 2$ and $K = 1$

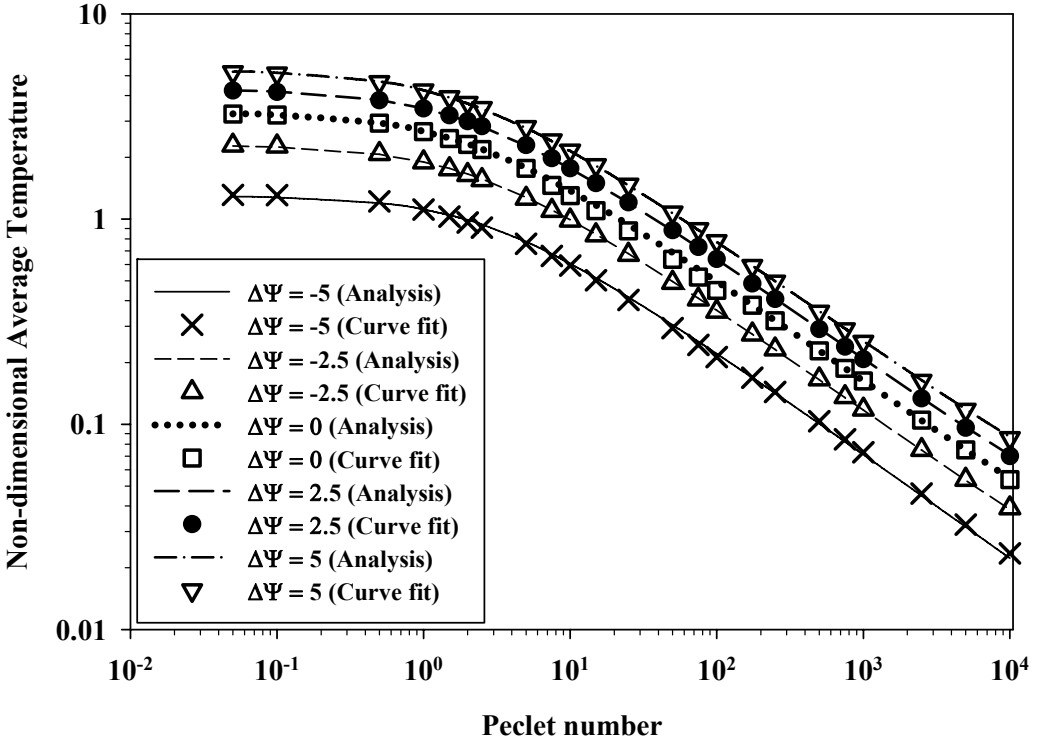

Figure 3.13 Validation of curve fit relations for average interface temperature relative to Ψ_2, for $K = 1.5$ and ellipticity of 0.8

Table 3.8 Coefficients for calculating maximum temperature for $\Delta\Psi \neq 0$

$c = b/a$	$0 < Pe \leq 15$		
	α	β	δ
2.0	0.74	0.76	1
1.5	0.63	0.755	1
1.25	0.57	0.75	1
1.0	0.49	0.748	1
0.9	0.485	0.745	1
0.8	0.445	0.725	1
0.7	0.42	0.722	1
0.6	0.385	0.72	1
0.5	0.35	0.71	1
0.4	0.325	0.68	1
0.25	0.265	0.665	1

It should be noted that Barber [55] conducted a related analysis wherein he presented an equation for computing the interfacial temperature in the presence of friction when the remote boundaries of the two bodies are maintained at different temperatures. However Barber does not distinguish the function that relates surface temperature rise to surface heat flux from the function that relates remote boundary temperature rise to surface heat flux. Moreover, the author feels that it is more physically sound to analyze bodies that begin at different initial temperatures and then reach steady-state in the vicinity of the contact, than to envisage bodies whose remote boundaries are maintained (somehow) at a fixed temperature.

3.7 Comparions with Kuhlmann-Wilsdorf

In this section the predictions of the average and the maximum temperature from Kuhlmann-Wilsdorf [12] (hereon referred to as K-W) are compared with the results of the curve fit equations presented in Section 3.4. The equations used by K-W were based on asymptotic values of temperature rise at very low and very high sliding velocities. An equation accounting for the shape of the contact region was presented, which, as the author herself pointed out, is not accurate for elliptical contact geometry. The author defined the flash temperature over the contact area to be proportional to the average temperature of the volume under the contact spot that receives the heat during the time interval it remains in contact. The equations presented in [12] suggest that the average flash temperature rise is $\pi/4$ times the maximum flash temperature rise irrespective of the thermal conductivities of the bodies in contact and the geometry of the contact.

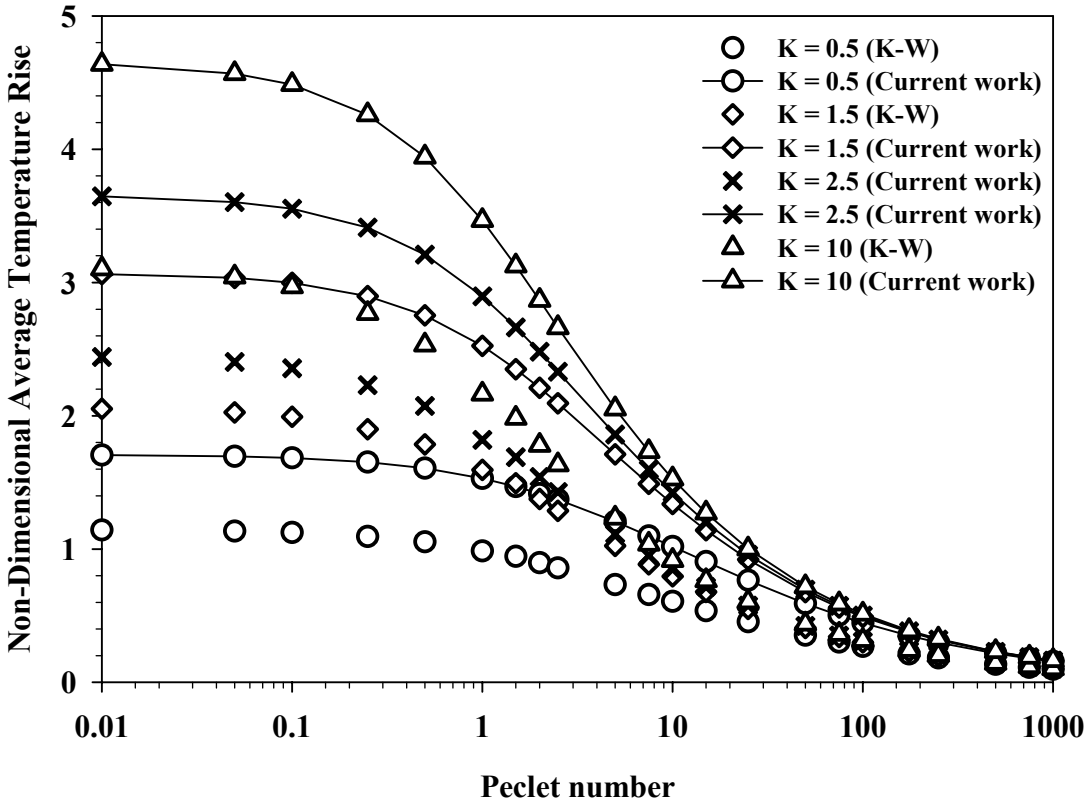

Figure 3.14 Comparison of average interface temperature with Kuhlmann-Wilsdorf [12] for ellipticity of 0.7

In this section we compare the average flash temperature and the maximum flash temperature using K-W's equations with the average and the maximum temperature of the interface as computed form the curve fit equations presented in the previous section.

Figure 3.14 provides a comparison of average temperature rise obtained from the curve fit equations presented earlier of with those of K-W for an elliptical contact with ellipticity of 0.7 for several Peclet numbers and thermal conductivity ratios. It is observed that at a thermal conductivity ratio of 0.5 the average temperature predicted by K-W's analysis is 33 – 40% lower than the average temperature obtained from the current work.

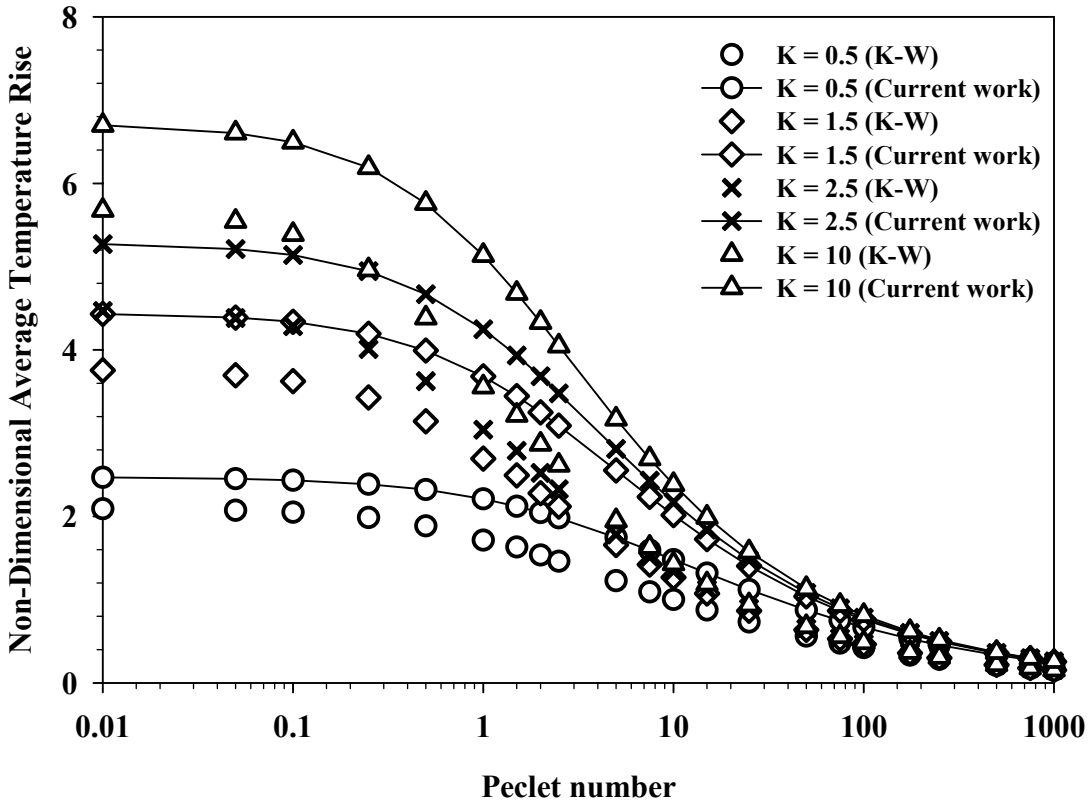

Figure 3.15 Comparison of maximum interface temperature with Kuhlmann-Wilsdorf [12] for circular contact

Figure 3.15 illustrates the comparison between the maximum flash temperature computed from K-W's analysis and maximum interface temperature obtained from the current work for the case of a circular contact for several Peclet numbers and thermal conductivity ratios. It is observed that for a circular contact, the K-W analysis under predicts the maximum temperature by 15 – 35% over the entire range of Peclet numbers and this error is independent of the thermal conductivity ratio.

It is also noted here that for ellipticity ratios greater than 1, the K-W analysis was found to over-predict the average and the maximum temperatures by 4 – 20% at low Peclet number (Pe < 1.5).

3.8 Summary

A least squares regression-based methodology is implemented for obtaining the steady-state temperature distribution at the interface of two sliding bodies. The local frictional dissipation rate at the interface was assumed to be the product of the friction coefficient, the pressure and the sliding velocity. Circular and elliptical contacts with semi-ellipsoidal (Hertzian) pressure distribution are considered. Integral equations were developed, expressing the temperatures of each body in terms of an unknown heat partition function. By assuming a polynomial form for the heat partition function and optimizing the coefficients to obtain the least squares difference in temperature at the interface between the two bodies, an estimate for the heat partition function was obtained. Calculations were performed for several ellipticity ratios between 2 and 0.25, thermal conductivity ratios ranging from 0.25 to 10 and various Peclet nos. ranging from 0 to 10,000. Based on the values of maximum and average temperature rise obtained from the computational analysis, several reasonably simple, but highly accurate curve fit equations were developed. It is envisioned that these equations will aid designers in correctly estimating temperature rise in elliptical contacts.

CHAPTER 4. HEAT PARTITION IN ELECTRICAL CONTACTS

4.1 Introduction

When two engineering bodies with rough surfaces are brought into contact, they make contact at asperity peaks called "*a*-spots". Each a-spot represents a local reduction in the cross-sectional area for electrical conduction and the added electrical resistance due to this constriction is referred to as constriction resistance. The overall constriction resistance is a function of the sizes and shapes of the a-spots as well as their relative locations. The total interface or contact resistance is then given by the sum of the constriction resistance and the film resistance due to any oxide or high-resistivity film on the surfaces [14, 56]. The heating of the interface due to Joule heat dissipation is of importance in assessing the performance reliability of the electrical contacts. In the scenario of sliding electrical contacts the presence of Coulomb heat in addition to the Joule heat causes further increase in the interface temperature.

Holm [14] was the first to present his analytical analysis of distribution of current density at the interface of elliptical and circular shapes. One can also determine the maximum interface temperature, knowing the potential drop across the interface, using Kohlraush's equation [57] or using Viedemann-Franz-Lorenz law [14, 58]. Kuhlmann-Wilsdorf [11] presented approximate relations for obtaining maximum interface temperature in sliding electrical contacts, accounting for both Coulomb and Joule heating components. There exists no model to quantify the heat partition and evaluate interface temperature distribution at the interface due to Coulomb and Joule heating.

In this chapter the heat partition model presented in Chapter 2 and [53] is extended to evaluate the heat partition and interface temperature rise due to the presence of both Coulomb and Joule heating.

4.2 Heat partition model

In addition to the assumptions for the model as listed in Chapter 2 few more assumptions are made here:

i. The contact resistance is the source of Joule heat generation

ii. Joule heat is uniformly distributed over the contact area while the Coulomb heat distribution follows the Hertzian pressure distribution

iii. Bulk Joule dissipation is neglected

iv. The electrical resistivity and thermal conductivity do not vary with temperature

Now the total heat generated at the interface is then given as:

$$q = q_f + q_j \tag{4.1}$$

where q_f and q_i are the Coulomb and the Joule heat dissipation respectively and are given as

$$\begin{aligned} q_f &= \mu p_m U \frac{3}{2}\sqrt{1-\frac{x^2}{a^2}-\frac{y^2}{b^2}} = q_o f(x,y) \\ q_j &= \frac{I^2 R_c}{\pi a b} \end{aligned} \tag{4.2}$$

where a and b are the semi-major and semi-minor axes of the contact region (for a circular contact $a = b$), $q_o = \mu p_m U$ and $f(x,y) = \frac{3}{2}\sqrt{1-\frac{x^2}{a^2}-\frac{y^2}{b^2}}$.

Note that for simplicity, uniform current density distribution has been assumed. A more realistic distribution, as given by Holm [14] for a circular contact, is of the form:

$$j(r) = \frac{I}{2\pi a^2} \frac{1}{\left(1 - r^2 / a^2\right)^{1/2}} \tag{4.3}$$

where *j(r)* is the current density as the function of the radial location *r* and *a* is the contact radius. However, using this form of heat generation in temperature rise Eq. (2.5) causes convergence issues with numerical integration.

Let q_1 and q_2 be the heat flow rates per unit area into Bodies 1 and 2, respectively, and $q(x,y)$ be their sum such that

$$q(x, y) = q_1(x, y) + q_2(x, y) \tag{4.4}$$

Let the heat partition factor, $\sigma(x, y)$, between the two bodies be defined as the ratio of the heat transfer into the moving body (Body 2) at *(x,y)* to the total heat generated at *(x,y)*, i.e.,

$$\sigma(x, y) = \frac{q_2(x, y)}{q(x, y)} \tag{4.5}$$

Using the Eqs. (2.4) and (2.5) the temperature at the interface for the bodies 1 and 2 can then be expressed as

$$\begin{aligned} T_1(x, y) = {} & \frac{q_o}{2\pi K_1} \iint \frac{\left(1 - \sigma(x', y')\right) f(x', y')}{\sqrt{(x - x')^2 + (y - y')^2}} dx' dy' \\ & + \frac{q_j}{2\pi K_1} \iint \frac{\left(1 - \sigma(x', y')\right)}{\sqrt{(x - x')^2 + (y - y')^2}} dx' dy' + T_{1i} \end{aligned} \tag{4.6}$$

$$T_2(x,y)=\frac{q_o}{2\pi K_2}\iint\sigma(x',y')f(x',y')\frac{\exp\left\{-\frac{U}{2\alpha_2}\left(\sqrt{(x-x')^2+(y-y')^2}-(x-x')\right)\right\}}{\sqrt{(x-x')^2+(y-y')^2}}dx'dy'$$
$$+\frac{q_j}{2\pi K_2}\iint\sigma(x',y')\frac{\exp\left\{-\frac{U}{2\alpha_2}\left(\sqrt{(x-x')^2+(y-y')^2}-(x-x')\right)\right\}}{\sqrt{(x-x')^2+(y-y')^2}}dx'dy'+T_{2i} \tag{4.7}$$

Introducing dimensionless variables according to

$$X=\frac{x}{a}\qquad Y=\frac{y}{a}\qquad \xi=\frac{x'}{a}\qquad \eta=\frac{y'}{a}$$
$$\mathrm{Pe}=\frac{Ua}{2\alpha_2}\qquad K=\frac{K_2}{K_1} \tag{4.8}$$

we can rewrite Eqs. (4.6) and (4.7) as

$$\left(\frac{2\pi K_2}{a}\right)\frac{T_1}{(q_o+q_j)}=K\frac{q_o}{(q_o+q_j)}\iint\frac{(1-\sigma(\xi,\eta))f(\xi,\eta)}{\sqrt{(X-\xi)^2+(Y-\eta)^2}}d\xi d\eta$$
$$+K\frac{q_i}{(q_o+q_j)}\iint\frac{(1-\sigma(\xi,\eta))}{\sqrt{(X-\xi)^2+(Y-\eta)^2}}d\xi d\eta+\left(\frac{2\pi K_2}{a}\right)\frac{T_{1i}}{(q_o+q_j)} \tag{4.9}$$

$$\left(\frac{2\pi K_2}{a}\right)\frac{T_2}{(q_o+q_j)}=\frac{q_o}{(q_o+q_j)}\iint\sigma(\xi,\eta)f(\xi,\eta)\frac{\exp\left\{-\mathrm{Pe}\left(\sqrt{(X-\xi)^2+(Y-\eta)^2}-(X-\xi)\right)\right\}}{\sqrt{(X-\xi)^2+(Y-\eta)^2}}d\xi d\eta$$
$$+\frac{q_j}{(q_o+q_j)}\iint\sigma(\xi,\eta)\frac{\exp\left\{-\mathrm{Pe}\left(\sqrt{(X-\xi)^2+(Y-\eta)^2}-(X-\xi)\right)\right\}}{\sqrt{(X-\xi)^2+(Y-\eta)^2}}d\xi d\eta$$
$$+\left(\frac{2\pi K_2}{a}\right)\frac{T_{2i}}{(q_o+q_j)} \tag{4.10}$$

Introducing the additional non-dimensional parameters

$$\Theta_1(X,Y)=T_1(x,y)\frac{2\pi K_2}{(q_o+q_j)a} \qquad \Theta_2(X,Y)=T_2(x,y)\frac{2\pi K_2}{(q_o+q_j)a}$$
$$\Psi_1=T_{1i}\frac{2\pi K_2}{(q_o+q_j)a} \qquad \Psi_2=T_{2i}\frac{2\pi K_2}{(q_o+q_j)a} \tag{4.11}$$
$$\beta_c=\frac{q_o}{(q_o+q_j)} \qquad \beta_j=\frac{q_j}{(q_o+q_j)}$$

the non-dimensional form of the temperature rise can then be written as

$$\Theta_1(X,Y)=K\beta_c\iint\frac{(1-\sigma(\xi,\eta))f(\xi,\eta)}{\sqrt{(X-\xi)^2+(Y-\eta)^2}}d\xi d\eta + K\beta_j\iint\frac{(1-\sigma(\xi,\eta))}{\sqrt{(X-\xi)^2+(Y-\eta)^2}}d\xi d\eta+\Psi_1 \tag{4.12}$$

$$\Theta_2(X,Y)=\beta_c\iint\sigma(\xi,\eta)f(\xi,\eta)\frac{\exp\left\{-\mathrm{Pe}\left(\sqrt{(X-\xi)^2+(Y-\eta)^2}-(X-\xi)\right)\right\}}{\sqrt{(X-\xi)^2+(Y-\eta)^2}}d\xi d\eta + \beta_j\iint\sigma(\xi,\eta)\frac{\exp\left\{-\mathrm{Pe}\left(\sqrt{(X-\xi)^2+(Y-\eta)^2}-(X-\xi)\right)\right\}}{\sqrt{(X-\xi)^2+(Y-\eta)^2}}d\xi d\eta+\Psi_2 \tag{4.13}$$

The singularity in the Eqs. (4.12) and (4.13) can be removed by applying change of variable as described in Chapter 3 and [59], and the final non-dimensional equations are

$$\Theta_1(\rho,\theta)=K\beta_c\int_{\phi=0}^{2\pi}\int_{s=0}^{s_b(\rho,\theta,\phi)}(1-\sigma(s,\phi))f(s,\phi)\,ds\,d\phi + K\beta_j\int_{\phi=0}^{2\pi}\int_{s=0}^{s_b(\rho,\theta,\phi)}(1-\sigma(s,\phi))\,ds\,d\phi+\Psi_1 \tag{4.14}$$

$$\Theta_2(\rho,\theta)=\beta_c\int_{\phi=0}^{2\pi}\int_{s=0}^{s_b(\rho,\theta,\phi)}\sigma(s,\phi)f(s,\phi)\exp\{-\mathrm{Pe}\,s(1+\cos\phi)\}\,ds\,d\phi + \beta_j\int_{\phi=0}^{2\pi}\int_{s=0}^{s_b(\rho,\theta,\phi)}\sigma(s,\phi)\exp\{-\mathrm{Pe}\,s(1+\cos\phi)\}\,ds\,d\phi+\Psi_2 \tag{4.15}$$

Applying the condition of continuity of temperature across the interface at each point within the contact region, we set $\Theta_1(\rho,\theta)=\Theta_2(\rho,\theta)$, which, after rearrangement, leads to

$$\Psi_1-\Psi_2+K\beta_c\int_{\phi=0}^{2\pi}\int_{s=0}^{s_b(\rho,\theta,\phi)} f(s,\phi)\,ds\,d\phi+K\beta_j\int_{\phi=0}^{2\pi}\int_{s=0}^{s_b(\rho,\theta,\phi)} ds\,d\phi=$$
$$\beta_c\int_{\phi=0}^{2\pi}\int_{s=0}^{s_b(\rho,\theta,\phi)} f(s,\phi)\,\sigma(s,\phi)\left[K+\exp\left\{-\mathrm{Pe}\,s\left(1+\cos\phi\right)\right\}\right]ds\,d\phi \qquad (4.16)$$
$$+\beta_j\int_{\phi=0}^{2\pi}\int_{s=0}^{s_b(\rho,\theta,\phi)} \sigma(s,\phi)\left[K+\exp\left\{-\mathrm{Pe}\,s\left(1+\cos\phi\right)\right\}\right]ds\,d\phi$$

The implementation of the least squares regression methodology to obtain the heat partition and the interface temperature rise has been discussed in detail in Chapter 2.

4.3 Interface temperature rise due to Joule heating

In this section we analyze the interface only with the presence of Joule heating $(q_o=0\rightarrow\beta_c=0)$. For the sake of simplicity it is assumed that both the bodies have the same initial temperatures, i.e $T_{1i}=T_{2i}$ or $\Psi_1=\Psi_2$. With these assumptions the Eq. (4.16) simplifies to

$$K\int_{\phi=0}^{2\pi}\int_{s=0}^{s_b(\rho,\theta,\phi)} ds\,d\phi=\int_{\phi=0}^{2\pi}\int_{s=0}^{s_b(\rho,\theta,\phi)} \sigma(s,\phi)\left[K+\exp\left\{-\mathrm{Pe}\,s\left(1+\cos\phi\right)\right\}\right]ds\,d\phi \qquad (4.17)$$

The non-dimensional temperature (from Eqs. (4.14) and (4.15)) is then expressed as:

$$\Theta_1(X,Y)=K\iint\frac{\left(1-\sigma(\xi,\eta)\right)}{\sqrt{(X-\xi)^2+(Y-\eta)^2}}d\xi\,d\eta \qquad (4.18)$$

$$\Theta_2(X,Y) = \iint \sigma(\xi,\eta) \frac{\exp\left\{-\mathrm{Pe}\left(\sqrt{(X-\xi)^2+(Y-\eta)^2}-(X-\xi)\right)\right\}}{\sqrt{(X-\xi)^2+(Y-\eta)^2}} d\xi d\eta \qquad (4.19)$$

Note that the above equations are similar to Eqs. (2.12) and (2.13) when $f(\xi,\eta) = 1$. Hence the results presented here are similar to those presented in Chapter 2 for uniform Coulomb heat distribution at the interface.

4.3.1 Effect of Peclet number

Figure 4.1 illustrates the non-dimensional temperature rise along the centerline of the contact region for several Peclet numbers. The non-dimensional temperature decreases as Peclet no. is increased and the maximum temperature occurs towards the trailing edge of the contact. Since the Joule heat generated at the interface is independent of the sliding velocity the non-dimensional temperature is directly correlated with the Peclet no. and the dimensional temperature is directly correlated to the sliding velocity. In other words, the non-dimensional temperature and the dimensional temperature follow the same trend with respect to Peclet no. It is seen that the interface temperature decreases as the Peclet no. is increased. As the Peclet no. is increased the time for which the part of the surface of Body 2 that remains in contact with the Body 1 decreases. This means that the heat generated at the interface is partitioned between existing hot surface of the Body 1 and the fresh surface of Body 2, or in other words Body 2 conducts the heat away from the interface and thus the lower interface temperature.

4.3.2 Effect of thermal conductivity ratio

Figure 4.2 presents variation of non-dimensional maximum temperature with Peclet no. for several values of thermal conductivity ratios K. It is seen that as the thermal conductivity ratio K is increased the non-dimensional maximum interface temperature rise also increases. At lower Peclet nos. (Pe < 5) the change in maximum temperature rise with K is substantial while, at the higher Peclet nos. (Pe > 100) little increase is observed. If K is increased solely by decreasing K_1 then the trend of dimensional temperature would be identical to that of dimensionless temperature, as seen from Eqs. (2.11) and (4.11). On the other hand, if K is increased solely by increasing K_2 the dimensional temperature would *decrease* with increasing K_2. This result is justified physically, as one would expect that a greater thermal conductivity of Body 2 would more effectively extract heat from the interface, thereby maintaining a lower temperature.

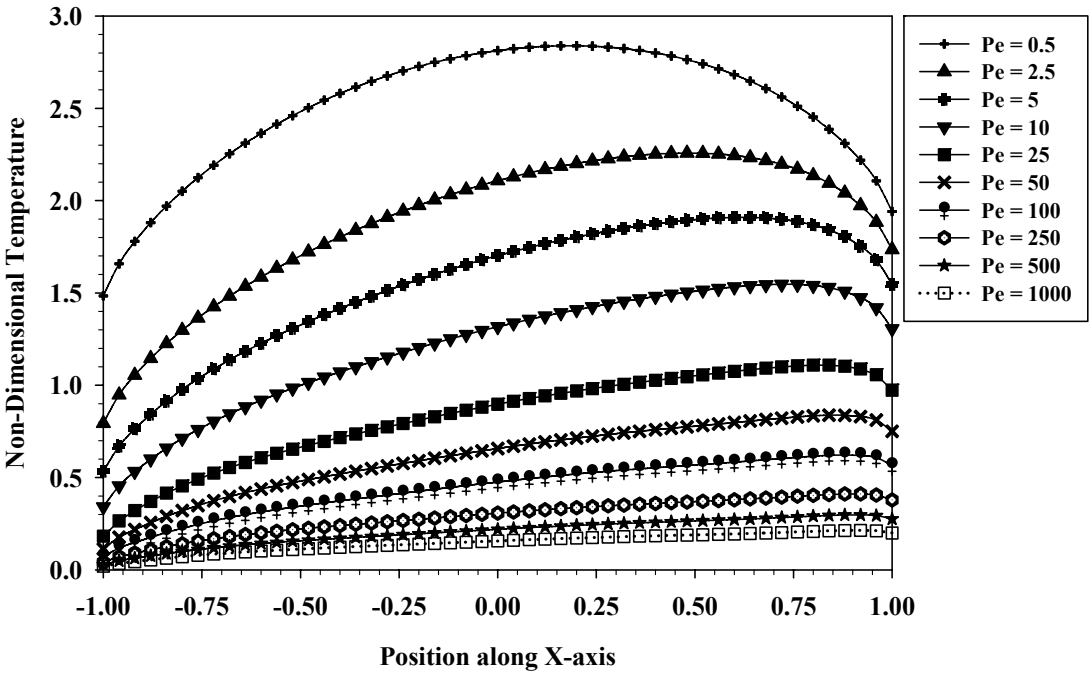

Figure 4.1 Centerline temperature for several Peclet numbers

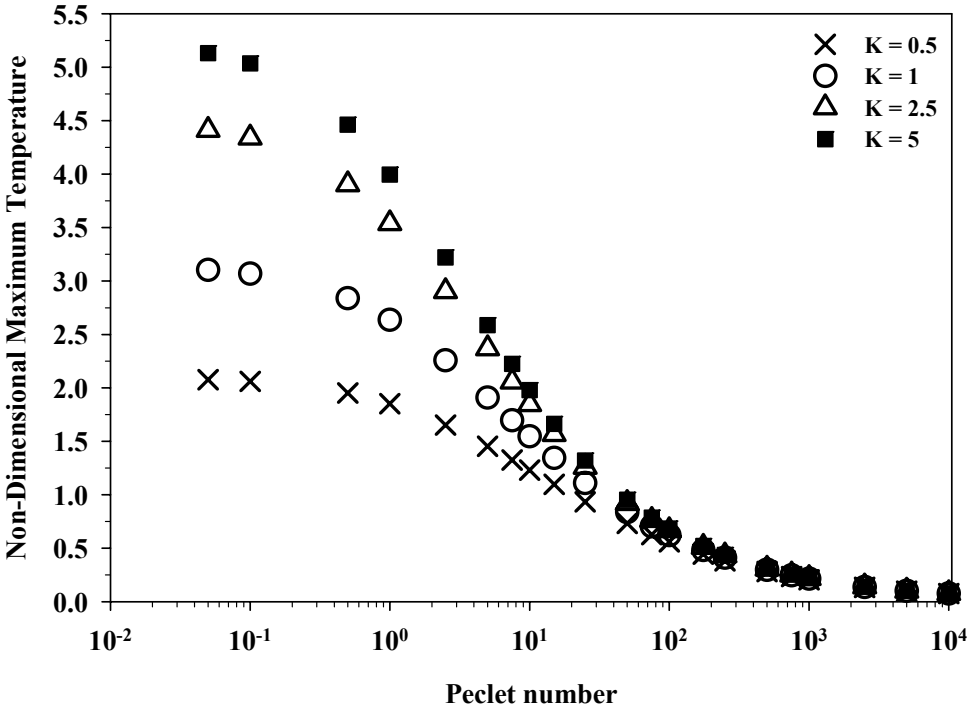

Figure 4.2 Dimensionless temperature vs. Peclet no. for several values of *K*

4.4 Interface temperature rise due to Coulomb and Joule heating

In this section the interface with the presence of both Coulomb heat and Joule heat is analyzed, i.e. of a sliding electrical contact. For the sake of simplicity it is assumed that both the bodies have the same initial temperatures, i.e $T_{1i} = T_{2i}$ or $\Psi_1 = \Psi_2$. Figure 4.3 (a) and (b) present the temperature distributions at the interface for the Peclet nos. of 0.5 and 10 respectively and $\beta_c = \beta_j = 0.5$. The maximum non-dimensional temperature is 3.11 for the Peclet no. of 0.5 and is 1.68 at the Peclet no. of 10.

Figure 4.4 shows the non-dimensional temperature rise along the centerline of the contact region for the case of interface with different combinations of Joule heat and Coulomb heat. It is observed that the non-dimensional temperature is highest for the case of interface with only Coulomb heat. As the percentage of the Joule heat is increased,

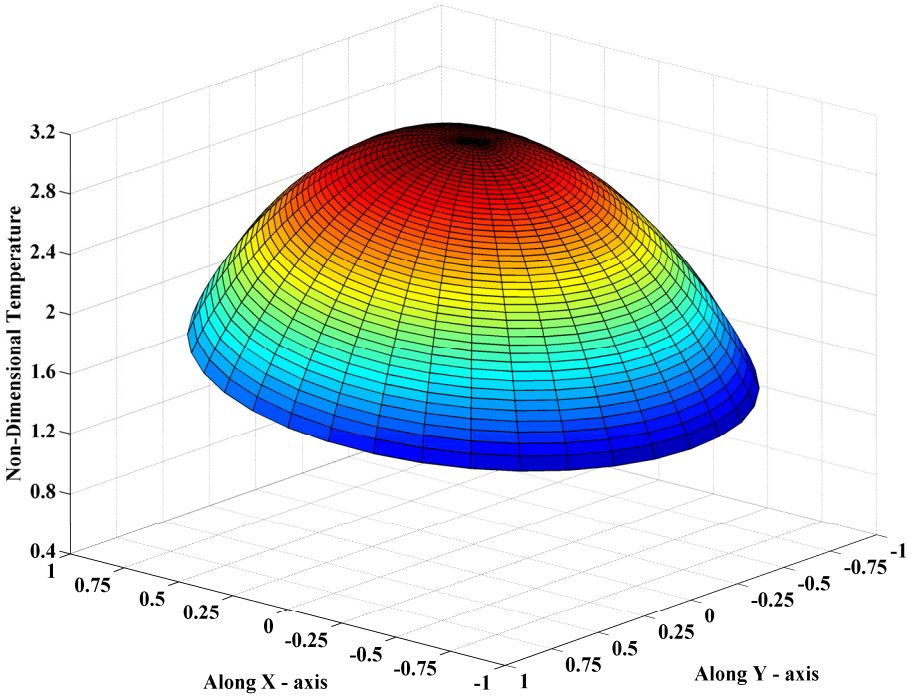

(a)

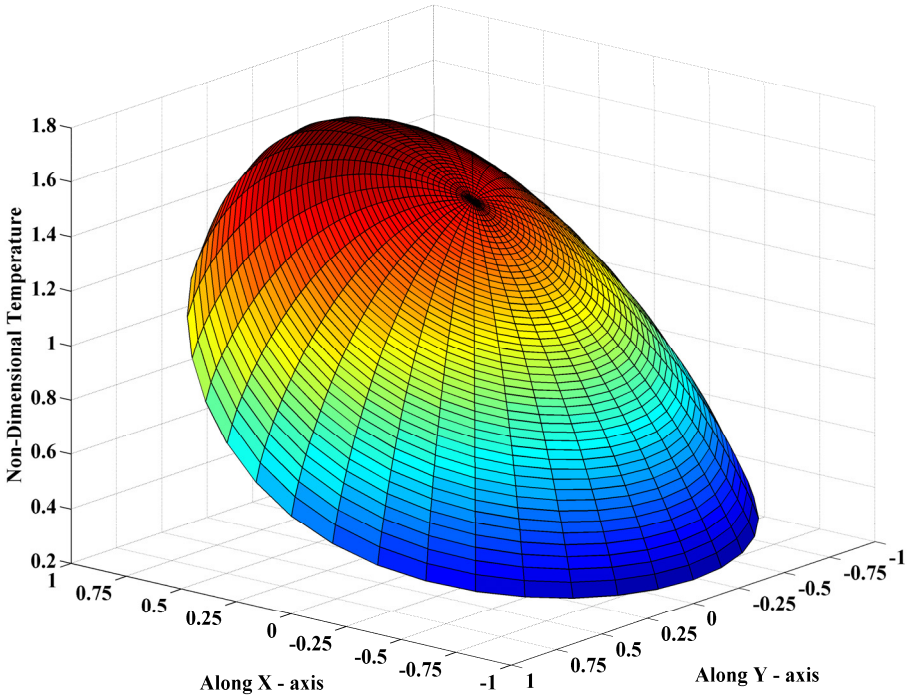

(b)

Figure 4.3 Interface temperature distribution for $\beta_c = \beta_j = 0.5$ and (a) Pe = 0.5, (b) Pe = 10

(keeping $\beta_c + \beta_j = 1$), the maximum interface temperature decreases and the position of the maximum temperature moves towards the edge of the contact as compared to the case of $\beta_c = 1, \beta_j = 0$. This is further explained by Figure 4.5 which presents the maximum interface temperature against Peclet no. for different percentages of Joule heat and Coulomb heat at the interface.

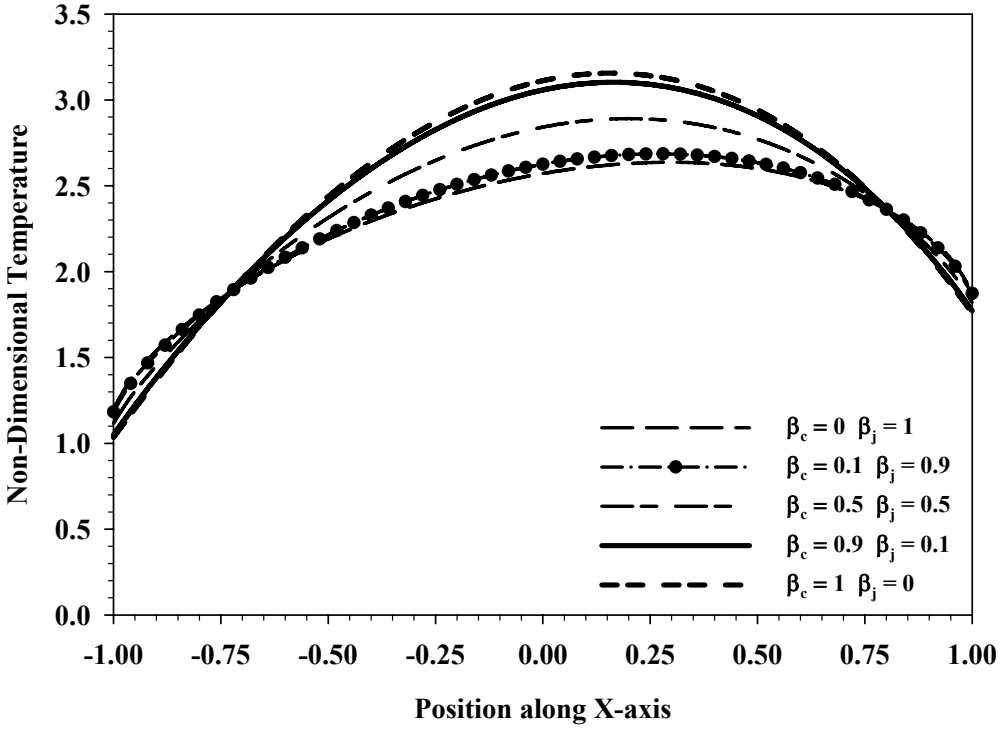

Figure 4.4 Temperature along the centerline of the contact for Peclet no. of 1 for varying proportions Coulomb and Joule heat

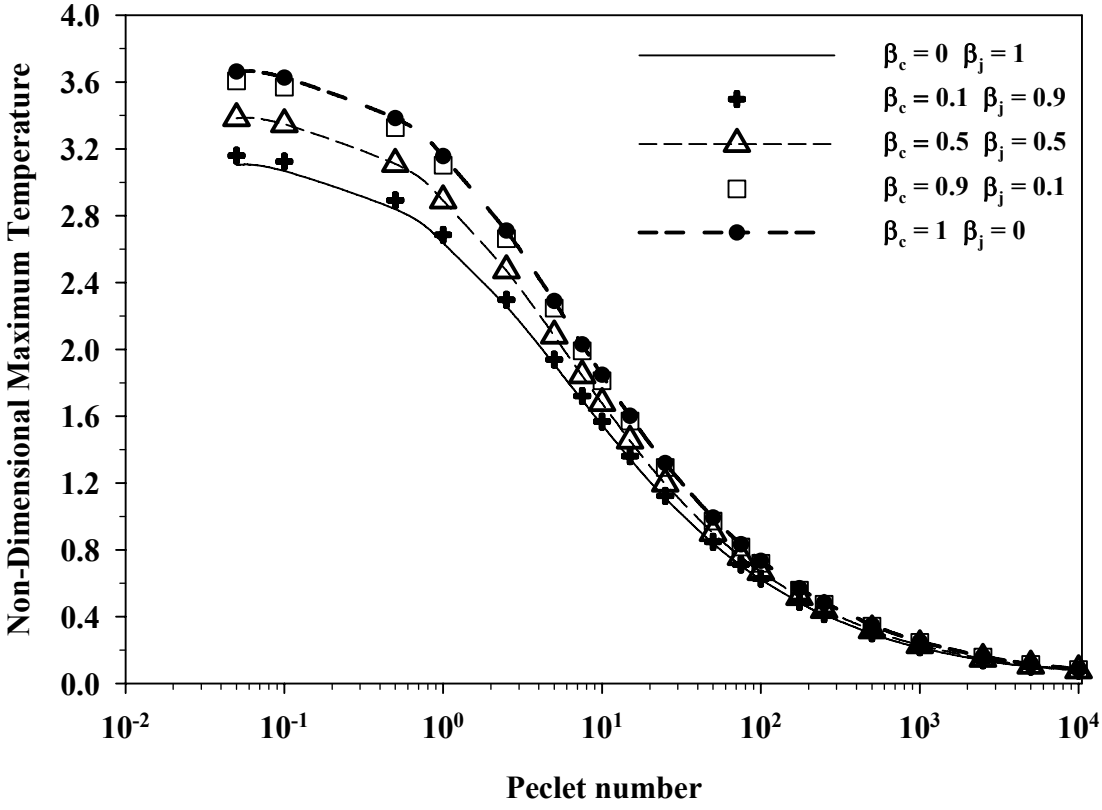

Figure 4.5 Dimensionless maximum interface temperature vs. Peclet no. for varying proportions of Coulomb and Joule heat

4.5 Summary

In this chapter the linear regression methodology for evaluating the heat partition and the interface temperature rise was extended to the case of sliding electrical contacts. The current model is a macro-scale model wherein the knowledge of interface parameters such as nominal contact dimensions, contact resistance, and contact pressure is used to determine the interface temperature. Although the model ignores the surface roughness and therefore the presence of *a*-spots within the nominal contact region it does provide qualitative insights into the temperature rise at the interface due to presence of both Coulomb and Joule heating.

CHAPTER 5. MULTI-SCALE CONTACT RESISTANCE MODEL

5.1 Introduction

The surfaces of all engineering bodies or components exhibit roughness at different length scales from macro-scale (waviness) to roughness at micro and nano scales. Each scale of roughness is associated with a corresponding real area of contact. The roughness pattern or surface texture can be described as random, either isotropic or anisotropic, and Gaussian or non-Gaussian [60]. When two engineering surfaces are brought into contact they make contact at the peaks of the asperities thereby establishing a real area of contact. This real area of contact dictates the conductance of heat and electrical current through the interface. In the context of electrical contacts these touching asperities are referred to as *a*-spots [14]. Most surfaces are covered with oxide or contaminant films which may or may not be thermally and/or electrically conducting. These *a*-spots reduce the available volume for electrical conduction, and the electrical resistance due to this constriction is referred to as constriction resistance. The constriction resistance is a function of size and shape of the *a*-spots as well as their distribution across the interface. The total interface or contact resistance is a function of the surface roughnesses and the electrical resistivities of the materials and is given by the sum of the constriction resistance and the film resistance due to any oxide or non-conducting film on the surfaces [14, 56, 61].

Several models have been put forth to estimate the real area of contact between two contacting bodies and the associated electrical contact resistance. Here a summary of the literature on different studies for approximating real area of contact and contact resistance is presented.

5.2 Literature review on modeling of real area of contact

Greenwood and Williamson [62] put forth one of the first statistical based model for frictionless contact between two rough surfaces. The (GW) model idealized the scenario as contact between a rough elastic surface and a rigid flat plane. They assumed that all the asperities have the same radius of curvature, all asperities behave independently and deform according to Hertzian contact theory [63], and their heights follow Gaussian distribution. A mathematical/statistical formulation was presented to determine the real area of contact based on the contact load and the above mentioned assumptions. They also defined a parameter accounting for plasticity in the interface called "plasticity index." This plasticity index accounted for the topographical and the material properties of the surfaces in contact and acted as an indicator determining the onset of plasticity. However this formulation had inherent flaws, since what is calculated for the average radius of curvature – as required by the model – is sensitive to the sampling resolution.

A fully plastic or truncation model was presented by Abbott and Firestone [64] to describe the wear process. The model of Abbott and Firestone ("AF model") assumed that under the conditions of complete plasticity, the area of contact ($\bar{A}_{AF}$) of a hemispherical asperity pressed against a moving rigid flat with an interference ω can be given as:

$$\bar{A}_{AF} = 2\pi\zeta\omega \tag{5.1}$$

The average contact pressure in this case is equivalent to the hardness, due to the conditions of complete plasticity. The contact load ($\bar{F}_{AF}$)can then be calculated as:

$$\bar{F}_{AF} = 2\pi\zeta\omega H \tag{5.2}$$

where ζ is the radius of curvature of the asperity and H is the hardness.

Greenwood and Tripp [65] investigated the difference between modeling the contact between two rough surfaces and between a rough and a smooth surface. Based on their mathematical analysis, they concluded that idealizing the contact between two rough surfaces as contact between a rough and a smooth surface, as done by Greenwood and Williamson [62], does not alter the results. They used Gaussian distribution for asperity heights along with Hertz's theory for the elastic contact and the AF truncation model for the plastic contact. They concluded that the height distribution on the two surfaces can be different and only the combined height distribution has bearing on the contact analysis.

Bush, Gibson and Thomas [66], hereon referred to as BGT model, developed an elastic contact model for isotropically rough surface. Their model used the assumptions of Nayak's microgeometry analysis [67] and approximated asperities as elliptical paraboloids with random principal axis orientation and aspect ratio. BGT model also used Hertz's solution [63] for the contact of two elastic paraboloids for calculating area of contact and load for each asperity. The results presented were function of the bandwidth parameter α, which is given as:

$$\alpha = \frac{m_0 m_4}{m_2^2} \tag{5.3}$$

where m_i are the spectral moments. The authors reported that their theory breaks down at small surface separations and the limiting surface separation increases with increasing α. The break down was attributed to interaction between the neighboring asperities as the

surfaces approach and its dependence on α implies that α cannot simultaneously account for asperities of different scales of sizes.

Whitehouse and Archard [68] developed a model of rough surface contact based on the asperity height distribution and the surface auto correlation length. This was based on the understanding that all important geometric characteristics of the surface profile can be computed from the r.m.s of height distribution and the correlation length. In their model, the distribution of peaks was assumed to be Gaussian and the distribution of peak curvatures was dependent upon the heights.

McCool [69] presented a very useful summary and numerical comparisons of some of the prevalent contact models in the early 1980's. The models considered were: GW [65] and BGT model [66] for isotropic surfaces, BGK model [70] which is anisotropic version of BGT model, isotropic version of GW model as suggested by Sayles and Thomas [71]. It was reported that GW and BGT models had good agreement for the area of contact but for the contact pressure GW was in agreement with the asymptotic case of BGT model (large surface separation). Comparison of BGK model with the asymptotic case of BGT model revealed that the anisotropic contact area was 2% lower and the nominal pressure was 28% lower for the same mean plane separation. The anisotropic version of GW model gave lower values of the contact area and nominal pressure when compared with BGK model. McCool recommended the use of GW model based on its simplicity and in comparison with asperity simulation model.

Johnson et al. [72] (hereon referred to as JGH model) presented relations for average pressure and contact area for the case of elastic contact of a bi-sinusoidal surface with a flat surface. Unlike Westergaard's [73] closed form solution of elastic contact

between one dimensional sinusoid and flat surface, JGH model gave relations for the contact area for the asymptotic cases, i.e., (1) during early stages of contact, and (2) for near complete contact. At very light loads Hertz's solution was implemented, while, at the other extreme of almost full contact, the non-contact zone was treated as a pressurized "penny-shaped" crack in an infinite solid. The following two pressure terms are defined in their analysis: $\overline{p}$ as the mean pressure in the interface (with respect to the nominal contact area), and p^* is a reference mean pressure that causes complete contact and is given by

$$p^* = \sqrt{2}\pi E \Delta f \tag{5.4}$$

where Δ is the waviness amplitude, f is the reciprocal of the wavelength and E is the equivalent elastic modulus given as:

$$\frac{1}{E} = \frac{1-\nu_1^2}{E_1} + \frac{1-\nu_2^2}{E_2} \tag{5.5}$$

where E_1, E_2, ν_1, and ν_2 are the modulus and Poisson's ratio for both the materials. The relations for the single–asperity contact area for the two asymptotic cases, for the unit cell with dimensions of $\lambda \times \lambda$, are then given as:

For $\overline{p} \ll p^*$

$$\left(\overline{A}_{JGH}\right)_1 = \frac{\pi}{2f^2}\left(\frac{3}{8\pi}\frac{\overline{p}}{p^*}\right)^{2/3} \tag{5.6}$$

For $\overline{p} \to p^*$

$$\left(\overline{A}_{JGH}\right)_2 = \frac{1}{2f^2}\left(1 - \frac{3}{2\pi}\left(1 - \frac{\overline{p}}{p^*}\right)\right) \tag{5.7}$$

A 2D Fourier cosine series was used to represent the contact pressure distribution. In order to determine the Fourier coefficients the authors used the variational principle of minimum complementary energy.

Chang et al. [74] developed an elasto-plastic contact model (CEB model) by applying the principle of volume conservation to the plastically deformed portion of the hemispherical asperity. They used the results from single asperity analysis to apply it to elasto-plastic deformation of the entire surface using the assumptions similar to GW model. The main assumptions of CEB model are: (i) asperity deformation is localized near its tip (vicinity of contact), (ii) asperity behaves elastically below critical interference and fully plastic beyond it and, (iii) the volume of the plastically deformed asperity is conserved. The CEB model suffers from the shortcoming of having a discontinuity in the contact load at critical interference. The contact load jumps from 2/3*KH* in the elastic regime to *KH* in the plastic regime, where *K* is the hardness factor.

A model incorporating a smooth transition from elastic to fully plastic regime was put forth by Zhao et al. [75] (ZMC model). The ZMC model uses Hertz's solution for the elastic regime ($\omega < \omega_c$), AF model for fully plastic regime ($\omega \geq 54\omega_c$), and for the elasto-plastic regime ($\omega \leq \omega_c \leq 54\omega_c$) following equations were put forth:

$$\begin{aligned} \overline{A}_{ZMC} &= \pi\zeta\omega\left[1-2\left(\frac{\omega-\omega_c}{53\omega_c}\right)^3+3\left(\frac{\omega-\omega_c}{53\omega_c}\right)^2\right] \\ \overline{F}_{ZMC} &= \overline{A}_{ZMC}\left[H-H\left(1-\frac{2}{3}K\right)\frac{\ln 54\omega_c-\ln\omega}{\ln 54}\right] \end{aligned} \tag{5.8}$$

where ω_c is the interference at which the plasticity sets in. These equations satisfy the continuity of the function and its slope at the two transitional regimes. This model was extended for elliptical asperity contacts by Jeng and Wang [76]

Zhao and Chang [77] presented a micro contact model including the effect of asperity interaction in an elasto-plastic rough contact. Their analysis assumed that each asperity has its own territory of influence surrounding the surface area which is directly related to the asperity load, and the sum of the territory areas of all the contact asperities is equal to the total nominal area. The deformation at an asperity due to pressures at all other contacting asperities was calculated using Love's equations [78]. The authors then used ZMC model to incorporate asperity interaction and plastic deformation simultaneously.

Kogut and Etsion [79] (KE model) presented a finite element analysis of frictionless contact between a deformable sphere with a rigid flat. The authors divided the deformation into four regimes: $\omega < \omega_c$, $1 \le \omega/\omega_c \le 6$, $6 \le \omega/\omega_c \le 110$, $\omega/\omega_c > 110$. Hertz's solution was used to the complete elastic regime ($\omega < \omega_c$) and AF model for fully plastic regime ($\omega/\omega_c > 110$). They provided empirical relations for the contact area, the contact force and the average contact pressure for the remaining deformation regimes.

For $1 \le \omega/\omega_c \le 6$

$$\begin{aligned} \bar{F}^*_{KE} &= 1.03\left(\frac{\omega}{\omega_c}\right)^{1.425} \\ \bar{A}^*_{KE} &= 0.93\left(\frac{\omega}{\omega_c}\right)^{1.136} \\ \left(\frac{\bar{F}}{AY}\right)_{KE} &= 1.19\left(\frac{\omega}{\omega_c}\right)^{0.289} \end{aligned} \tag{5.9}$$

For $6 \le \omega/\omega_c \le 110$

$$\bar{F}^*_{KE} = 1.4\left(\frac{\omega}{\omega_c}\right)^{1.263}$$
$$\bar{A}^*_{KE} = 0.94\left(\frac{\omega}{\omega_c}\right)^{1.146} \tag{5.10}$$
$$\left(\frac{\bar{F}}{AY}\right)_{KE} = 1.61\left(\frac{\omega}{\omega_c}\right)^{0.117}$$

where $\bar{F}$ is the contact load, $\bar{F}^*$ is the ratio of contact load to critical load (point of initial yielding), A is the contact area, and A^* is the ratio of contact area to the critical contact area. The critical load and critical contact area are given as:

$$\bar{F}_c = \frac{4}{3}\left(\frac{\zeta}{E}\right)^2\left(\frac{\pi KH}{2}\right)^3$$
$$\bar{A}_c = \pi^3\left(\frac{KH\zeta}{2E}\right)^2 \tag{5.11}$$

where ζ is the equivalent radius of curvature computes as:

$$\frac{1}{\zeta} = \frac{1}{\zeta_1} + \frac{1}{\zeta_2} \tag{5.12}$$

Here hardness is related to the yield stress by $H = 2.8Y$ [80] and K, the hardness coefficient is related to the Poisson ratio as $K = 0.454 + 0.41\nu$ [74]. KE model suffered from an inherent shortcoming as it has a discontinuity at $\omega/\omega_c = 6$.

Jackson and Green [81] (JG model) performed a finite element analysis of elasto-plastic contact between a deformable hemisphere and a rigid flat. They used Von Mises yield criterion to arrive at the critical interference, which was given as

$$\omega_c = \left(\frac{\pi CY}{2E}\right)^2 \zeta \tag{5.13}$$

where,

$$C = 1.295\,\mathrm{e}^{0.736\nu} \tag{5.14}$$

and the Poisson's ratio used is of the material that yields first. The corresponding critical contact force ($\bar{F}_c$) and contact area ($\bar{A}_c$) are given as:

$$\bar{F}_c = \frac{4}{3}\left(\frac{\zeta}{E}\right)^2\left(\frac{\pi CY}{2}\right)^3 \tag{5.15}$$

$$\bar{A}_c = \pi^3\left(\frac{CY\zeta}{2E}\right)^2 \tag{5.16}$$

Based on the results of the FEA the authors reported that the contact behaves elastically for $0 \le \omega/\omega_c \le 1.9$, and hence Hertz's solution was used to describe deformation in this regime. For interference ratio $\omega/\omega_c \ge 1.9$ following elasto-plastic relations were put forth:

$$\bar{A}_{JG} = \pi\zeta\omega\left(\frac{\omega}{1.9\omega_c}\right)^B \tag{5.17}$$

$$\frac{\bar{F}_{JG}}{\bar{F}_c} = \exp\left(-\frac{1}{4}\left(\frac{\omega}{\omega_c}\right)^{5/12}\right)\left(\frac{\omega}{\omega_c}\right)^{3/2} + \frac{4H_G}{C.Y}\left[1-\exp\left(-\frac{1}{25}\left(\frac{\omega}{\omega_c}\right)^{5/9}\right)\left(\frac{\omega}{\omega_c}\right)\right] \tag{5.18}$$

where,

$$B = 0.14\exp\left(23\,Y/E\right) \tag{5.19}$$

$$\frac{H_G}{Y} = 2.84\left[1-\exp\left(-0.82\left(\frac{a}{\zeta}\right)^{-0.7}\right)\right] \tag{5.20}$$

where *a* is the radius of contact for an asperity. Eq. (5.20) describes the varying geometric hardness of the hemispherical asperity during the deformation process. The authors also pointed out that their model was in good agreement with the experimental results published by Johnson [82].

Jackson and Green [83] extended the applicability of their micro contact model [81] by applying it to contact between two rough surfaces. They assumed Gaussian distribution for the asperity heights.

Since numerical integration of the integrals associated with the Gaussian distribution can be cumbersome, many researchers have resorted to much simpler exponential distribution for the asperity height to obtain closed form solutions [62, 84-88]. Green [89] presented the analytical solutions for the Gaussian height distribution for CEB model, which was used in [83, 90]. Green [89] used mean value theorem to approximate the integrals for the elastic regime and performed complete integration for the plastic regime.

Krithivasan and Jackson [91] (referred to as KJ model) employed finite element analysis to extend the JGH [72] elastic model for three-dimensional elastic-plastic sinusoidal contact. The authors pointed out that the hardness of the sinusoidal surface will show negligible changes in the initial stages of deformation but will increase as the flattening process continues. Based on the parametric study conducted using FEA, the authors presented relations for the elasto-plastic contact area and contact pressure, which are presented in Section 5.4.1.3.

Almost all the models presented above, except JGH and KJ models, use the results of single asperities to stochastically model the contact between two rough surfaces. Another approach involving discretization of the real surface and then simulating the contact between them is called deterministic modeling. Solving the constitutive equations of elasticity at every point in the domain requires large computing power and time. Lee and Cheng [92] presented a 2D model for contact between

longitudinally oriented rough surfaces. Three dimensional deterministic analysis were conducted by Ren and Lee [93, 94] (elastic contact) and by Lee and Ren [95] for elasto-plastic contact. Techniques like fast Fourier transform (FFT) [96, 97] and Variational methods [98] have been suggested to expedite the computation time.

Fractal based contact models have been developed using Weierstrass-Mandelbrot fractal function. The results of the fractal analysis are insensitive of the resolution of the surface scan and the surface is represented in terms of fractal parameters. Fractal characterization is discussed in detail in [99, 100] and some elastic-plastic contact analyses are presented in [101-103].

Jackson and Streator [104] have developed a non-statistical multi-scale contact model based on the concept of "protuberance upon protuberance", as suggested by Archard [105]. This model computes the FFT of the surface scan and arranges the asperities of higher frequencies upon asperities of lower frequencies. One of the biggest advantages of the Jackson-Streator (JS) model is that its predictions are not sensitive to the horizontal sampling resolution used to measure the surface, unlike the GW, CEB, ZMC models. This model will be discussed in detail in the subsequent section.

5.3 Literature review on modeling of contact resistance

The presence of surface roughness impedes the conduction of heat and current through the interface. Here a brief summary of the literature on modeling of interface resistance to electrical current is presented.

Holm [14] presented simple analysis for estimating the constriction resistance due to the presence of *a*-spots at the interface. He proposed a simple relation for estimating

the constriction resistance, assuming that all the *a*-spots are circular in shape and lie at distances much greater than their individual radii, given as:

$$R_c = \frac{\rho_1 + \rho_2}{4\sum a_i} \tag{5.21}$$

where ρ_1 and ρ_2 are the resistivities of both the bodies and *a* is the radius of *a*-spot. The above equation finds limited practical application, since the number and the size of *a*-spots cannot be determined.

Greenwood [56] derived an equation for the contact resistance based on the principle that the current distributes itself across the interface so as to minimize the heat production. Greenwood's analysis accounted for self resistance of the *a*-spots and also the resistance due to interactions between the clusters of *a*-spots. The relation for the resistance due to one contacting member or resistance between a rough and a smooth surface was:

$$R_c = \frac{\rho}{2\sum a_i} + \frac{\rho}{\pi}\left(\sum\sum_{i\neq j}\frac{a_i a_j}{s_{ij}}\right)\Bigg/\left(\sum a_i\right)^2 \tag{5.22}$$

where s_{ij} is the distance between the *a*-spots within a cluster. The first term in the above equation represents the self resistance of the *a*-spots and the second term accounts for the interaction resistance between the *a*-spots in the clusters. Greenwood provided a simplified version of the above equation by making following assumptions: the size and the locations of the *a*-spots are uncorrelated and $\sum a_i = n\bar{a}$, where *n* is the number of *a*-spots and $\bar{a}$ is the average radius of the *a*-spots. The above equation can then be written as:

$$R_c = \frac{\rho}{2n\bar{a}} + \frac{\rho}{\pi n^2}\sum\sum_{i\neq j}\frac{1}{s_{ij}} \tag{5.23}$$

Boyer et al. [106] put forth a simple model for calculating the constriction resistance for cases when the number of contact spots is small and the real area of contact approaches the apparent area of contact. They considered the case of two semi-infinite electrodes and showed that the expressions for the constriction resistance given by Holm [14] and Greenwood [56] gives inaccurate results when the real area of contact is close to the apparent area, as those expressions were derived assuming the spot size to be very small compared to the distance between them.

Malucci [107] developed a contact resistance model to account for the effects of surface degradation and interface motion for stationary contacts. An insulating film whose thickness was a statistical function of the asperity deformation was introduced to simulate the aging/degradation of contacts. In a subsequent study [108], he included the effects of contact force, microhardness, and geometry on the performance of aging electrical contacts.

Nakamura [109], using boundary element method (BEM) showed that the shape of contacting spots has negligible effect on the constriction resistance if their areas are comparable. In a later study [110], he used BEM to calculate the constriction resistance of contact spots of regular forms, like circle, square, hexagon etc., and irregular forms. A self avoiding random walk process on a square mesh was applied to obtain irregular forms of the conducting spots.

Jang and Barber [111] put forth an expression for constriction resistance in which they replaced the double summation in Greenwood's [56] expression by an integral over the nominal contact area whose kernel depends on the bearing area ratio. Their analysis yielded good results for the bearing ratio less than 10% and the results were in good

agreement with Nakamura's [110] results for square contacting spot shape. However, their analyses suffered from being sensitive to the resolution scale and it yielded lower contact resistance at finer resolution.

Majumdar and Tien [112] presented a model to calculate the thermal resistance to the heat flow between two rough surfaces using the fractal theory. In principle this model could be extended to determine electrical contact resistance between two surfaces. In their model, they idealized the real surfaces as homogenous, isotropic and self-similar, and developed a network of resistances arranged in series and parallel configuration for a 1-D surface profile. The resistance network was akin to the model proposed by Greenwood [56] as the resistance of each asperity and the interaction between all the asperities was considered as the part of the network model. In order to obtain the relationship between the real area of contact and the contact force they used the power law equation proposed by Majumdar and Bhushan [100]. The authors pointed out that their analyses could not be readily applied to anisotropic surfaces generated using most machining processes.

Kogut and Komvopoulos [113] derived an expression for the contact resistance from first principles based on a fractal model of the surface topography, including the effects of elastic-plastic asperity deformation and size dependent constriction resistance of the microcontacts. The electrical contact resistance contained the contributions due to Sharvin's mechanism and to a scattering mechanism. In most real cases it is relatively easy to measure the electrical contact resistance and thus the authors provided an expression to evaluate the real area of contact based on such measurement. They also pointed out that their analysis was applicable only to static contacts since, for dynamic

contacts, it is difficult to determine the surface topography during the operation. The authors subsequently extended their model to include the effect of surface contaminant/insulating films in contact resistance modeling [114, 115].

Based on the above literature review on the modeling of real area of contact and the electrical contact resistance, it is seen that there are no experimentally validated models for determining the real area of contact and electrical contact resistance for rough surfaces. The JS model provides a convenient framework wherein different combinations of single-asperity deformation models can be used to predict the real area of contact while considering the various spatial frequencies comprising the surface topography. In this thesis the JS model is extended to predict contact resistance between two rough surfaces.

5.4 Description of the multi-scale contact resistance model

The assumptions for the multi-scale contact resistance model are essentially the same as those for JS model [104],

1. Asperities with higher frequencies are superimposed on asperities with lower frequencies,
2. Each frequency level of asperities carries the same load, which is equally shared among all the contacting asperities at the given frequency,
3. Any elastic or elasto-plastic asperity deformation model can be applied to each frequency level, irrespective of the higher frequency asperities on top,
4. The contact area at a given frequency level cannot be greater than the contact area at frequency level below it,

In order to extend this model to evaluate the electrical contact resistance following assumptions are made:

5. Contacting asperities of a given frequency level can be visualized as resistors connected in parallel,
6. If a given frequency level has the same area of contact as that of the frequency level below it, it contributes no resistance (i.e., it is assigned a resistance value of zero).
7. The equivalent resistance of a given frequency level acts in series with the equivalent resistance of the frequency level below it.

Assumptions # 5–7 are the contributions of the current work and extend the JS model to predict electrical contact resistance. The implementation of the multi-scale contact resistance model is discussed in detail below and graphically explained in the flowchart illustrated in Figure 5.1.

A representative scan length L is selected and the surface scans of both the contacting surfaces are obtained from the profilometry measurements. The mean plane for each of the surfaces, calculated using a least squares method, is subtracted from the surface scans. The resulting surface profiles are then added to simulate a contact between an equivalent rough surface and a smooth surface.

$$z = z_1 + z_2 \tag{5.24}$$

where z_1 and z_2 are the mean plane subtracted profiles of surfaces 1 and 2, and z is the equivalent surface profile.

A two-dimensional FFT of the resulting surface is performed according to the following equation:

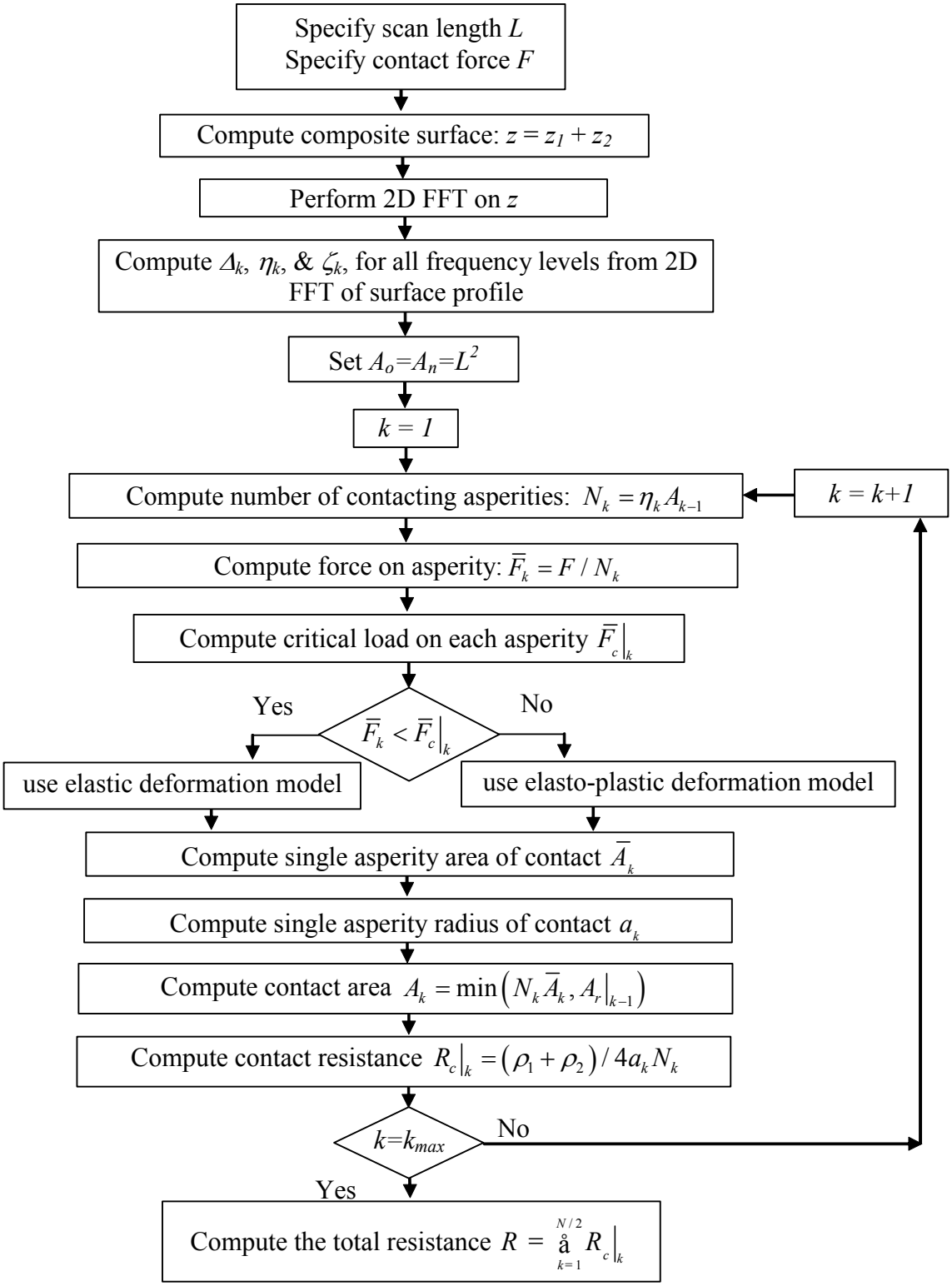

Figure 5.1 Flow chart of multi-scale contact resistance model

$$Z_{pq} = \frac{1}{MN}\sum_{r=0}^{M-1}\sum_{s=0}^{N-1} z\left(r\Delta x, s\Delta y\right)\exp\left(-i2\pi\left(m\frac{r}{M}+n\frac{s}{N}\right)\right) \tag{5.25}$$

where M and N are number of samples and m and n are frequency numbers and Δx and Δy are the grid spacing along the x and y direction respectively, and Z_{pq} are the FFT coefficients. For the sake of symmetry, we set $M = N$. Using the Nyquist criterion the cutoff (k_{max}) frequency is set at $N/2$.

As the JS model requires specification of single amplitude with a given frequency, it becomes important to accurately represent the amplitude information from a 2D FFT in 1D representation. In this regard, the following relations are used to obtain the signal amplitude (Δ_k) at given frequency level:

$$\begin{aligned}
\Delta_k &= \sqrt{\sum_{q=0}^{N-1}\left|Z_{kq}\right|^2} + \sqrt{\sum_{p=0}^{N-1}\left|Z_{pk}\right|^2} \qquad \text{for } 1 < k < N/2\text{-}1 \\
\Delta_k &= \frac{1}{2}\left(\sqrt{\sum_{q=0}^{N-1}\left|Z_{kq}\right|^2} + \sqrt{\sum_{p=0}^{N-1}\left|Z_{pk}\right|^2}\right) \qquad \text{for } k = N/2
\end{aligned} \tag{5.26}$$

where Z_{kq} is the FFT coefficient for a given y_q and Z_{pk} is the FFT coefficient for a given x_p. The derivation for the above relations is detailed in Appendix A. The above equations calculate the signal amplitude at a given frequency based on the r.m.s averages over x and y axes. Now the areal asperity density (η_k) and the radius of curvature (ζ_k) at frequency level k can be calculated using following equations:

$$\eta_k = 2f_k^2 \tag{5.27}$$

$$\zeta_k = \frac{1}{4\pi^2\Delta_k f_k^2} \tag{5.28}$$

where f_k is the frequency. The critical contact load for each asperity at a given frequency level can be calculated as:

$$\overline{F}_c\big|_k = \frac{4}{3}\left(\frac{\zeta_k}{E}\right)^2\left(\frac{C\pi Y}{2}\right)^3 \tag{5.29}$$

where C is given in Eq. (5.14).

At the first frequency level, identified with $k = 1$, the nominal contact area (A_o) is just equal to L^2 (L is the length of scan). The total number of asperities (N_1)at the first frequency level is then computed as:

$$N_1 = \eta_1 A_o = 2 f_1^2 A_o = 2\left(\frac{1}{L}\right)^2 L^2 = 2 \tag{5.30}$$

Note that both asperities are assumed to be in contact.

For each higher frequency level (k), the "nominal" area of contact is the contact area at the previous frequency level, and the number of contacting asperities (N_k) is given by

$$N_k = \eta_k A_{k-1} = 2 f_k^2 A_{k-1} = 2\left(\frac{k}{L}\right)^2 A_{k-1} \tag{5.31}$$

where A_{k-1} is the contact area at the preceding frequency level. The contact load is then equally divided among all the contacting asperities at the given frequency level

$$\overline{F}_k = \frac{F}{N_k} \tag{5.32}$$

and the average pressure at a given frequency level with respect to nominal contact associated with that frequency is computed as:

$$\overline{p}_k = \frac{\overline{F}_k}{A_{k-1}} \tag{5.33}$$

The contact load is then compared with the critical load at that frequency level (Eq. (5.29)), and the single asperity area of contact is then determined using appropriate

asperity deformation model (e.g., Hertz, JGH, JG etc.). Multiplying the single asperity area with the number of asperities at that frequency level gives a provisional contact area for that frequency level. Following the Assumption #4, this contact area is checked against the contact area predicted at the preceding frequency level and the smaller value is selected as the contact area for the given frequency level.

$$A_k = \min\left(N_k \overline{A}_k, A_{k-1}\right) \tag{5.34}$$

where $\overline{A}_k$ is the area of contact for a single asperity. Keeping with Assumption # 5, the equivalent resistance of the contacting asperities at a given frequency level is then computed as

$$R_c\big|_k = \frac{\left(\rho_1 + \rho_2\right)}{4 a_k N_k} \tag{5.35}$$

where a_k is the radius of contact of each asperity at that frequency level, and ρ_1 and ρ_2 are the resistivities of Surfaces 1 and 2 respectively. However, if the contact area of a given frequency level is equal to or less than the contact area in the preceding frequency level, then the equivalent resistance of that frequency level is set to zero.

The iterative procedure continues until all the desired frequency levels are considered, resulting in the prediction of the real area of contact. The overall electrical contact resistance of the interface is then determined by summing in series the equivalent resistances of all frequency levels.

5.4.1 Asperity deformation models

If the critical load at a given frequency level is greater than the force on a single asperity at that frequency level, elastic contact models (Hertz, JGH) are implemented.

Otherwise elasto-plastic (JG, KJ) contact models are implemented to determine the contact area. Three combinations of asperity deformation models are used for comparison, in the current work, which are listed below

1. JGH (elastic) – JG (elasto-plastic)
2. Hertz (elastic) – JG (elasto-plastic)
3. JGH (elastic) – KJ (elasto-plastic)

5.4.1.1 ***JGH and JG***

JGH model put forth by Johnson et al. [72] has been discussed in detail in section 5.2. Johnson et al. presented equations for the contact area for elastic contact between a bi-sinusoidal elastic and a rigid flat surface. The equations presented were for the asymptotic cases of contact under very light loads and for complete contact, as described by Eqs. (5.6) and (5.7). Jackson and Streator [104] provided a polynomial curve fit equation between the two extremes based on the experimental data provided by Johnson et al. [72]. The piecewise curve fit equations are:

For $\overline{p}_k / p_k^* < 0.8$

$$\overline{A}_k = \left(\overline{A}_{JGH}\right)_1 \left(1 - \left(\frac{\overline{p}_k}{p_k^*}\right)^{1.51}\right) + \left(\overline{A}_{JGH}\right)_2 \left(\frac{\overline{p}_k}{p_k^*}\right)^{1.04} \tag{5.36}$$

For $\overline{p}_k / p_k^* \geq 0.8$

$$\overline{A} = \left(\overline{A}_{JGH}\right)_2 \tag{5.37}$$

where $\left(\overline{A}_{JGH}\right)_1$ and $\left(\overline{A}_{JGH}\right)_2$ are given by Eqs. (5.6) and (5.7) respectively and p_k^* is given by Eq. (5.4).

The JG model [81] describing the contact between a elastic, perfectly plastic hemisphere and a rigid flat is discussed in section 5.2. The parameter H_G termed as "hardness geometric limit" which is given by Eq. (5.20), is valid for interferences for which $a/\zeta < 0.41$. Jackson and Streator [104] provided a polynomial fit for H_G/Y for $0.41 \le a/\zeta \le 1$, which is given as

$$\begin{aligned} \frac{H_G}{Y} &= 7.32\left(\frac{a_k}{\zeta_k}\right)^3 - 14.1\left(\frac{a_k}{\zeta_k}\right)^2 + 6.28\left(\frac{a_k}{\zeta_k}\right) + 1.52 \qquad \text{for } 0.41 \le a_k/\zeta_k < 1 \\ \frac{H_G}{Y} &= 1 \qquad\qquad\qquad\qquad\qquad\qquad\qquad\qquad\qquad\qquad\qquad\qquad \text{for } a_k/\zeta_k = 1 \end{aligned} \tag{5.38}$$

here the subscript *k* denotes the values at a given frequency level.

5.4.1.2 ***Hertz and JG***

Hertz's solution for elastic contact between a sphere and a flat are given as [47, 63]:

$$a_k = \left(\frac{3\overline{F}_k\zeta_k}{4E}\right)^{1/3} \tag{5.39}$$

$$\overline{A}_k = \pi a_k^2 \tag{5.40}$$

The JG model is used for the case when $\overline{F}_k > \overline{F}_c\big|_k$, and the implementation of this model has been discussed in Sections 5.2 and 5.4.1.1.

5.4.1.3 ***JGH and KJ***

The implementation of the JGH is discussed in detail in Sections 5.2 and 5.4.1.1. The relevant equations for the KJ model are presented below. The area of contact for an asperity at a given frequency level is computed as:

$$A'_k = \overline{A}_{ep}\left[1-\left(\frac{\overline{p}_k}{p^*_{ep}}\right)^{1.51}\right]+\frac{1}{2{f_k}^2}\left[1-\frac{3}{2\pi}\left(1-\frac{\overline{p}_k}{p^*_k}\right)\right]\left(\frac{\overline{p}_k}{p^*_{ep}}\right)^{1.04} \tag{5.41}$$

$$\overline{A}_k = \min\left(A'_k, \lambda_k^2/2\right) \tag{5.42}$$

where A_{ep} was derived from [79],

$$\overline{A}_{ep} = A_c^{\frac{1}{1+d}}\left(\frac{3\overline{p}_k}{4CY{f_k}^2}\right)^{\frac{d}{1+d}} \tag{5.43}$$

where A_c is given by Eq. (5.16) and the parameter d was determined by curve fitting the FEM results and is given as:

$$d = 3.8\left(\frac{E\Delta f_k}{Y}\right)^{0.11} \tag{5.44}$$

and p^*_{ep} the average pressure that causes complete contact is computed as:

$$\frac{p^*_{ep}}{p^*_k} = \left(4.172\frac{Y}{E}+0.0173\right)\sqrt{\frac{\lambda_k}{\Delta_k}} \tag{5.45}$$

where p^* is given by Eq. (5.4).

5.5 Experimental contact resistance measurements

An experimental study to measure the contact resistance between two surfaces and to validate the multi-scale contact resistance was conducted on a precision test setup. Figure 5.2 presents the schematic of the experimental setup. As seen from the figure, a

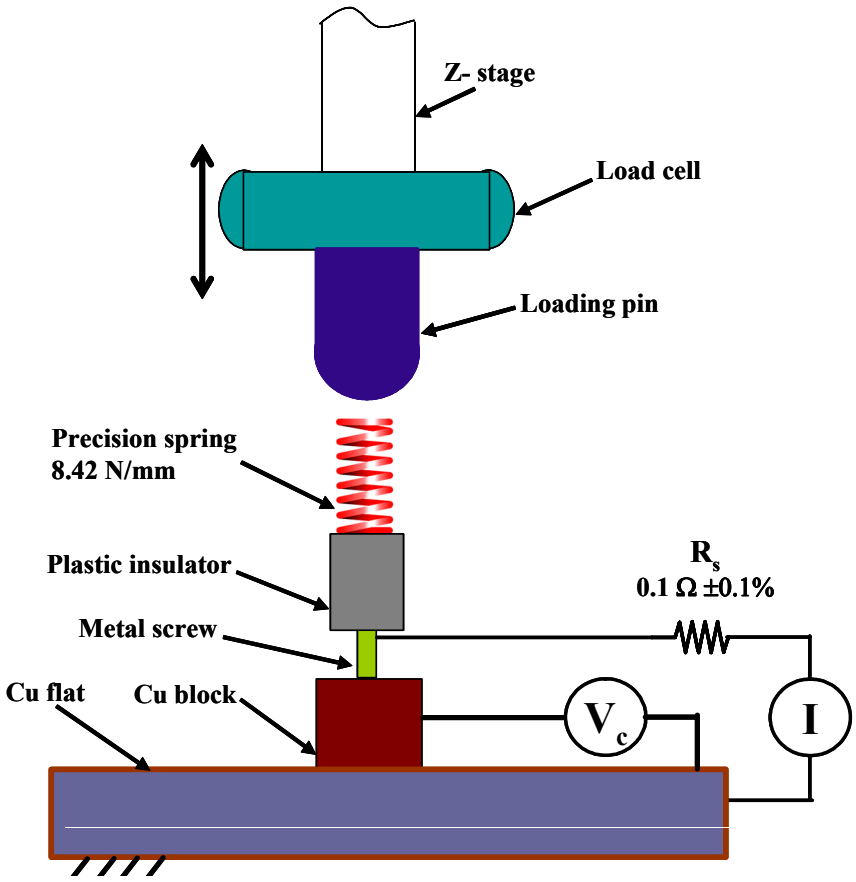

Figure 5.2 Schematic of the experimental setup for contact resistance measurement

copper block (Cu 110) block, 5mm ×5mm×6.4mm was loaded against a copper (Cu 110) flat. The 4–probe voltage measurement technique was used to measure the contact resistance between the block and the flat. The tests were conducted under constant current conditions. Two probes were used to determine the prescribed interface current (I) by measuring the voltage drop (V_s) across a known resistor (R_s) of 0.1Ω (±0.1%). A

separate pair of probes was used to measure the voltage drop (V_c) across the interface. Note that V_c includes the voltage drop across an appreciable length of the upper and lower contact specimens. However, since the bulk resistance (about 1 μΩ) is orders of magnitude less than the total contact resistance, its contribution was neglected. The load is applied by a computer controlled precision vertical stage (Z-stage) pressing down on a precision spring with stiffness of 8.42 N/mm. A load cell is used to measure the applied load. During the contact resistance measurements, the load was gradually increased by moving the Z-stage down in incremental steps while compressing the spring. After reaching the solid length of the spring the Z-stage was raised back up in incremental steps. Specifically, the contact resistance was measured at a constant current of 0.5 A, while the interface was subject to an increasing–decreasing load cycle. Three blocks with similar surface roughness were machined and tested against three flats with different surface roughness. Table 5.1 lists the surface roughness parameters of the blocks and the flats.

Figure 5.3 (a) and (b) illustrates the surface profiles of a block and a flat as measured under Zygo™ white light interferometer with spatial resolution of 2.2 μm. The surfaces of the blocks were scanned under the profilometer before and after the tests.

Table 5.1 Surface roughness parameters for Cu blocks and flats

Interface no.	Block		Flat		Equivalent
	R_a (μm)	R_q (μm)	R_a (μm)	R_q (μm)	R_q (μm)
1	0.53	0.86	0.913	1.2	1.47
2	0.495	0.64	0.337	0.443	0.78
3	0.535	0.7	0.049	0.064	0.7

In order to check the repeatability of the measurements, the contact resistance between the block and the flat was checked at three different locations on the flat. Figure 5.4 presents the experimental measurements of the contact resistance as a function of the

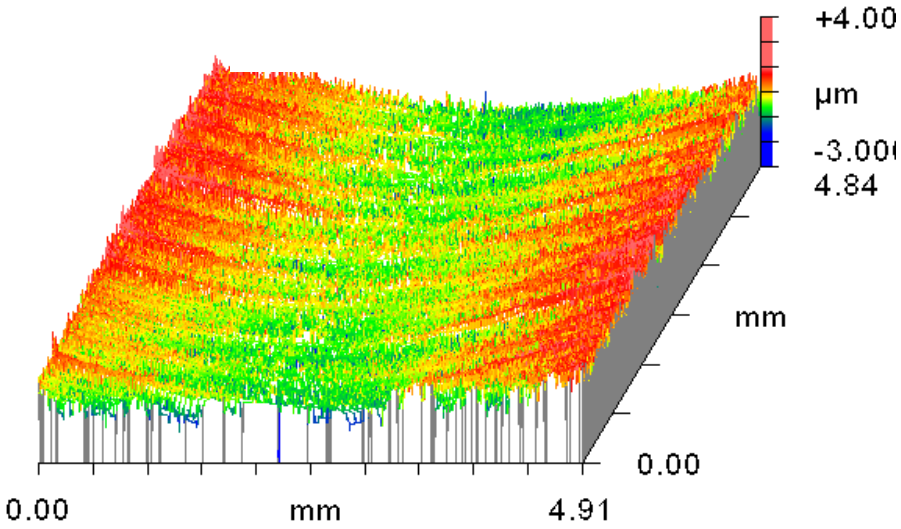

(a)

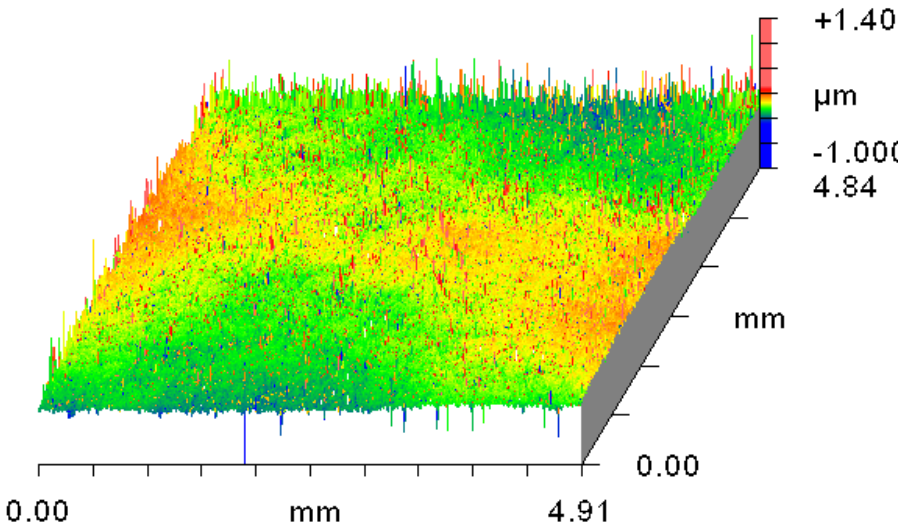

(b)

Figure 5.3 Representative surface profile of: (a) block, and (b) flat from Interface #3

load for the Interface # 1. The error bars indicate the standard deviation measured over three test runs. It is observed that the scatter between the runs is very minimal (standard deviation less than 1%), and hence for the sake of readability of the plots only one representative test run is shown in the subsequent plots.

From Figure 5.4 it is evident that the contact resistance traces different paths during the increasing–load and decreasing–load part of the load cycle. This indicates the presence of hysteresis in contact resistance–load behavior. This can be explained as: as the load on the interface is increased some asperities undergo elastic deformation and some undergo plastic deformation. Hence when the load is decreased not all asperities return to their original configuration and this gives thus the contact resistance is lower, for a given load, during the decreasing–load part of the load cycle.

Figure 5.5 presents the comparison between the contact resistance measurements and the predictions of the multi-scale contact resistance model, for Interface #1. Note that experimental results correspond to the increasing load process. Three different micro-contact models (as described in Section 5.4.1) were used within the framework of the multi-scale contact resistance model. It is seen that among all three micro-contact models, JGH-KJ model predictions are closer to the experimental results. The JGH-JG and Hertz-JG model over predict the contact resistance by almost 100% up to the load of 10 N, after which the model predictions are within 50% of the experimental values. On the other hand JGH-KJ model under predicts the contact resistance values by almost 85% up to the load of 5 N after which the model almost 70% lower than the experimental values.

Figure 5.6 (a), (b) and (c) shows the amplitude versus frequency plot, as calculated using Eq. (5.26), of the blocks (1, 2 and 3) before and after the tests with

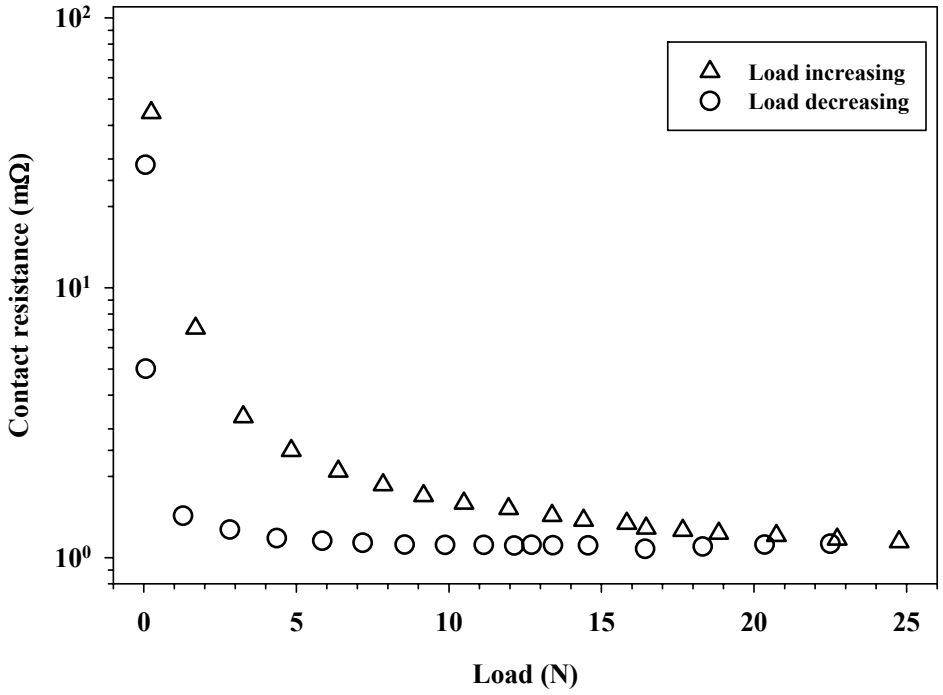

Figure 5.4 **Variation of contact resistance with load for three different load cycles**

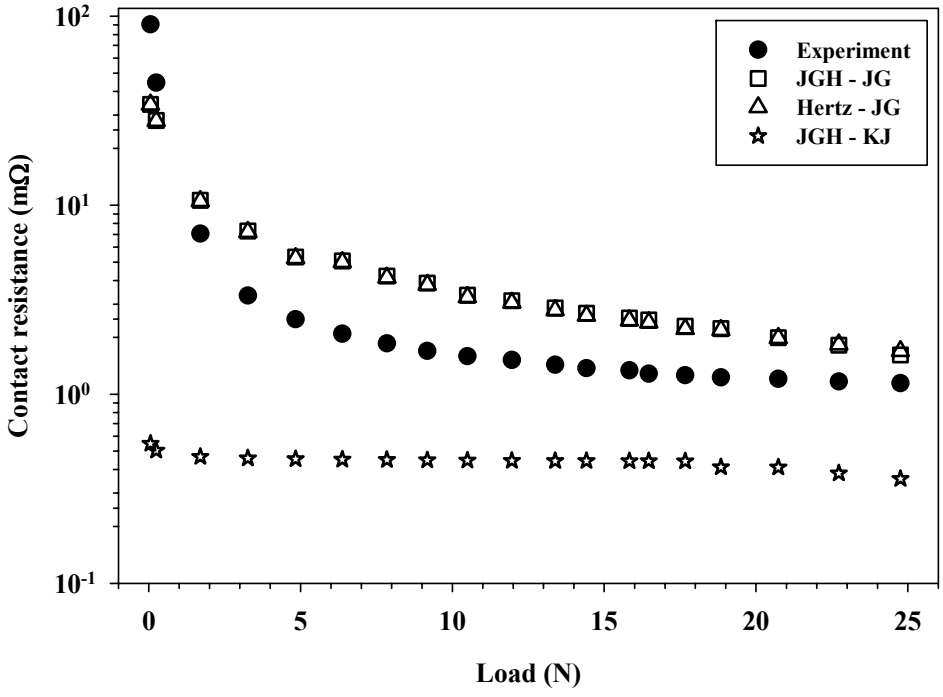

Figure 5.5 **Contact resistance vs. load: comparison of multi-scale contact resistance model with experimental for Interface # 1**

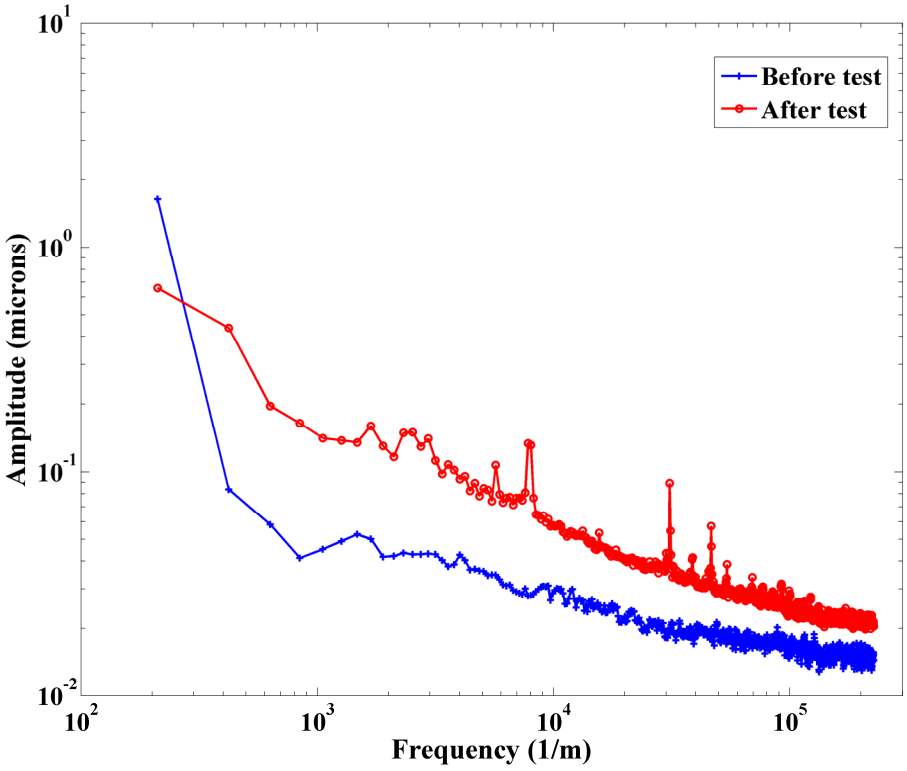
Before test
After test
Amplitude (microns)
Frequency (1/m)
10^{1}
10^{0}
10^{-1}
10^{-2}
10^{2}
10^{3}
10^{4}
10^{5}

(a)

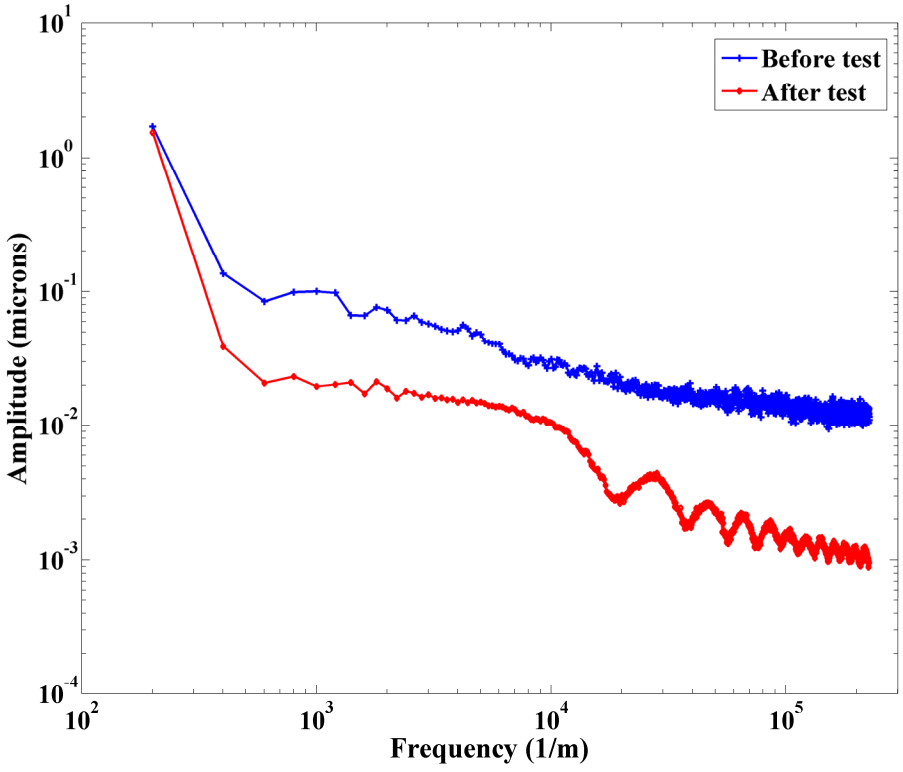
Before test
After test
Amplitude (microns)
Frequency (1/m)
10^{1}
10^{0}
10^{-1}
10^{-2}
10^{-3}
10^{-4}
10^{2}
10^{3}
10^{4}
10^{5}

(b)

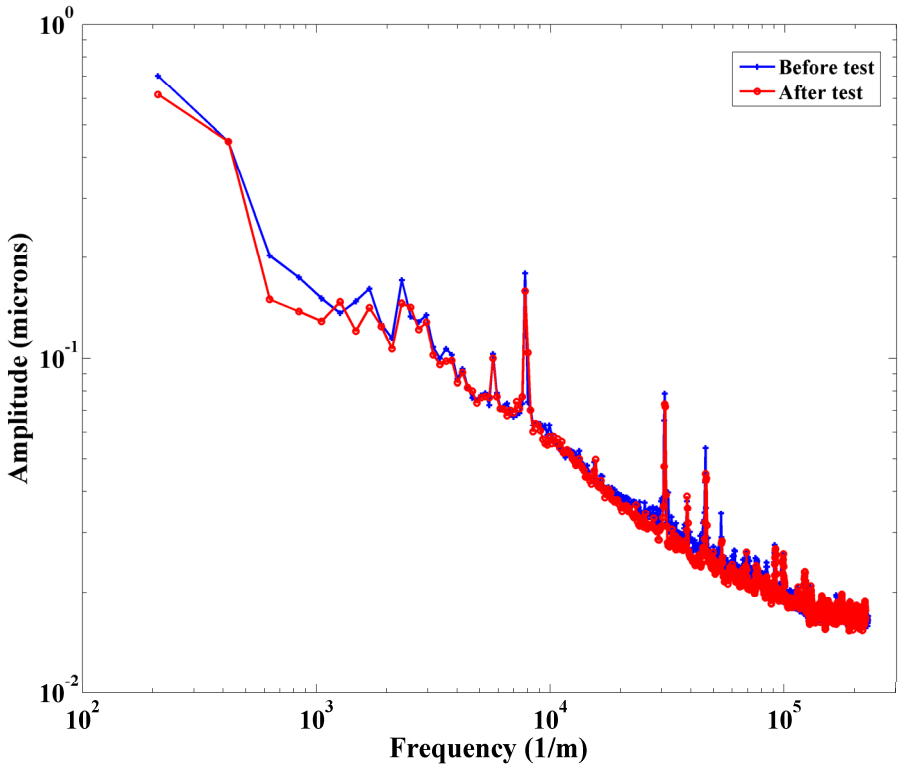

(c)

Figure 5.6 Amplitude vs. frequency before and after test for: (a) Block # 1, (b) Block # 2, and (c) Block #3

Interface #1, Interface #2 and Interface #3 respectively. It is seen that the there is a distinct difference in the amplitude vs. frequency before and after the loading cycle for Interface #1 and Interface #2, but no distinct difference is observed for Interface #3. For the Block #1 the amplitude increased after the tests while for the Block #2 this trend was reversed. Block #1 was in contact with the roughest polished flat (R_q = 1.2 μm) and this could have led to roughening of the surface of the block during the load cycles. Block #2 was in contact with a flat with comparable R_q (roughness). Block #3 on the other hand was in contact with a very smooth surface and this could have been the reason behind negligible change in the amplitude of the surface heights before and after tests. It is to be

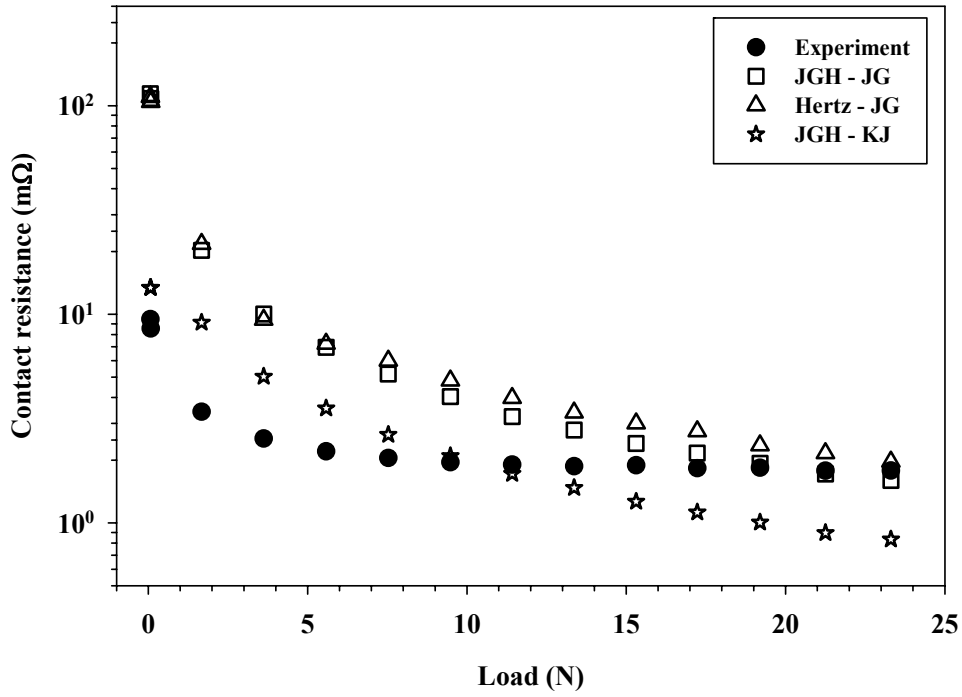

Figure 5.7 **Contact resistance vs. load: comparison of multi-scale contact resistance model with experimental for Interface #2**

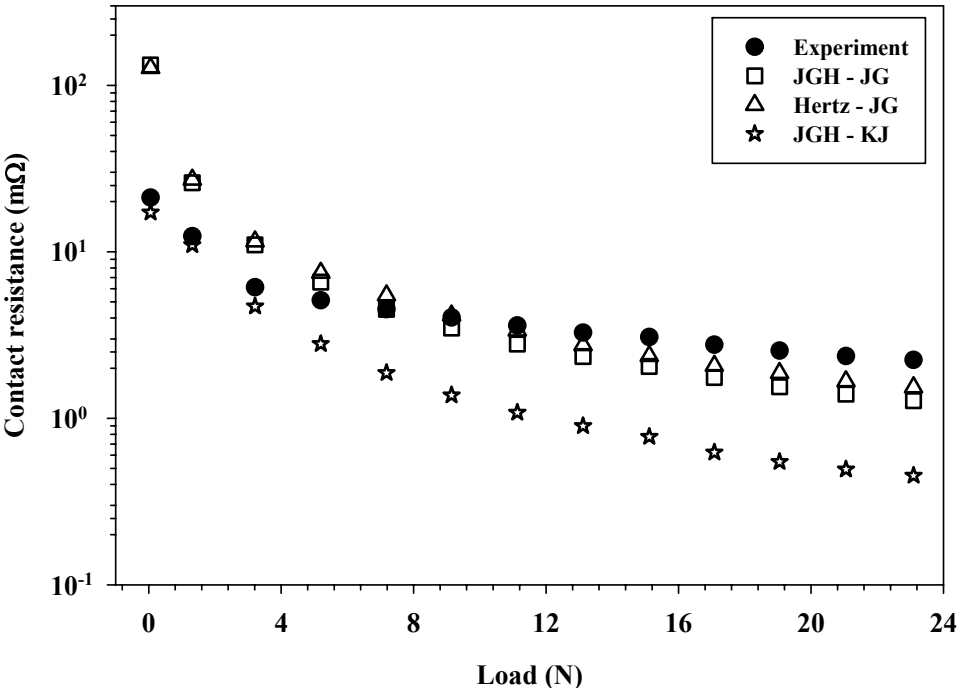

Figure 5.8 **Contact resistance vs. load: comparison of multi-scale contact resistance model with experimental for Interface #3**

noted that the surface of the flats were not scanned after the tests and hence any conclusions derived about the state of the interface from Figure 5.6 are incomplete.

Figure 5.7 shows the comparison of the experimental measurements of the contact resistance for Interface #2. It is observed that at the lowest load of 0.06 N the predictions from JGH-JG and Hertz-JG models are an order of magnitude greater than the experimental values. As the load is increased the agreement between the ECR predictions from JGH-JG and Hertz-JG models and the experimental measurements improve. After the load of 14N the difference in the predictions from the model and the experimental values is less than 50%. It is also observed that JGH-KJ model over predicts the ECR values by almost 50% at lower loads (up to 7 N) and as the load is increased the model under predicts the ECR values. It is also seen that as the load is increased the predictions from the JGH-KJ model diverge from the experimental values.

Figure 5.8 presents the contact resistance measured during Interface #3 and the values are compared with the predictions of the multi-scale contact resistance model. At the lowest load (weight of the block) the JGH-JG and Hertz-JG models over predicts the ECR values by almost an order of magnitude. But as the load is increased the difference between the ECR predictions from the JGH-JG and Hertz-JG models and the experimental values decreases to about 35% at the highest load of 23N. On the other hand, the JGH-KJ model agrees very well with the experimental observations at low loads (up to 5N), but as the load is increased the difference between the model and the experimental results increases. Beyond the load of 11 N the JGH-KJ model under predicts the ECR values by almost 75% when compared to the experimental results.

From the above Figures 5.5, 5.7 and 5.8 it can be concluded that the multi-scale contact resistance model captures the overall trend of variation of contact resistance with load.

The JGH-JG and Hertz-JG combinations of asperity deformation models behave identically as JGH model is identical to Hertz's theory in elastic regime. Both of these models show good agreement with the experimental observations over a wide range of loads and three vastly different surface roughnesses of the copper flats considered. The JGH-KJ combination appears to be sensitive to become increasingly sensitive to load as the value of R_q (surface roughness) is decreased.

5.6 Summary

In this chapter a brief literature review on the modeling of real area of contact and electrical contact resistance was presented. The multi-scale model proposed by Jackson and Streator [104] was extended to predict the electrical contact resistance. The JS model has the advantage of the ease of applicability of different asperity deformation models within its framework. The multi-scale contact resistance model captures the overall trend of decreasing contact resistance with increasing contact load. The model does not account for the presence of oxide layer and it is hypothesized that determination of the oxide layer thickness and its resistance would substantially improve the model predictions. Copper oxide being soft is easily disrupted by applying contact loads [116]. The predictions of the multi-scale ECR model using JGH-JG and Hertz-JG models are in good agreement, within 50%, with the experimental results. The multi-scale ECR model is also computationally more efficient, providing orders of magnitude of savings in

computational time when compared to deterministic model for the same number of grid points.

CHAPTER 6. EFFECT OF CURRENT ON STATIC ELECTRICAL CONTACTS

6.1 Introduction

The subject of electrical contact resistance between two current carrying conductors has been studied extensively. Holm [14] presented an detailed study on electrical contacts, which was reviewed in detail [58, 116, 117]. When two rough surfaces are brought into contact to form an electrical junction they make contact at asperity peaks called '*a*-spots'. As compared to the nominal contact area, these *a*-spots reduce the available cross-sectional area for electrical conduction, and the electrical resistance due to this constriction is referred to as constriction resistance. The constriction resistance is a function of size and shape of the *a*-spots as well as their locations. The total interface or contact resistance is a function of the surface roughnesses and the electrical resistivities of the materials and is given by the sum of the constriction resistance and the film resistance due to any oxide or non-conducting film on the surfaces [56, 61, 118].

The constriction of current through *a*-spots forces the current lines to realign thereby increasing the current density and thus leading to Joule heat generation [58, 119]. The heating of the interface raises the concerns for the performance reliability and structural integrity of the electrical contact or the members therein. Mass transport due to electromigration at high current densities has been reported to be one of the reasons for the degradation of the contacts [120-123], among the other causes like oxidation, corrosion [124, 125], contact load relaxation [126], and sintering in Al-Al contacts [127].

The variation of the contact resistance with load has been studied experimentally [14, 128, 129] and several mathematical/analytical models [56, 62, 113, 114, 130, 131] have been put forth to explain the same. It is a well established fact that the contact resistance is strongly influenced by the contact load. However few studies have been conducted investigating the effect of current through the interface on the contact resistance [119, 132-134]. Here a brief literature review on the effect of current on the potential drop and contact resistance is presented.

6.2 Literature review

Bowden and Williamson [61] studied the effect of short duration (1.2 ms) pulses of current on the constriction resistance between gold surfaces under the load of 1g. The objective of their study was to ascertain if the constriction resistance is influenced by the total energy dissipated at the interface or by the maximum value of the current. The authors measured the constriction resistance by passing an alternating current, before and after the pulse lasting 0.1, 1.0 and 5 ms with same maximum current value. The authors found that the constriction resistance was a strong function of the maximum current pulsing through the interface and not of the duration of the pulse. The authors concluded that for a given current level the interface has a critical contact resistance below which the current will pass without inducing any permanent changes in the interface. If the interface resistance is greater than this critical value then the current will lower the interface resistance until it becomes equal to the critical value associated with that current level. This is also explained by the softening and collapsing of the asperities, due to heat generation at or near the interface, and the associated increase in the real area of contact.

The interface cools and re-hardens during the decay of the pulse without changing the area of contact. The authors observed the evidence of melting on the surfaces (gold) when the potential drop across the contact exceeded 380 mV and the corresponding temperature, as calculated from the Kohlrausch's theory [135] was 950 °C while the metallurgical evidence showed that the melting temperature of 1063 °C was attained.

In the subsequent study Greenwood and Williamson [57] provided mathematical equations to explain the observations made in [61]. The equations revealed that for materials for which thermal conductivity and electrical resistivity increases with temperature, there exists a threshold for the potential drop for the interface to remain in thermal equilibrium. If the current through the interface is such that the potential drop across it is greater than the threshold the thermal equilibrium cannot be attained. The interface then undergoes softening or melting thereby increasing the contact area and arriving at a new threshold for the potential drop. The authors also recommended to use the product of current and "cold" resistance (resistance at very low currents) instead of voltage drop in the Kohlrausch's equation [135]. This modification helps to connect the maximum interface temperature to the level of current flowing through it.

Tamai and Tsuchiya [132] studied the effect of current on contact resistance and contact area for the case of thin (1 mm diameter) metal wires on a conductive film of SnO_2 and 1.3% Sb under very small loads (few milligrams). They made direct observations of the contact area and contact voltage while increasing the current (0 – 200 mA) through the interface. Although it is not explicitly stated in the paper if the tests reported were conducted under constant current or constant voltage conditions, based on the description of few figures therein it is assumed that the tests were conducted under

constant voltage conditions. The authors reported that the contact area increased markedly for low hardness metals (In, Pb, Sn, Zn, In-Sn alloy) as the current was increased through the contact while the increase in contact area was very gradual for harder metals (Mo, W, Cu, Ni, Au, Ag). They used the Wiedman-Franz-Lorenz law [14] to get an estimate of the interface temperature from the contact voltage measurement and attributed the softening of the interface at higher contact voltage (and current) to increase in contact area.

The validation of the Kohlrausch's voltage-temperature relation [135] was put to test by Timsit [136]. Based on the experimental measurements, Timsit concluded that the Kohlrausch's equation is applicable for contacts with radius greater than 10 μm and the relation becomes invalid for contacts with radius smaller than 30 nm. The deviation of the measured voltage drop from the predicted voltage was attributed to the significant heat losses by thermal conduction through surface oxide film and more importantly to Knudsen resistance.

In another study Runde et al. [133] investigated the material transfer across Al and Al_{85}-Zn_{15} interface, wherein Zn was used a tracer material. The tests were conducted under a load of 20 N with nominal contact area of 3 mm^2. The authors observed that the contact softening process initiated at around 100 mV and accelerated as the current through the contact was increased. At the end of the experiments the voltage drop was in the range of 115 – 220 mV and contact resistance in the range of 1.6 – 8.2 mΩ. It was also observed that the mass transfer across the contact increased with the duration of the passage of current. This was attributed to high current density at the interface leading to

electro-migration (Zn into anode) and the asymmetrical fracture of the intermetallic bridge during the contact separation.

In a study on gold-gold and copper-copper contacts, Bennett [137] demonstrated that the contact voltage initially increases linearly with current (Ohmic behavior), but after a certain current level the contact voltage remains constant with increase in current. This constant contact voltage was similar to the "softening voltage" as reported by Holm [14]. He suggested that electromigration, and not thermally induced yielding or recrystallization, is the significant phenomena controlling the contact behavior at temperatures below the melting point of the contact materials.

In another study on current induced aging, i.e. passing the current through the contact over an extended period of time, of the Al-Al contacts Runde et al. [119] reported that the electromigration of Al into anode is a significant mass transport phenomena. This leads to a high vacancy concentration at some distance inside the cathode and ensues into clustering of vacancies and forming of voids inside the cathode and thus impairing the mechanical properties of the contact. This can lead to reduction in contact resistance, due to increase in contact size, but even the newly developed contact undergoes the degradation process by electromigration.

Runde et al. [134] experimentally studied the aluminum contact interface correlating the contact voltage to the contact area measured after the tests under scanning electron microscopy (SEM). The current across the Al-Al interface was increased very gradually to avoid any transient affects and then kept constant for 5 hours. For certain test specimens the contact voltage was constant during the course of the test while some tests showed increasing and decreasing contact voltage measurements with transient peaks up

to 300 mV. The authors attributed the increasing resistance to the oxidation and corrosion of the *a*-spots, as suggested by Williamson [138]. The melting of the *a*-spots at around 300 mV and subsequent spreading of the liquid metal was reasoned to be the cause of decrease in the contact resistance and contact voltage. The periods of decreasing contact resistance was attributed to the softening of the interface which led to increase in contact area. The authors observed that the interface exhibiting high and unstable contact voltages were associated with larger contact spots, which is contrary to the relationship between the resistance and contact size (Holm's relation) and thus reasoned that the interface went through an aging process.

Timsit [139] performed experimental study on the melting voltages for several metal-metal contacts and compared the results with the theories presented by Greenwood and Williamson in [57] and also using Wiedman-Franz-Lorenz law [14]. The difference between the two theories is that Wiedman-Franz-Lorenz law uses the voltage drop across the conductors/interface to arrive at the maximum temperature while Greenwood and Williamson used the product of the current and cold resistance instead. Timsit defined the contact melting by the onset of instability in the potential drop measurement. The maximum temperature corresponding to this voltage drop, as calculated from the theory of Greenwood and Williamson in [57], was in good agreement with the values of melting temperature for the materials in contact. However the voltage drop corresponding to the melting temperature as calculated from the Wiedman-Franz-Lorenz law was found to be much higher than the observed melting voltage.

It can thus be summarized that the literature on the effect of current on electrical contact behavior does not offer strong explanation of melting voltages as reported by

Holm [14]. The behavior of the interface at the softening voltage and the melting voltage has been explained using Kohlrausch's equation [135] or Greenwood-Williamson's cold resistance – temperature relation [57]. Both of those equations are independent of the thermo-mechanical properties of the interface, or in other words they ignore the effect of temperature on the mechanical properties of the interface. Although softening voltage has been linked to the recrystallization temperature [132, 140] and electromigration [137], these explanations continue to discount the influence of temperature on the mechanical properties of the interface.

In this chapter experimental results are presented that demonstrate the phenomenon of voltage saturation in electrical contacts. This phenomenon, which is linked to the so-called softening voltage is then explained by considering the effect of temperature rise at the interface on the mechanical properties of the interface.

6.3 Experimental setup

The experiments investigating the effect of current cycling through the interface on the voltage and contact resistance are discussed here. The experiments were conducted on Al-Al and Cu-Cu interfaces under constant current conditions.

Figure 6.1 presents the schematic of the electrical circuit. A four-point voltage measurement was used to determine the electrical contact resistance. Two probes were used to determine the interface current (I) by measuring the voltage drop (V_s) across a known resistor (R_s) of 0.1Ω (±0.1%). A separate pair of probes was used to measure the voltage drop (V_c) across the interface. Note that V_c includes the voltage drop across an appreciable length of the upper and lower contact specimens. However, since the bulk

resistance (about 1 μΩ) is orders of magnitude less than the total contact resistance, its contribution was neglected. This arrangement was used for experiments at lower current (0 – 5 A). For the higher current range (0 – 225 A) the resistor R_s (for current measurement) was replaced by an inductive current sensor.

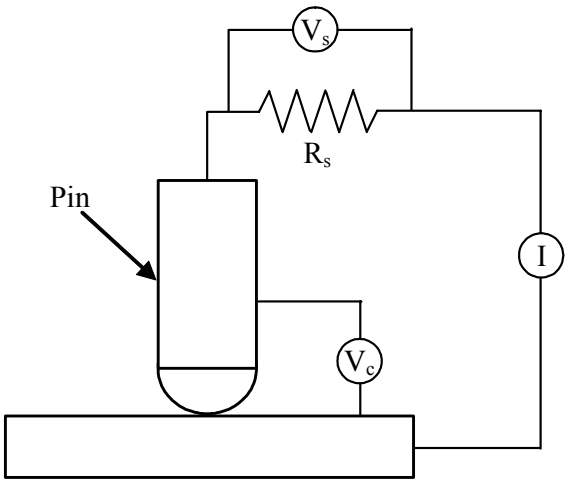

Figure 6.1 Electric circuit for contact resistance measurement

6.4 Study on Al-Al electrical interface

The experiments were conducted by loading a hemispherical pin having radius of curvature of 6.35 mm against a flat. The material of both the pin and the flat was Al 6061. The influence of varying test conditions on the contact voltage and the contact resistance is studied here.

6.4.1 Effect of current cycling – contact broken between cycles

The contact resistance measurements between the pin and the flat were made under three different current ranges: 0.01 A – 1 A, 0.02 A – 5 A, and 1 A – 50 A. The current was applied in a stepped fashion: at each step the current was maintained for 15

seconds and the average voltage over that time period is presented in the subsequent plots.

Figure 6.2 presents the contact voltage as a function of current through the interface on log-log scale. Here the current was first increased from 0.01 A – 1 A and then decreased back to 0.01 A, while keeping the load constant at 1 N during the experiment. The pin was raised at the end of each current cycle and then lowered back to the same location for the next current cycle. It is observed for all cycles that the contact voltage increases initially but then saturates around 160 – 170 mV beyond a current of 0.6 A. During the decreasing part of a cycle the voltage is seen to immediately decrease below the saturation level and it ends up at a value much lower than at the start of the cycle. It is hypothesized that the observed reduction in contact resistance is associated with increased contact area through interface heating and softening of the interface material. That the voltage is seen to increase between the end of one cycle and the beginning of another, suggests any enhanced surface conformity is lost upon breaking the contact. It is noted that no change in surface roughness due to current cycling was found.

Figure 6.3 illustrates the variation of contact resistance ($R_c = V_c/I$) with current for the same set of tests. It is seen that the contact resistance decreases as the current is increased. Interestingly for all three current cycles, the contact resistance converges to a value around 160–170 mΩ at 1 A.

Figure 6.4 illustrates the variation in contact voltage with current for the current range of 0.02 A–5 A on a log-linear scale for two current cycles. The pin was raised and lowered into contact at the same location between the current cycles and the load was

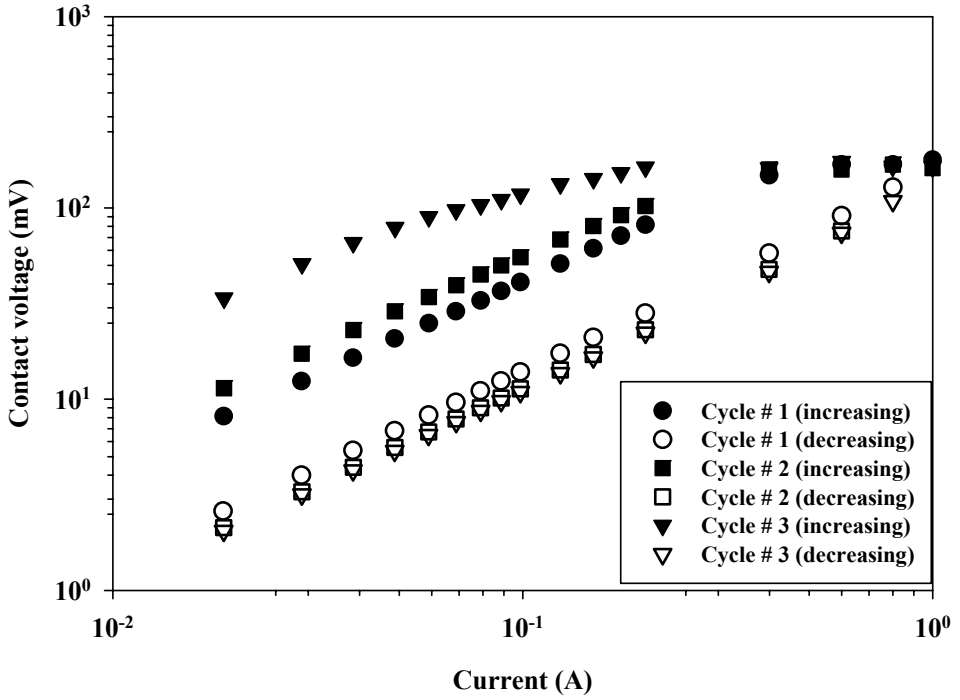

Figure 6.2 **Variation of contact voltage with current for 3 current cycles (0.01 A – 1 A). Pin raised and lowered between cycles**

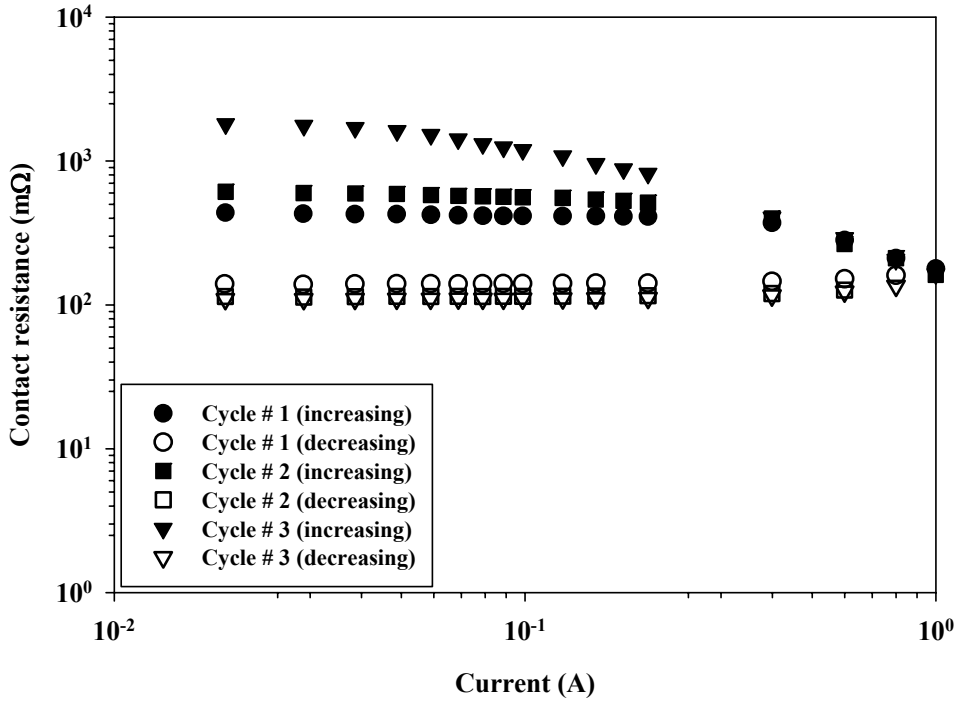

Figure 6.3 **Variation of contact resistance with current for 3 current cycles (0.01 A – 1 A) for conditions of Figure 6.2**

maintained at 1 N. Trends similar to Figure 6.2 are observed here i.e., contact voltage increases with current initially and then saturates around 150–160 mV at 1.25 A in the first and the second current cycle, and in the third current cycle the voltage saturates around 165–175 mV starting at 0.75 A. Figure 6.5 shows contact voltage versus current for the range of 1–50 A at a contact load of 1N. It is observed that in the voltage drop across the interface has a very gradual rate of increase with current. The contact voltage saturates at about 175–185 mV when the current is around 5–10 A. The contact voltage decreases as soon as the current is reduced and, for all three current cycles, the decreasing–current parts of the curves nearly coincide.

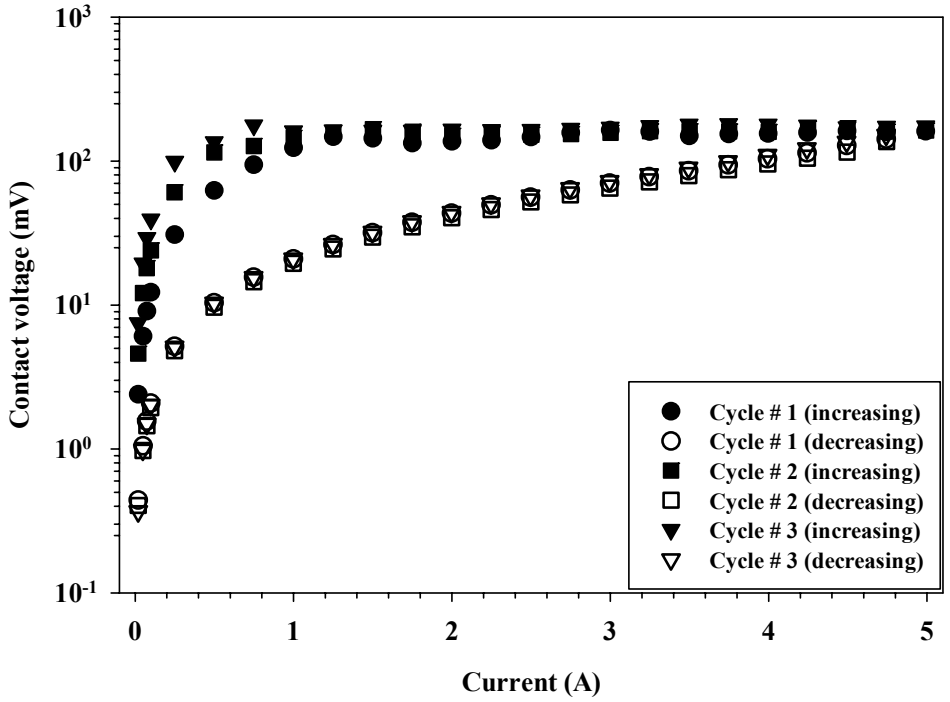

Figure 6.4 Variation of contact voltage with current for 3 current cycles (0.02 A – 5 A). Pin raised and lowered between cycles

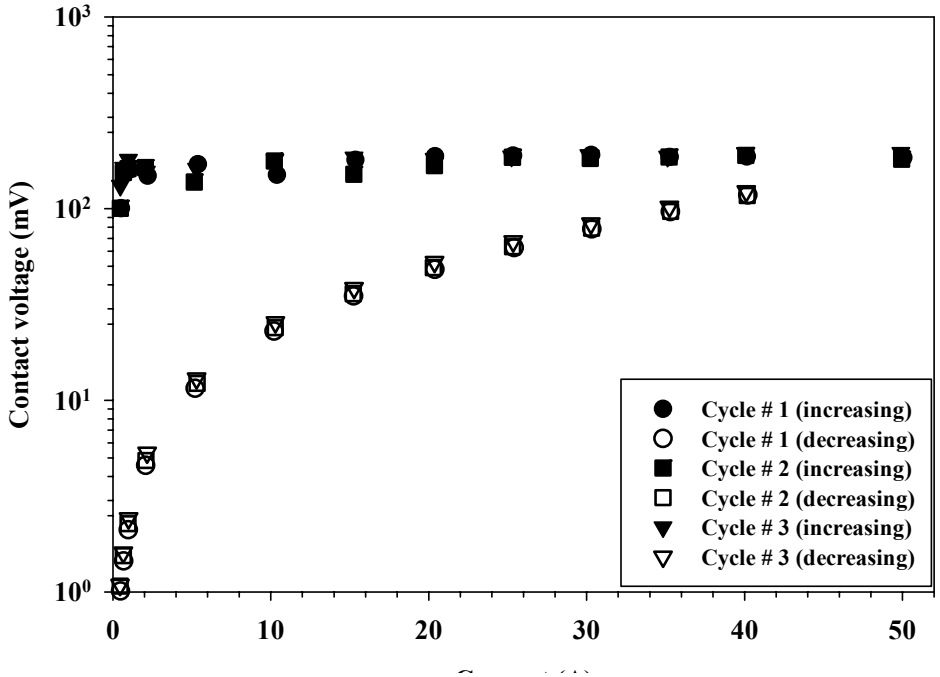

Figure 6.5 Variation of contact voltage with current for 3 current cycles (1 A – 50 A). Pin raised and lowered between cycles

In the subsequent set of experiments the current was cycled up to different peak currents, the first current cycle being limited to 25 A, the second one to 50 A, and the third one to 100 A. Between each current cycle the pin was raised and lowered back to the same location on the flat and the contact load was maintained at 1 N. Figure 6.6 illustrates the variation in contact voltage with current on a log-linear scale. In the first cycle, it is seen that the saturation voltage of 160–170 mV is reached after 7.5 A while, in the second current cycle the contact voltage reaches 165 mV at 7.5 A and then saturates around 185–195 mV after 10 A. In the third current cycle the contact voltage reaches 160 mV at 10 A and then saturates around 180 – 190 mV after reaching a current of 20 A. It is also seen that during the decreasing–current part of the cycles, the voltage at a given current depends on current history—i.e., it is a function of the peak current that was applied during the increasing–current part of the cycle. The higher the peak current, the

lower is the subsequent voltage at a given current. Figure 6.7 presents the variation in contact resistance with current for the test conditions of Figure 6.6. It is seen that the lowest contact resistance is different for each current cycle and it decreases as the peak current in the cycle increases.

In all of the above experiments the pin was raised and lowered back into the contact between current cycles. As it was seen that the voltage–current behavior for repeat cycles was quite similar to the initial cycle (see Figures 6.2–6.5), it can be inferred that the re-formed interface behaves as a "new" interface, showing little or no influence of the previous current cycling. This observation is significant given that, during a given current cycle, the contact resistance may decrease by orders of magnitude. It can thus be concluded that whatever morphological changes the interface experiences during current cycling do not persist once the contact is broken.

6.4.2 Effect of current cycling - pin kept in contact

For the following experimental results the pin was kept in contact with the flat between the current cycles. Figure 6.8 illustrates the variation in contact voltage with current for current cycles up to 5 A while the pin was kept in contact under load (1 N). It is seen that the contact voltage saturates around 150 – 160 mV starting at 0.5 A during the increasing–current part of the first cycle. During the increasing–current part of the second current cycle the contact voltage retraces the path followed during the decreasing–current part of the first current cycle. This indicates that the changes that interface goes through during the decreasing part of the current cycle are reversible, if the pin is

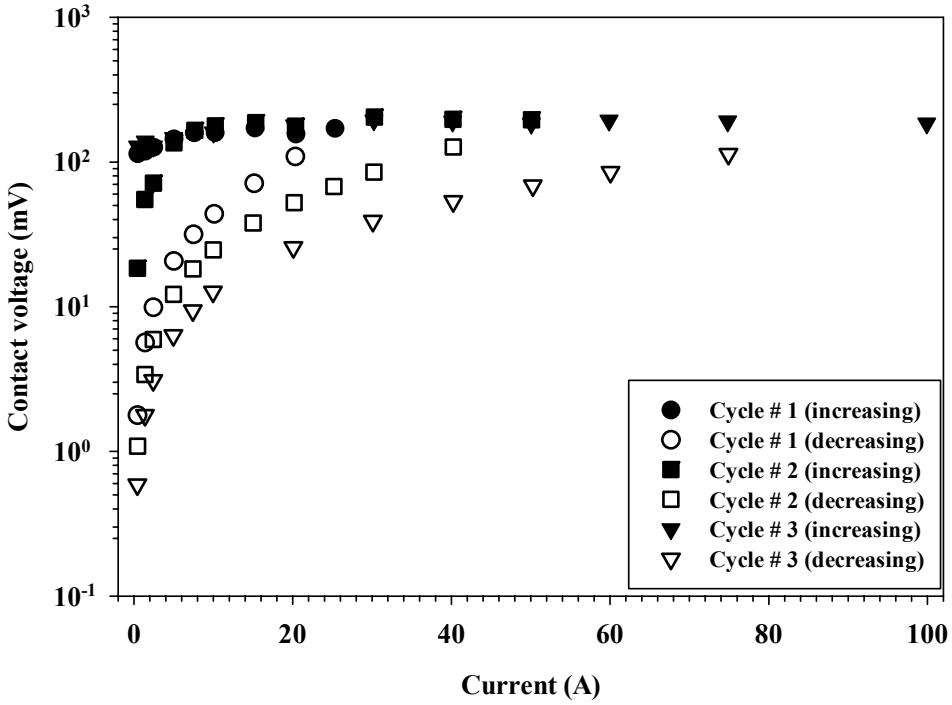

Figure 6.6 Variation of contact voltage with current for 3 current cycles with varying peak current values

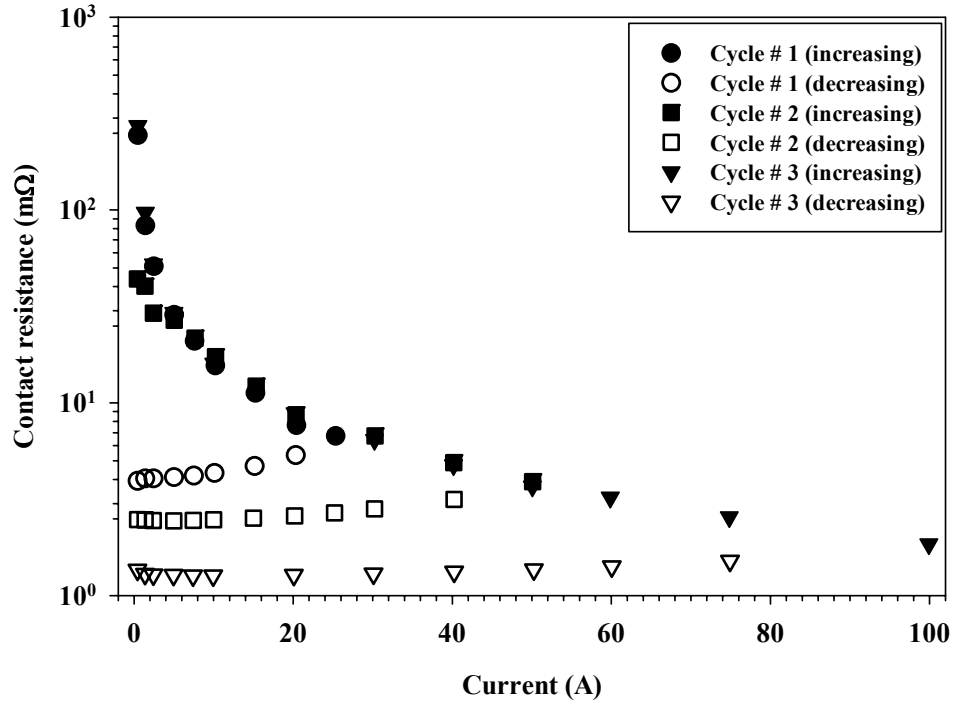

Figure 6.7 Variation of contact resistance with current for 3 current cycles with varying peak current values

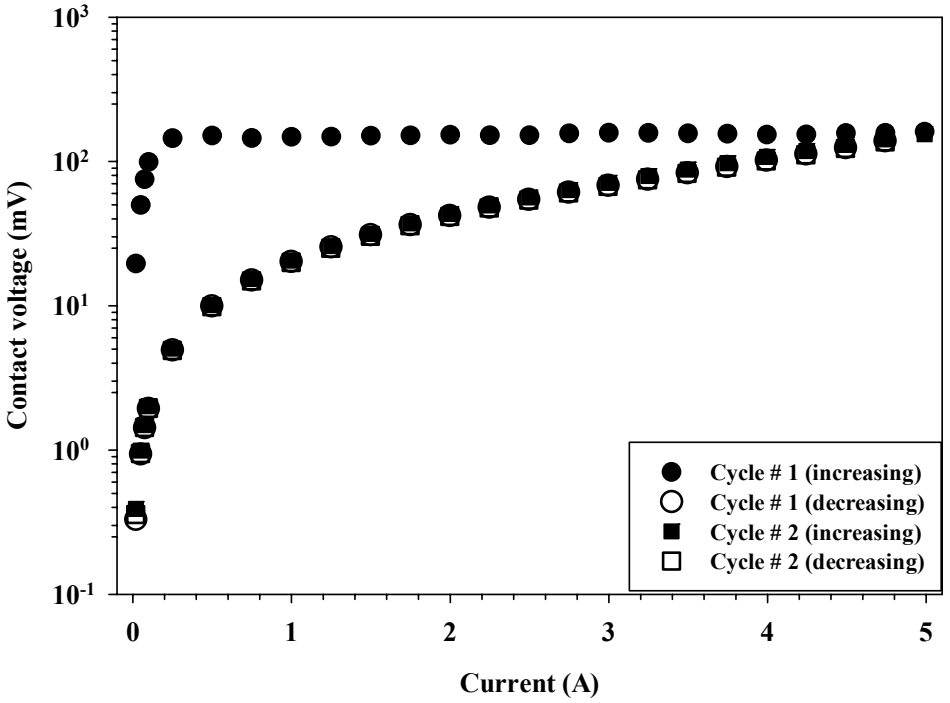

Figure 6.8 Variation of contact voltage with current for 2 current cycles while pin kept in contact between the cycles at 1 N

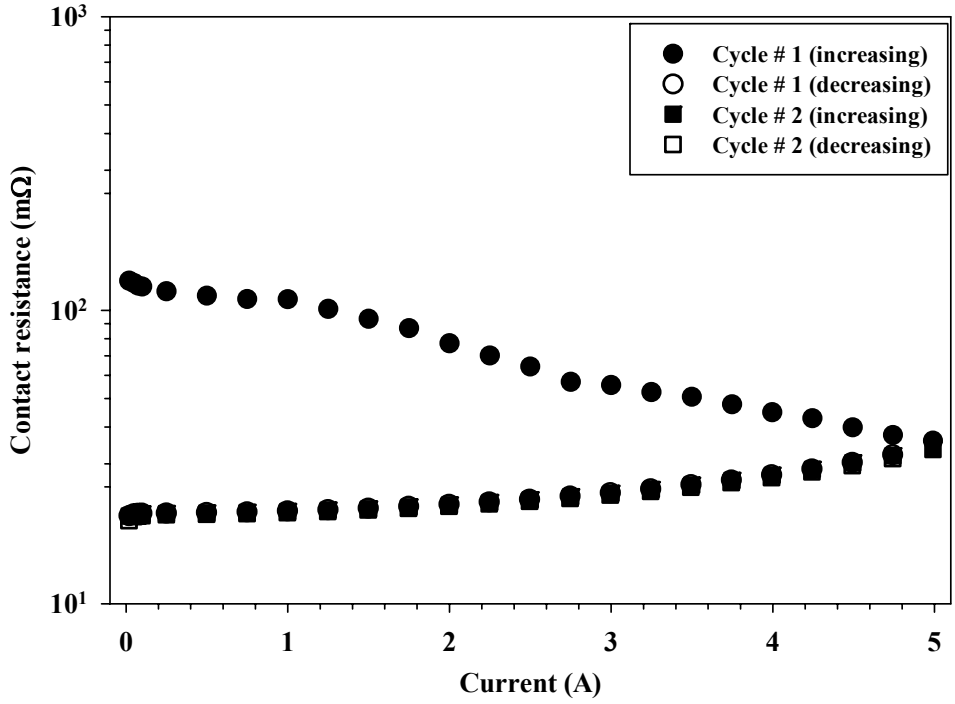

Figure 6.9 Variation of contact resistance with current for 2 current cycles while pin kept in contact between the cycles at 10 N

maintained in contact under load. This reversible nature of the contact resistance after an initial half-cycle was also noticed by Holm [14]. Similar observations were made at the contact load of 10 N, Figure 6.9 shows the variation in contact resistance with current for the same. The contact resistance is reversible for the second current cycle when the pin is maintained in contact.

In the next set of tests the current was cycled to different lowest values while keeping the peak current the same. The pin was kept in contact between successive cycles of current under the contact load of 5 N and the current was maintained constant for 10 seconds at each step. Figure 6.10 illustrates the time history of the contact voltage. After the first cycle (1A to 50A to 1A) the subsequent current cycles go to different minimum current levels but share the same peak current level of 50 A.

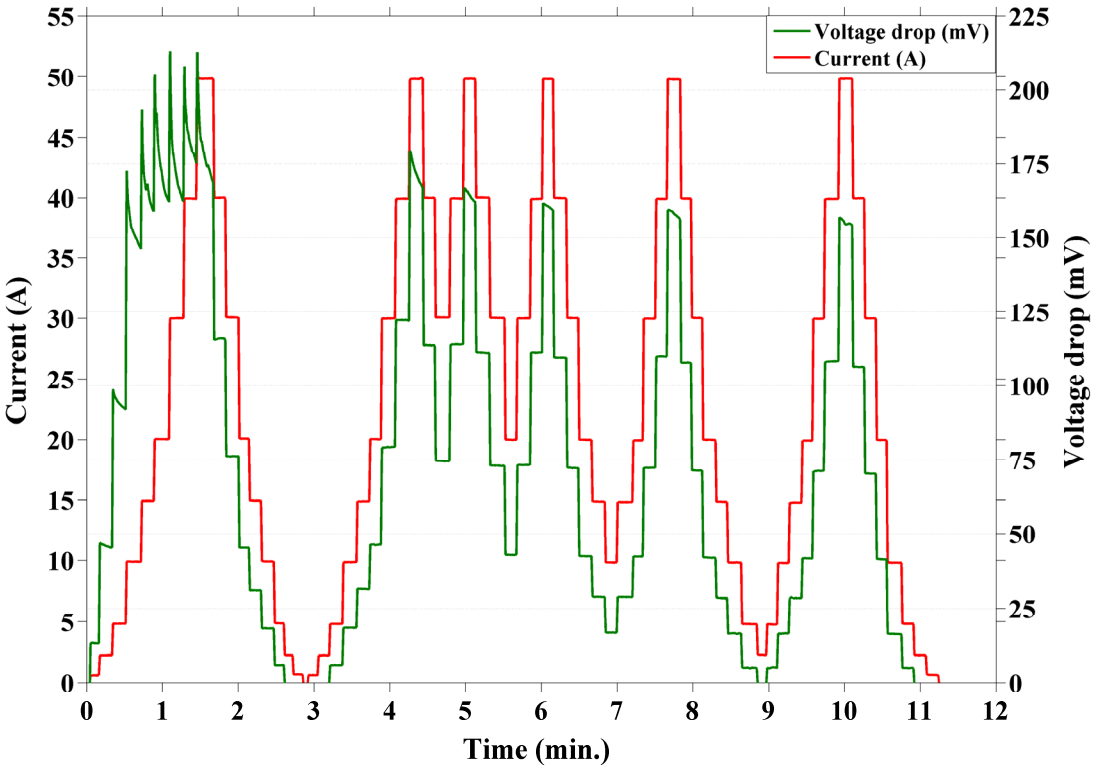

Figure 6.10 Time history of contact voltage and current

Figure 6.11 presents the variation in contact resistance for the test conditions of Figure 6.10. Trends similar to those observed in Figure 6.9 are observed here. Even though the current is cycled up to different minimum values of current, the interface behaves reversibly. The values of the contact voltage differ by a small for a given current level for different current cycles. However the contact voltage in the decreasing–current part of one cycle is nearly the same as the contact voltage during the increasing–current part of the subsequent current cycle, at a given value of current.

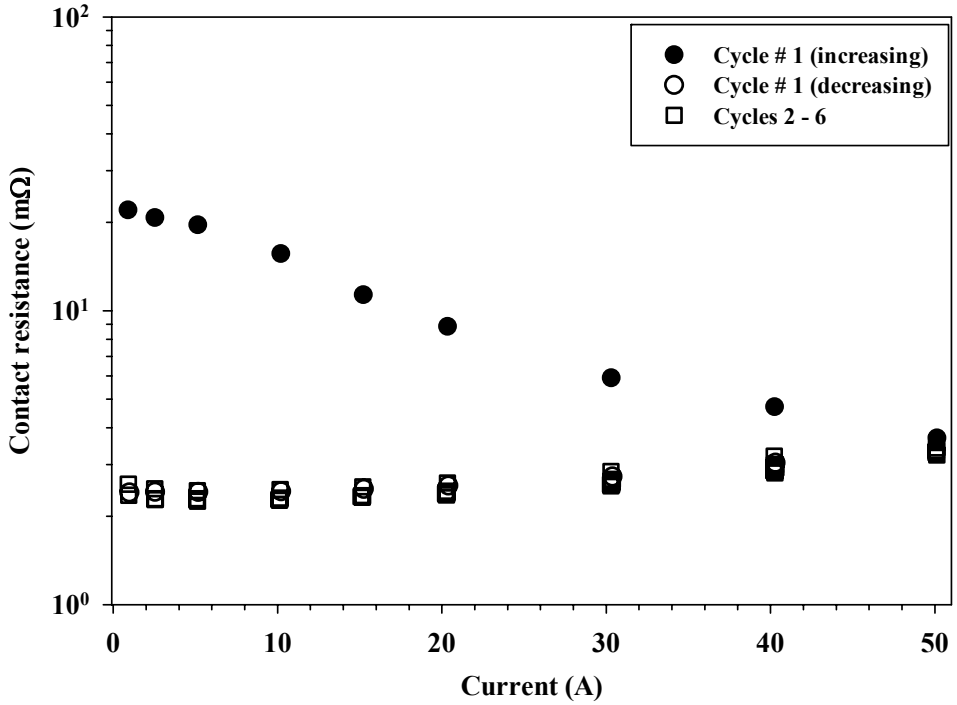

Figure 6.11 Variation of contact resistance with current for test conditions of Figure 6.10

6.4.3 Effect of load

The effect of load on the saturation voltage was investigated. Tests were conducted at different loads with a new pin for each load on a new location on the flat. Table 6.1 lists the contact loads and the corresponding Hertzian contact radii and

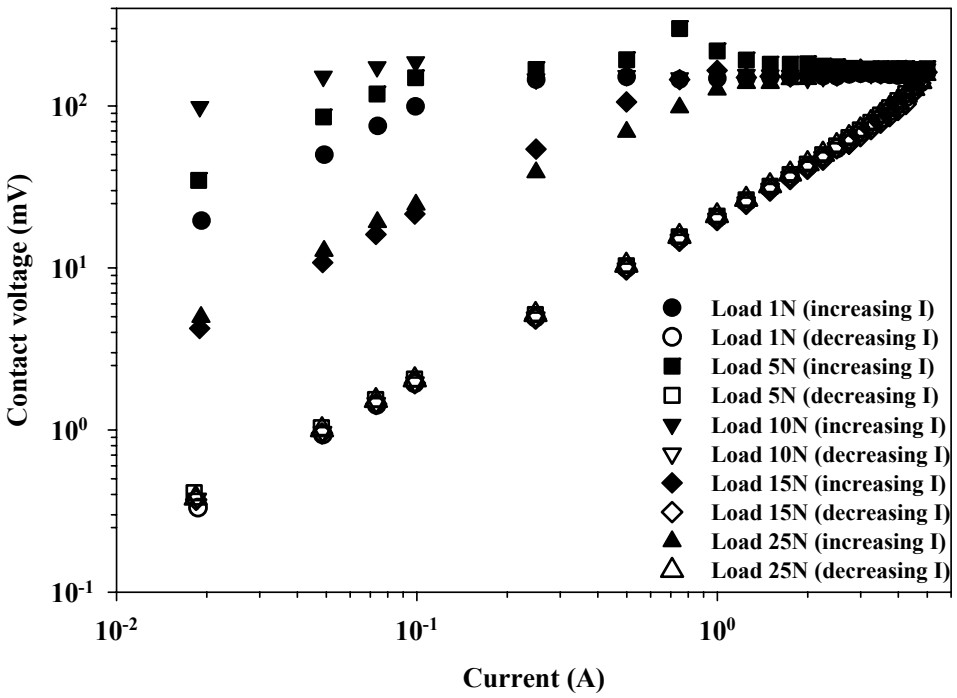

Figure 6.12 Variation in contact voltage with current for different contact loads

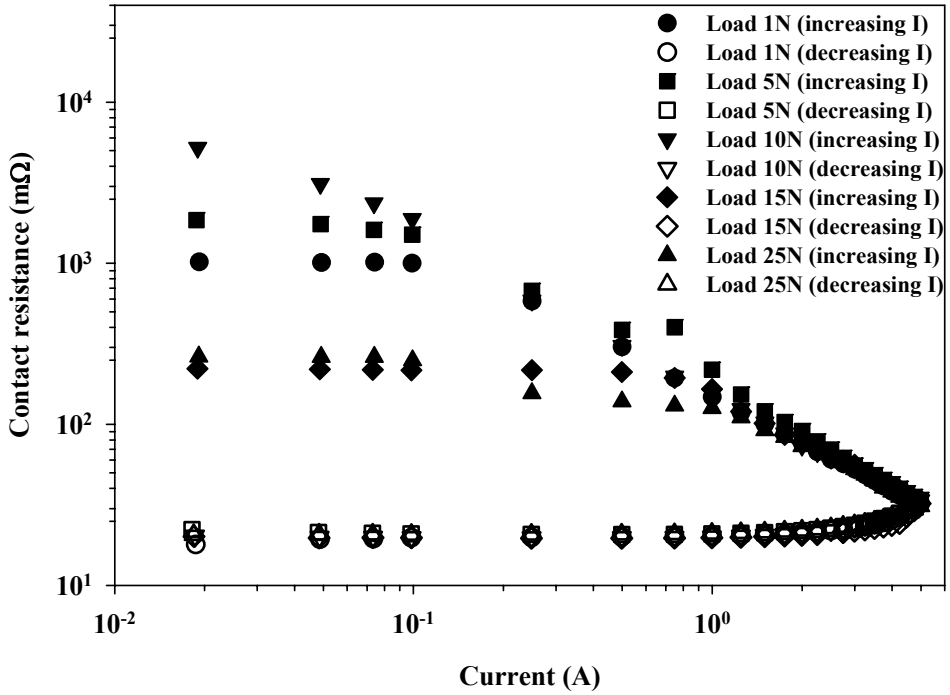

Figure 6.13 Variation in contact resistance with current for different contact loads

pressures. Figure 6.12 presents the comparison of contact voltages at different contact loads as the function of current. For the contact loads of 1 N, 5 N and 10 N the voltage saturation point is reached at very low currents (0.2 A). It is observed that at loads greater than 15 N the voltage saturation point is delayed. At 15 N load the voltage saturates around 160 mV starting at the current of 0.75 A, while the saturation point is reached at the current of 2 A at the contact load of 25 N. For all the contact loads the saturation voltage was in the range of 160 – 170 mV. Once the saturation voltage point is reached the interface behaves identically under all the loads. The decreasing–current part of the current cycle is virtually identical at all the contact loads, which suggests that this part of the current cycle is influenced more by the current history rather than the load. Figure 6.13 illustrates the variation in contact resistance with current at the various contact loads.

Table 6.1 Contact parameters for Al-Al contact

Contact load (N)	Hertzian contact radius (μm)	Average Hertzian contact pressure (MPa)	Maximum Hertzian contact pressure (MPa)
1	49.8	128.6	192.9
5	85.1	219.9	329.9
10	107.2	277	415.5
15	122.7	317.1	475.7
25	145.5	376	564

6.4.4 Effect of surface roughness

Here the effect of the surface roughness of the flat on voltage saturation is investigated. Pins with nominally the same surface finish were tested against flats having different surface roughnesses. Flats with three different surface roughnesses were

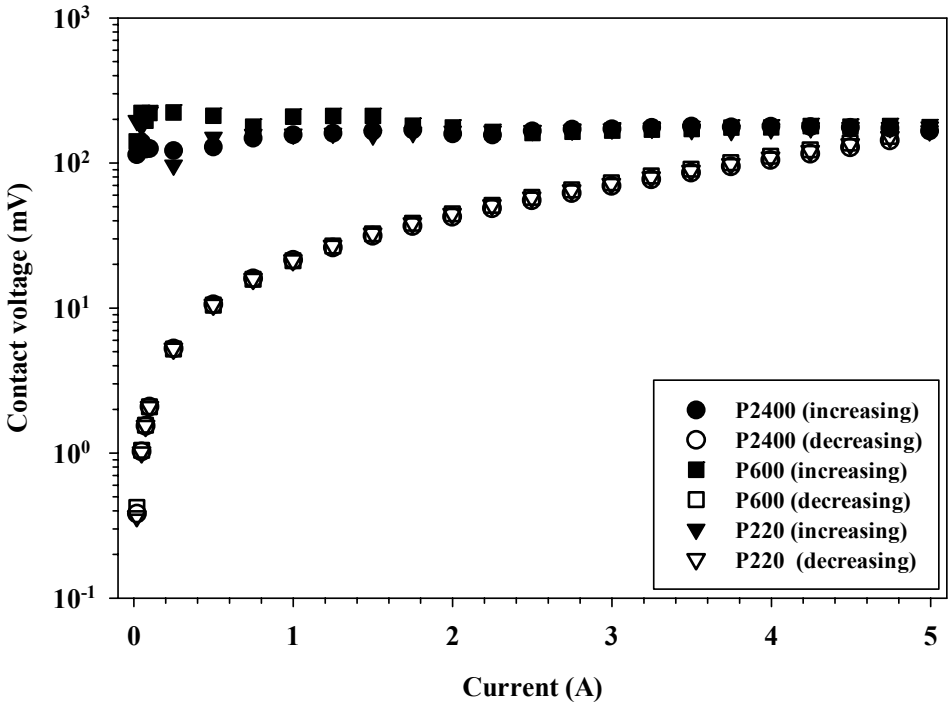

Figure 6.14 Variation in contact voltage drop with current for flats with different surface roughnesses at 1 N load

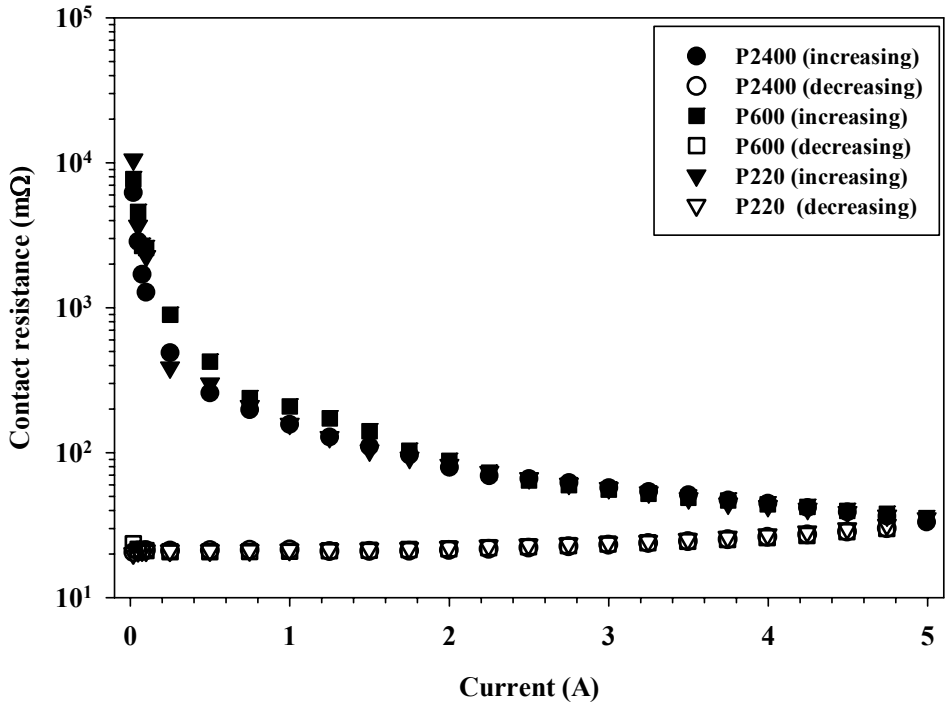

Figure 6.15 Variation in contact voltage drop with current for flats with different surface roughnesses at 1 N load

Table 6.2 Surface roughness parameters of pins and flats

Pin				Flat		
Before Tests		After Tests		Before Tests		Sand paper grit
R_a (μm)	R_q (μm)	R_a (μm)	R_q (μm)	R_a (μm)	R_q (μm)	
0.11	0.17	0.109	0.17	0.26	0.38	P2400
0.151	0.224	0.15	0.221	0.24	0.33	P600
0.13	0.18	0.121	0.156	0.46	0.62	P220

prepared by polishing those with sand papers of different grits, viz P220, P600 and P2400 while the load was set at 1 N for all the tests. Table 6.2 lists the surface roughness parameters of the pins and the flats before and after the tests.

Figure 6.14 illustrates the contact voltage as a function of the current through the interface for tests performed with flats of different surface roughnesses. A new pin was used for each test case and the repeated (3–5 times) test runs resulted in similar observations, hence only one representative test run is shown in the above figures. It can be inferred that surface roughness of the flat has little influence on the voltage saturation; once the saturation point is reached the interface behaves identically irrespective of the surface roughness. The onset of saturation also seems to be independent of the surface roughness. Figure 6.15 shows the variation in contact resistance as a function of current for the test conditions of Figure 6.14. It is observed that the smoothest surface (polished with P2400) yields the highest contact resistance at the lowest current while the roughest polished flat yields the lowest contact resistance.

6.4.5 A note on voltage transients in Al-Al contacts

During the increasing–current part of the current cycle through the interface, after a certain current level when the current was increased a voltage spike was observed. The contact voltage then decreased rapidly followed with a more gradual decrease towards the saturation voltage point. Figure 6.16 shows the time history of current and contact voltage while the current was maintained constant for 3 minutes at each step.

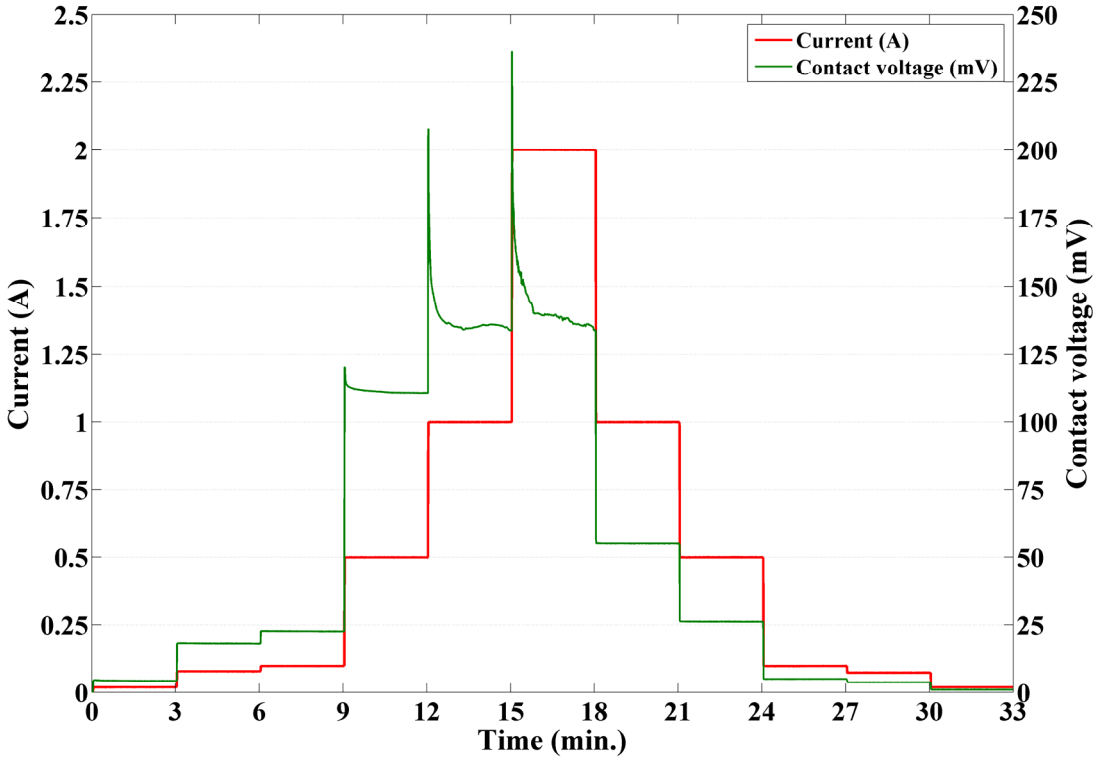

Figure 6.16 Time history plot of current and voltage

The voltage spike above 200 mV is observed for current levels greater than 0.5 A. This can be explained as: after a given current level the interface reaches its saturation voltage and for any additional current to pass through, the interface has to undergo some change. The voltage spike and associated temperature rise causes permanent changes in

the interface morphology and thus allows the interface to conduct this higher current at a lower contact resistance. This explanation is different to the one proposed by Bowden and Williamson [61], wherein they suggested that the interface has a critical resistance associated with a current level. In this study it is observed that there is a saturation voltage associated with the interface and once that voltage is reached, any additional increase in current causes the interface to change so that the contact voltage reaches back to the saturation level. The steady decrease in the contact voltage, while the current is maintained constant, suggests that the interface is undergoing physical changes. These spikes are absent during the decreasing part of the current cycle. This indicates that the interface equilibrates with the new current level without requiring additional changes in the area of contact.

Referring back to Figure 6.10 wherein the current is cycled while keeping the pin in contact, it is seen that voltage spikes are absent in the current cycles after the first current cycle. This further substantiates the hypothesis that whatever changes the interface went through during the first increasing–current cycle persist in the interface and the subsequent current cycles, up to the same maximum current, cause no further changes in the interface morphology.

The voltage-temperature relation for mono metal contact is given as [58]

$$V^2 = 8k_o\rho_o\left\{\left(T_m - T_1\right) + \left(\alpha - \beta\right)\left(T_m^2 - T_1^2\right)/2 - \alpha\beta\left(T_m^3 - T_1^3\right)/2\right\} \tag{6.1}$$

where V is the contact voltage, T_1 is the remote boundary temperature, T_m is the maximum temperature in the interface, k_o is the thermal conductivity at the room temperature, ρ_o is the electrical resistivity at room temperature, α is the temperature coefficient of electrical resistivity and β is the temperature coefficient of the thermal

conductivity. The dependence of thermal conductivity and electrical resistivity on temperature can be expressed using following equations:

$$k = k_o\left(1-\beta T\right) \tag{6.2}$$

$$\rho = \rho_o\left(1+\alpha T\right) \tag{6.3}$$

Table 6.1 [58, 141] lists the values of the parameters for pure Al used in Eq. (6.1).

Table 6.3 Parameters for Al-Al contact for voltage-temperature relation Eq. (6.1)

α (1/ °C)	β (1/ °C)	k_o (W/m.K)	ρ_o (Ω.m)
6.01×10^{-3}	-3.58×10^{-4}	167	3.99×10^{-8}

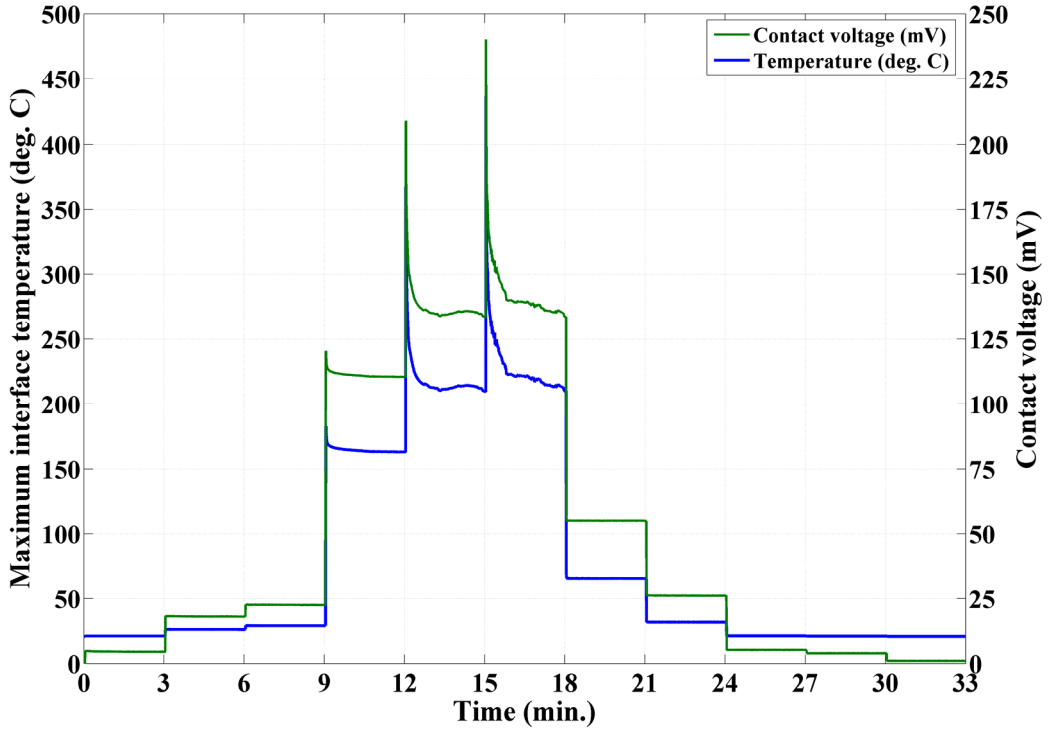

Figure 6.17 Time history of maximum theoretical interface temperature

The maximum interface temperature can be calculated from the above equation by solving it iteratively for a known contact voltage. Figure 6.17 illustrates the time

history of the maximum interface temperature as calculated from Eq. (6.1). It is seen that the voltage spikes causes the temperature to spike to values greater than 400° C. Although this could be a very localized phenomenon in the interface, i.e. occurring within few *a*-spots, it can influence the strength of the interface and thus modify it (discussed in Section 6.6).

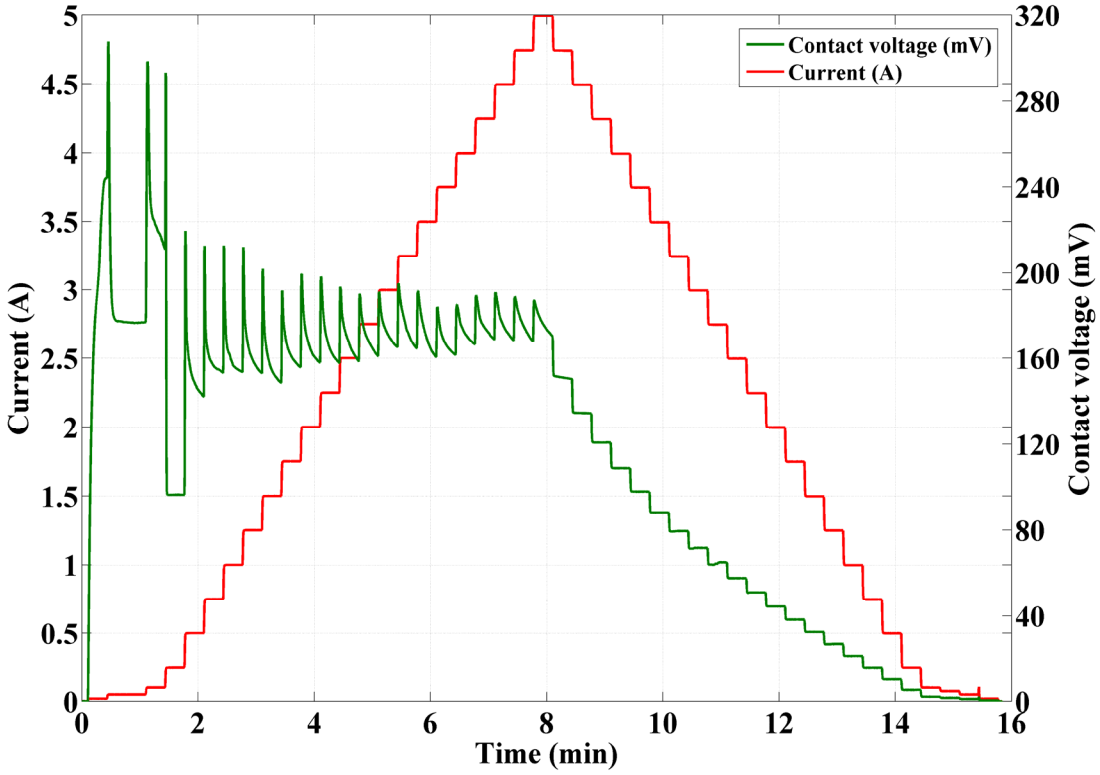

Figure 6.18 Time history plot of current and voltage

Figure 6.18 shows the time history plot of current and contact voltage for pin tested on the flat polished with P220 grit sand paper with load of 1 N. Voltage spikes up to 300 mV are seen for the first couple of current steps in the increasing part of the current cycle. The contact voltage does not exhibit steady behavior and spikes up to 200 mV are observed throughout during the increasing part of the current cycle. During the

decreasing part of the current cycle the contact voltage exhibits steady behavior. Figure 6.19 presents the time history plot of maximum interface temperature as calculated using Eq. (6.1). It is seen that the temperature spikes greater than 580° C for the first couple of current steps and then spikes up to 350° C are seen during the increasing part of the current cycle. The maximum interface temperature remains around 300° C throughout the course of increasing part of the current cycle.

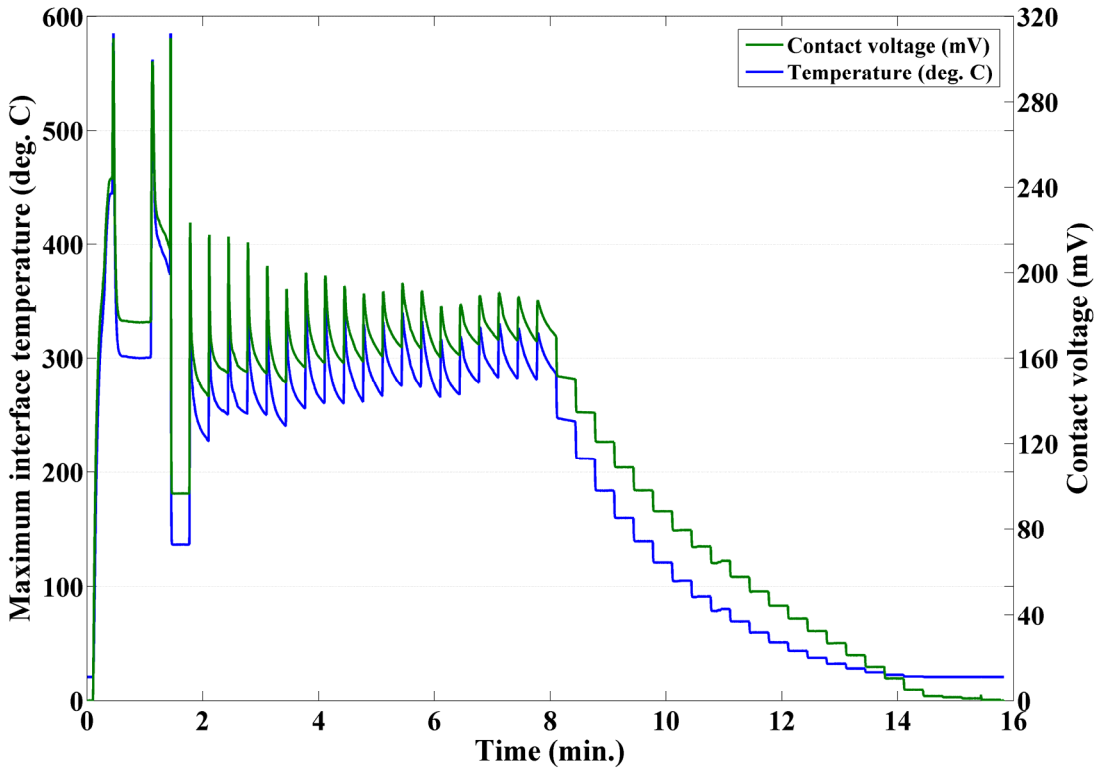

Figure 6.19 Time history plot of maximum interface temperature and contact voltage

6.5 Study on Cu-Cu electrical interface

The phenomena of voltage saturation in Cu-Cu contacts was investigated by conducting experiments with copper (C110) pins on copper (C110) flat. The pin had a radius of curvature of 5.3 mm. The following sub-sections discuss various factors influencing the voltage saturation in Cu-Cu contacts.

6.5.1 Effect of current cycling – contact broken between cycles

Here the effect of cycling the current through the interface up to different peak currents is investigated. Figure 6.20 illustrates the variation in contact voltage with current under the load of 2.2 N for the current range of 0.01 − 0.3 A. The pin is raised and lowered back into the contact between the current cycles. The current was increased in steps and maintained constant for 10 seconds at each step. The average values of the contact voltage and contact resistance over 10 seconds are presented in the subsequent plots. It is seen that the voltage drop across the contact increases linearly with current and retraces its path during the decreasing part of the current cycle. No sign of hysteresis is observed between the two current cycles. Figure 6.21 presents the variation in the contact resistance with current for the same test conditions. The contact resistance does not vary appreciably with current and the subsequent test runs exhibit similar behavior. It can thus be concluded that the contact is behaving in perfectly "Ohmic" sense. Similar observations of linear dependence of contact voltage on interface current are made for the experiments with current range of 0.02 – 5 A at 1 N load, as shown in Figure 6.22. Interestingly the contact resistance decreases by almost 50% from 0.02 A to 0.75 A, and then remains steady around 7.6 mΩ up to the peak current of 5 A. The contact resistance

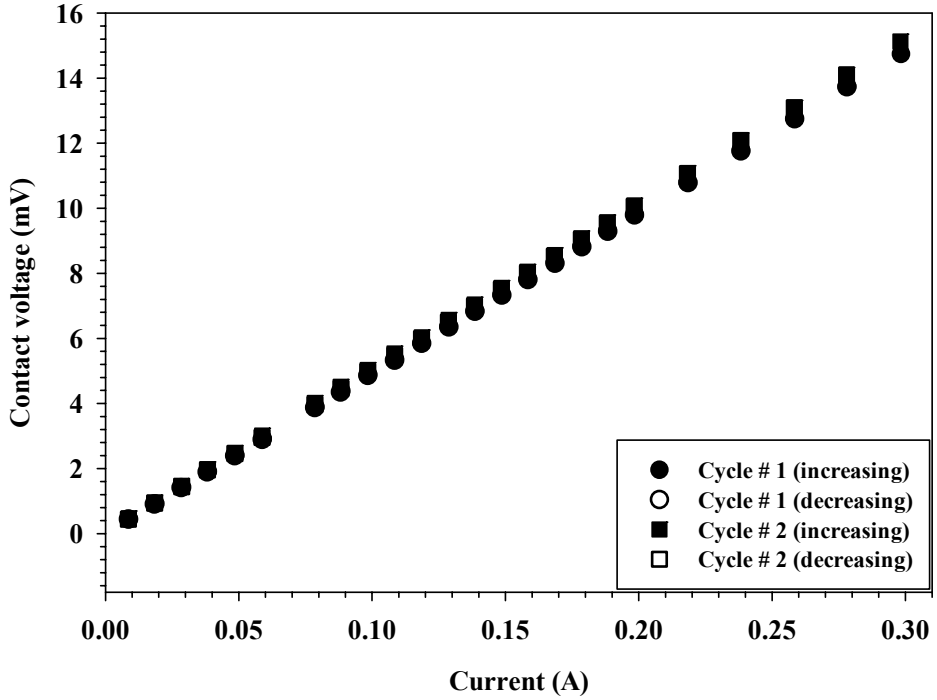

Figure 6.20 Variation in contact voltage with current for current range of 0.01 – 0.3 A. Pin raised between current cycles

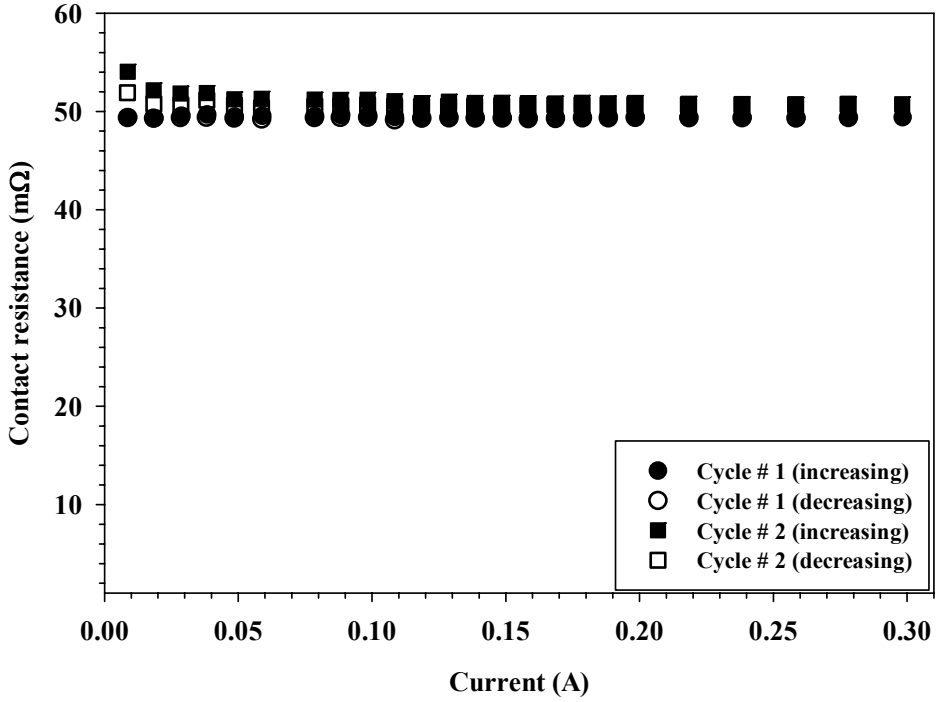

Figure 6.21 Variation in contact resistance with current for current range of 0.01 – 0.3 A. Pin raised between current cycles

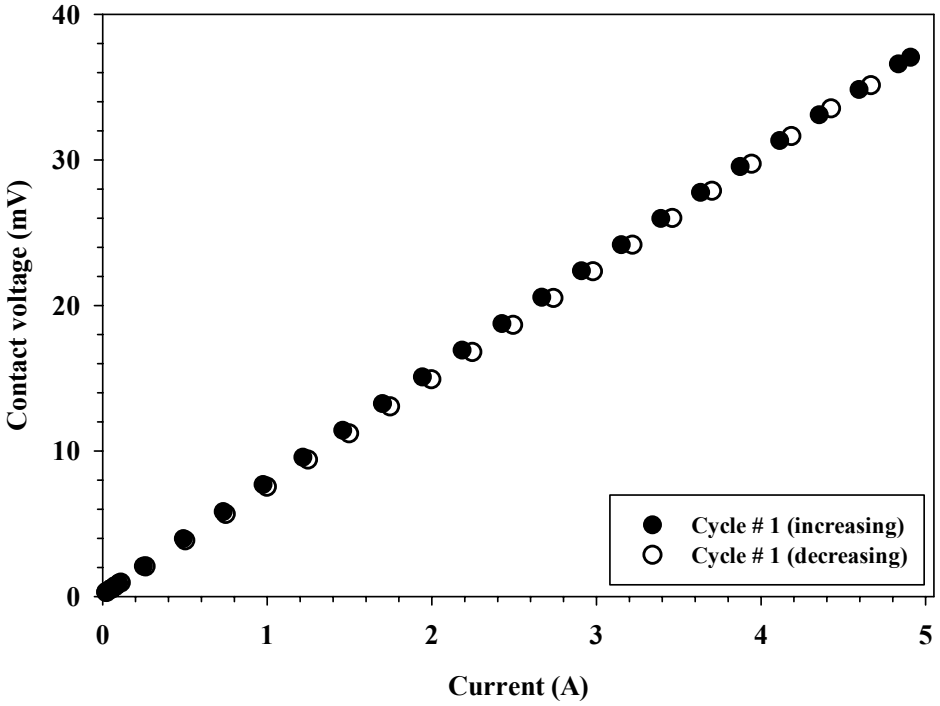

Figure 6.22 Variation in contact voltage with current for current range of 0.02 – 5 A

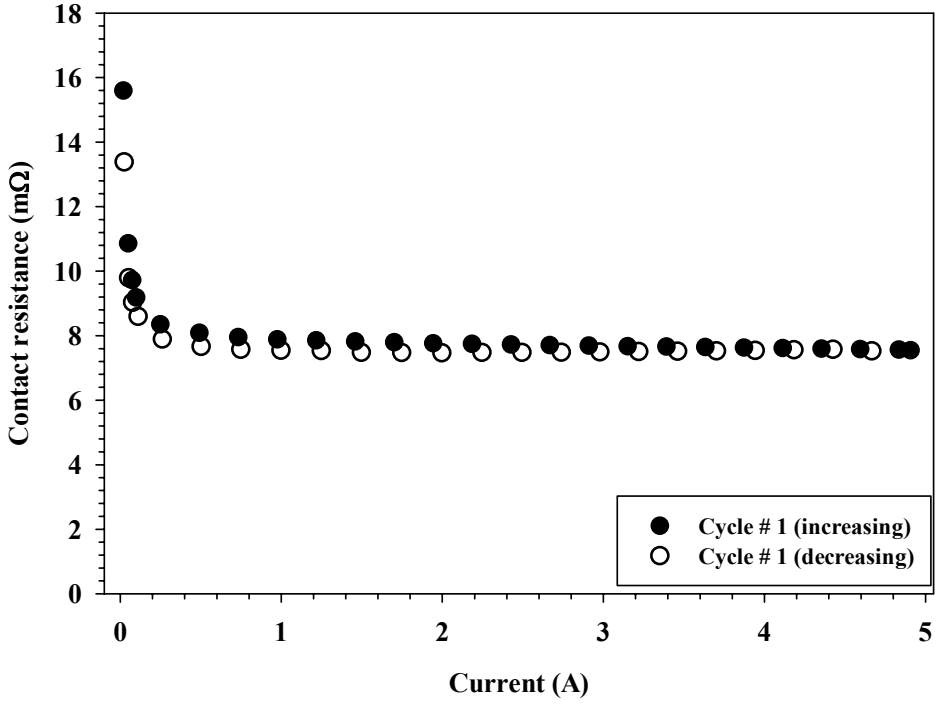

Figure 6.23 Variation in contact resistance with current for current range of 0.02 – 5 A

during the decreasing part of the current cycle follows the same path as during the increasing part of the cycle, but ends up at a value 14% lower at the current of 0.02 A.

Figure 6.24 illustrates the variation in the contact voltage with current for current cycles with peak current of 50 A. The contact load was maintained at 1 N throughout and the pin was raised and lowered back in to the contact between the current cycles. The current was increased in steps and maintained constant for 10 seconds at each step. It is observed that, in the first current cycle the voltage begins to saturate around 110 mV starting at 10 A and in the second current cycle this saturation point occurs around 20 A, while in the third current cycle this saturation point occurs around 45 A. In the decreasing–current part of each cycle the contact voltage decreases with decreasing, and for a given current the contact voltage takes a value lower than the value during the increasing part of the cycle. Figure 6.25 presents the contact resistance as function of the interface current for the experimental conditions of Figure 6.24. The contact resistance is highest at the beginning of each cycle and it decreases with increasing current for every current cycle.

Figure 6.26 presents contact voltage as function of current for current cycles with different peak currents. Cycle 1 has the peak current value of 25 A, cycle 2 of 50 A, cycle 3 of 100 A, and cycle 4 of 150 A. The pin was raised and lowered back into the contact between the cycles and the load was maintained at 1 N throughout the experiment. In the first cycle the contact voltage increases up to 142 mV at 4 A and then starts to gradually decrease and steadies itself around 130 mV. As soon as the current was decreased the contact voltage decreased and followed a different path. In the subsequent current cycle the contact voltage increases with current and saturates around 130 mV starting at the

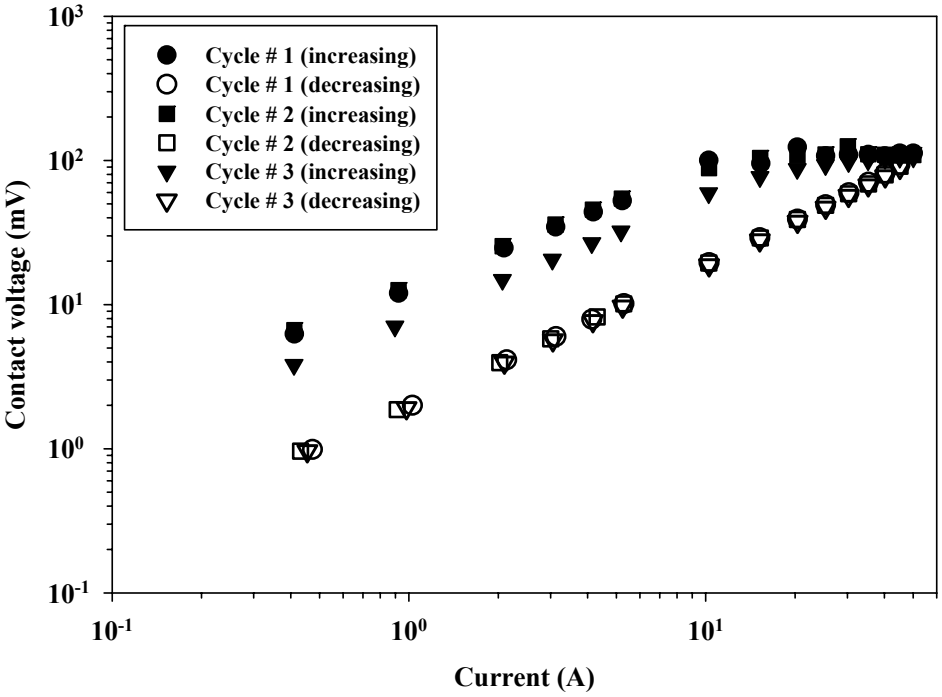

Figure 6.24 Variation in contact voltage with current for current range of 0.5 – 50 A. Pin raised between current cycles

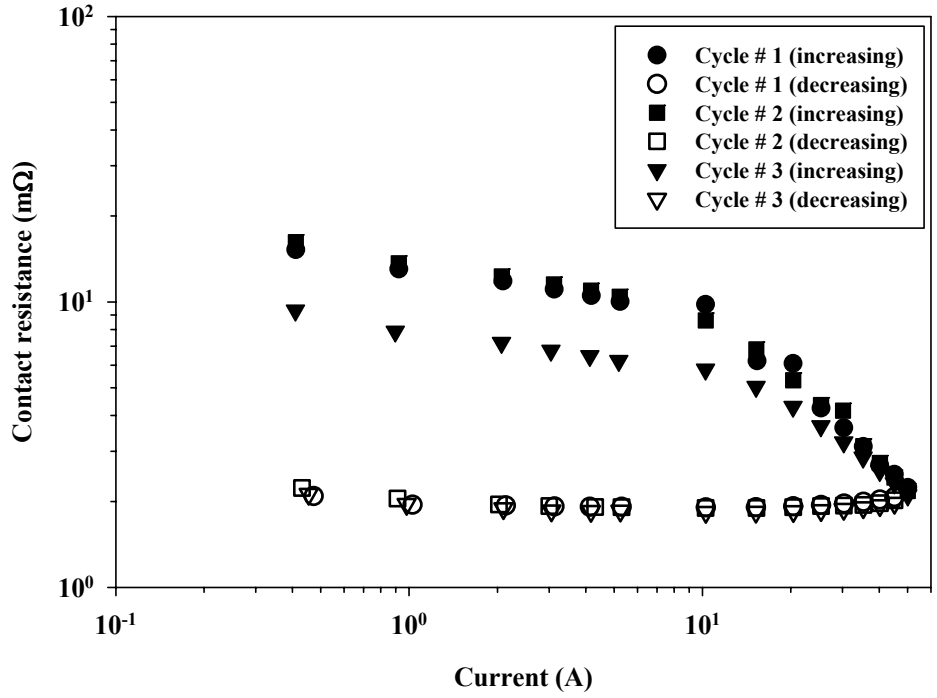

Figure 6.25 Variation in contact resistance with current for current range of 0.5 – 50 A. Pin raised between current cycles

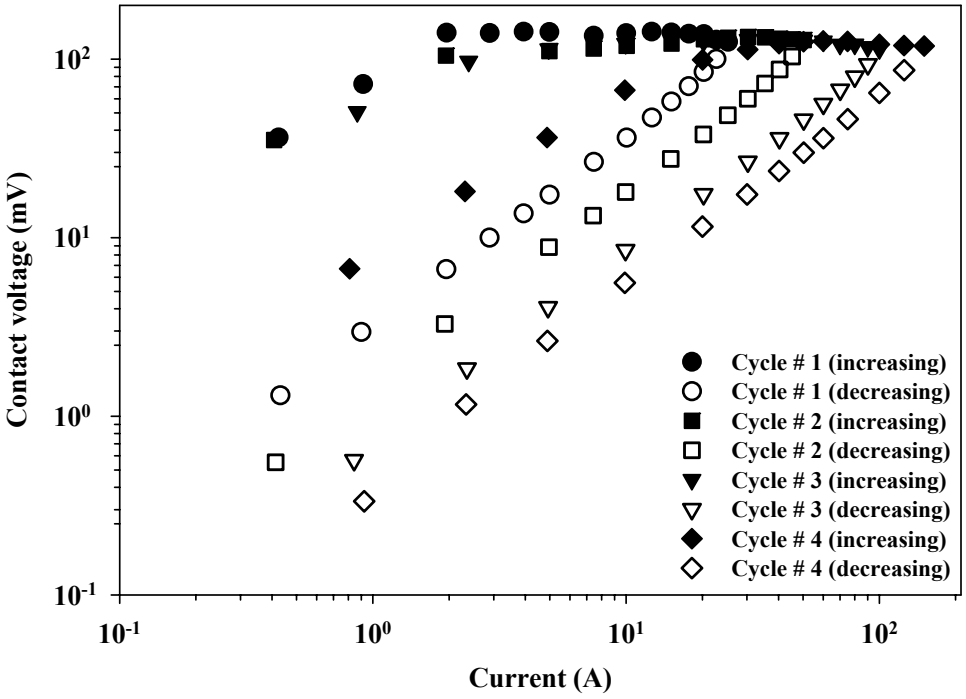

Figure 6.26 Variation in contact voltage with current for current cycles with different peak currents. Pin raised between cycles

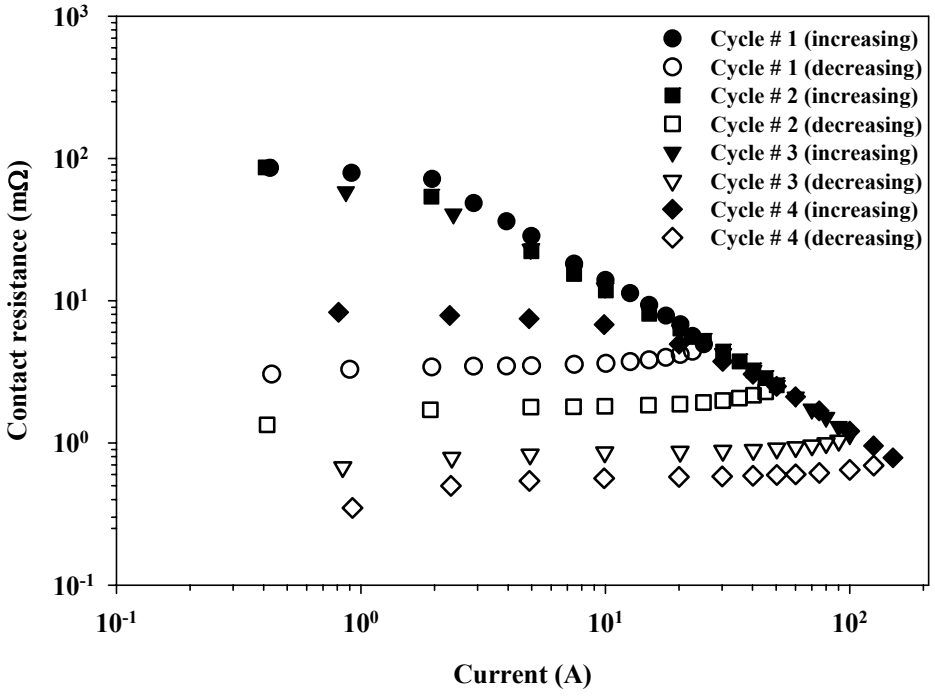

Figure 6.27 Variation in contact resistance with current for current cycles with different peak current levels. Pin raised between cycles

current of 20 A. In the third current cycle the contact voltage increases up to 130 mV at 40 A, but then decreases and saturates around 120 mV. In the fourth current cycle the voltage starts out a bit lower than in the previous three cycles and saturates around 120 mV. Interestingly the contact voltage follows a new path for each current cycle when the current is decreased; this is because each current cycle has a different peak current, which modifies the surfaces to a greater degree than the previous current cycle. This results in permanent changes in the surface and when the contact is re-established for the subsequent current cycle the interface behaves as a "new" interface. Figure 6.27 illustrates the variation in contact resistance with current for the same test conditions as in Figure 6.26. It is seen that the contact resistance during the increasing–current part of the current cycles traces the same paths except for the cycle with peak current of 150 A. The lowest contact resistance during the increasing–current part of the cycle is different for each cycle as the peak current is different, and the contact resistance follows different curves during the decreasing–current part of the cycle for each cycle. It is observed that the contact resistance during the increasing–current part for the Cycle # 4 is much lower than the previous cycles. This could be due to the morphological changes the pin surface would have gone through due to heating in the previous cycles.

6.5.2 Effect of current cycling – pin kept in contact

In the following experiment the pin was maintained in contact, under the load of 1 N, while the current was cycled up to different peak currents. For the first current cycle the peak current was set at 10 A, 25 A for the second current cycle, 50 A for the third current cycle, 100 A for the fourth current cycle and the peak current was 150 A for the

fifth current cycle. Figure 6.28 presents the contact voltage for the different current cycles while the pin was maintained in contact. It is observed that the saturation voltage of 140 mV is reached in the first current cycle at a current of 5 A. For the second current cycle the contact voltage retraces the same path as during the decreasing part of the first current cycle and reaches a contact voltage of 140 mV at 12 A. The contact voltage then decreases to 130 mV at 25 A. In the third current cycle the contact voltage during the increasing part of the current cycle retraces the same path as during the decreasing part of the second current cycle. This behavior is observed for all the subsequent current cycles. During the increasing part of the second current cycle the contact voltage reaches 130 mV at 35 A but then starts to decrease and saturates around 125 mV at 45 A. In the fourth current cycle the contact voltage reaches a peak value of 123 mV at 60 A and then starts decreasing and saturates around 115 mV at 90 A. In the fifth current cycle the saturation voltage of 119 mV is reached at the peak current of 150 A. Figure 6.29 illustrates the variation in contact resistance as a function of current for the same test conditions of Figure 6.28. It is observed that, after the first cycle, the contact resistance during the increasing part of a current cycle retraces the same path as during the decreasing part of the preceding current cycle. However for each current cycle the contact resistance reaches a new minimum as the peak current in a given current cycle is higher than that in the preceding cycle.

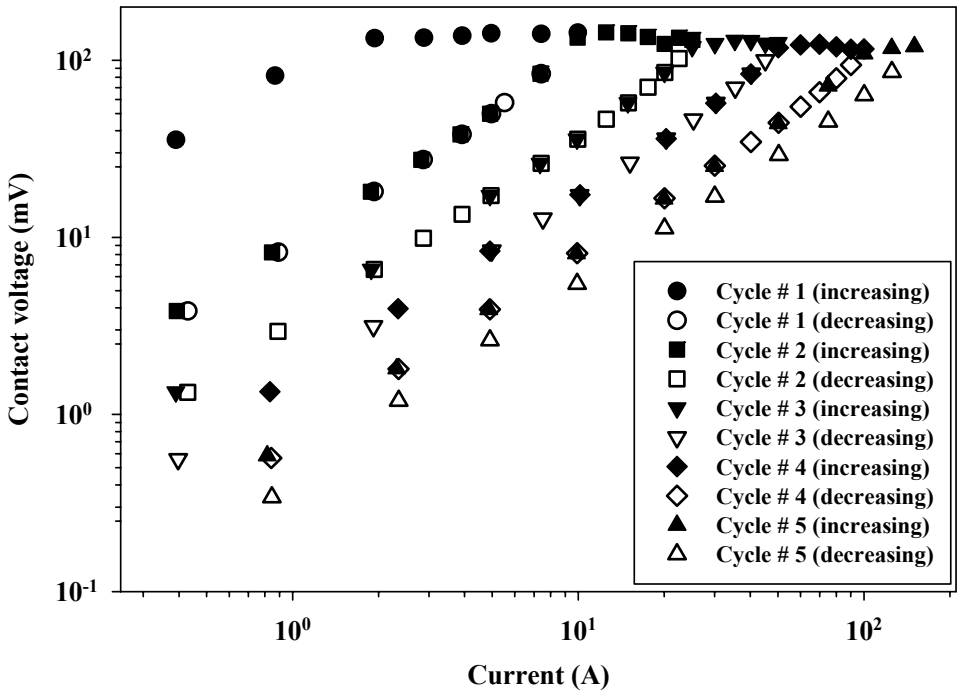

Figure 6.28 Variation in voltage drop with current for Cu-Cu contact. Pin maintained in contact at 1 N

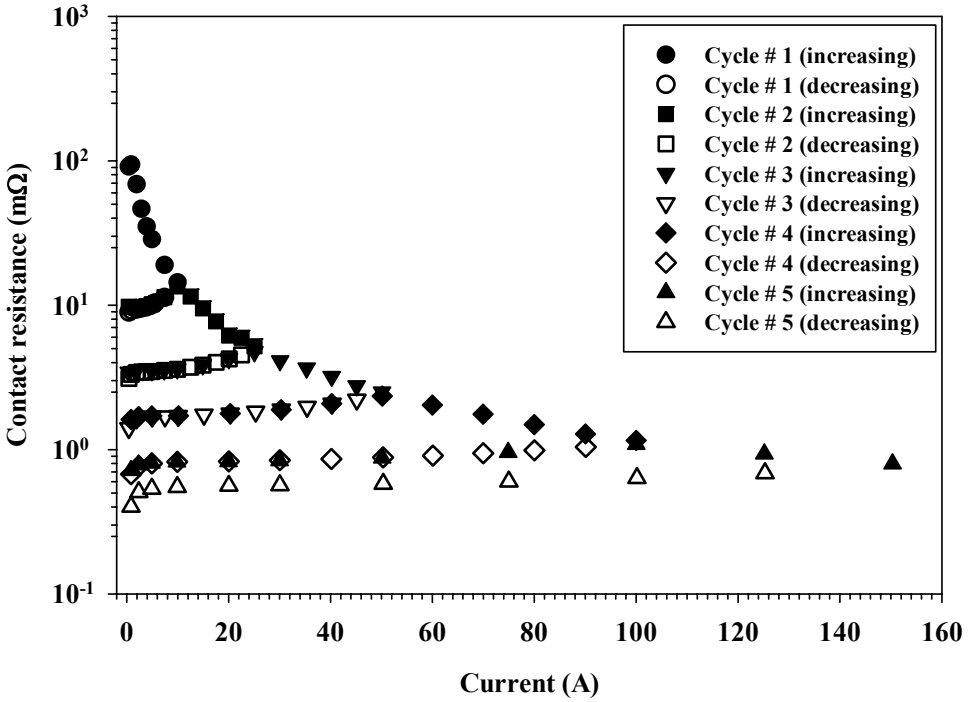

Figure 6.29 Variation in contact resistance with current for Cu-Cu contact. Pin maintained in contact at 1 N

6.5.3 Effect of load

In this section the results on the effect of contact load on the voltage saturation in Cu-Cu contacts are presented. Table 6.4 lists the contact loads used in the experiments and the corresponding Hertzian contact radii and pressures.

Table 6.4 Contact parameters for Cu-Cu contact

Contact load (N)	Hertzian contact radius (μm)	Average Hertzian contact pressure (MPa)	Maximum Hertzian contact pressure (MPa)
1	39.7	201.8	302.7
2	50	254.3	381.5
3	57.3	291.1	436.7
4	63	320.5	480.7
5	68	345.2	517.8
7.7	78.4	399	598.5

Figure 6.30 illustrates the contact voltage as a function of current through the interface for the contact listed in the above table. For the sake of visual clarity only the increasing–current part of the cycles are shown. It is seen that for the load of 1 N the voltage increases with current initially and then saturates around 130 mV starting at the current of 25 A. For all the loads considered the saturation voltage was around 130 mV but the onset of saturation was delayed as the load increased. Figure 6.31 presents the contact resistance as function of current through the interface for different loads (test conditions same as in Figure 6.31). Tests were also conducted with higher loads and the variation of contact voltage with current is shown in Figure 6.32. It is to be noted that in this case (for a different pin) the saturation voltage at 1 N load is around 105 mV. For higher loads the contact voltage continues to increase with current throughout, although

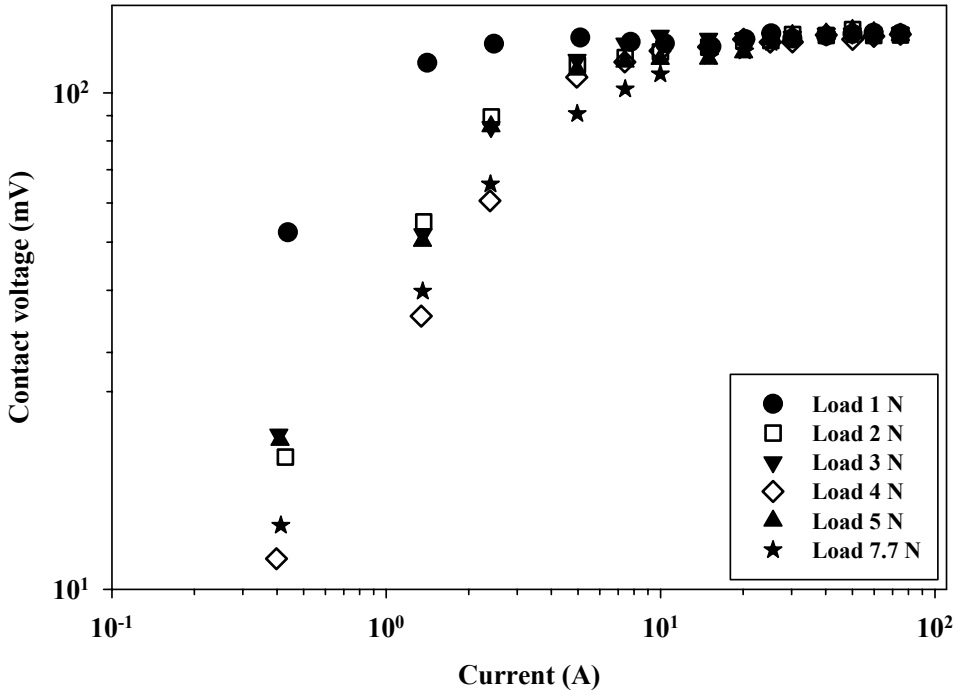

Figure 6.30 Variation in contact voltage with current for different contact loads (1–7.7 N)

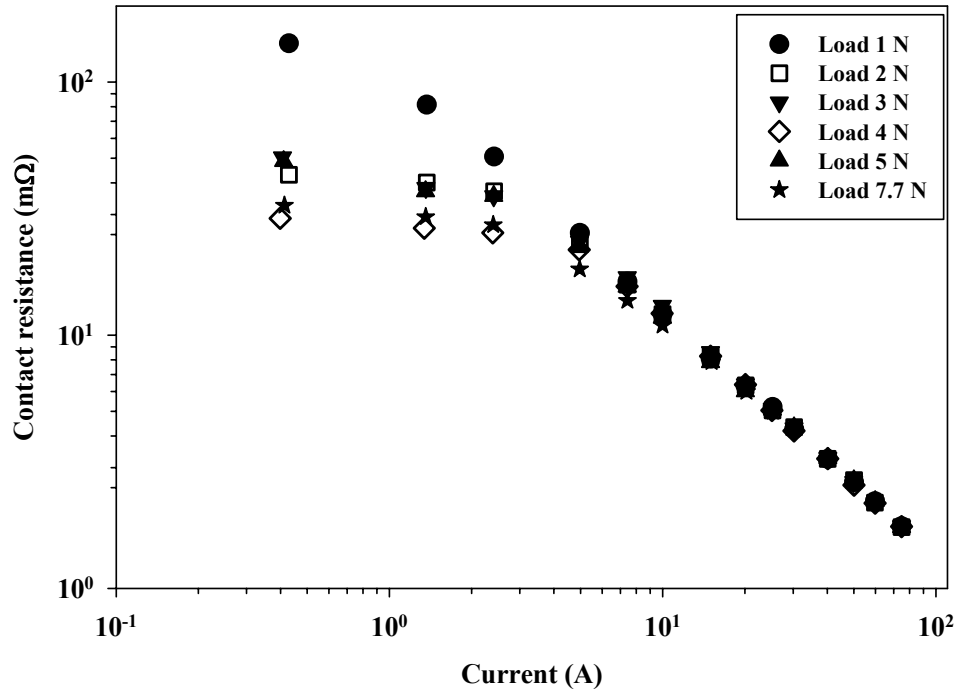

Figure 6.31 Variation in contact resistance with current for different contact loads (1–7.7 N)

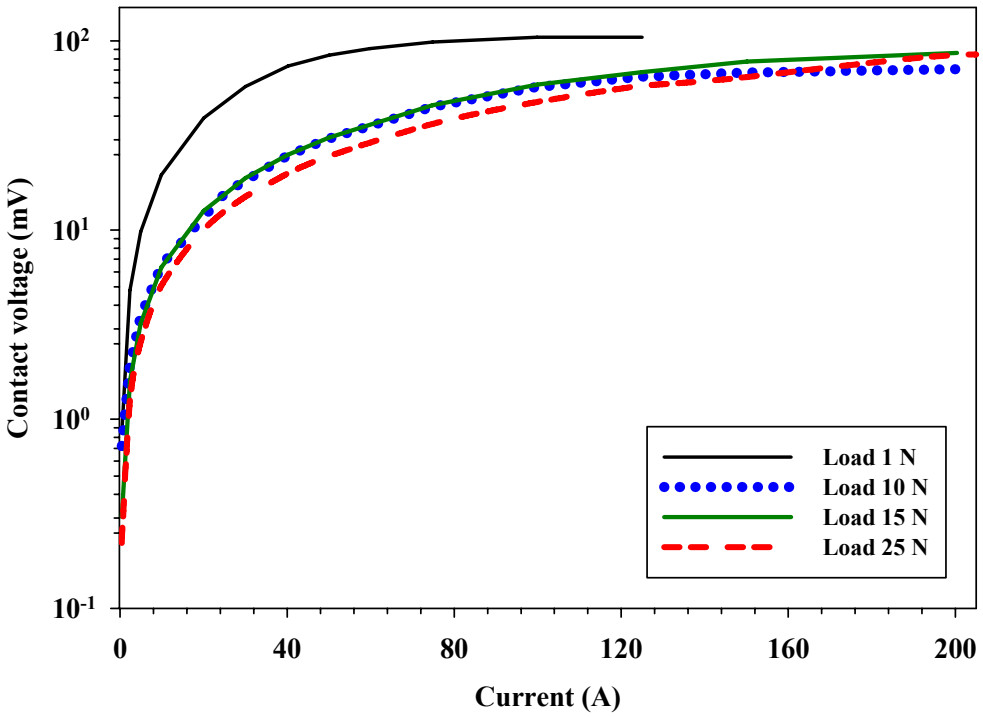

Figure 6.32 Variation in contact voltage with current for different contact loads (1 – 25 N)

at a very gradual rate beyond a current of 100 A. This result implies that a higher current is required to reach the saturation voltage at higher loads.

6.5.4 Effect of surface roughness

In this section the results on the effect of surface roughness of the flat on voltage saturation in Cu-Cu contacts are presented. Pins with nominally identical surface finish were tested against flats having different surface roughnesses. Flats with three different surface roughnesses were prepared by polishing those with sand papers of different grits, viz P220, P600 and P2400 while the load was set at 1 N for all the tests. Table 6.5 lists the surface roughness parameters of the pins and the flats before and after the tests.

Each test condition was run three times and the variation in the contact voltage measurement was found to be less than 7%. For the sake of visual clarity only one representative test run for each case is shown. Figure 6.33 illustrates the contact voltage

Table 6.5 Surface roughness parameters of pins and flats (Cu-Cu contact)

Pin				Flat		
Before Tests		After Tests		Before Tests		Sand paper grit
R_a (μm)	R_q (μm)	R_a (μm)	R_q (μm)	R_a (μm)	R_q (μm)	
0.65	0.828	0.645	0.814	0.074	0.133	P2400
0.633	0.801	0.637	0.807	0.28	0.37	P600
0.645	0.814	0.633	0.801	0.54	0.86	P220

as a function of current through the interface for three different surface roughnesses of the flats. It is observed that for the flat polished with P2400 the voltage saturates around 110 mV starting at 10 A, while for the flat polished with P600 the voltage saturates around 130 mV at 30 A and for the flat polished with P220 sand paper the voltage saturates around 110 mV starting at 20 A. It is observed that surface roughness of flat has a small influence on saturation voltage. Figure 6.34 presents the variation in contact resistance with current for the same tests. It can be seen that the flat polished with P220 grit sand paper yielded in the lowest contact resistance, at all the current levels, when compared to the flats polished with smoother sand papers.

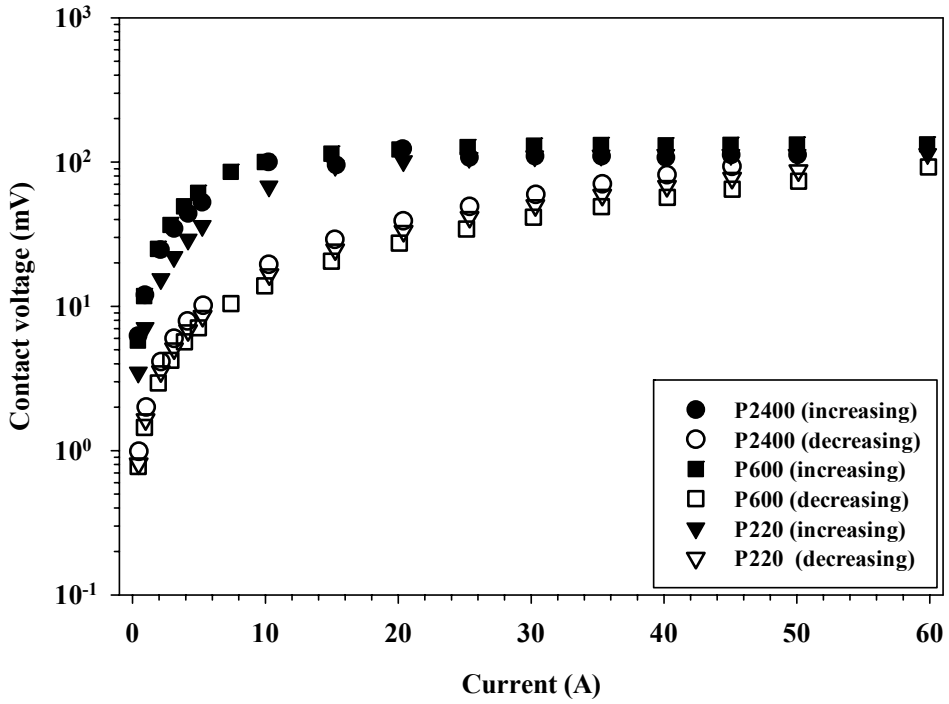

Figure 6.33 Variation in contact voltage with current for flats with different surface roughnesses at 1 N load

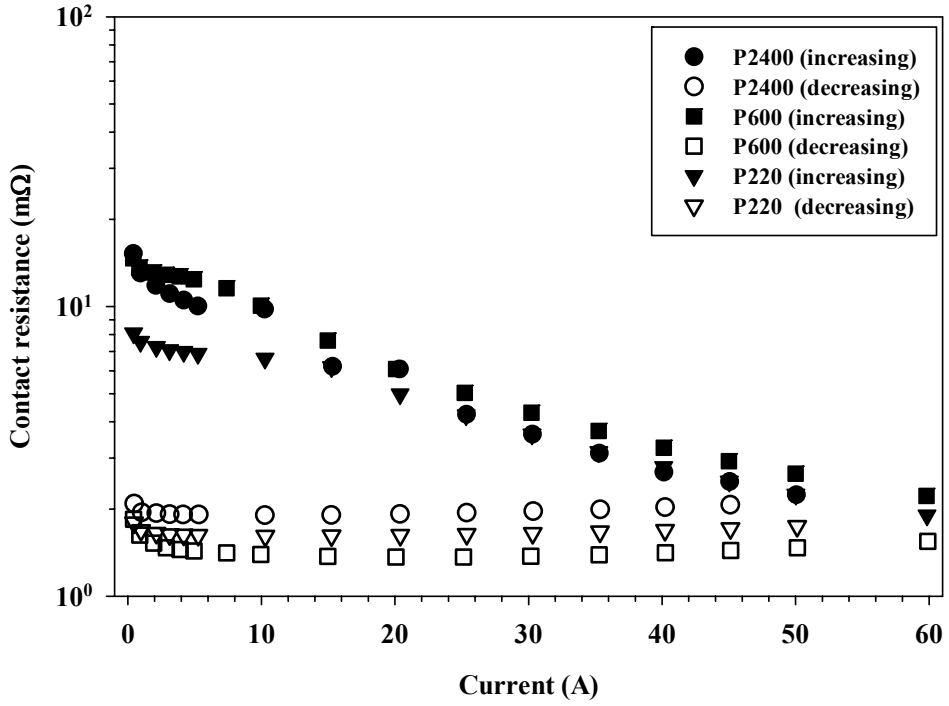

Figure 6.34 Variation in contact resistance with current for flats with different surface roughnesses at 1 N load

6.5.5 A note on voltage transients in Cu-Cu contacts

Figure 6.35 illustrates the time history plot of current and contact voltage across Cu-Cu contact at 1 N load. It is seen that for currents greater than 10 A the contact voltage initially spikes and then decreases. During the increasing part of the current cycle, as the current is increased through the interface, the contact voltage shows a spike and then gradually starts decreasing.

Using the voltage–temperature relation (Eq. (6.1)) and the parameters for Cu, as listed in the Table 6.6 [142], the maximum theoretical interface temperature can be calculated. Figure 6.36 presents the time history of the maximum interface temperature as calculated using Eq. (6.1). It is seen that when the voltage spikes to 125 mV the temperature spikes up to 220 °C.

Table 6.6 Parameters for Cu-Cu contact for voltage-temperature relation Eq. (6.1)

α (1/ °C)	β (1/ °C)	k_o (W/m.K)	ρ_o (Ω.m)
3.97×10^{-3}	3.27×10^{-4}	388	1.69×10^{-8}

Figure 6.37 presents the time history plot of current and contact voltage for Cu-Cu contact under the load of 15 N, while Figure 6.38 presents the time history plot of maximum theoretical interface temperature and contact voltage. It is seen that the maximum voltage spike observed is less than 100 mV and it occurs at the maximum current of 200 A, and the corresponding temperature spike is around 165 °C. Comparing Figures 6.37 and 6.39 it can be said that at higher loads the voltage spikes occur at much higher current levels.

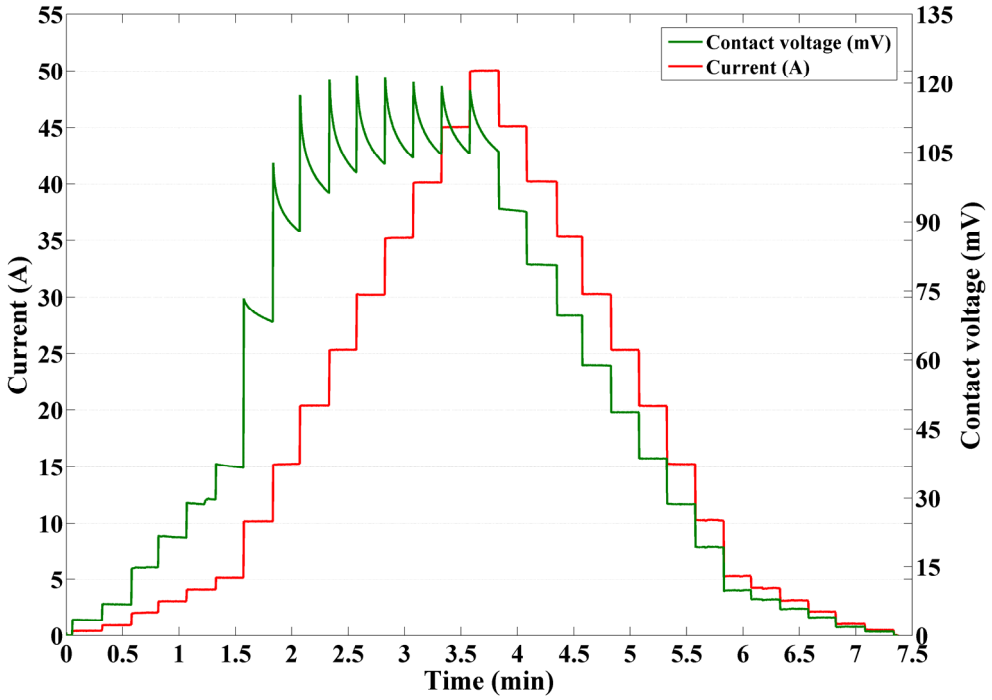

Figure 6.35 Time history plot of current and voltage for Cu-Cu contact at 1 N

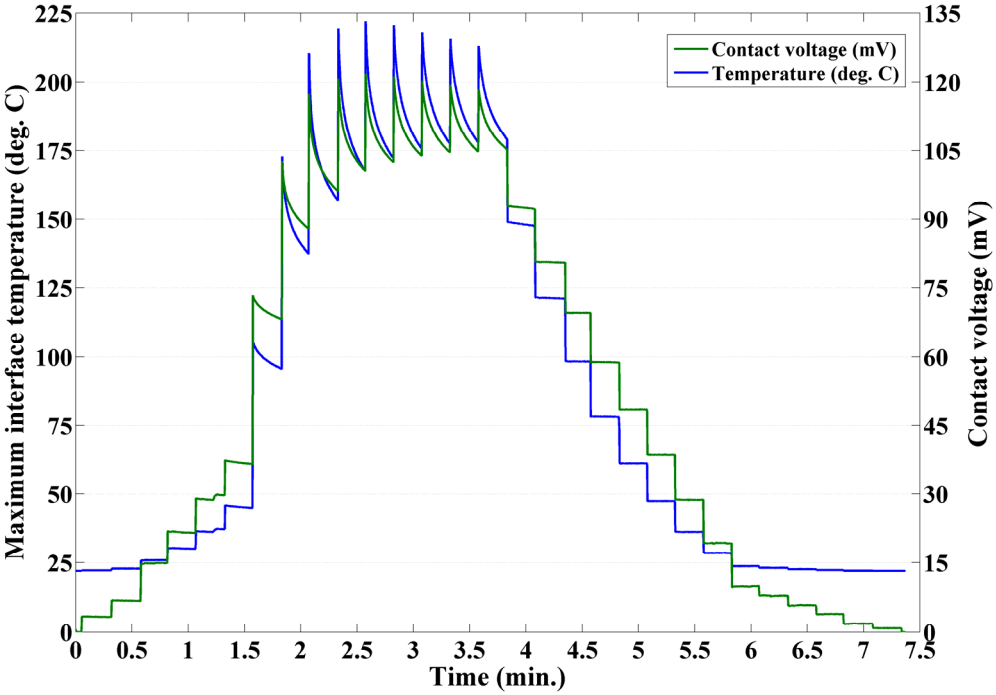

Figure 6.36 Time history plot of maximum interface temperature and voltage for Cu-Cu contact at 1 N

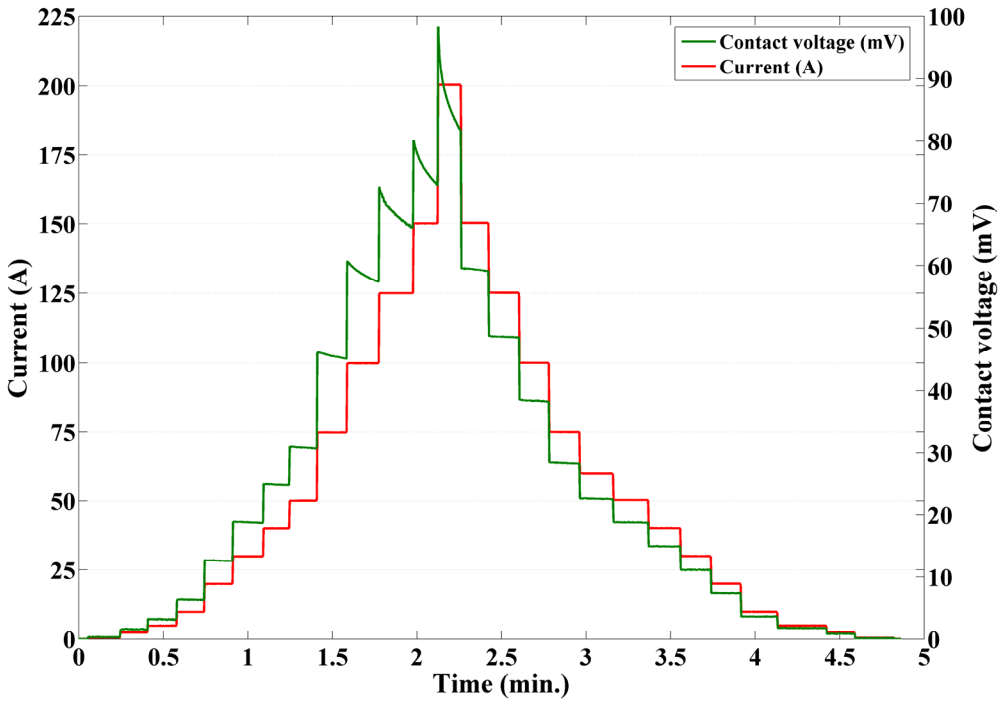

Figure 6.37 Time history plot of current and voltage for Cu-Cu contact at 15 N

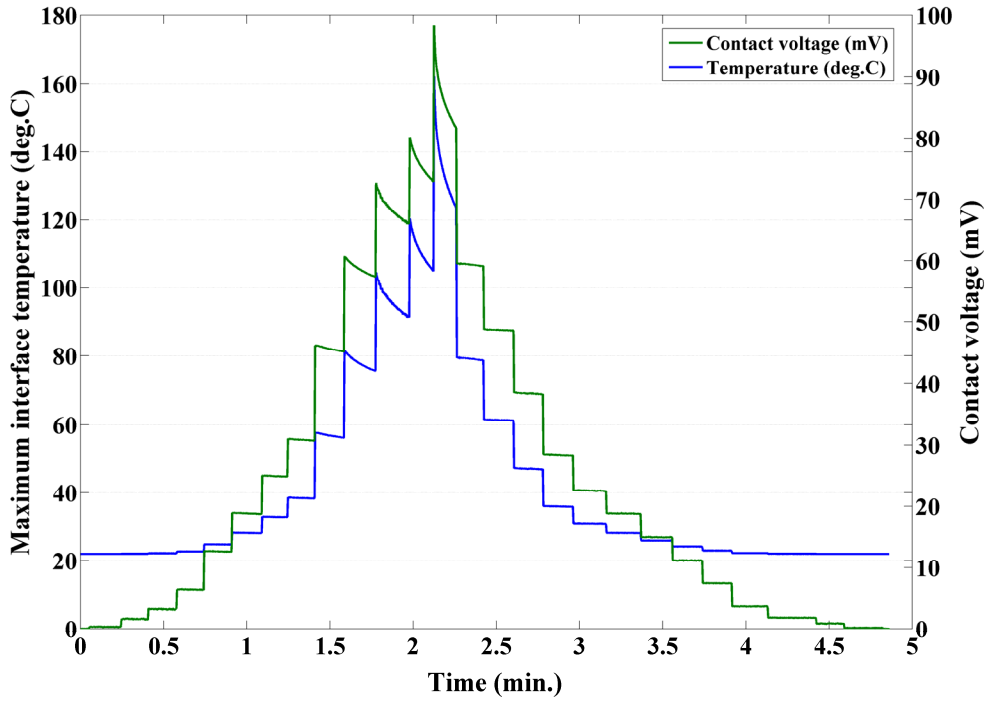

Figure 6.38 Time history plot of maximum interface temperature and voltage for Cu-Cu contact at 15 N

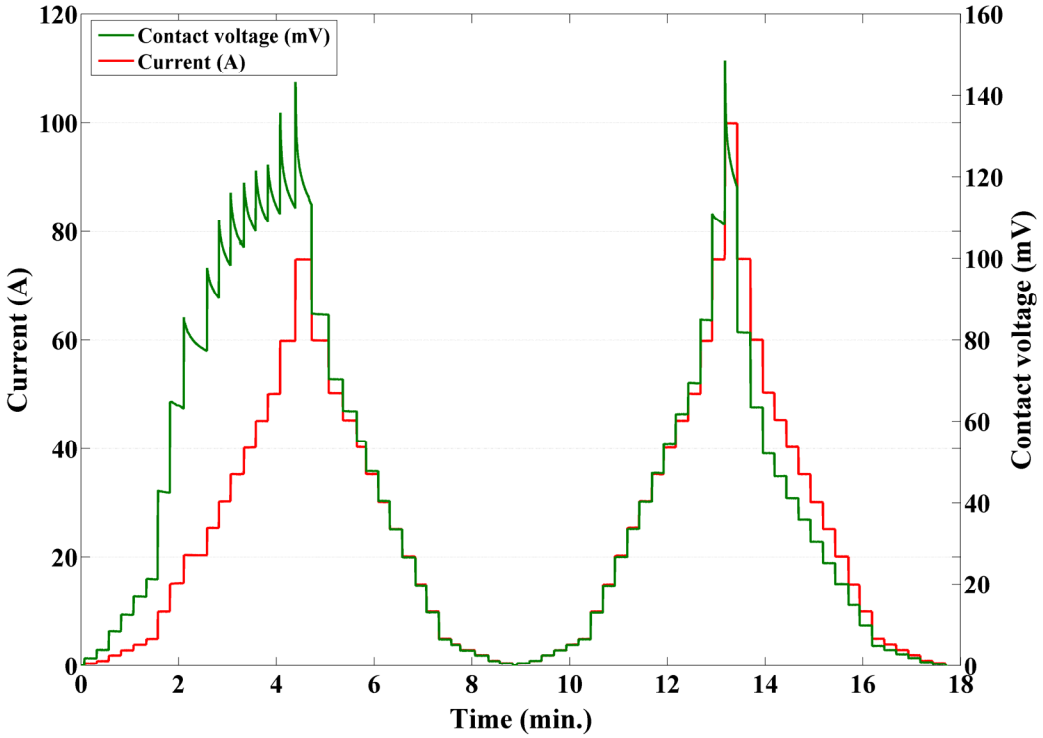

Figure 6.39 Time history of current and contact voltage for Cu-Cu contact with pin kept in contact

Figure 6.39 illustrates the time history plot of current and contact voltage for two current cycles when the pin was maintained in contact in between the cycles. It is seen that in the increasing–current part of the first cycle voltage spikes are seen for current levels greater than 30 A. These voltage spikes are absent in the increasing–current part of the second cycle until the peak current is reached (which is greater than the peak current of first cycle). This observation is similar to the one made for Al-Al contact and discussed in Section 6.4.5.

6.6 Discussion

The phenomenon of voltage saturation and hysteresis with current cycling in aluminum and copper contacts was demonstrated in Sections 6.4 and 6.5. Both of these phenomena can be explained by considering the effect of temperature on the mechanical and electrical properties of the contact materials. The saturation voltage observed here is likely connected to the "softening voltage" articulated first by Holm [14] and later associated with the recrystallization temperature [132, 140]. However, since the recrystallization process depends on time and degree of cold work, in addition to the temperature [143], it is believed that the onset of recrystallization does not adequately explain the voltage saturation observed in this study.

Figures 6.18, 6.19 and 6.35 illustrate the time history plots of contact voltage and current. It is seen that during the increasing part of the current cycle the contact voltage spikes before settling at a value much lower than the peak of the spike. This voltage spike is responsible for changing the morphology of the interface. As the contact voltage increases the interface temperature follows the same trend (Figures 6.20 and 6.36). The resistivity of the materials increases with temperature and this increases the Joule heat dissipation at the interface. Depending on the relationship between the thermal conductivity and temperature this can cause increase or decrease in the interface temperature. The hardness and the yield stress of most materials (ductile) decreases with increasing temperature [144, 145]. Note also, in Hertzian contact, when the mean contact pressure is less than the yield stress, the contact remains elastic [47]. Thus if the yield stress at the new interface temperature is greater than the mean contact pressure, then the interface will remain in the elastic regime and the contact area does not change. On the

other hand, if the yield stress at the new interface temperature is lower than the contact pressure, then the interface undergoes plastic deformation and the contact area increases. This in turn will reduce the contact resistance and hence the contact voltage (current is maintained constant). This explains the voltage spike and the subsequent decrease in the contact voltage while the current is maintained constant. As the current is increased to the next level the contact voltage spikes again and this increases the real area of contact. The contact voltage then stabilizes around the saturation voltage as the area of contact has been modified to lower the contact resistance and conduct the increased current. This explains the phenomena of voltage saturation. As the current is decreased the contact voltage also decreases but to a much lower value as compared to the contact voltage for the same current level during the increasing–current part of the cycle. This is because the real area of contact is sufficiently big to conduct this current without inducing any changes in the interface. As the current and contact voltage across the interface decrease so does the interface temperature. This increases the strength and the hardness of the interface; in other words the interface rehardens. As long as the pin is maintained in contact the deformation that the interface goes through during the increasing–current part of the cycle persists in the interface. In other words the real area of contact at the end of the increasing–current part of the cycle is the maximum area of contact. This explains the lower contact resistance during the decreasing–current part of the cycle.

Once the pin is raised the conformity attained by the surfaces of the pin and the flat, due to thermal softening, is destroyed and the surfaces are re-roughened. This causes the contact resistance to be higher when the same pin is brought into contact again. The interface then behaves as a “new” interface and goes through a similar cycle as in the

preceding current cycle. On the other hand if the pin is maintained in contact between the current cycles the topographical changes in the interface are sustained and the contact voltage during the subsequent current cycles retraces the same path as during the decreasing part of the first current cycle.

It can be concluded that the contact resistance depends on the current history apart from load and surface roughness. It can also be stated that the contact voltage is a function of the thermal conductivity, electrical resistivity, area of contact, and mechanical properties of the interface. Temperature has a strong influence on the thermal, electrical and mechanical properties of the materials. The variations in the mechanical and electrical properties with temperature for aluminum (Al 6061) and copper (C 110) are presented in Figures 6.40–6.43 [141, 142]. Figure 6.40 illustrates the variation in tensile strength, yield stress and hardness with temperature for Al 6061, while Figure 6.42 presents the same scenario for Cu 110. The hardness values in the plots are computed from the relation $H = 2.8Y$ [80]. The variation of thermal conductivity and electrical resistivity with temperature for Al 6061 and Cu 110 are plotted in Figures 6.41 and 6.43 respectively. It should be noted that the thermal conductivity of Al 6061 increases with increasing temperature while that of Cu 110 decreases with increasing temperature.

Let us consider the case of Al 6061 contact under the load of 1 N. From Figure 6.17 it is seen that voltage spikes greater than 200 mV are obtained for a couple of current steps and correspondingly the temperature spikes to values greater than 400 °C. At this temperature the hardness and yield stress decrease by more than 95% based on Figure 6.40. Voltage spikes around 300 mV are observed for first couple of current steps that the reduction in the interface strength leads to an increase in the contact area, as the

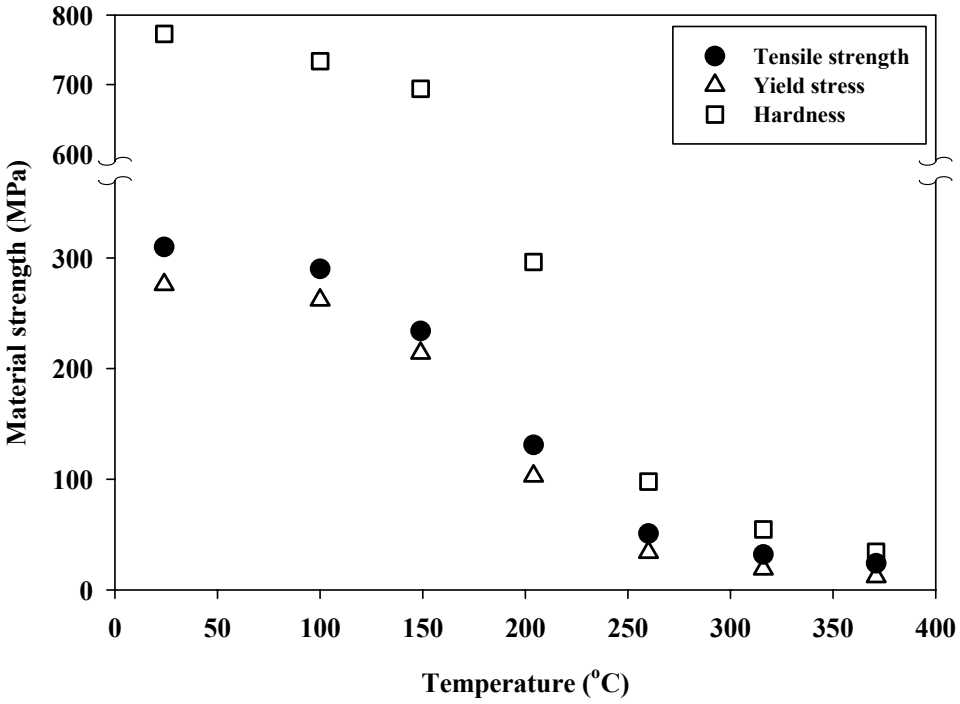

Figure 6.40 Variation in mechanical properties with temperature for Al 6061

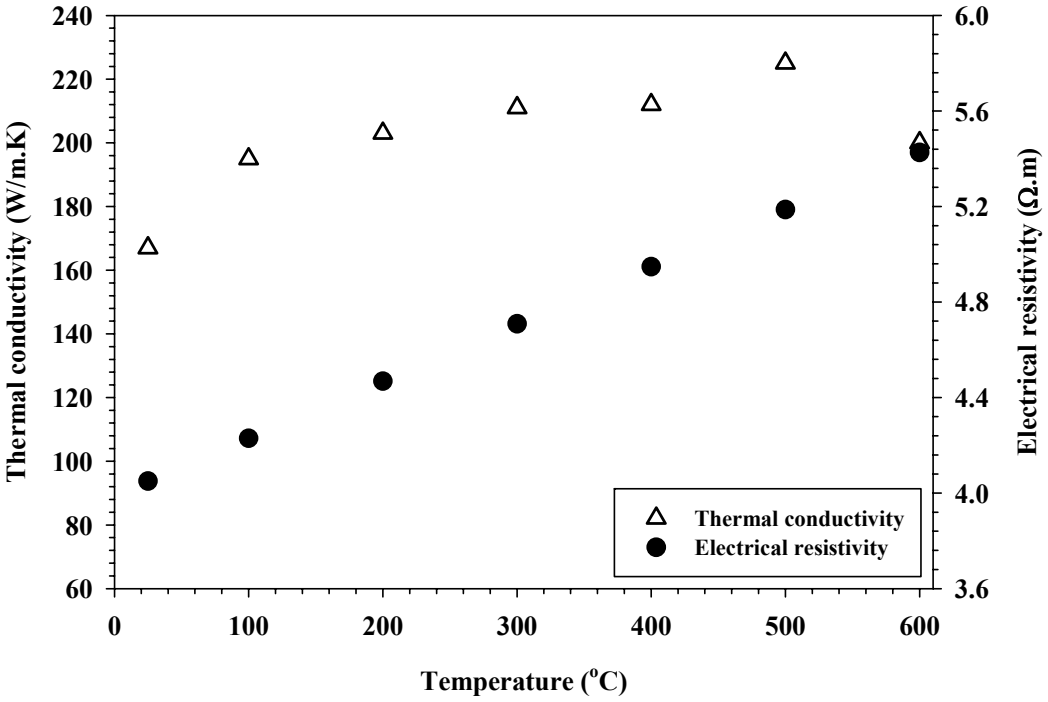

Figure 6.41 Variation of thermal and electrical properties with temperature for Al 6061

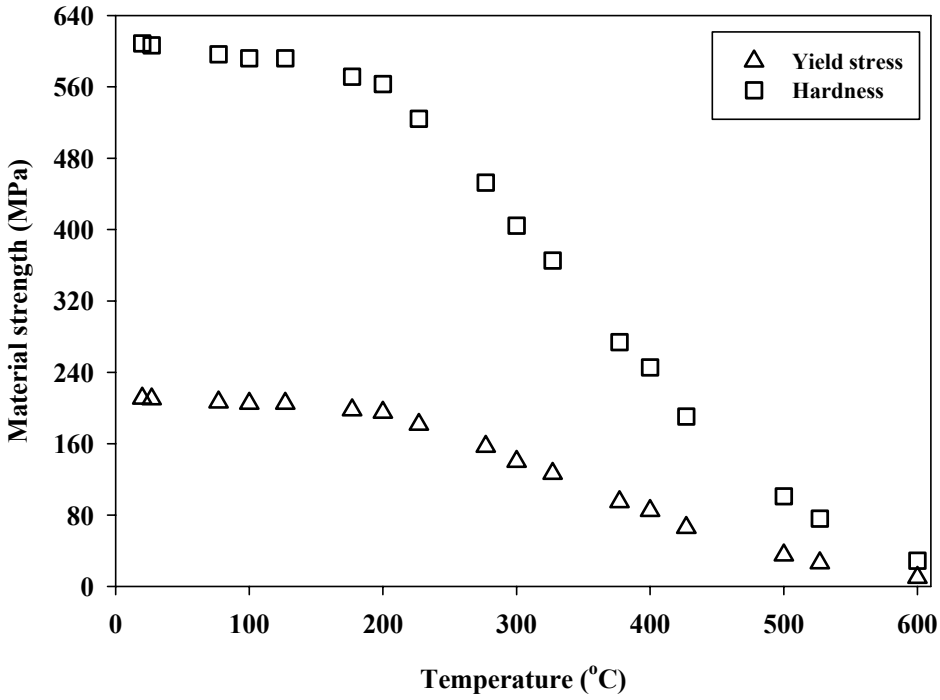

Figure 6.42 Variation in mechanical properties with temperature for Cu 110

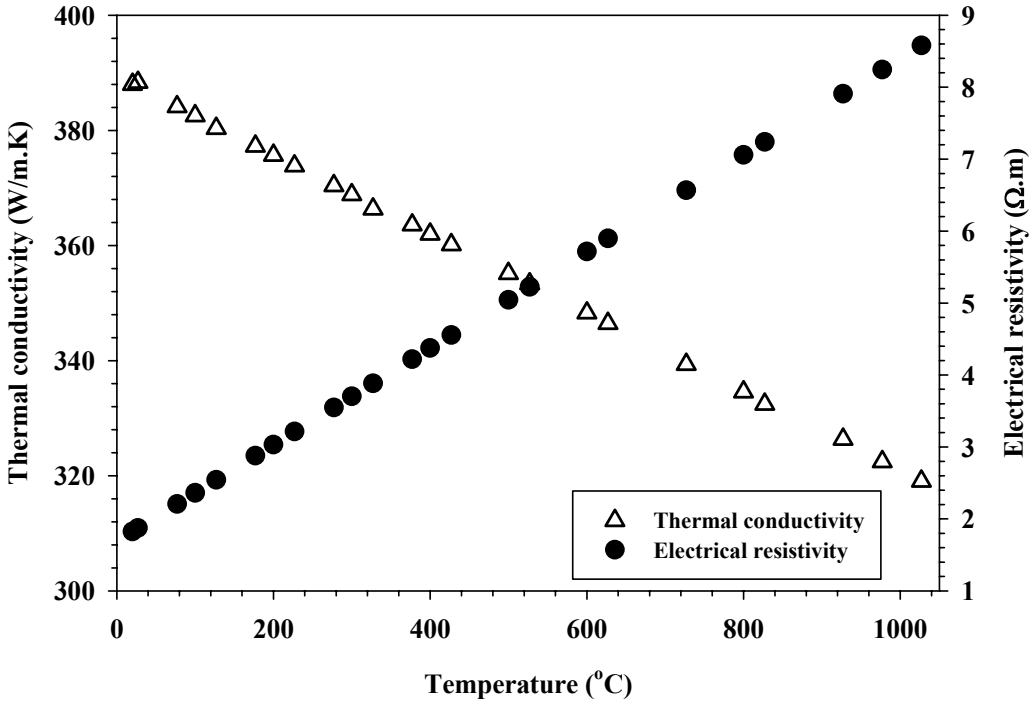

Figure 6.43 Variation of thermal and electrical properties with temperature for Cu 110

average contact pressure (128 MPa) is greater than the hardness at that temperature by more than 73%. It should be noted that contact pressure experienced by asperities would be much greater than the average Hertzian pressure. But the average pressure argument presents a much conservative analysis and further substantiates the hypothesis that asperities undergo thermally induced plastic deformation. In Figure 6.19 the average voltage saturates around 160 mV and the temperature around 300 °C. Even at this temperature the initial average contact pressure is greater than the hardness by 53%. This means that the interface continues to increase in size and thereby reduces the contact resistance.

Now consider the Cu110 interface under the load of 1 N. Voltage spikes greater than 120 mV are seen in Figure 6.36, and the corresponding maximum interface temperature spikes to values around 220° C. The yield stress corresponding to this temperature is around 181 MPa while the contact pressure is around 201 MPa. This means that the interface yields plastically and the contact area increases. The average temperature during those current steps is around 185° C and the corresponding yield stress is 196 MPa, and hence it can be argued that the interface continues to grow in size.

At higher contact loads the average contact pressure is higher and so is initial contact area. This leads to lower contact resistance, lower contact voltage and lower interface temperature rise and hence the interface can conduct higher currents before reaching the saturation stage. Once the voltage saturates the interface responds mechanically in similar fashion as discussed above.

The above discussed phenomena, of increasing contact area with time during voltage transients, can be viewed from the perspective of creep and/or viscoplastic

deformation at the interface. On atomic scale the viscoplasticity in a material occurs via the dislocation mobility, diffusion of atoms, relative displacement of grains by grain boundary sliding and mechanical twinning [146]. However, based on the creep data map for copper presented by Frost and Ashby [146] it is unlikely that viscoplasticity occurs, as the strain rates obtained from the maps are less than 10^{-10} 1/s. The effect of electrical current on dislocation motion has been studied and it is well established that the flow of electrons may assist the dislocations in overcoming obstacles to their motion [147-150]. This effect is more commonly referred to as "electroplasticity" in metals. The presence of electric field is also known to influence the diffusion of atoms [151, 152]. Almost all of the studies in the literature study the effect of passing a short electric pulse on the deformation response of materials [149, 152-158], in order to exclude the effect of Joule heating. There exists no study to knowledge of the author which studies the viscoplastic deformation or the creep behavior of metals under the presence of continuous current supply over a time period of several seconds and minutes. In the current study the effect of Joule heating along with the increased dislocation mobility, in presence of electric current, can be hypothesized to be the reason for creep like behavior of the interface during voltage transients. With the lack of creep data for metals in presence of electric current this hypothesis cannot be quantified easily, but this certainly is an interesting opportunity for further investigation.

6.7 Summary

The effect of current cycling through static Al 6061 and Cu 110 contacts was studied in this chapter and the key finding can be summarized as follows:

1. The voltage drop across the contact initially increases with current until a certain critical voltage is increased. Beyond this critical point any increase in the current causes essentially no increase in steady-state contact voltage. This critical voltage is thus termed as "saturation voltage."
2. The saturation voltage for Al 6061 interface was found to be in the range of 160 – 190 mV and that for Cu 110 interface was in the range of 100 – 130 mV.
3. The contact voltage as a function of the interface current traces different paths during the increasing and decreasing parts of the current cycle, if saturation voltage is attained during the current cycling.
4. The interface loses its memory and behaves as a "new" interface if the contact is broken between the current cycles.
5. Voltage spikes are observed as the current is increased in a stepped fashion when the voltage approaches the time–averaged saturation point.
6. The temperature rise during the voltage spike decreases the strength of the interface and causes the real area of contact to increase. This increase in area decreases the contact resistance.

CHAPTER 7. TRIBOLOGICAL STUDY OF SLIDING ALUMINUM-COPPER ELECTRICAL INTERFACE

7.1 Introduction

Aluminum and copper are the most widely used materials in electrical machines due to their good electrical properties [159, 160]. The electrical connectors in power generators and motors can be subjected to fretting [161, 162], sliding [163, 164] or rotating motion [165, 166] during their operation or could even be static [167, 168].

The temperature rise at the interface of the connectors has direct bearing on the life and performance of the connectors. The temperature of the connectors is dependent on several factors like the physical and electrical properties of the materials in contact, surface roughness, current density and voltage potential across the contact, relative motion between the contact pair and several others. The high contact temperatures can accelerate the corrosion and the wear process [169, 170] thus damage their surfaces. The contact resistance of the interface between current–carrying conductors increases drastically due to the surface damage and in the severe conditions can lead to an open-circuit condition [161]. This leads to a cascading process of the degradation of the contacts leading to further increase in contact resistance and Joule heat dissipation which may ensue in the breakdown of the machine/components.

The armature-rail interface in an electro-magnetic launcher (EML) presents a classic example of extreme conditions of high velocity and high current densities. An EML, in a very broad sense, can be described as an electro-magneto-mechanical device used to propel projectiles at very high velocities. An EML has two parallel conductors

that act as rails over which the armature slides. Typically current is supplied to one of the rails, from discharging capacitor banks, which passes through the armature and out through the other rail. The direction of the current and arrangement of the conductors is such that magnetic fields are set up around each of the rails, which are in opposite directions. This results in a Lorentz force acting on the armature and is responsible for the acceleration imparted to it.

The following study was motivated by the ongoing research on wear and friction phenomenon in an EML, conducted by the MURI program at Georgia Tech. Here a brief literature review is presented highlighting the tribological study conducted on EML's.

7.2 Literature review

The armature-rail interface in an EML is characterized by frictional and Joule heating and the associated energy losses. The interface heating and current concentration at the armature-rail contact leads to localized melting and removal of material from the interface during sliding [171]. The outflow of material from the contact region leads to loss in electrical contact and the low voltage (<50 volt) sliding contact transforms to a high voltage (hundreds of volts) contact, a phenomenon known as "transition" [172].

Young and Hughes [173] and Parks [174] modeled the current flow/distribution in armature-rail interface and inferred that the velocity skin effect (VSE) is one of the factors leading to contact transition. Barber and McNab [175] suggested that when the magnetic blow-off force, developed due to current concentration at the armature-rail contact, exceeds the applied contact force then transition can occur. Persad et al. [176] suggested that a liquid metal film at the armature-rail interface gets disrupted when the

balance between viscous drag and magneto-hydrodynamic forces is affected by the magnetic pinch forces. This leads to reduction in contact pressure and deformation of the armature due to thermal stresses. Stefani and Parker, [177] from their experiments, concluded that at high speeds viscous heating dominates Joule heating and 800-1000 m/s is the threshold for the onset of a liquid film generation. Another mechanism that causes transition is called “negative I-dot transition”, which is dominant only if there is a well-developed liquid film at the interface and the driving current is reduced rapidly [171, 172]. Stefani et al. [172] proposed the theory of negative I-dot transition in which the reversal of the Lorentz force, due to a rapidly decreasing driving current, begins to lift off the trailing legs of the armature.

Contact transition and interface melting has a significant effect on the wear of the rail conductors. The mechanical and metallurgical response of the material pair to the extreme conditions during a launch process also dictates the performance of an EML. Large thermal gradients, such as change of 1000 °C over a distance of 200 microns [178], and pressures on the order of 300 MPa [179] have been reported to exist at the interface. These conditions can lead to crack initiation and propagation in the rails.

Several copper alloys have been used for rails with and without electroplated metals. Bedford [180] evaluated Cu-0.6% Cd with electrodeposited Cr, Ni, Sn, Rh and Zn, as well as Cu-0.6% Cd without any coating, 25Cu-25W, mild steel, aluminum, and stainless steel with a plasma armature. The tests revealed that Cu-Cd rails had molten damage at beginning of the shot, which decreased in the direction of the muzzle, eventually resulting in tracks formed by electrical arcing. All the coating materials were melted and spread around on the rails but with various characteristics: the shot with a Rh

coating left a smooth surface; the Cu rails with Zn coating showed less damage than the bare Cu rails and the coating remained over the entire length of the rails; the Sn coating was melted and pushed around severely leaving a wavy surface. The stainless steel rails had damage only in the first half of their lengths while the aluminum rails were deformed and severely damaged.

Several authors have studied the behavior of Cu-Al couple and their alloys in an EML environment. Persad et al. [181] tested Al 7075 armature against ETP (electrolytic tough pitch) copper and, upon analyzing the muzzle wear debris under X-ray diffraction, observed a copper rich matrix and the presence of the intermetallic compound Cu_9Al_4. Wolfe et al. [182] tested Cu-Cr-Zr alloy rails (8m long) with aluminum plasma driven and solid armatures for 88 shots and studied the changes in electrical conductivity, microstructure and microhardness. Low magnification surface examination of the rails revealed that aluminum striations existed on the rails with no severe damage until the muzzle end, where the rail showed signs of severe pitting. The authors also observed that the electrical conductivity varied along the length of the rail (after firing the shot) which they attributed to the changes in distribution of Cr and Zn in Cu due to heat input during the firing of shots. The microhardness measurements did not show any marked effect of heating or softening of the surface.

Gee and Persad [183] compared different strengthening mechanisms by evaluating the multi-shot performance of solution strengthened Be-Cu (beryllium-copper) and Cu-Cr (copper-chromium), powder metallurgy infiltrated Cu-W (copper-tungsten) and dispersion strengthened Cu rails at the armature (Al 7075-T6) starting position. Be-Cu rails showed furrows with re-solidified Al at the start up location, while the other rails

only had aluminum deposits at the start up location. None of the rails exhibited significant changes in subsurface hardness. Dispersion hardened copper had the lowest voltage drop while Cu-W had the highest voltage drop. Be-Cu, even though the hardest material was also the most electrically resistive, leading to softening and the formation of grooves due to Joule heating.

Several studies conducted in a non-EML type environment were found in literature. Brailsford [184] studied the influence of alternating current (AC) on static coefficient of friction, under light loads, for aluminum, copper, brass and tin and their combinations. He reported that when one of the mating surfaces was aluminum, the friction coefficient decreased with increasing current. For the combinations of brass-brass, copper-copper no significant influence of current on friction coefficient was observed, whereas for tin-tin surfaces friction coefficient increased with increasing current.

Chen and Vook [185] studied the behavior of sliding Al-Cu electrical contacts in high vacuum. The authors tested Al wire brushes on rotating Cu slip rings and Cu wire brushes on Al slip rings, rotating at 250 rpm for 10,000 rotations under a maximum current of 30 A. The authors observed that for the case of an Al brush on a Cu slip ring the contact resistance was almost 10 times greater than that of a Cu brush sliding on an Al slip ring. The SEM analysis showed that Al had transferred onto the Cu brush, thus forming a homogenous Al-Al contact, leading to smaller contact resistance. Additionally, the wear particles collected were composed only of Al. In the case of an Al brush on a Cu slip ring, it was observed that Al had transferred onto the Cu slip ring and Cu had

transferred onto the Al brush, while the wear particles collected were comprised of an Al-Cu alloy.

Paulmier et al. [186] investigated the wear behavior of copper and chrome steel couple under currents up to 40 A, sliding speed up to 7.2 m/s and contact load of 10N on a pin-on-disc tirbometer. They observed that currents below 40 A have little influence on the friction coefficient. However, the wear of copper was greatly affected by the magnitude and the polarity of the current. The wear rate of copper was higher when it was maintained as cathode. The authors explained this behavior using the oxidation theory put forth by Cabrera and Mott [187]. It was reasoned that copper oxidizes faster than steel when it is anode and the wear mode is adhesive, while in the reverse scenario the high oxidation of steel leads to formation to hard iron and chrome oxides which leads to abrasive wear of copper.

Similar observations were made by Bouchoucha et al. [188] and Senouci et al. [189] in their study on copper–steel interface. Microscopic and X-ray analysis performed by Bouchoucha et al. [188] revealed that the rate of iron transfer onto the copper wire increased with the current intensity especially when the Cu wire was anode. Senouci et al. [189] also found that wear rate of copper increases with load and under oxygen environment when compared to tests in ambient atmosphere and in argon environment. In the argon environment the polarity of the current had no effect on wear as the oxidation process was absent.

The current study is aimed at understanding the behavior of aluminum and copper in an environment of high current densities and contact pressures at low sliding velocities. The extreme velocities in an EML lead to phenomena like velocity skin effect

[173, 174] and viscous drag forces [172] which modify the distribution of the current at the interface and influence the onset of transition. In both these scenarios the critical factor that remains is how the materials respond to such extreme conditions. The study is divided in two parts: in the first part the tribological interface of aluminum–copper is considered, and in the second part the aluminum–aluminum tribological interface is considered (Chapter 8).

7.3 Experimental setup

The wear and friction studies on sliding electrical contacts were performed on a specially designed tribo-simulator. A line schematic of the tester is shown in Figure 7.1 and Figure 7.2 (a) and (b) shows the actual setup. The tribo-simulator essentially

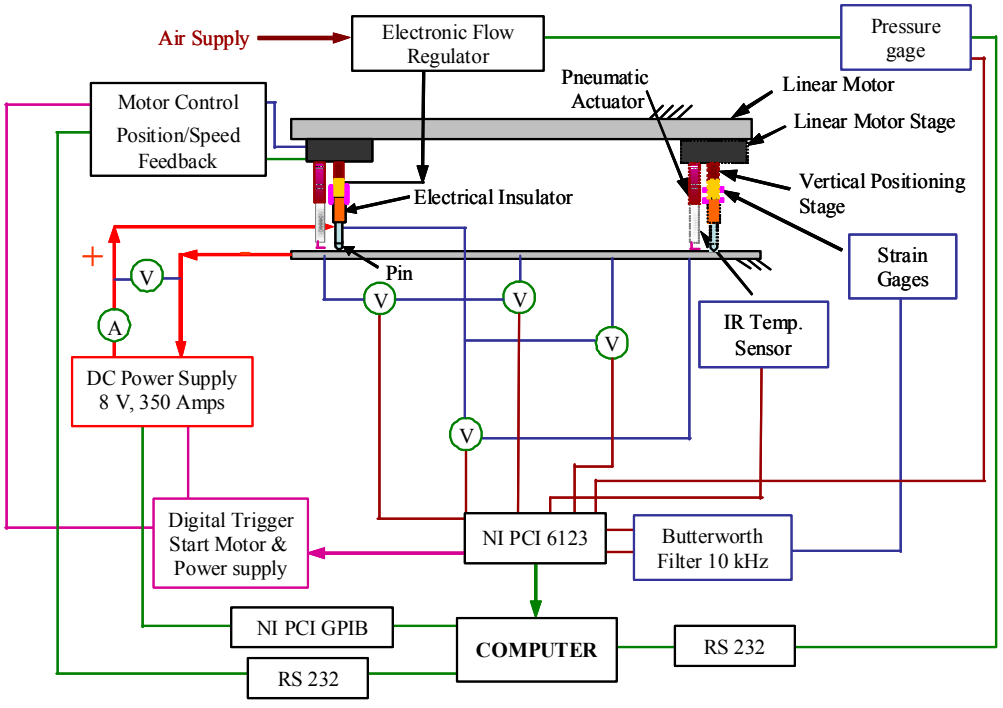

Figure 7.1 Line schematic of the linear tribo-simulator

comprises of a computer controlled linear motor, capable of accelerating up to 2.5g's, driving a stage that slides the pin along a flat surface over a maximum travel length of 2 meters. The load is applied, to the pin, using a pneumatic actuator controlled via an electronic pressure regulator. The loading mechanism consists of a vertical positioning stage carrying a flexural frame along with a low-friction pneumatic actuator (piston diameter of 10 mm). The vertical positioning stage is used to gradually bring the pin into contact with the stationary flat (rail surface). The normal force and the friction force at the interface are measured by the means of strain gages mounted in the half-Wheatstone bridge configuration on the flexural frame. The geometry of the pin can be configured so as to achieve either Hertzian or flat-on-flat type of contact configuration. A D.C. power supply rated at 8V/350A supplies the current to the interface. An infrared temperature sensor measures the temperature of the rail surface lagging the interface by a distance of 25 mm. The tester allows for real time measurements of normal force, friction force, current and voltage drop at the interface. The signals from all the sensors are sampled at 18 kHz and filtered using a low pass Butterworth with a cut-off frequency set at 8 kHz.

To begin the experiments the pin is lowered into the contact by means of the vertical positioning stage. After the contact is established the data acquisition is started and the prescribed load is applied via the pneumatic actuator. Then the power supply is triggered to ramp up the current to a pre-set value and the linear motor is triggered to start. At the end of the sliding motion of the linear motor the data acquisition is stopped, the current and the load are reduced to zero and the pin is raised from the contact.

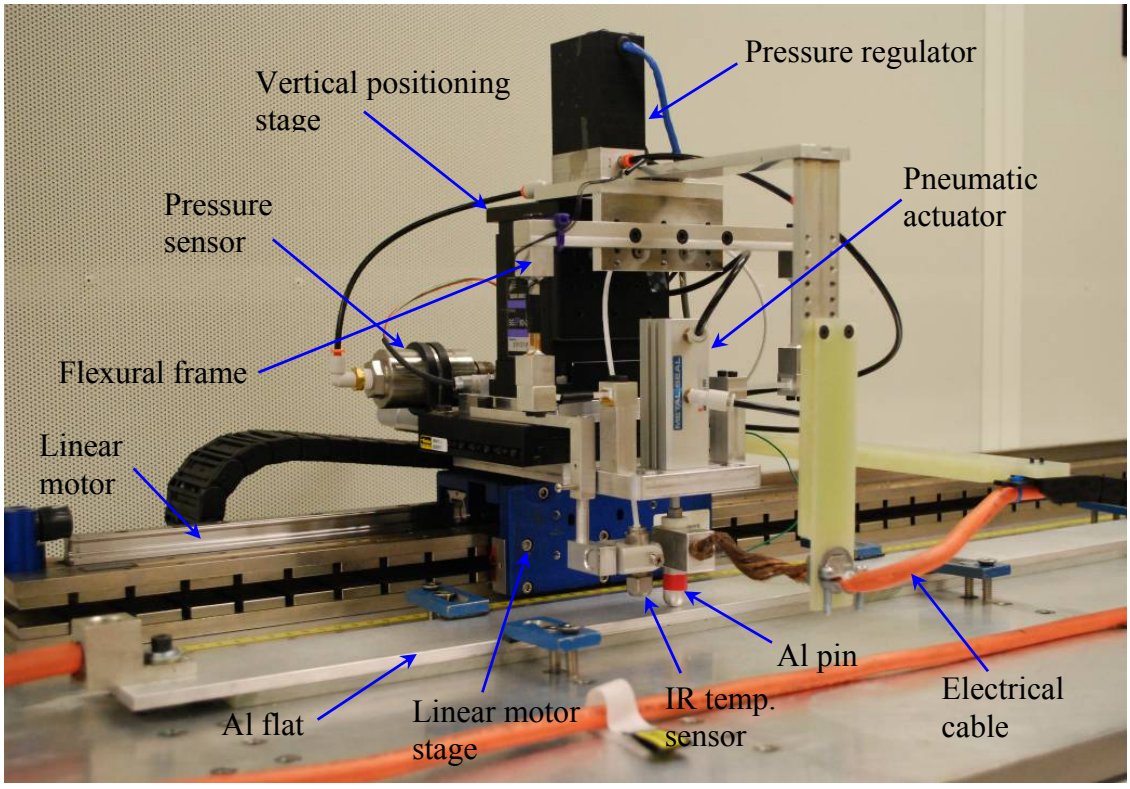

(a)

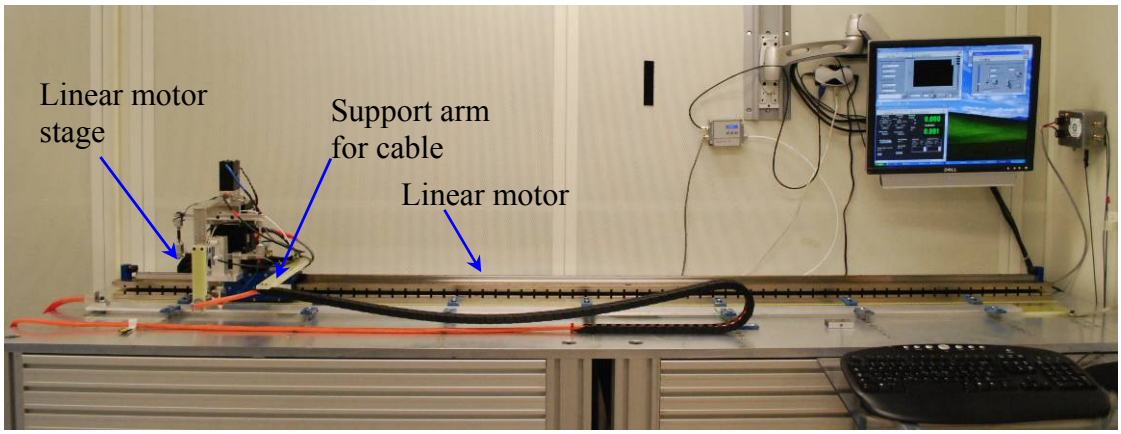

(b)

Figure 7.2 Linear tribo-simulator

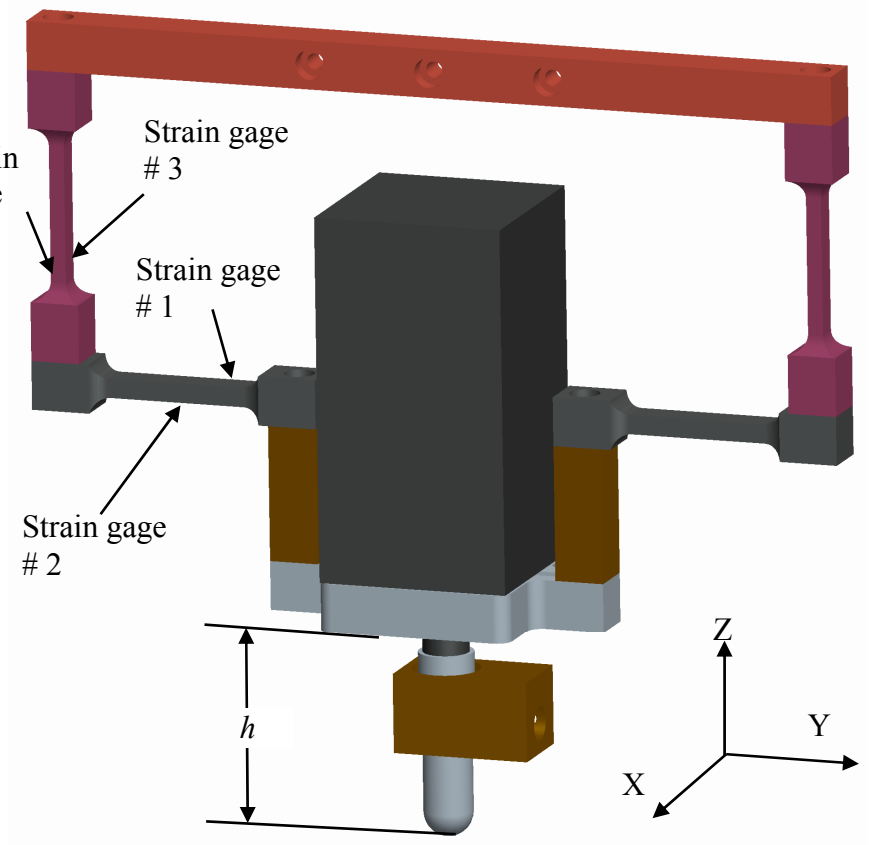

Figure 7.3 Schematic of the flexural frame for the force measurement

7.3.1 Force measurement frame

As mentioned above a flexural frame with strain gages was used to measure the forces at the interface. A schematic of the frame is shown in Figure 7.3. The frame was designed so that the strain gages experience bending force due to the normal force and the frictional force. The location of the strain gages is pointed out in the Figure 7.3. Strain Gages #1 and #2, comprising half-Wheatstone Bridge #1, were mounted primarily to measure the normal force, while the Strain Gages #3 and #4, forming half-Wheatstone Bridge #2, were mounted to measure the frictional force. However all of the strain gages were found to be influenced by both normal axial forces. The force measurement system

was calibrated by applying forces along the Y and the Z direction independently while measuring those forces simultaneously using a load cell. The voltage output from both the strain gages was recorded for each applied force. As a result of the calibration process following matrix relation is obtained:

$$\begin{Bmatrix} V_1 \\ V_2 \end{Bmatrix} = \begin{bmatrix} C_{11} & C_{12} \\ C_{21} & C_{22} \end{bmatrix} \begin{Bmatrix} N \\ F \end{Bmatrix} \tag{7.1}$$

where N, and F are the applied forces along Z and Y direction respectively, V_1 and V_2 are the voltages measured from the half-Wheatstone Bridges # 1 and # 2 respectively and C_{ij} are the force-voltage coefficients (Volts/Newton). In order to determine unknown forces due to known voltage measurements V_1 and V_2, the above matrix equation is inverted.

$$\begin{Bmatrix} N \\ F \end{Bmatrix} = \begin{bmatrix} Y_{11} & Y_{12} \\ Y_{21} & Y_{22} \end{bmatrix} \begin{Bmatrix} V_1 \\ V_2 \end{Bmatrix} \tag{7.2}$$

here Y_{ij} are the calibration coefficients obtained by inverting the matrix in Eq. (7.1). The calibration coefficients depend on the height (h) of the frame above the flat and hence the calibration was performed for several values of h and their dependence on h is illustrated in Figure 7.4.

The above described calibration is for static case and in principle cannot be applied to dynamic scenario (i.e., when significant inertial forces are present due to vibration). Hence the time-averaged values of the normal force, friction force and the coefficient of friction are reported.

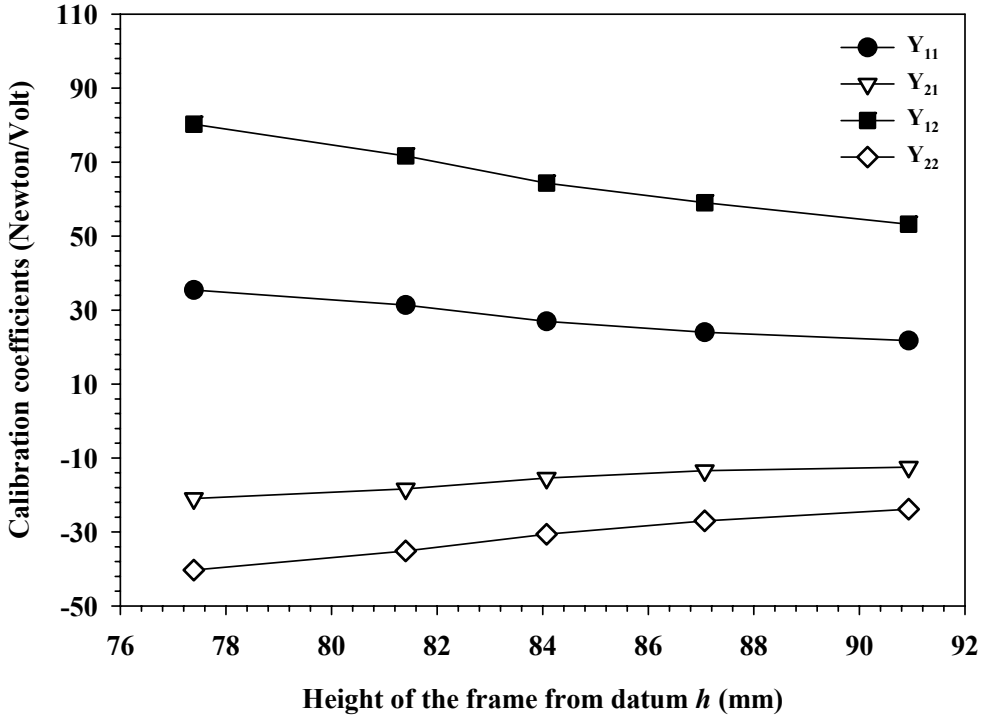

Figure 7.4 Variation of calibration coefficients

7.4 Tribological study of Al-Cu sliding interface

The EML research group at the Georgia Institute of Technology uses copper-110 for rails and aluminum 6061 for armatures. The current study was aimed at understanding the behavior of these two materials in an environment of high current densities and contact pressures.

The experimental matrix is detailed in Table 7.1 along with the contact pressures and the current densities at each load and current level. The test matrix consists of two separate normal loads and six current settings for a speed of 0.15 m/s and travel distance of 1.7 m. In all the test cases, the pin was maintained at positive polarity with respect to the rail. Since the tests are of destructive nature (in regards to the pins), not all tests were repeated. Most of the tests were repeated twice (i.e., a total 3 runs per test) and the ones

Table 7.1 Experimental test matrix for Al-Cu sliding interface

Test No.	Load (N)	Current (A)	Contact pressure (MPa)		Current density (GA/m^2)	
			Flat ended	Hemisph. ended	Flat ended	Hemisph. ended
1*	4.1	0	9	260	0	0
2*	4.1	60	9	260	0.13	3.8
3	4.1	120	9	260	0.26	7.61
4	4.1	180	9	260	0.39	14.06
5	4.1	240	9	260	0.53	15.22
6	4.1	300	9	260	0.66	19.02
7*	12.2	0	26.75	374	0	0
8	12.2	60	26.75	374	0.13	1.84
9	12.2	120	26.75	374	0.26	3.68
10	12.2	180	26.75	374	0.39	5.52
11	12.2	240	26.75	374	0.53	7.36
12	12.2	300	26.75	374	0.66	9.2

that were not repeated are marked with "*" in Table 7.1. As indicated, all 12 combinations of load and current were executed for flat ended and hemispherical pins. The acceleration and the deceleration phases of the linear motor stage velocity profile were set at a magnitude of 7.4 m/s^2. The radius of curvature of the hemispherical pins was 5.7 mm (0.225 inches) while the radius of the cylindrical shank of the flat ended pins was 0.38 mm (0.015 inches). Figure 7.5 (a) and (b) presents the pictures of the hemispherical ended and flat ended pins respectively.

In the case of hemispherical pins the initial contact configuration is of sphere-on-flat type and thus Hertz's theory is used to calculate the initial average contact pressure (Eq. (7.3)) and current density. For flat ended pins the contact pressure was calculated by dividing the normal force by the nominal area of contact (Eq. (7.4)). Thus for hemispherical pins, we have

$$p_{avg} = \left(\frac{6NE^2}{\pi^3 R^2} \right)^{1/3} \tag{7.3}$$

while for flat ended pins,

$$p_{avg} = \frac{N}{A_{nom}} \tag{7.4}$$

where E is the equivalent modulus of elasticity, N is the normal load, R is the radius of curvature, and A_{nom} is the nominal area of contact.

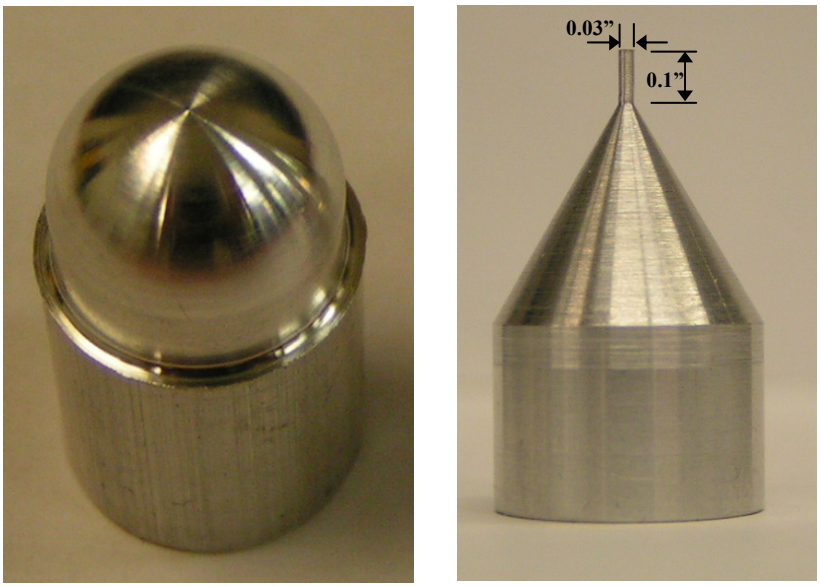

(a) (b)

Figure 7.5 (a) Hemispherical ended pin, (b) Flat ended pin

The copper flats were polished using 116 μm, 60 μm, and 30 μm abrasive size sand papers in the same order to achieve smoother surface finish. The surface roughness parameters, of copper flats, as measured on Zygo NewView 6200 optical profilometer were R_q = 0.92 μm and R_a = 0.65 μm. In order to prevent contact misalignment, the flat ended pins were run-in by rubbing them across 14.5 μm abrasive size sand paper, glued

onto the rail surface, while being held in the tribo-tester. As a result of running-in process the pin tip obtained rounded edges, as seen in Figure 7.6(a).

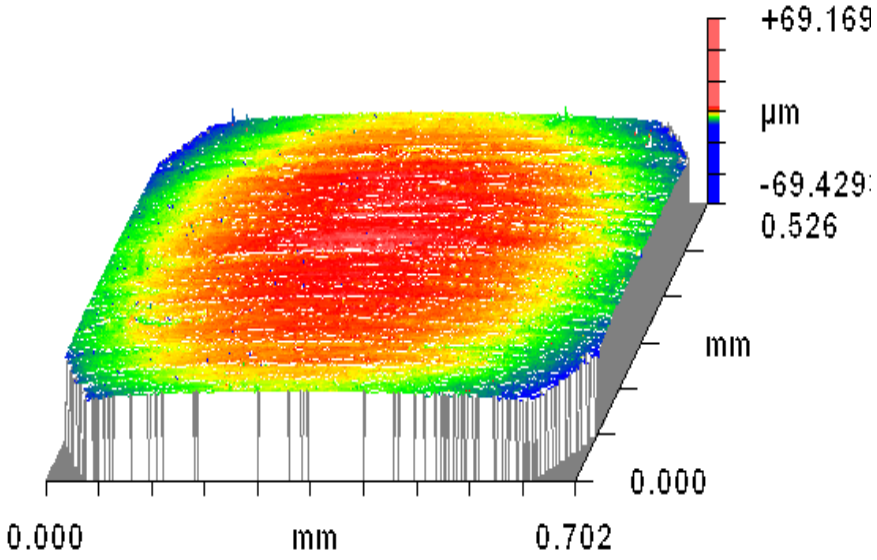

(a)

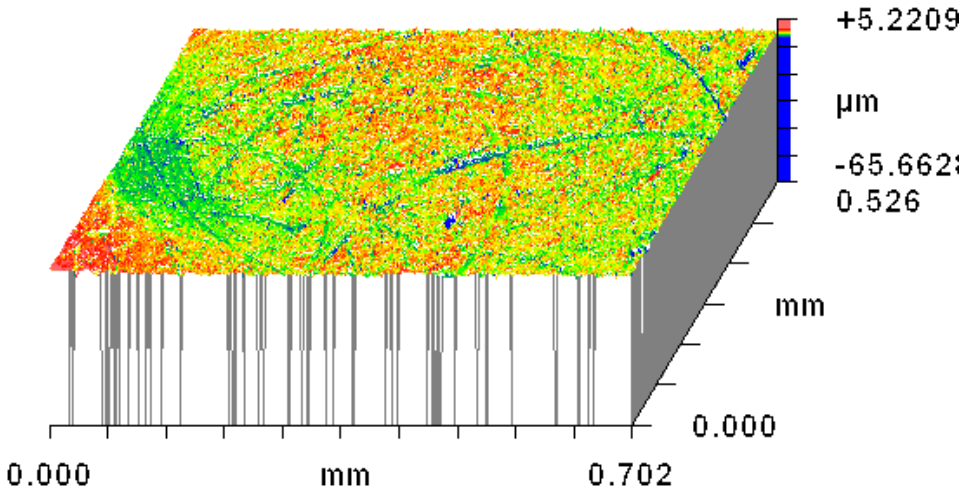

(b)

Figure 7.6 Surface profile of: (a) the flat ended pin, and (b) the hemispherical pin

A representative set of data recorded during Test # 6 (see Table 7.1), which involves a hemispherical pin, is shown in Figure 7.7. As seen from the Figure 7.7, the friction force starts decreasing after 1.5 seconds and the voltage drop shows an increasing trend thereafter. This trend is visible for all the tests and shows that the friction force and the voltage drop across the interface are negatively correlated. One possible explanation is that high contact voltage during the initial part of sliding increases the interface temperature which in turn leads to deterioration of the material strength. The material at the interface softens and this leads to stronger adhesion at the interface and increase in real area of contact. This in turn leads to high friction coefficient and low contact resistance.

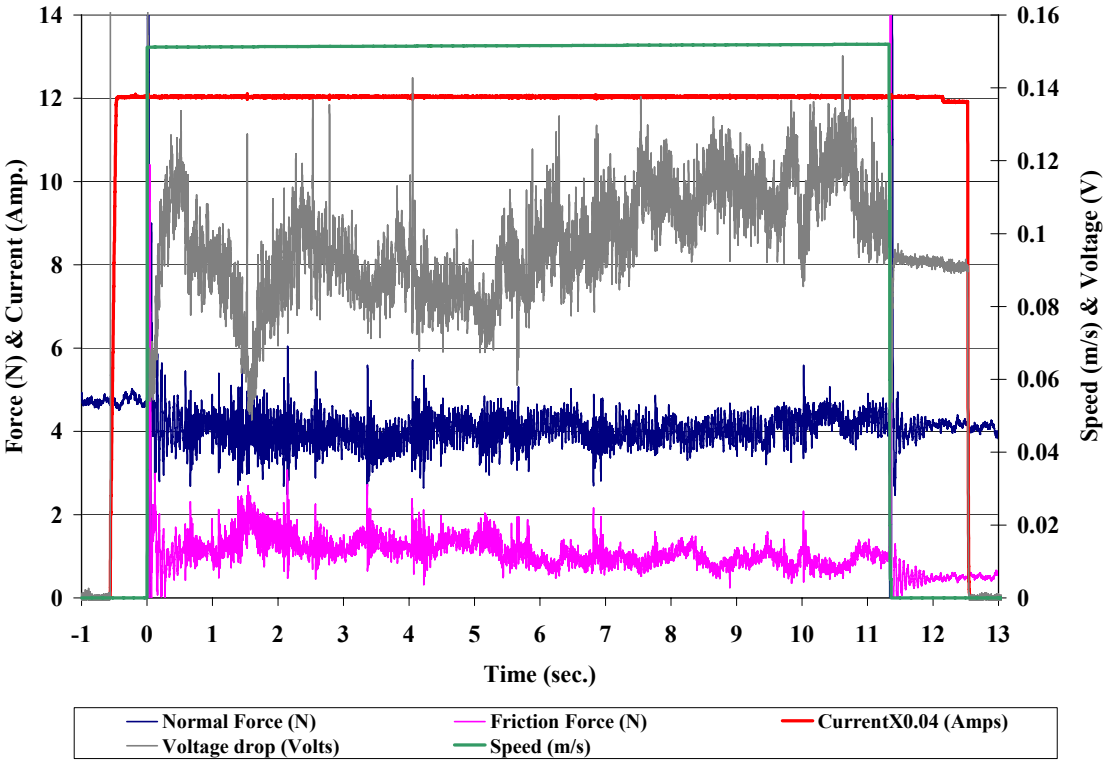

Figure 7.7 Representative test measurement for Test # 6 for hemispherical pin

7.4.1 Effect of current on coefficient of friction

The average coefficient of friction is computed by normalizing the average friction force during the sliding by the average normal force. The average of all three test runs is plotted and the standard deviation is shown by error bars. Figure 7.8 and 7.9 illustrate the variation in the coefficient of friction with current for the flat ended pins and the hemispherical pins respectively.

As seen from the above figure, the coefficient of friction at the normal load of 4.1 N has almost a constant value of around 0.29 – 0.31 for all current levels except for 120 A for which the coefficient of friction drops to a value of 0.23. For the normal load of 12.2 N the coefficient of friction remains steady around 0.22 – 0.23 until 240 A but increases to 0.26 at 300 A.

For the hemispherical pins, at a load of 4.1 N, the coefficient of friction is 0.34 at no current, but jumps to 0.44 at 60 A and then starts to decrease as the current is increased. At a normal load of 12.2 N the coefficient of friction remains constant around 0.32 for all the current levels.

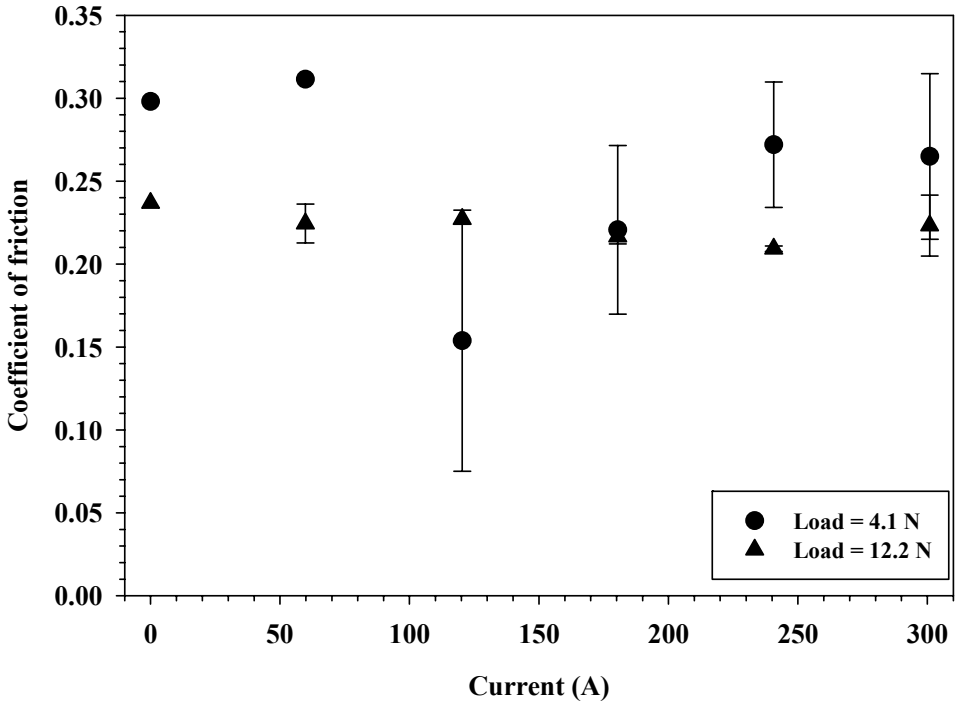

Figure 7.8 Variation in coefficient of friction with current for flat ended pins

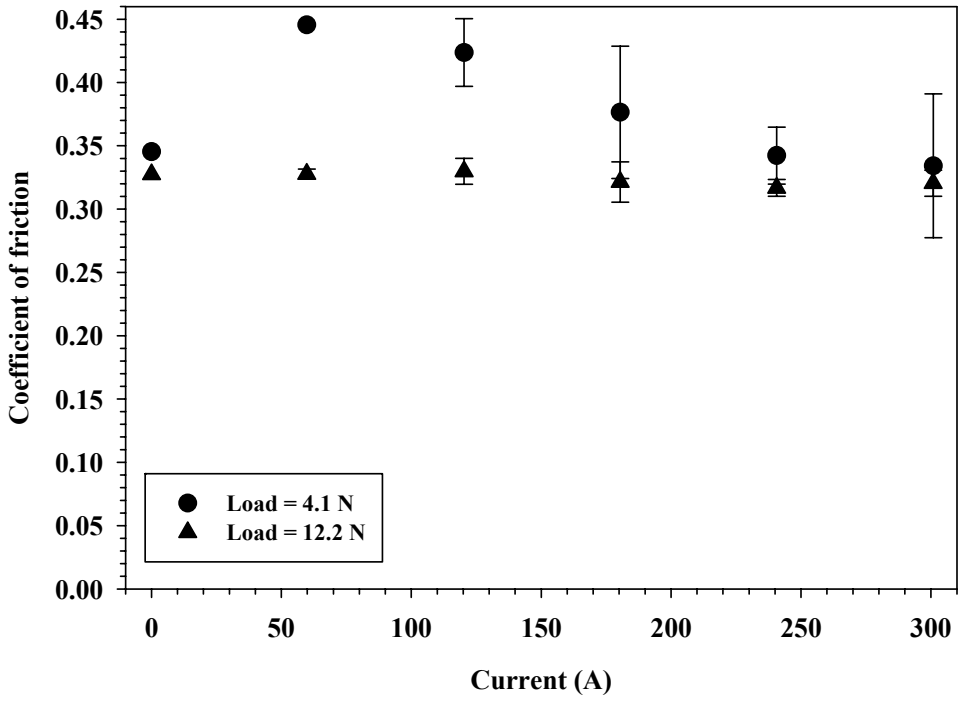

Figure 7.9 Variation in coefficient of friction with current for hemispherical ended pins

7.4.2 Effect of current on contact voltage and contact resistance

The effect of current on the contact voltage, averaged over the sliding distance, is presented here. For the flat ended pins, as seen in Figure 7.10, the contact voltage increases with current. Similar trends are observed for the hemispherical ended pins, as seen in Figure 7.11. Negligible difference in the contact voltage is observed at the two loads for the flat ended pins. However for the hemispherical ended pins the contact voltage was lower at the higher load. This can be explained as: for the hemispherical pins at the higher load (12.2 N) the nominal contact area increases by almost 106% from the load of 4.1 N, while for the flat ended pin the nominal contact area does not change. It is also noticed that the contact voltages are higher for the flat ended pins when compared to those for the hemispherical ended pins for the same current levels.

Figure 7.12 illustrates the variation in average contact resistances for both the flat ended and the hemispherical pins under the loads of 4.1 N and 12.2 N. For flat ended pins the contact resistance decreases with increasing the current but there is little difference between the contact resistances under the two loads for a given current level. In the case of hemispherical pins the contact resistance is lower at the load of 12.2 N as compared to its value at 4.1 N.

In the case of hemispherical pins the original Hertzian area of contact increases by 106% on increasing the load from 4.1 N to 12.2 N. This increase in area of contact is the biggest contributor in lowering the contact resistance under the higher load for any given current level. Very little variation in contact resistance is observed, for the load of 12.2 N, from the current level of 120 A to 300 A whereas for the load of 4.1 N the contact resistance is showing a decreasing trend.

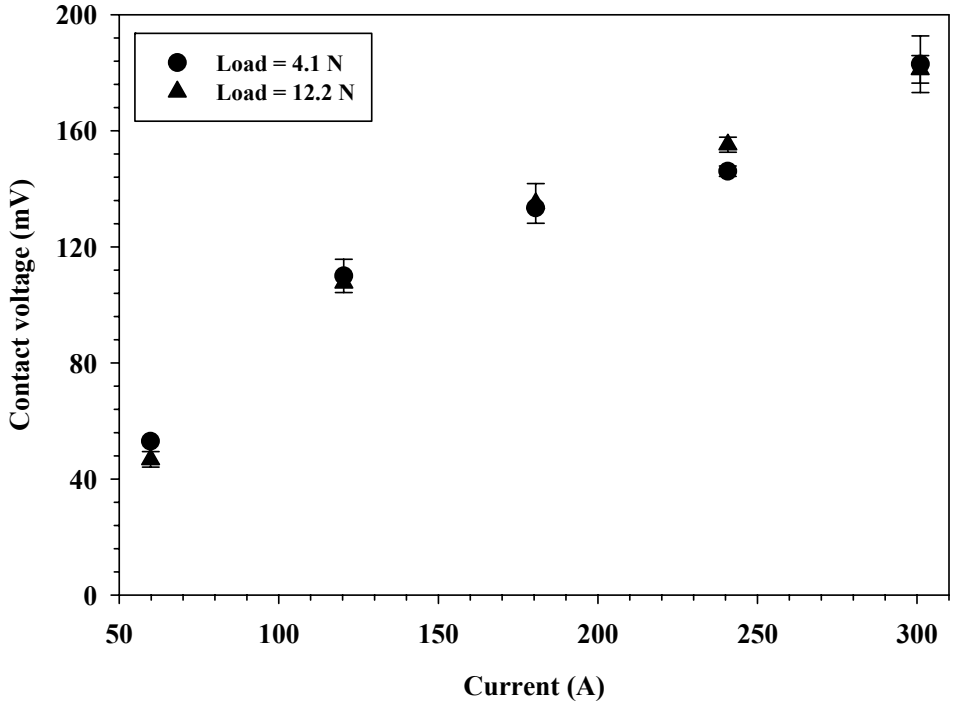

Figure 7.10 Variation in contact voltage drop with current for flat ended pins

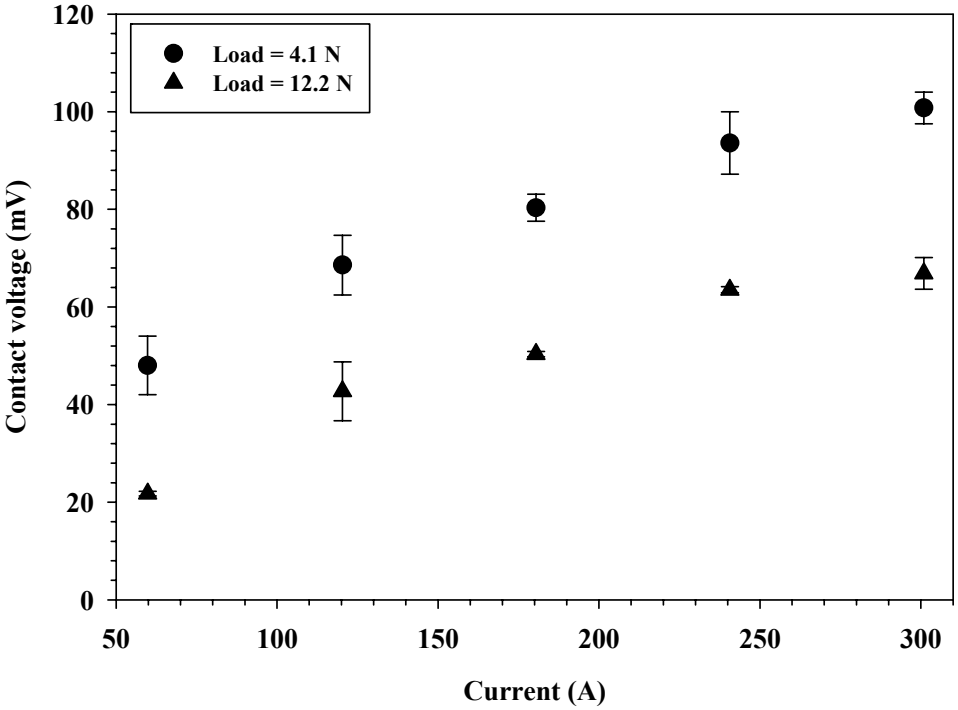

Figure 7.11 Variation in contact voltage drop with current for hemispherical ended pins

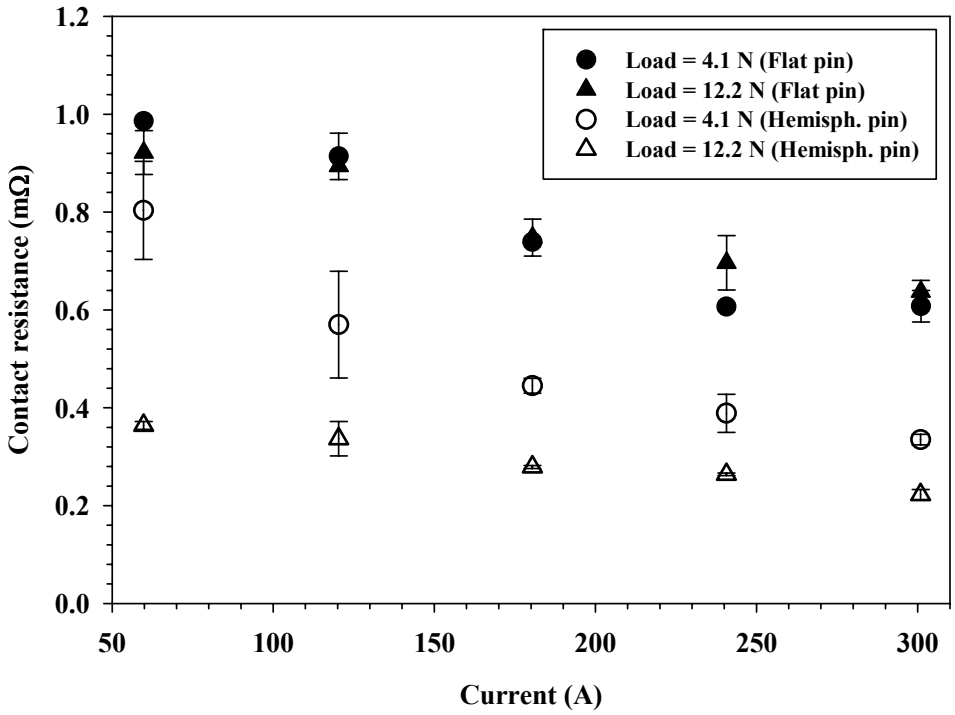

Figure 7.12 Variation in contact resistance with current for both the pins types and load levels

In comparing the contact resistance data of Figure 7.12 to the friction coefficient data of Figure 7.9 as it pertains to the hemispherical pins, we find similar trends: At the lower load, both contact resistance and friction coefficient decrease significantly with increasing current while, at the higher load, these quantities show significantly less variation.

7.4.3 Effect of current on wear of pins

Conducting wear analysis of pins and rail is not trivial, as there is material transfer occurring from pin onto the rail and vice versa. Different techniques like measuring the change in mass of the pins, scanning electron microscopic (SEM) and optical microscopic analysis and energy dispersion spectroscopy (EDS) of the pin surface

were employed to perform the wear analysis. Figure 7.13 shows the change in mass of the hemispherical pins averaged for all three runs of each test condition. It is important to note that although there is transfer of copper onto the aluminum pins, the pins still register decrease in their masses.

As seen from the Figure 7.13 at the lower load of 4.1 N there is little variation in loss in masses of pins over the entire current range, although a decreasing trend is observed. However, at the load of 12.2 N the loss in masses of pins increases with increasing current. The diameter of the wear patch on the tip of the hemispherical pins was measured under an optical microscope to investigate the effect of current on wear. Figure 7.14 plots the diameter of the wear patch for different current levels. It is to be noted that the wear diameter under all the current levels is greater than the initial predicted Hertzian contact diameter and the size of the wear patch increases with increasing current.

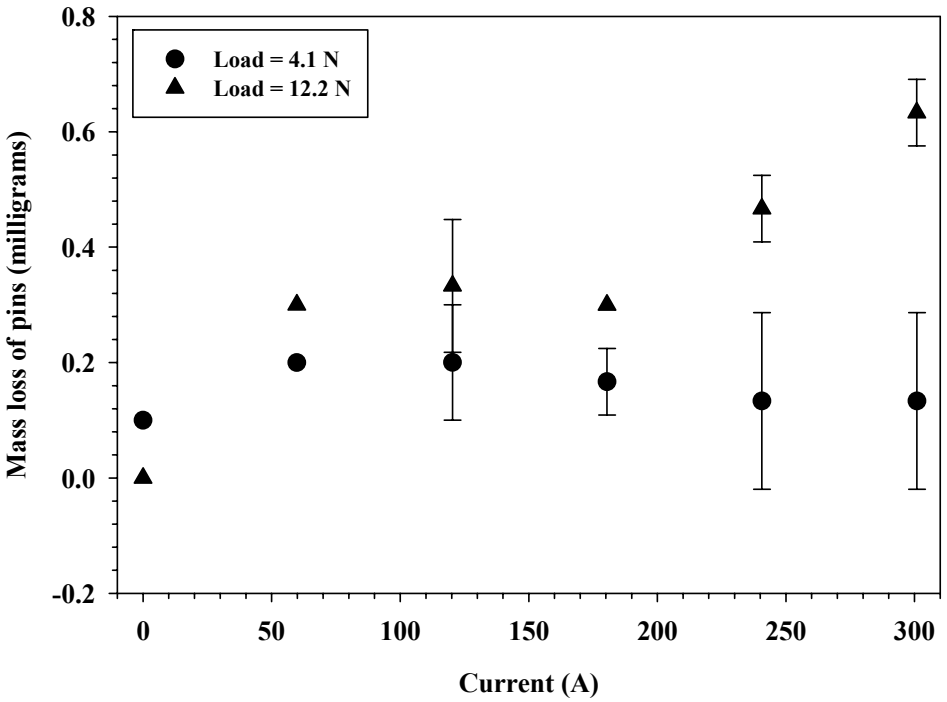

Figure 7.13 Loss in mass of the hemispherical pins at different currents

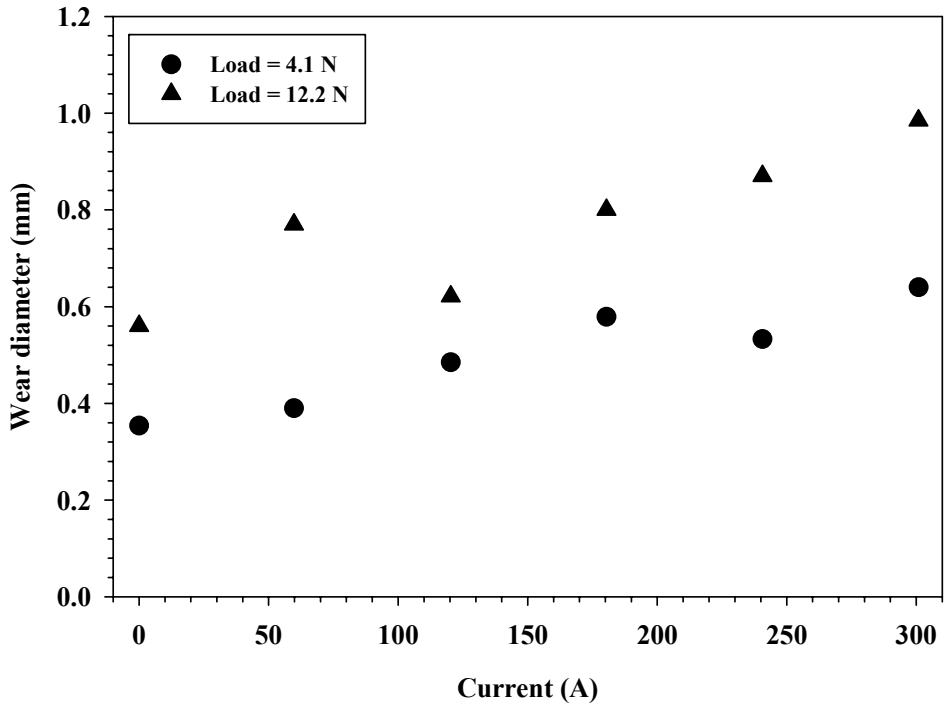

Figure 7.14 Wear diamter v/s current, for the two load levels, for hemispherical ended pins

7.4.3.1 ***Optical microscopy***

Optical microscopy of the pin surface shows interesting trends in transfer of copper onto the aluminum pins. Figure 7.15 shows the flat ended pins for tests under the normal load of 4.1 N, at all the current levels. Under no current there is a very thin film of copper smeared onto the surface, and as the current is increased through the interface the spread and the thickness of the copper film increases. At currents of 240 and 300 amperes the build up of copper is very distinct. Similar behavior is observed for the hemispherical pins. Figure 7.16 shows the hemispherical pin surface under the normal load of 4.1 N for all the current levels.

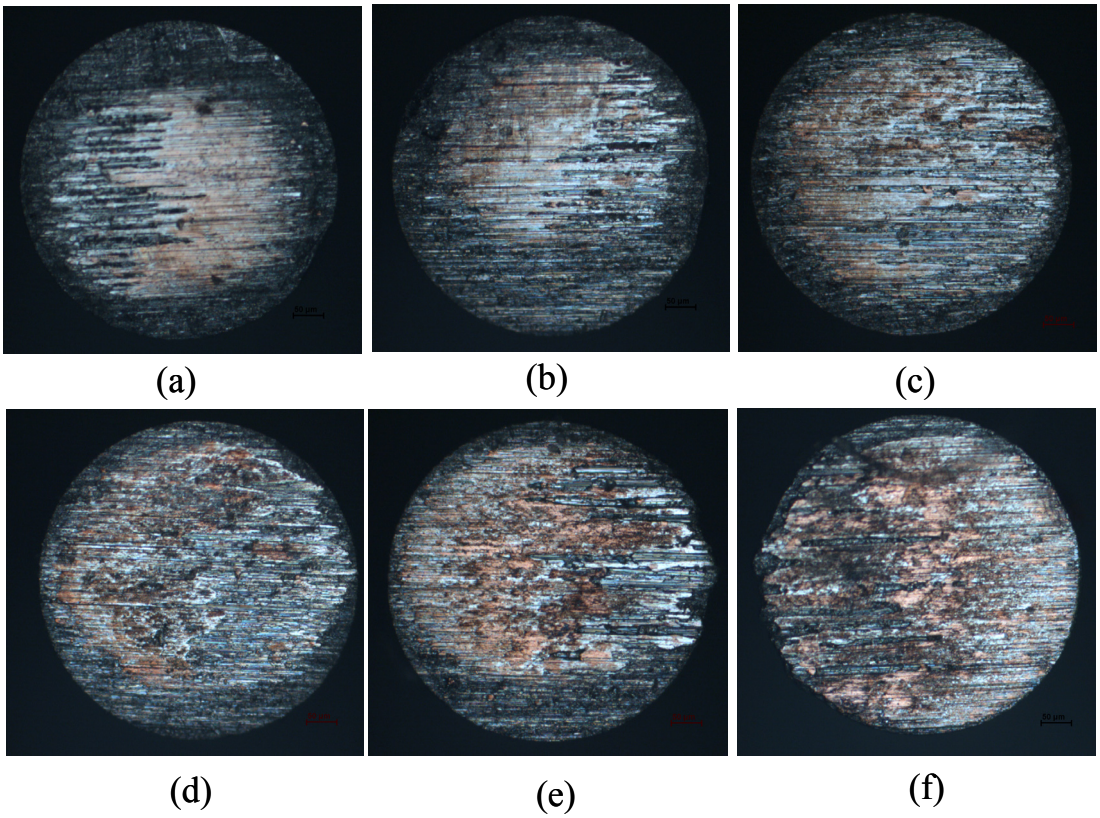

Figure 7.15 Optical images of flat ended pins showing copper transfer onto the aluminum pins,under 4.1N load and currents of (a)0, (b) 60, (c) 120, (d) 180, (e) 240 and (f) 300 amperes

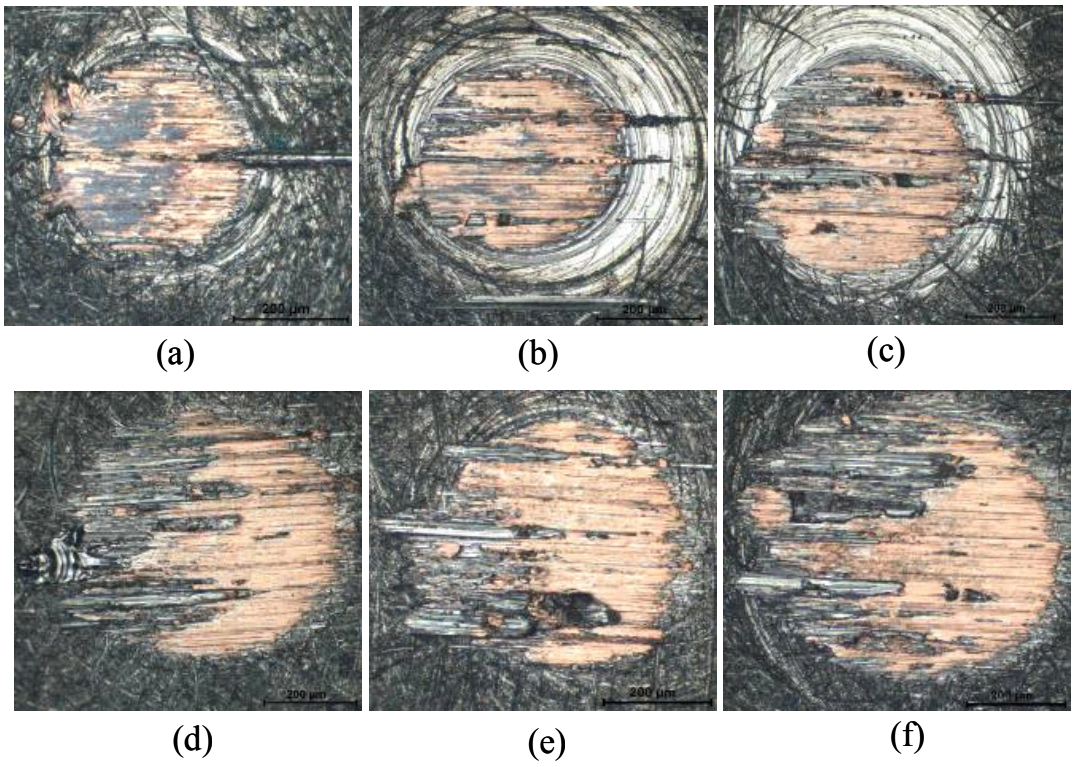

Figure 7.16 Optical images of hemispherical pins showing copper transfer onto the aluminum pins, under 4.1N load and currents of (a)0, (b) 60, (c) 120, (d) 180, (e) 240 and (f) 300 amperes

7.4.3.2 ***Scanning Electron Microscopy and Energy Dispersion Spectroscopy***

SEM and EDS analyses of the pins were conducted to investigate the transfer of copper onto the aluminum pins. In order to check the repeatability of the measurements all three pins from Test #5 (for the flat ended pins), were scanned. The percentages of copper found on the surface were 28%, 33%, and 30%, suggesting a good degree of repeatability. Figure 7.17 illustrates a SEM image of a pin surface (left image), tested under a current of 240 amperes and a normal load of 4.1 N, along with the EDS maps of the aluminum (middle image) and the copper distribution (right image). Consistent with the optical images of Figure 7.16, copper (from the rail) is identified on the pin surfaces.

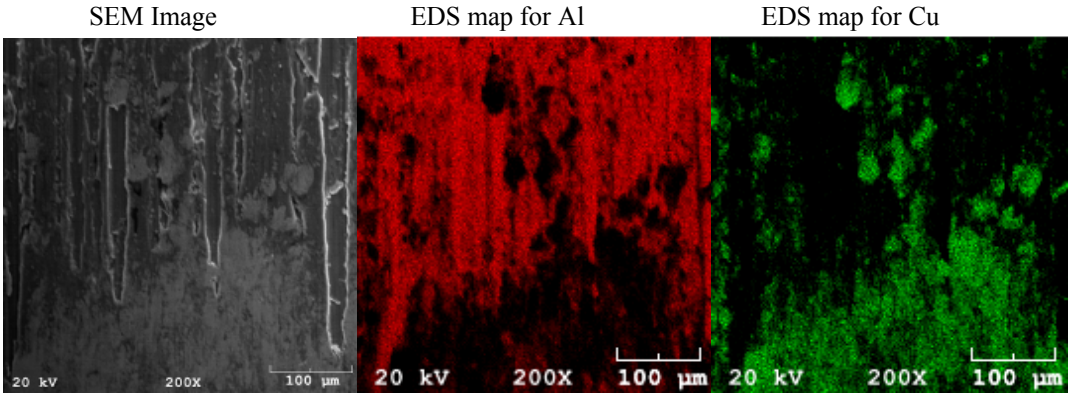

Figure 7.17 SEM and EDS maps of the surface of a flat ended pin (Test # 5)

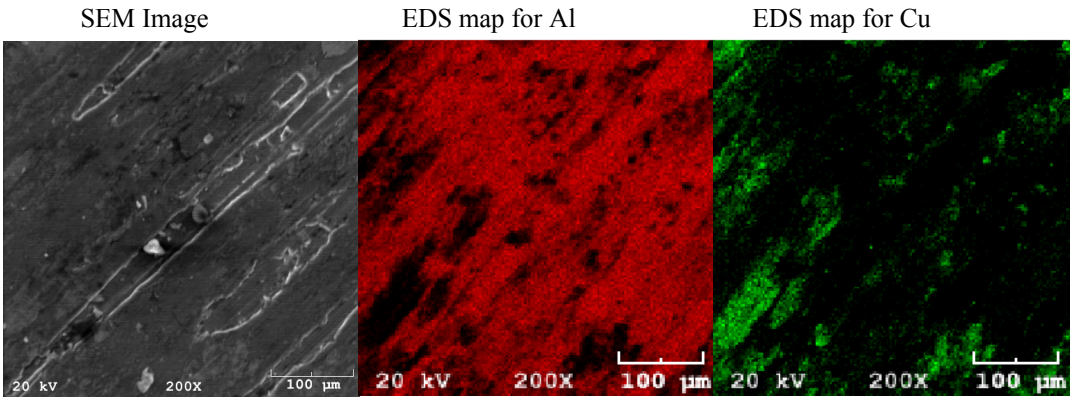

Figure 7.18 SEM and EDS maps of the surface of a flat ended pin (Test # 12)

Figure 7.19 illustrates the variation in the weight pct. transfer of copper onto the pins at different current levels as obtained from the EDS analysis. As expected, greater transfer of copper occurs with increasing current. Surprisingly, however, more copper transferred onto the pins for tests at 4.1 N as compared to the tests at 12.2 N, for the current levels considered. For example the weight percentage of copper on the pin was found to be 54% for current of 300 A at 4.1 N (Test #6) while the copper percentage was 22% for the same current at 12.2 N load (Test #12) (Figure 7.18).

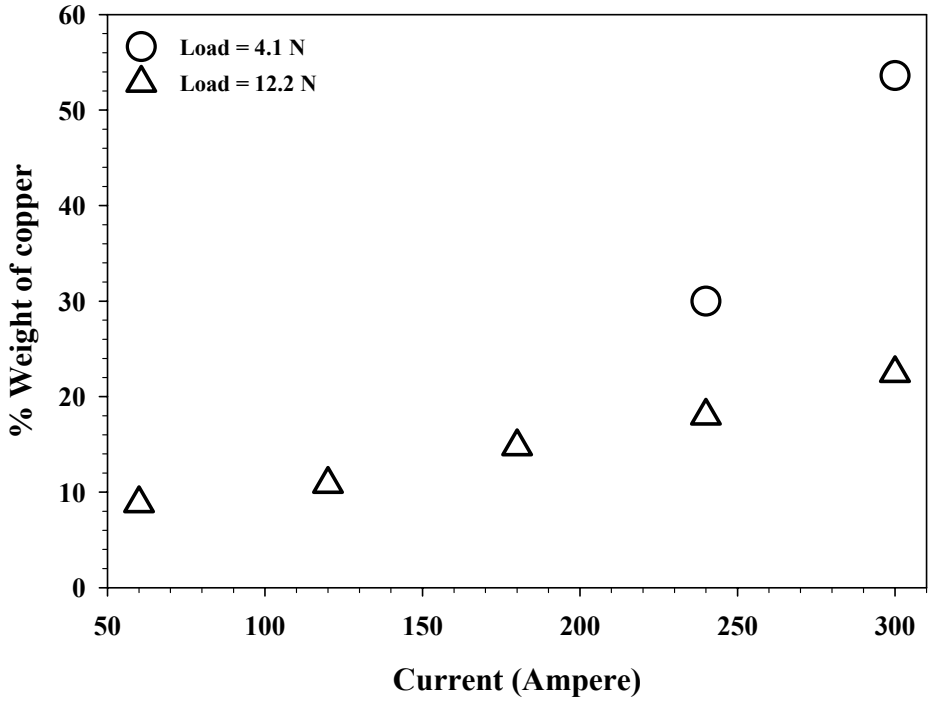

Figure 7.19 Variation in transfer of copper with current for flat ended pins

7.4.4 Discussion

From Figure 7.10 and 7.11 it is seen that the flat ended pins yield higher contact voltages. Figure 7.20 presents the time history plot of contact voltage for the tests at different current levels for flat ended pins for the load of 4.1 N. It is observed that the contact voltage increases with current. For currents greater than 120 A the contact voltage starts to increase towards the end of the sliding. Except for the visual evidence of the material transfer (Cu on Al pins) no other experimental measurement is indicative of the melting at the interface. Hence the paradigm of thermal softening of the interface is discussed here.

The "melting" voltages for Al and Cu as reported by Holm [14] are 0.3 and 0.43 V respectively. From Figures 7.10, 7.11 and 7.20 it is evident that the interface

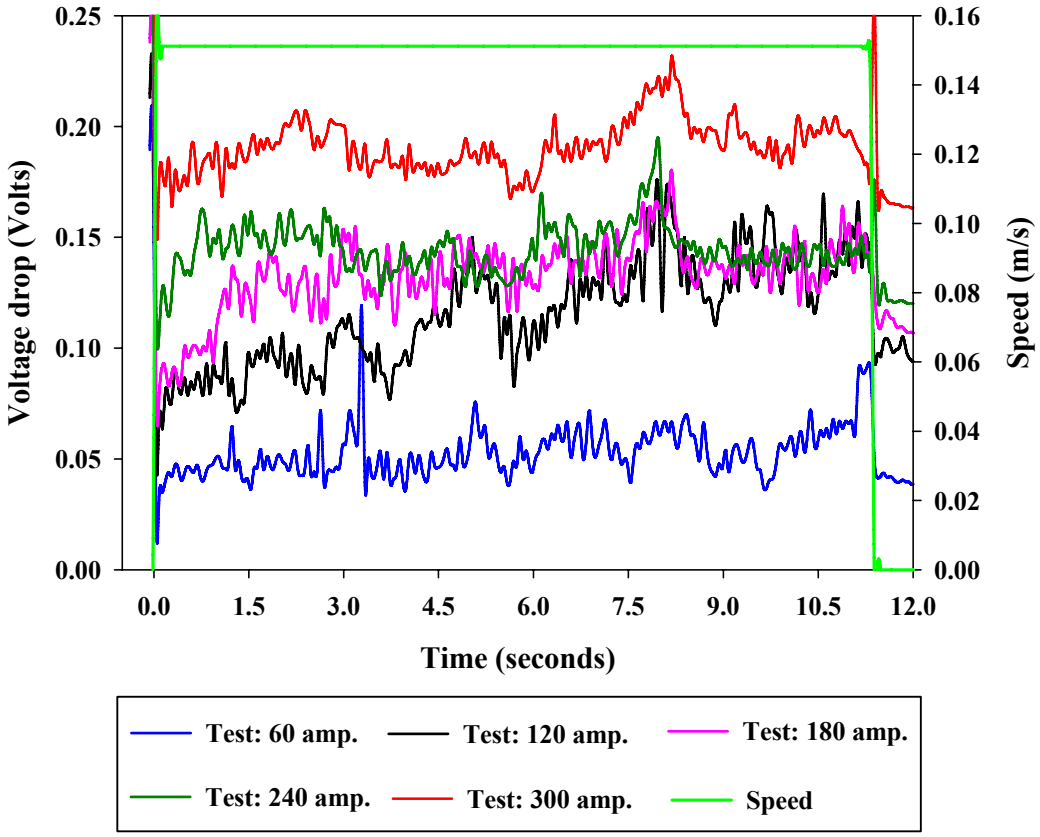

Figure 7.20 Time history plot of contact voltages for flat ended pins for the load of 4.1 N

does not reach the melting voltages. The softening voltages of Al 6061 and Cu 110, as reported in Chapter 6, are around 170 mV and 110 mV respectively. Even though the analysis in Chapter 6 considered similar materials in contact, based on Figures 7.10, 7.11 and 7.20 it can be stated that the interface temperatures are in excess of 200° – 300° C. The hardness of Al 6061 decreases by almost 90% and that of Cu 110 by 35%. This indicates that the interface is thermally softened and this also explains the transfer of Cu onto the Al pins (as seen in Figures 7.15 and 7.16).

7.5 Conclusions

The tests for Al 6061 pins on Cu 110 rails under low and very high current densities have shown interesting trends in the regards of coefficient of friction, electrical contact resistance and wear patterns. In particular, increasing the current: (1) tends to decrease the electrical contact resistance, (2) enhances the rate of transfer of copper from the rail to the pin, (3) increases the wear rate of the aluminum through thermal softening, and (4) may or may not decrease the friction coefficient, depending on the load level and the pin geometry. Additionally, increasing the load tends to decrease the contact resistance for hemispherical pins, but has little effect on flat ended pins.

CHAPTER 8. TRIBOLOGICAL STUDY OF ALUMINUM-ALUMINUM SLIDING INTERFACE

8.1 Introduction

The tribological interface of Al 6061–Al 6061 was studied under various currents, speeds, loads and surface roughness of the flat. Aluminum (Al 6061) hemispherical pins, with radius of curvature of 6.35 mm, were slid against Al 6061 flat for 2 m. Since the tests are of destructive nature, in the sense that the surfaces of the pin and the flat get altered during the test, test matrices were designed to optimize the total number of tests while still accommodating a wide range of test parameters.

8.2 Effects of load, speed and current

Tests were conducted at 6 currents, 3 sliding speeds and 2 loads as listed in Table 8.1. Each test case was repeated twice (total of 3 runs per test case) so that a total of 108 (36×3) tests were run. Each test, including the replicated runs, was run using a new pin on a new track on the surface of the aluminum flat. The values reported in the subsequent plots represent averages taken over the 3 test runs per test case while the error bars indicate the standard deviation in the measurement.

Table 8.1 Test matrix # 1 for Al-Al sliding pair

Current (A)	0	50	120	190	240	320
Speed (m/s)	0.05	0.15	1			
Load (N)	5	15.4				

The surfaces of the aluminum flats were polished using P400 grit sand paper while the surface of the pins were polished using P1200 grit sand paper. All the pins were scanned under the profilometer before the experiments and several different locations were scanned on the aluminum flats. The surface roughness parameters for the pins and the flats are listed in Table 8.2. The corresponding Hertzian contact parameters at the onset of the sliding are listed in Table 8.3. The results of test measurements, including the coefficient of friction, contact resistance, and theoretical interface temperature are presented as functions of contact load, sliding speed and interface current. The coefficient reported here is the ratio of the average friction force over the average normal force as measured over the entire sliding distance. The maximum theoretical interface temperature was calculated from the measured voltage drop using Eq. (6.1) and the parameters listed in Table 6.3.

Table 8.2 Surface roughness parameter for pins and the flats

	Pins		Flats	
	R_a (μm)	R_q (μm)	R_a (μm)	R_q (μm)
Minimum	0.10	0.119	0.38	0.55
Average	0.14	0.22	0.65	0.92
Maximum	0.21	0.29	1.22	1.73
Std. deviation	0.015	0.02	0.1	0.2

Table 8.3 Hertzian contact parameters for Al-Al contact

Current (A) / Load (N)	Contact radius (μm)		Average contact pressure (MPa)		Current density (GA/m^2)	
	5	15.4	5	15.4	5	15.4
0	85.1	124	219.9	320.6	0	0
50	85.1	124	219.9	320.6	2.2	1.0
120	85.1	124	219.9	320.6	5.3	2.5
190	85.1	124	219.9	320.6	8.4	3.9
240	85.1	124	219.9	320.6	10.5	4.9
320	85.1	124	219.9	320.6	14	6.6

The following sections discuss the effect of load, speed and current on the coefficient of friction, contact resistance, contact voltage and maximum interface temperature.

8.2.1 Influence on coefficient of friction

Figure 8.1 presents the coefficient of friction as a function of current through the interface for the load of 5 N. It is observed that at all the speeds the coefficient of friction decreases with increasing current. However, at the maximum current the coefficient of friction increases. This could be attributed to increased adhesion due to thermal softening at the interface which also leads to increase in real area of contact. Figure 8.2 illustrates the variation in coefficient of friction with current for the normal load of 15.4 N. In this case it is seen that the coefficient of friction decreases with increasing current for the speeds of 5 cm/s and 15 cm/s. At the maximum speed of 1 m/s the coefficient of friction seems to be independent of the current through the interface.

More observations on the effect of load on coefficient of friction can be drawn by comparing Figures 8.1 and 8.2. It is seen that, at no current, load has negligible influence on the coefficient of friction, a behavior observed at all 3 speeds. It is also observed that the coefficient of friction increases with load, for all speeds, in presence of current. The only anomalous behavior observed is at the current of 50 A and speed of 1 m/s where the coefficient of friction increases by almost 35% from the load of 5 N to 15.4 N.

It is observed that, at contact load of 5 N, for currents greater than 120 A the coefficient of friction decreases with increasing current. For currents lower than 120 A,

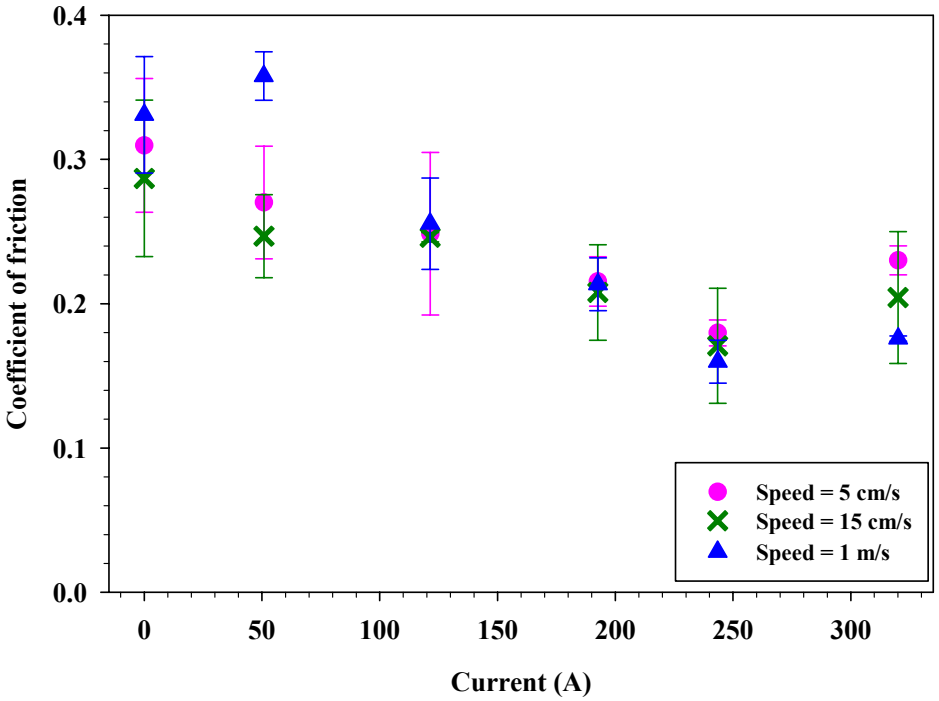

Figure 8.1 Variation of coefficient of friction with current at 5 N

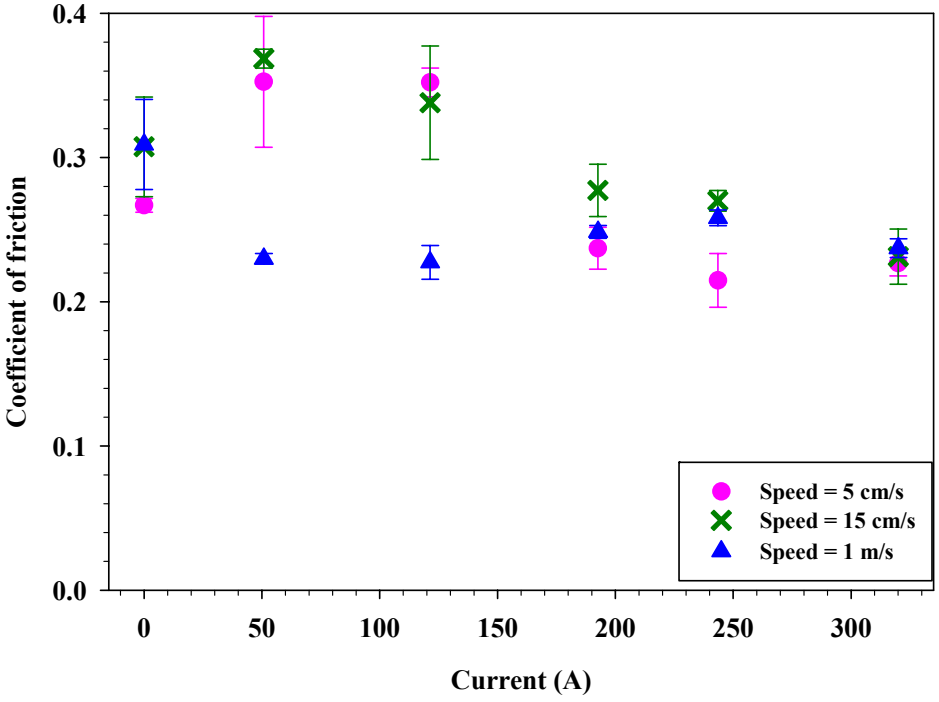

Figure 8.2 Variation of coefficient of friction with current at 15.4 N

speed has little influence on the coefficient of friction. At the load of 15.4 N the speed seems to have negligible influence on the coefficient of friction.

8.2.2 Influence on contact voltage

Figure 8.3 illustrates the variation in contact voltage with current for all 3 speeds at 5 N contact load, while Figure 8.4 presents the same scenario for the load of 15.4 N. From both the figures it is evident that the contact voltage (averaged over sliding distance) increases with current and for a given current level as the speed is increased the contact voltage also increases. At low speeds (5 cm/s and 15 cm/s) the percentage difference in the contact voltage decreases on increasing the load from 5 N to 15.4 N while the current is being increased through the interface. For example at 50 A the contact voltage at 5 cm/s for the load of 5 N is 72% greater than that for the load of 15.4 N, this difference reduces to 14% for the current of 320 A. Similar observations are made for the speed of 15 cm/s where the percentage difference in contact voltage for the 2 loads decreases from 63% at 50 A to 17% at 320 A. Interestingly for the sliding speed of 1 m/s this trend is reversed i.e., the percentage difference in contact voltage between the 2 loads increases from 1.5 % at 50 A to 10 % at 320 A.

Recalling from the observations made in Chapter 6, the saturation voltage for Al–Al contact is in the range of 160–190 mV. It is noted from Figures 8.3 and 8.4 that as the load is increased the onset of saturation is delayed as the current is increased. More interestingly, it is observed that as the speed is increased the interface reaches the saturation voltage as lower currents. For example, for the contact load of 5 N the contact voltage is around 155 mV at 320 A at 5 cm/s, whereas for the speed of 15 cm/s the

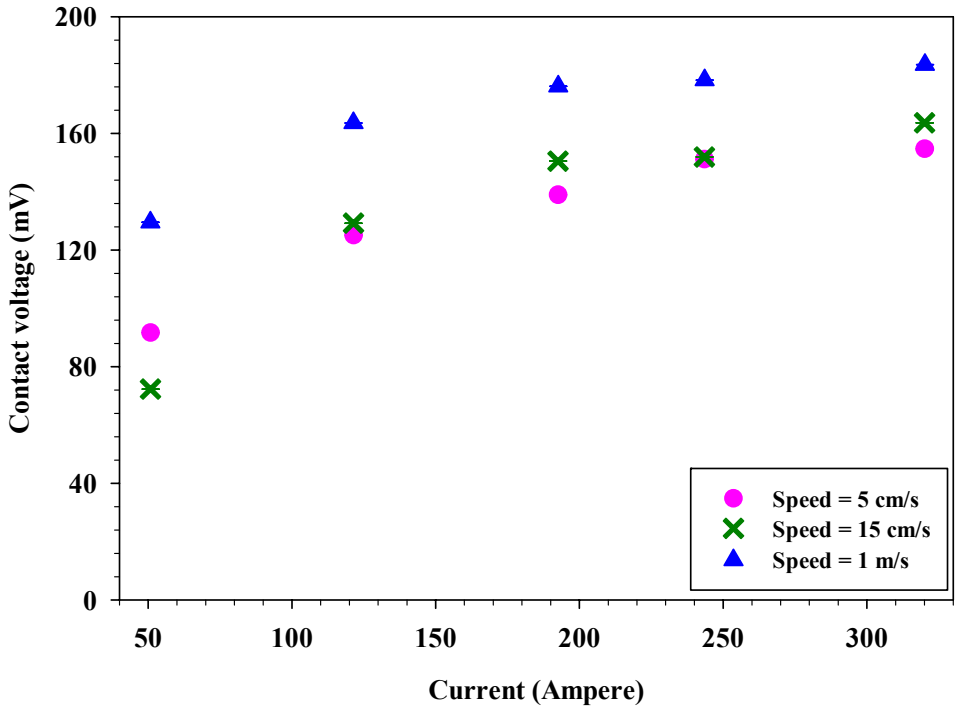

Figure 8.3 Variation of contact voltage with current at 5 N

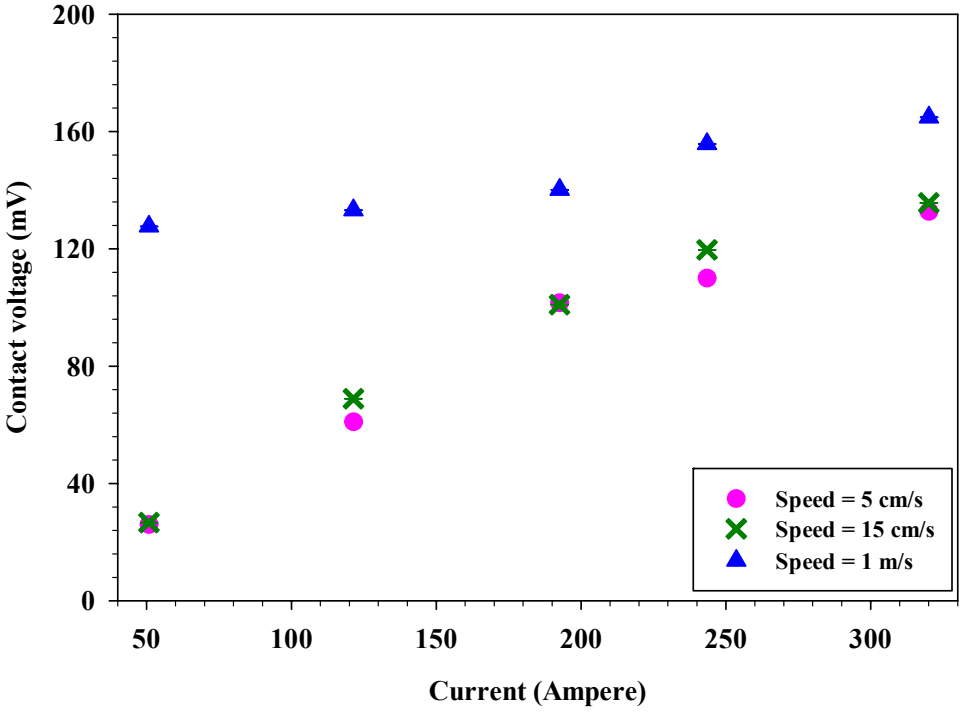

Figure 8.4 Variation of contact voltage with current at 15.4 N

contact voltage reaches 153 mV at 240 A and for the highest sliding speed of 1 m/s the contact voltage is 164 mV at 120 A.

8.2.3 Influence on contact resistance

Figure 8.5 presents the variation in contact resistance with current for all 3 speeds for the contact load of 5 N, while Figure 8.6 illustrates the same scenario for the contact load of 15.4 N. For both the cases of load it is observed that as the current is increased the contact resistance decreases. It is also observed that for a given current level the contact resistance decreases as the load is increased from 5 N to 15.4 N. The percentage decrease in contact resistance due to increase in load (from 5 N to 15.4 N) decreases as the current is increased, this behavior is observed at all 3 speeds. For example for the speed of 15 cm/s the contact resistance decreases by almost 64% on increasing the load at 50 A and this percentage difference reduces to 18% at 320 A. Another interesting observation made is that the contact resistance, for both the cases of load, increases as the speed is increased for a given current. This trend is seen more clearly when contact resistance is plotted as a function of speed. Figure 8.7 illustrates the variation in contact resistance with speed for 5 current levels at the load of 5 N. This plot is essentially obtained by replotting the data in Figure 8.5 as a function of speed. The only anomalous behavior observed is at 50 A where the contact resistance at 15 cm/s before increasing again at 1 m/s.

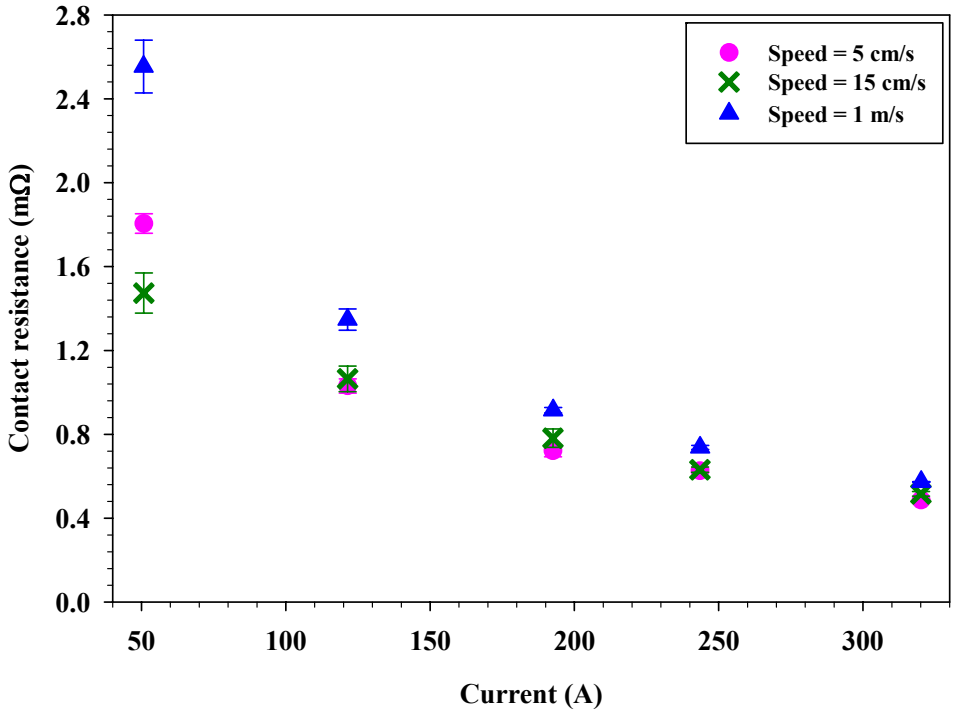

Figure 8.5 Variation of contact resistance with current at 5 N

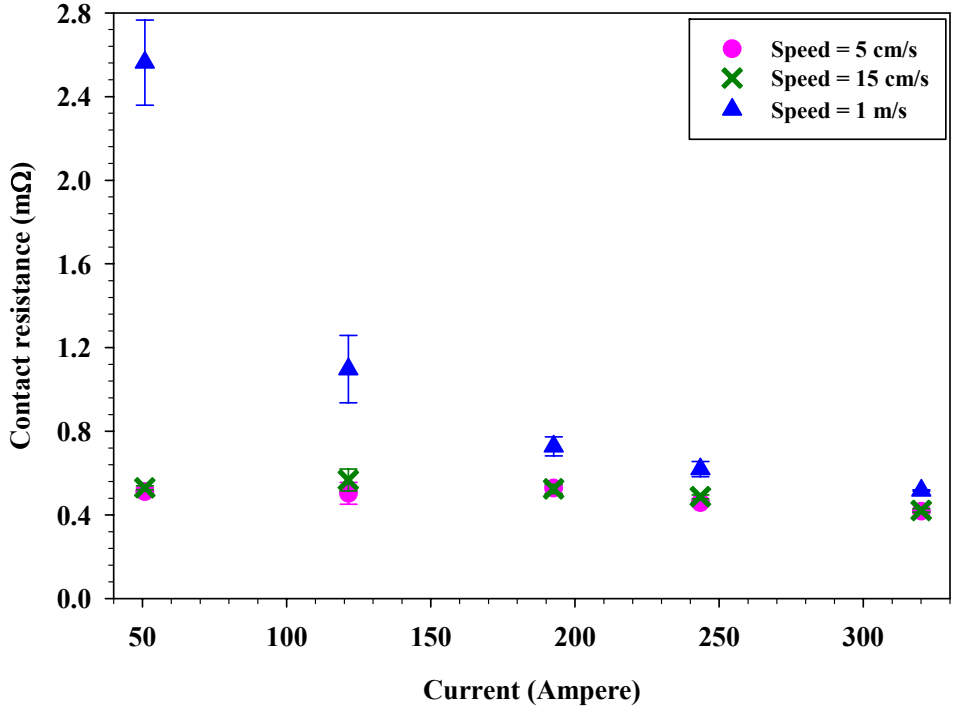

Figure 8.6 Variation of contact resistance with current 15.4 N

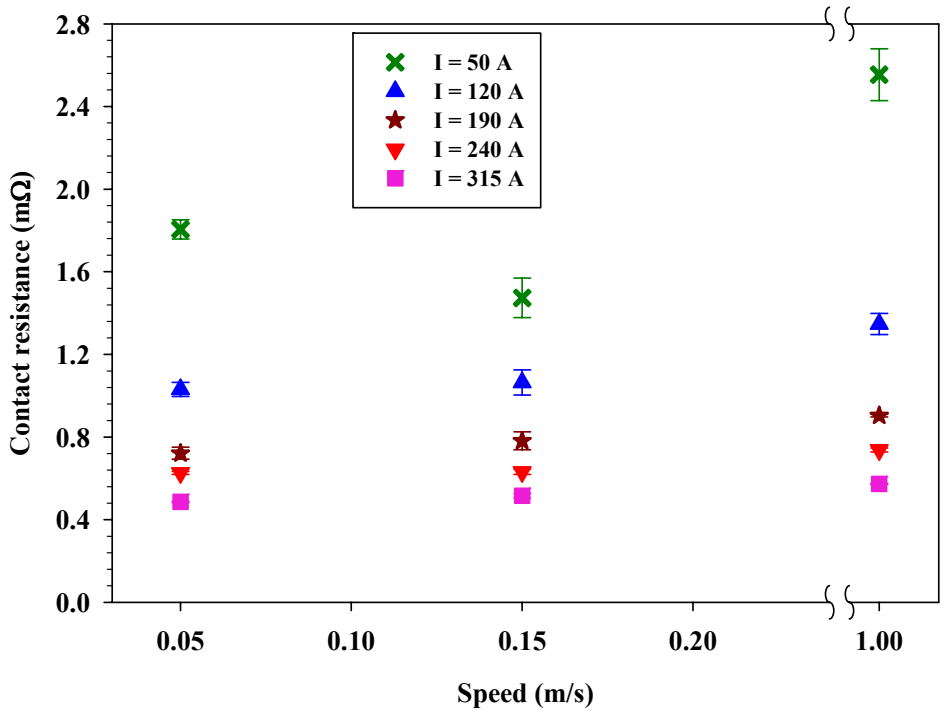

Figure 8.7 Variation of contact resistance with speed at 5 N

8.2.4 Influence on theoretical interface temperature

The interface temperature is estimated using the voltage–temperature as expressed in Eq. (6.1). In order to get a better understanding of the interface behavior it was decided to plot the maximum value of the interface temperature attained during the course of sliding along with the average interface temperature (averaged over the course of sliding). Figure 8.8 presents the maximum and the average theoretical interface temperature for 3 speeds at the contact load of 5 N, while Figure 8.9 presents the similar scenario for the contact load of 15.4 N. Since the occurrence of the maximum temperature could be an isolated incident, the average interface temperature is considered to be a conservative analysis tool. From Figure 8.8 and 8.9 it is seen that for a given current both the maximum and the average interface temperatures increase with speed.

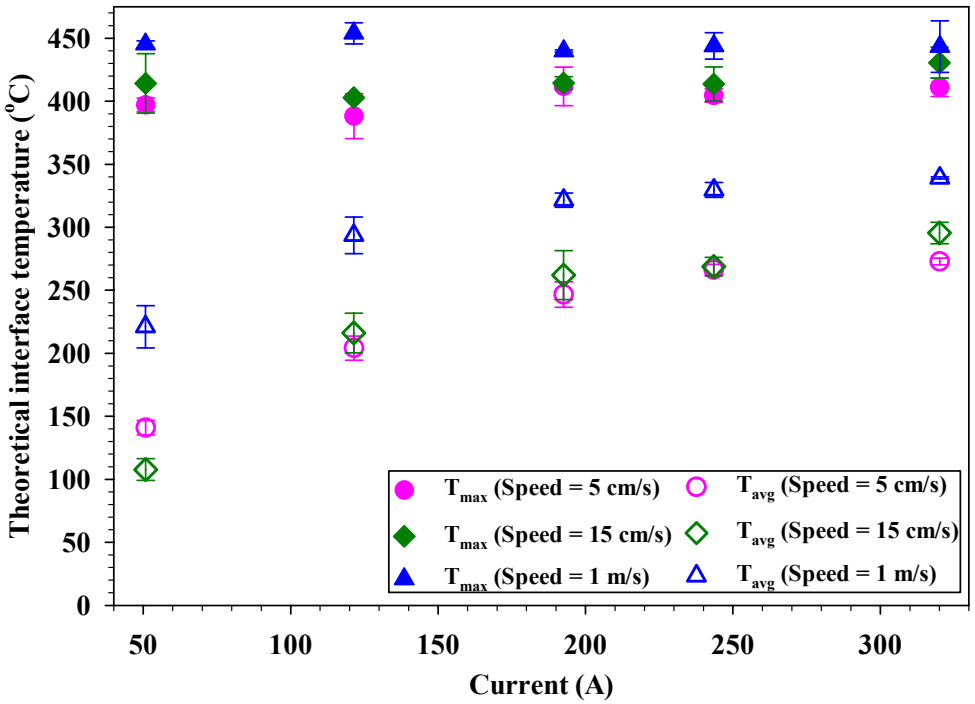

Figure 8.8 Variation of theoretical interface temperature with current at 5 N

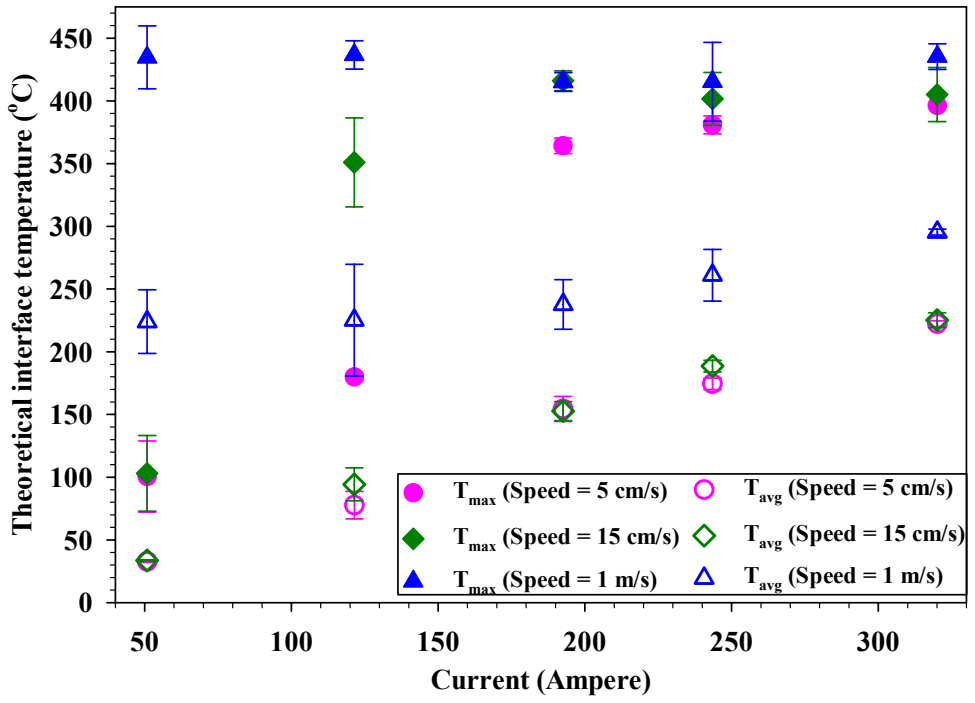

Figure 8.9 Variation of theoretical interface temperature with current at 15.4 N

For the contact load of 5 N, from Figure 8.8, there is negligible variation in the maximum interface temperature with current for all 3 speeds considered. However the average interface temperature increases with current for all 3 speeds.

At the contact load of 15.4 N, from Figure 8.9, it is seen that at sliding speed of 1 m/s the maximum interface temperature is insensitive to the current. However for the speeds of 5 cm/s and 15 cm/s the maximum interface temperature shows an increasing trend with increasing current. The average interface temperature for the load of 15.4 N follows the same trend as for the load of 5 N, i.e. it increases with increasing current.

8.2.5 Discussion (part 1)

As the current through the interface is increased the contact resistance decreases but the Joule heat dissipation increases because of marked increase in the I^2 term. Also contact voltage increases with current leading to rise in the interface temperature. From the dependence of the material strength with temperature (Chapter 6) it can be concluded that the interface is thermally softened. For example from Figure 8.8 it is seen that for currents greater than 150 A, for all the aluminum flats, the average interface temperature is in the range of 220 – 320° C, the corresponding reduction in material strength (hardness) is 63 – 90%.

As the speed is increased the asperities on the pin and those on the flat remain in contact for shorter duration. This leads to less intimate electrical contact between the pin and the flat and hence higher voltage drop across the contact, which can cause micro arcing at the interface.

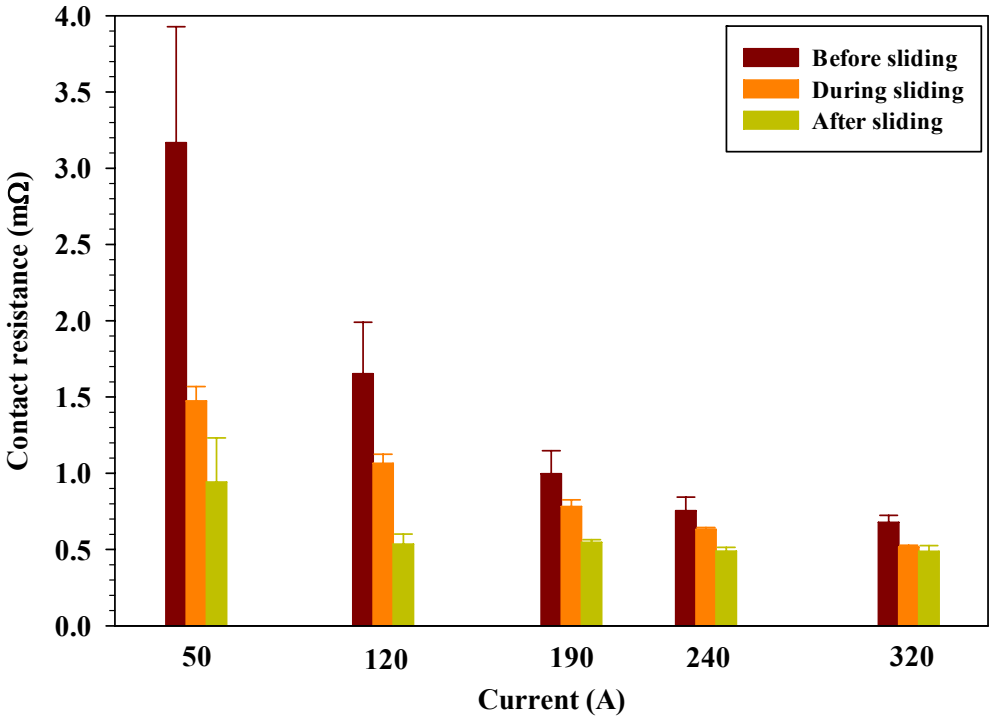

Figure 8.10 Variation in contact resistance with current at different stages of sliding at 5 N and 15 cm/s

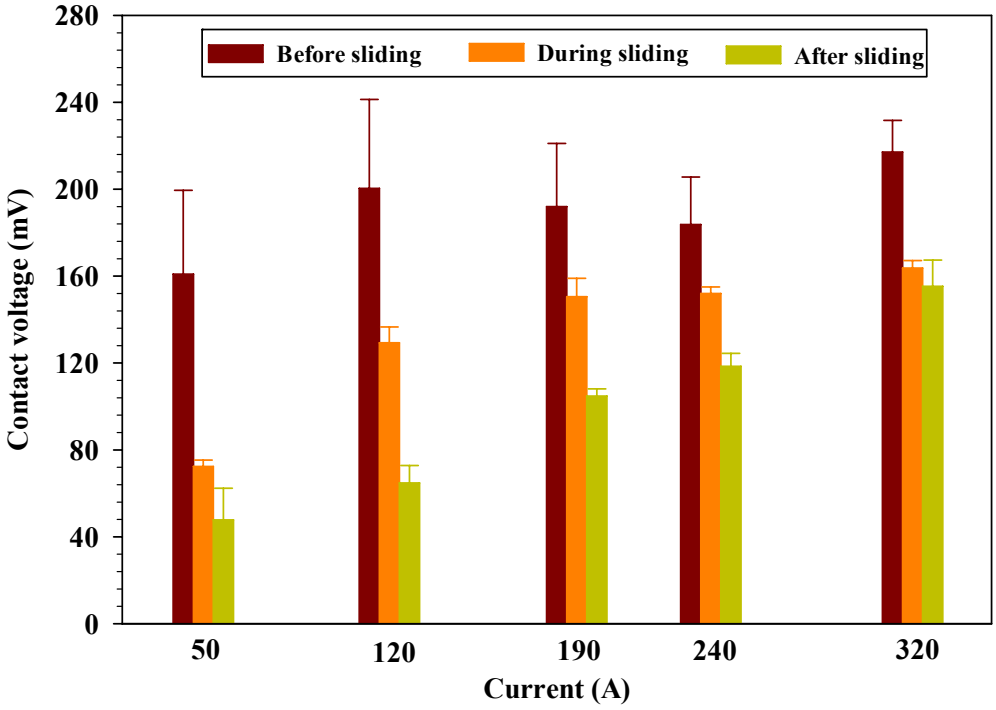

Figure 8.11 Variation in contact voltage with current at different stages of sliding at 5 N and 15 cm/s

The interface undergoes changes, morphological and mechanical, during the course of sliding, and contact resistance is a good indicator of this. Figure 8.10 illustrates the contact resistance at three stages of sliding, initial static, averaged over sliding, and final static after sliding, for the load of 5 N and sliding speed of 15 cm/s. It is observed that the contact resistance is highest when the contact is established (initial static stage). The average contact resistance during the course of sliding is lower than the initial static contact resistance and is higher than the final contact resistance after sliding. This indicates that the contact area has increased during sliding and the contact has become more conformal. Figure 8.11 presents the contact voltage at the three stages of sliding for the test conditions of Figure 8.10. It is observed that the contact voltage during the initial static stage is within the range of 165 – 215 mV. This is similar to the saturation voltage for Al 6061 as reported in Chapter 6 (Section 6.3). Hence it can be stated that when the contact is established the contact voltage is at the saturation state. The contact voltage, averaged over the sliding distance, is lower than the saturation voltage, and the final static contact voltage is the lowest. This also indicates that the contact area has increased, as a result of wear process, during the course of sliding and the contact has become more conformal and therefore electrically conductive.

Figure 8.12 illustrates the contact resistance versus current at three stages of sliding for the contact load of 15.4 N and speed of 1 m/s. Trends similar to Figure 8.10 are observed here too, i.e. contact resistance is highest before sliding and the lowest after sliding. Figure 8.13 presents the contact voltage as a function of current for the test conditions of Figure 8.12. Even here it is observed that the contact voltage before sliding is in the saturation regime and the contact voltage is lowest after the end of sliding.

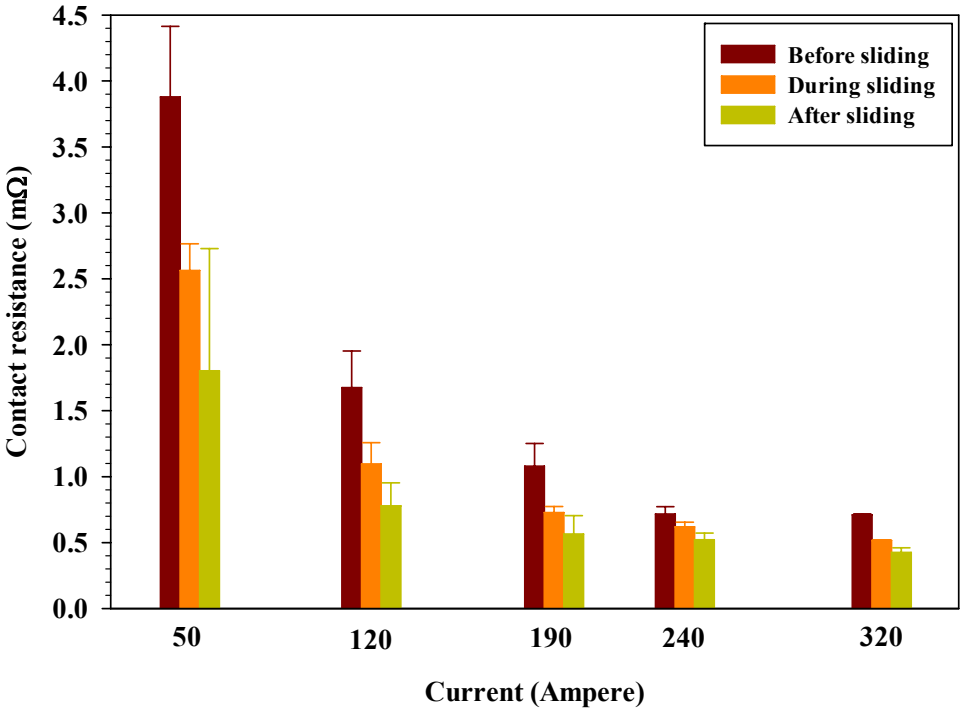

Figure 8.12 Variation in contact resistance with current at different stages of sliding at 15.4 N and 1 m/s

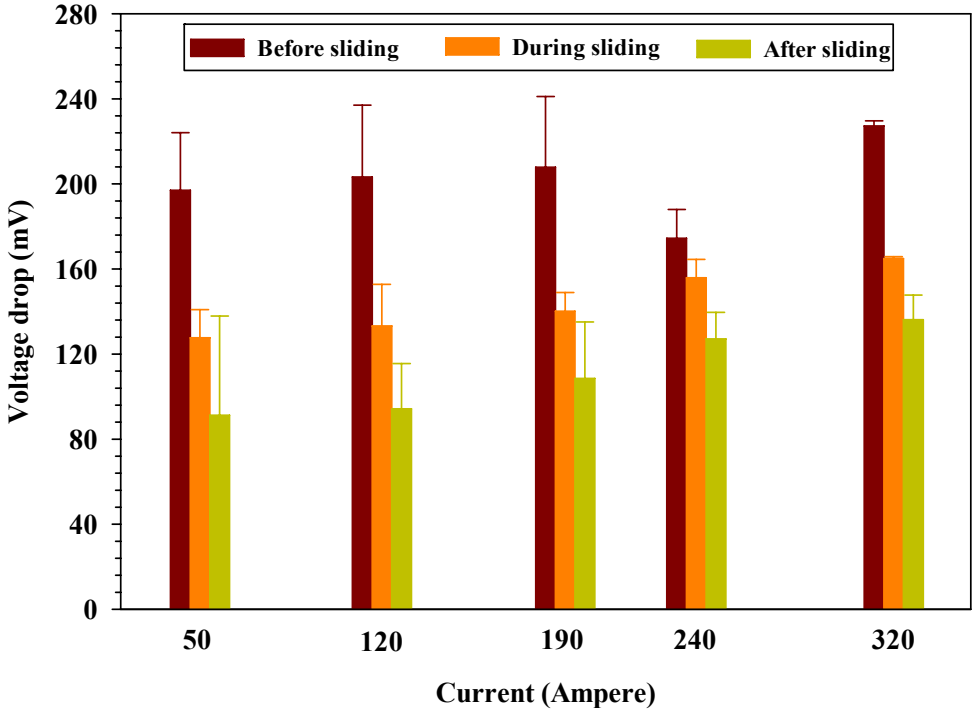

Figure 8.13 Variation in contact voltage with current at different stages of sliding at 15.4 N and 1 m/s

8.3 Study on the effect of surface roughness

Another study investigating the influence of surface roughness of the aluminum flat on the coefficient of friction, contact resistance and wear of the aluminum pins was performed. Based on the results of previous study (Section 8.2) it was decided to vary only current while keeping the load and sliding speed constant in this study. In this study the aluminum (Al 6061) pins with nominally identical surface finish were run against aluminum flats (Al 6061) with different surface roughnesses. Four aluminum flats were polished with four different sand papers to obtain four distinct surface roughnesses on the flats. The test conditions for the same are listed in Table 8.4. The surface roughness parameters for the aluminum flats are listed in Table 8.5, while those for the pins were identical to the values reported in Table 8.2.

Table 8.4 Test matrix # 2 for Al-Al sliding pair

Load (N)	5.25				
Sliding speed (cm/s)	15				
Sliding distance (m)	2				
Current (A)	0	75	150	225	300

Table 8.5 Surface roughness parameters for Al flats

	R_a (μm)				R_q (μm)			
	Min.	Avg.	Max.	St. dev.	Min.	Avg.	Max.	St. dev.
P120	1.17	1.53	2.0	0.19	1.5	2.05	2.62	0.24
P220	0.74	0.95	1.38	0.15	0.98	1.26	1.83	0.2
P400	0.4	0.65	1.22	0.11	0.55	0.92	1.73	0.2
P1200	0.17	0.25	0.42	0.04	0.24	0.36	0.57	0.08

Each test case was repeated twice for a total of three runs, and for each test (including the replicated runs) a new pin was run on a fresh track on the aluminum flat.

The following sections discuss the variation of coefficient of friction, contact resistance, contact voltage and wear of pins as a function of current for the aluminum flats with different surface roughnesses.

8.3.1 Influence on coefficient of friction

Figure 8.14 presents the variation in coefficient of friction, for aluminum flats polished with different sand papers, as a function of current. It is observed that for the smoothest aluminum flat (R_q = 0.36 µm) the coefficient of friction decreases with increasing current. For the aluminum flat polished with P400 (R_q = 0.92 µm) grit sand paper the coefficient of friction decreases with increasing current until 300 A where it increases by almost 15 % from its value at 225 A. It is also seen that the roughest polished aluminum

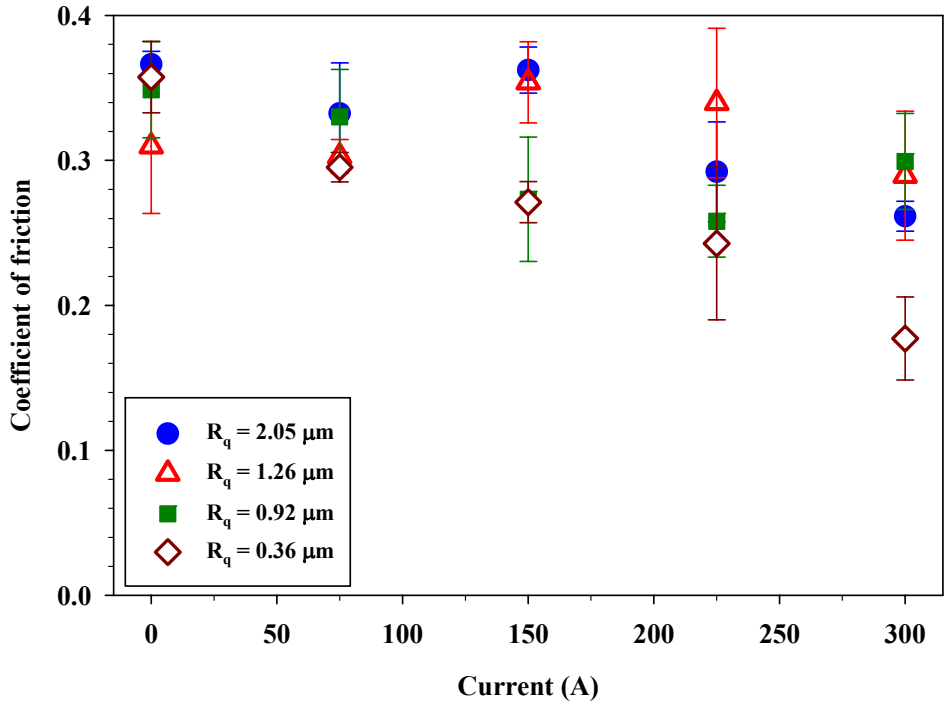

Figure 8.14 Variation in coefficient of friction with current for Al flats with different surface roughnesses

flat (R_q = 2.05 µm) yields the highest coefficient of friction at current levels up to 150 A, while the smoothest polished flat (R_q = 0.36 µm) yields the lowest coefficient of friction at currents greater than 75 A.

8.3.2 Influence on contact voltage

Figure 8.15 presents the contact voltage, averaged over the duration of sliding, versus current for different surface roughnesses of aluminum flats. It is observed that the roughest polished aluminum flat (R_q = 2.05 µm) yields the lowest contact voltage while the smoothest polished flat (R_q = 0.36 µm) yields the maximum voltage drop at all currents. For the other two aluminum flats, (R_q = 1.26 µm) and (R_q = 0.92 µm), the contact voltage shows negligible influence of current during sliding.

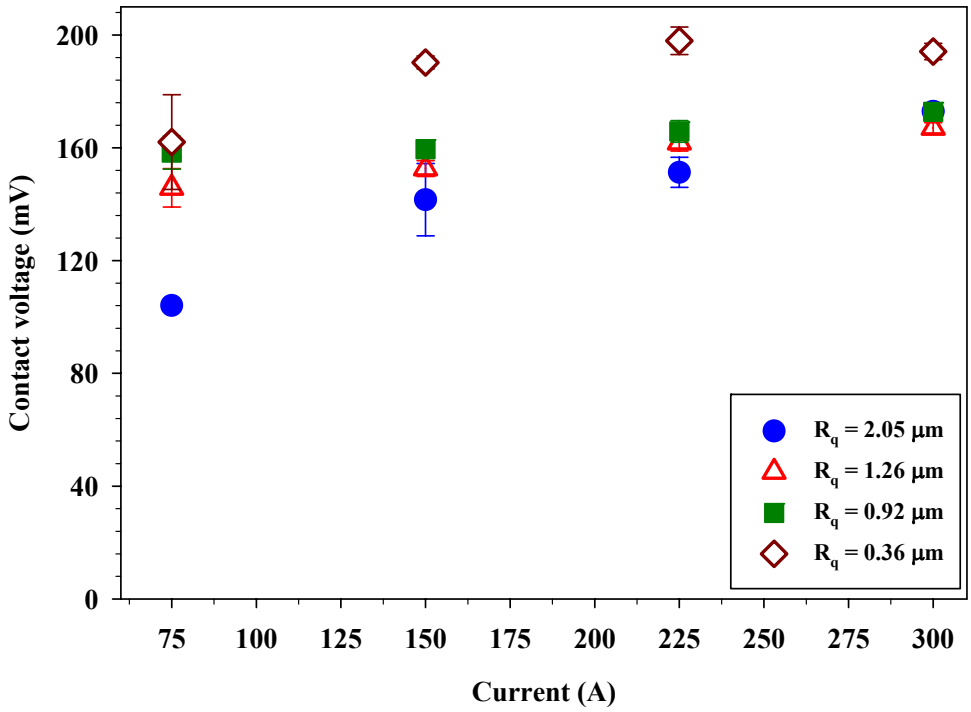

Figure 8.15 Variation in contact voltage with current for Al flats with different surface roughnesses

Figure 8.16 presents the contact voltage as a function of current for initial static (before sliding) stage. It is seen that for all the combinations of currents and surface roughness of the flats the contact voltage is in the saturation regime. It is also observed that the roughest polished aluminum surface (R_q = 2.05 µm) yields the highest voltage drop while smoothest polished aluminum surface (R_q = 0.36 µm) yields the lowest voltage drop at all currents.

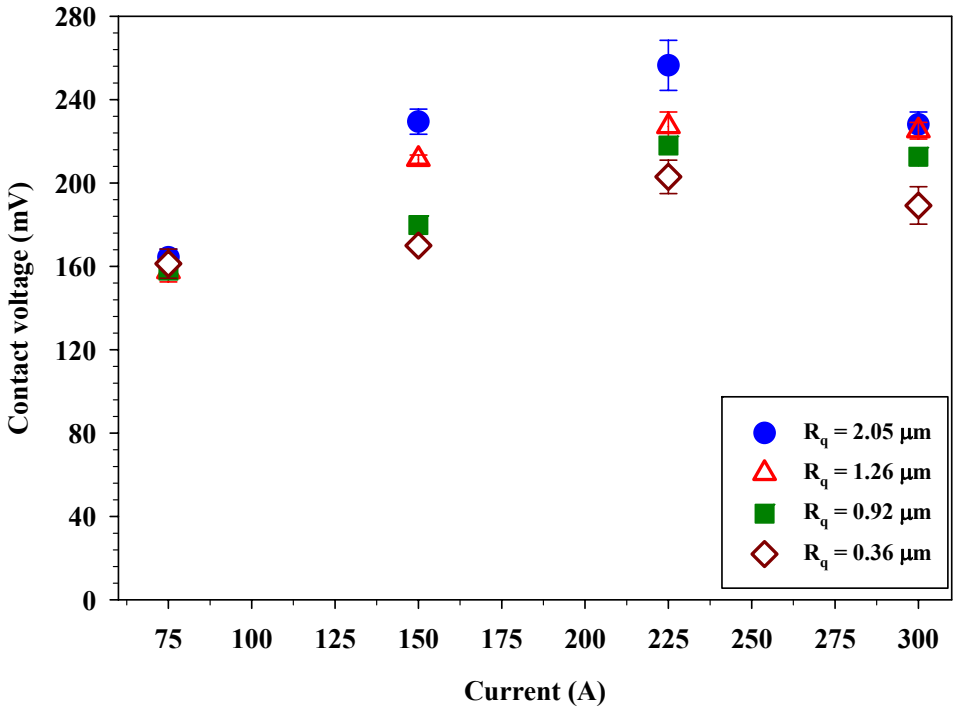

Figure 8.16 Variation in contact voltage with current for Al flats with different surface roughnesses: Before sliding

8.3.3 Influence on contact resistance

Figure 8.17 presents the variation of contact resistance, averaged over the sliding distance, with current for different surface roughness of the flats. It is observed that the contact resistance decrease with increasing current for all the flats with different surface

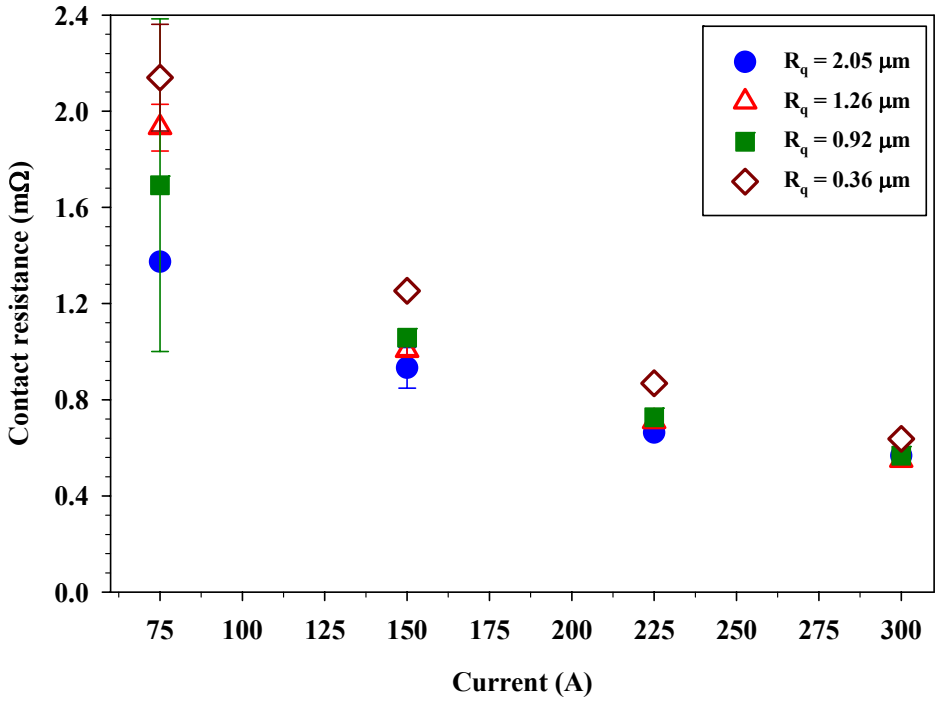

Figure 8.17 Variation in contact resistance with current for Al flats with different surface roughnesses

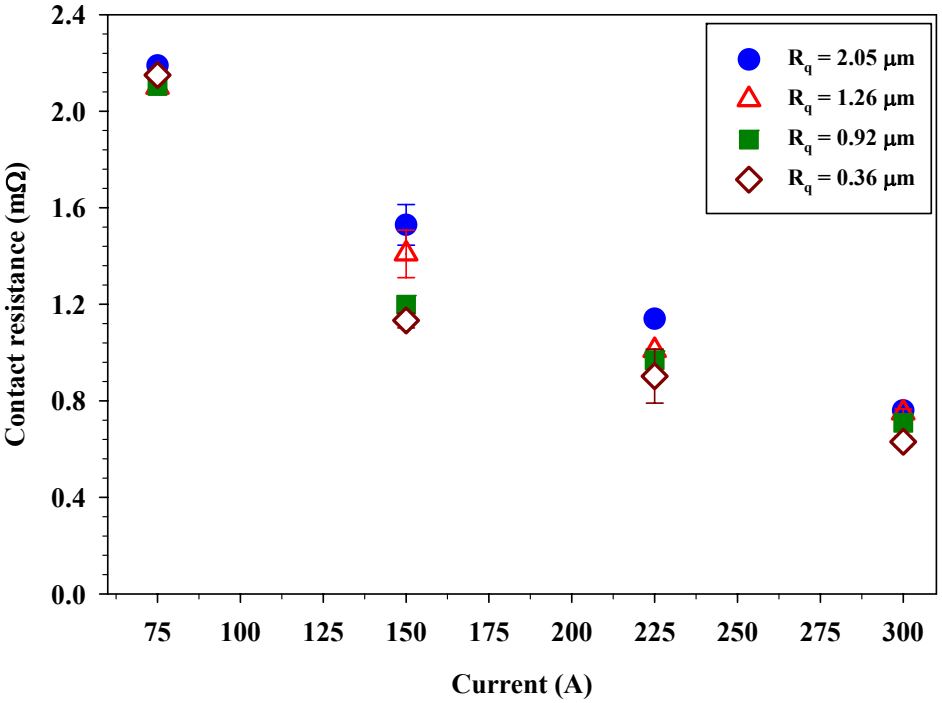

Figure 8.18 Variation in contact resistance with current for Al flats with different surface roughnesses: Before sliding

roughnesses. Interestingly the smoothest polished aluminum flat (R_q = 0.36 μm) yields the highest contact resistance while the roughest polished aluminum flat (R_q = 2.05 μm) yields the lowest contact resistance at all currents. As the current through the interface is increased the difference in the contact resistance, at a given current, decreases.

Figure 8.18 illustrates the initial static (before sliding) contact resistance for all 4 surface roughnesses of aluminum flats as a function of current. It is observed that in the static condition the roughest polished aluminum flat (R_q = 2.05 μm) yields the highest contact resistance at all the current levels when compared to the aluminum flats with other surface roughnesses. This trend is reversed during the course of sliding (as seen from Figure 8.17) which indicates that the interface with the roughest polished aluminum flat (R_q = 2.05 μm) undergoes maximum change. The contact resistance for this case decreases by 37% at 50 A and 25% at 300 A from initial static condition, whereas for aluminum flat with R_q = 0.36 μm the corresponding decrease in contact resistance is 0.5% at 50 A and 1% at 300 A.

8.3.4 Influence on interface temperature rise

Figure 8.19 plots the theoretical interface temperature rise, both maximum average values over the duration of sliding, versus current for aluminum flats with four different surface roughnesses as calculated using Eq. (6.1).

It is observed that both the maximum and the average interface temperature increase with current. This is similar to the trends of contact voltage with current as seen in Figure 8.15. The aluminum flat with smoothest finish (R_q = 0.36 μm) yields the

highest maximum interface temperature compared with flats with other surface roughnesses.

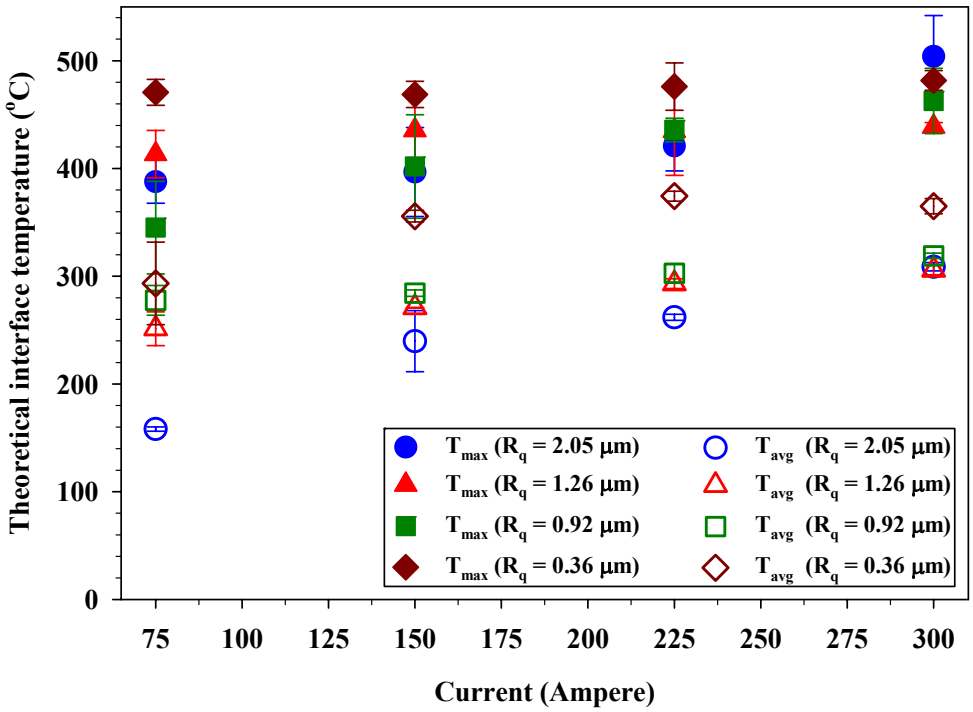

Figure 8.19 Variation in theoretical interface temperature with current for Al flats with different surface roughnesses

A more conservative indicator of the nature of the interface can be obtained by averaging the theoretical interface temperature over the course of sliding. It is seen that for all the aluminum flats excluding the roughest one (R_q = 2.05 µm) the average interface temperature is insensitive to the surface roughness at a given current. It should be noted that the percentage increase in average interface temperature with current decreases as the surfaces are made smoother. For example for the roughest polished aluminum flat (R_q = 2.05 µm) the average interface temperature increases by almost 95%

from 75 A to 300 A while the corresponding increase is 21% and 15% for aluminum flats with R_q = 1.26 µm and R_q = 0.92 µm respectively.

8.3.5 Influence on wear of pins

The wear of pins was quantified by measuring their masses before and after the tests. Figure 8.20 presents the measured loss in mass of pins versus current for tests with aluminum flats with four different surface roughnesses.

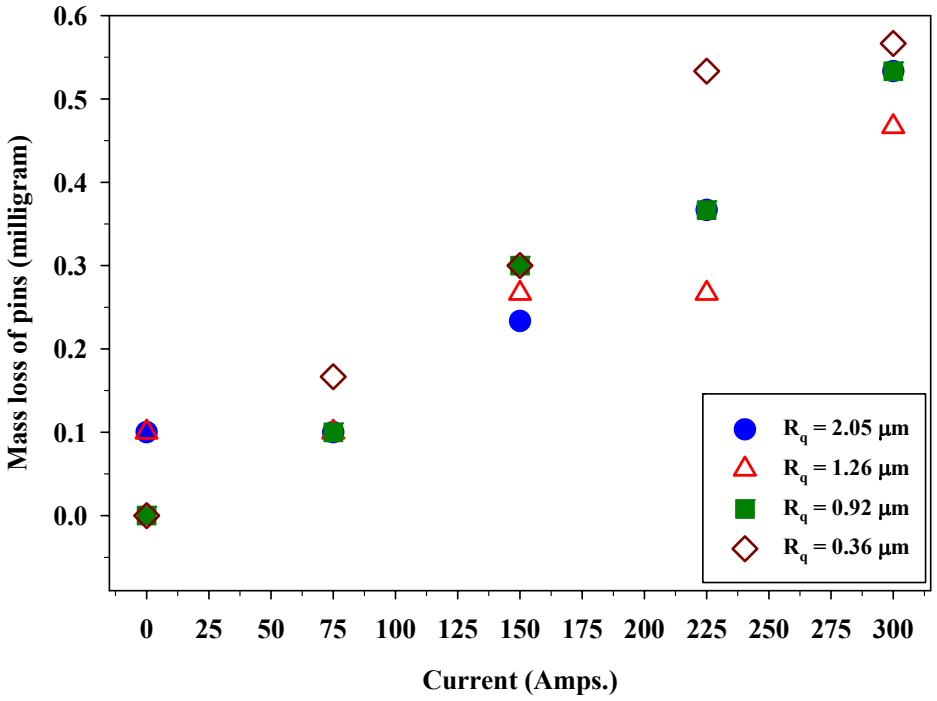

Figure 8.20 Variation in mass loss of pins with current for test against Al flats with different surface roughnesses

It is observed that the loss in mass of pins increases with current. At zero current the smoother polished aluminum flats R_q = 0.92 µm and R_q = 0.36 µm caused the least wear of the pins. As the current through the interface was increased the smoothest polished aluminum flat (R_q = 0.36 µm) caused higher loss in mass of pins when compared to tests with flats with rougher surface roughness. It should be noted that the

material transferred onto the pin during the course of sliding was not removed while measuring its mass after the test.

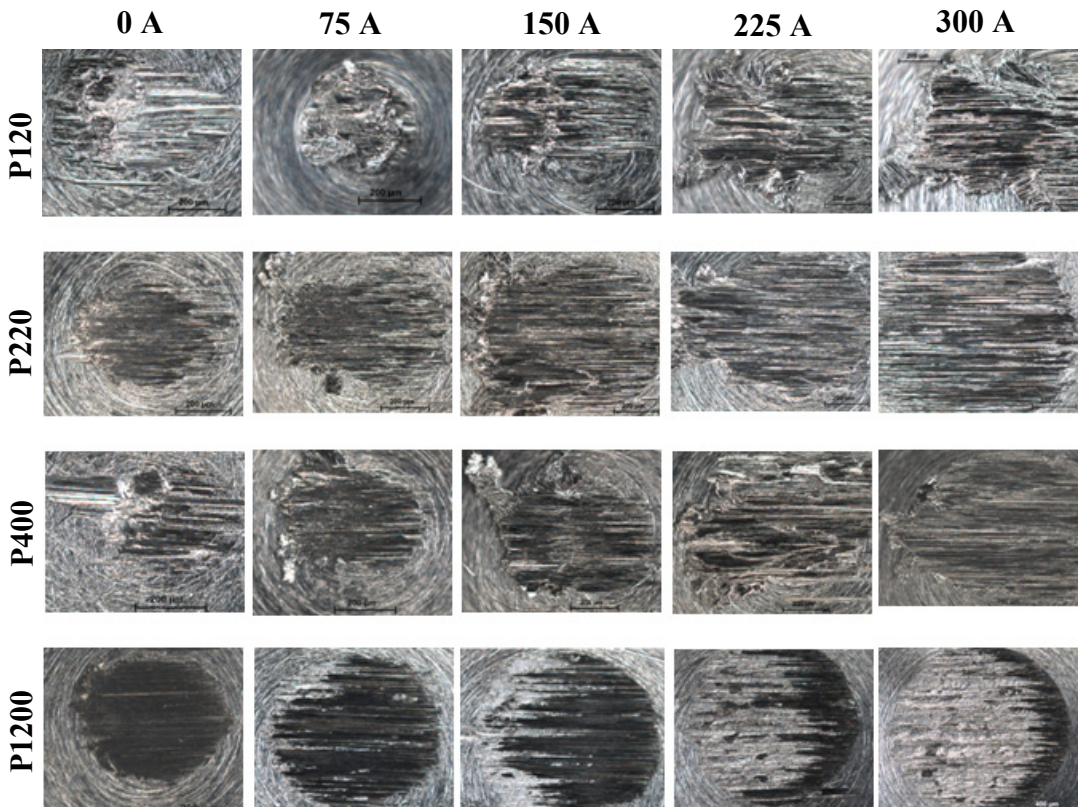

Figure 8.21 Images of pin surfaces under different currents for test against Al flats with different surface roughnesses flats

Figure 8.21 shows the microscope images of the representative pin surfaces for tests under different current levels and against aluminum flats polished with different grit sand papers. Each row of images is for tests performed against aluminum flats polished with different grit sand papers. Evidence of gross plastic flow due to thermal softening of the interface can be seen for currents greater than 75 A, for aluminum flats polished with P120 and P220 grit sand papers. For the smoothest polished aluminum flat (P1200) the pin surfaces indicate scuffing to be the dominant wear process. The occurrence of

scuffing wear can also be seen for the pin run against the aluminum flat polished with P400 sand paper at the current of 300 A.

It should be noted for tests with aluminum flats polished with P400 (R_q = 0.92 μm) and P1200 (R_q = 0.36 μm) at zero current the pins register no loss in mass (Figure 8.20), but the surface of pins shows wear scar and some material transfer (Figure 8.21). Since the material transferred onto the pin during sliding was not removed after the test, this implies that the mass of the material transferred onto the pin is same, or within the resolution of the weighing scale (0.1 mg), as the mass loss of the pin.

8.3.6 Discussion (part 2)

From the above presented results it can be concluded that surface roughness does influence the wear behavior, contact resistance, contact voltage and coefficient of friction. The contact voltage, for all combinations of surface roughnesses and current, is in saturation regime at the initial static stage. However surface roughness seems to influence the growth of the area of contact and wear process so that the average voltage drop over the course of sliding does not always remain in the saturation regime. For the cases of aluminum flat polished with P220 (R_q = 1.26 μm), P400 (R_q = 0.92 μm), and P1200 (R_q = 0.36 μm) the contact voltage remains in saturation regime during sliding while for the aluminum flat polished with P120 (R_q = 2.05 μm) the contact voltage reaches saturation at 225 A, during the course of sliding. The average interface temperature for currents greater than 150 A and for all 4 cases of surface roughnesses is in the range of 250 – 320° C. The corresponding reduction in material strength (hardness) is 70 – 90%. It can thus be concluded that the thermal softening at higher current levels

leads to accelerated wear. At higher currents the effect of surface roughness is mitigated and the wear behavior becomes independent of the surface roughness. Interestingly coefficient of friction does seem to show a weak influence of the surface roughness especially when comparing the results with the roughest (R_q = 2.05 μm) and the smoothest (R_q = 0.36 μm) polished aluminum flats.

8.4 Summary

The findings of the studies presented in Sections 8.2 and 8.3 can be summarized as follows:

- When there is no current, load has little influence on coefficient of friction
- The coefficient of friction increases with load for all speeds in the presence of current
- Contact resistance decreases with increasing current and load
- Contact voltage increases with speed for all currents and loads
- The roughest surface finish (R_q = 2.05 μm) on the aluminum flat yields the highest coefficient of friction while the smoothest surface finish (R_q = 0.36 μm) yields the lowest coefficient of friction for most of the current levels
- The wear of pins increases with increasing current through the interface
- The wear mode of pin changes from plastic flow due to thermal softening to scuffing as the surface of aluminum flat is made smoother
- Thermal softening of the interface at higher currents leads to higher wear of pins

CHAPTER 9. CONCLUSIONS AND INTELLECTUAL CONTRIBUTIONS

9.1 Conclusions

9.1.1 Chapters 2–4: Heat partition and temperature rise in sliding contacts

This section of the dissertation analyzed the interface from a macro-scale perspective. A macro scale model to evaluate interface temperature was developed. The effect of surface roughness and the deformation of the interface were neglected. A least squares regression-based methodology was developed for obtaining the steady-state temperature distribution at the interface of two sliding bodies, whose initial uniform temperatures may be the same or different. This model applies the condition of "temperature continuity" across the interface in the strictest sense. The local frictional dissipation rate at the interface was assumed to be the product of the friction coefficient, the pressure and the sliding velocity. Both uniform and Hertzian contact pressure distributions were considered. Integral equations were developed, expressing the temperatures of each body in terms of an unknown heat partition function. By assuming a polynomial form for the heat partition function and optimizing the coefficients to obtain the least squares difference in temperature at the interface between the two bodies, an estimate for the heat partition function was obtained.

The model was also used to develop curve fit equations for computing temperature rise at the interface of sliding Hertzian contact with similar and dissimilar initial uniform temperatures, over a wide range of thermal conductivity ratios, Peclet nos., and ellipticity ratios.

The model was extended to evaluate temperature distribution at the interface of an electrical contact wherein the Joule heat dissipation was taken to be product of I^2R_c and was assumed to be uniformly distributed. It is assumed that the value of contact resistance (R_c) is known and does not change during sliding. This provided qualitative predictions of the effect of Peclet no. and Joule heating on the interface temperature.

9.1.2 Chapter 5: Multi-scale electrical contact resistance

In Chapter 5, the multi-scale JS model [104] was extended to predict the "cold" contact resistance at the interface of two conductors. The predictions of the model were compared with the experimental results. It was observed that the model captures the overall trend of variation of the contact resistance with load and the model predictions compare very well with experiments for rougher surfaces. The discrepancy in the comparison for smoother surfaces was attributed to the presence of uniform oxide present on the smoother surface unlike the case for rougher surfaces.

9.1.3 Chapter 6: Voltage limits in static contacts

In Chapter 6, the phenomenon of voltage saturation in electrical contacts was demonstrated experimentally. This phenomenon, to some extent, was reported by Holm [14] and Bennett [137]. However the effect of current cycling on the interface was not discussed in earlier studies. This current study presents an extensive research on the effect of load, surface roughness, magnitude of the peak current in the current cycle, and breaking the contact in between the current cycles on the voltage saturation. The saturation voltage observed in the study is linked to the softening voltage reported by

Holm [14] and explained using the dependence of the material strength on the temperature. The study also demonstrates the hysteresis in contact voltage with current cycling.

9.1.4 Chapters 7–8: Sliding electrical contacts are high current densities

This section of the dissertation presented experimental study on sliding Al-Cu (Chapter 7) and Al-Al (Chapter 8) contacts at high current densities. A tribo-simulator for conducting the experiments was designed, built and characterized. For Al-Cu sliding contacts both flat-on-flat and sphere-on-flat type configurations were considered, whereas for Al-Al sliding interface only sphere-on-flat type of configuration was considered.

For Al-Cu sliding interface it was observed that increasing the current through the interface increased the wear rate of the Al pins and also increased the transfer of Cu from the rails onto the pins. The contact resistance was also found to be function of the interface current.

The effect of contact load, sliding speed, current and surface roughness on coefficient of friction, contact resistance and wear in Al-Al sliding interface were studied in Chapter 8. The phenomenon of voltage saturation was also observed in sliding contact akin to the one in static contacts. Surface roughness of the Al flats was found to strongly influence the wear behavior of the Al pins. Based on the optical microscopy of the pin surfaces it was concluded that the wear mode of pin changes from plastic flow due to thermal softening to scuffing as the surface of aluminum flat is made smoother. Current was once again found to strongly influence coefficient of friction, contact resistance and wear of pins.

9.2 Intellectual contributions

The major intellectual contributions of the current work are listed below:

1. A macro-scale model for determining heat partition and computing temperature rise at the interface of two sliding bodies due to the presence of Coulomb and Joule heating was developed. This model is first of its kind to apply to condition of temperature continuity at every point in the interface and also include the initial bulk temperature difference.
2. The heat partition model was used to develop curve fit equations for evaluating temperature rise at the interface of sliding Hertzian contact with Coulomb heat dissipation. The curve fit equations were extended to account for the case when both the bodies have dissimilar initial temperatures. These curve fits are valid over wide range of Peclet nos. (0.01–10,000), ellipticity ratios (0.25–2), and thermal conductivity ratios (0.25–10). It is believed that these curve fit equations will provide designers with a simple but accurate tool to evaluate interfacial temperature rise over a wide range of operating conditions.
3. A model was developed to predict the “cold” electrical resistance at the interface of two rough surfaces. This model based on the JS multi-scale contact model overcomes the sensitivity to sampling resolution inherent in many asperity based models in the literature.
4. The phenomenon of voltage saturation in both static and sliding electrical contacts was demonstrated experimentally. The effect of load and surface roughness on voltage saturation was also demonstrated experimentally. An explanation based on the softening of the interface was proposed rather than more widely referred

hypothesis of recrystallization. If the contact voltage is well below the saturation voltage then the interface behaves as an Ohmic resistor, or else the knowledge of current level also becomes important.

5. A new concept has been offered as to how voltage transients are responsible for the incremental softening of interface asperities and the associated decrease in electrical contact resistance. This concept also accounts for the presence and degree of hysteresis during current cycling.

APPENDIX A. DERIVATION OF 1D SIGNAL AMPLITUDES

Given *z(x,y)* sampled in a square grid with a uniform spacing Δx along *X* and Δy along *Y*. Let *M* and *N* be the number samples along *X* and *Y* axes. The two-dimensional (2D) FFT of the resulting surface is performed according to the following equation:

$$Z_{pq} = \frac{1}{MN}\sum_{r=0}^{M-1}\sum_{s=0}^{N-1} z\left(r\Delta x, s\Delta y\right)\exp\left(-i2\pi\left(p\frac{r}{M}+q\frac{s}{N}\right)\right) \tag{A.1}$$

Now let us consider the 1D FFT coefficient at a location along *y* axis, i.e.

$$X_k\left(s\Delta y\right) = \frac{1}{M}\sum_{r=0}^{M-1} z\left(r\Delta x, s\Delta y\right)\exp\left(-i\frac{2\pi kr}{M}\right) \tag{A.2}$$

Taking the 2-norm of the magnitude of X_k, considering all values of *s*

$$E\left\{\left|X_k\left(s\Delta y\right)^2\right|\right\} = \frac{1}{N}\sum_{s=0}^{N-1} X_k^*\left(s\Delta y\right)X_k\left(s\Delta y\right) = \frac{1}{N}\sum_{s=0}^{N-1} X_{ks}^* X_{ks} \tag{A.3}$$

Now consider

$$\phi_{kn} = \frac{1}{N}\sum_{s=0}^{N-1} X_k\left(s\Delta y\right)\exp\left(-i\frac{2\pi ns}{N}\right) = \frac{1}{N}\sum_{s=0}^{N-1} X_{ks}\exp\left(-i\frac{2\pi ns}{N}\right) \tag{A.4}$$

By the properties of FFT coefficients [190]

$$\sum_{n=0}^{N-1}\left|\phi_{kn}\right|^2 = \frac{1}{N}\sum_{s=0}^{N-1}\left|X_k\left(s\Delta y\right)\right|^2 = \frac{1}{N}\sum_{s=0}^{N-1}\left|X_{ks}\right|^2 \tag{A.5}$$

Thus,

$$\sum_{n=0}^{N-1}\left|\phi_{kn}\right|^2 = E\left\{\left|X_k\left(s\Delta y\right)^2\right|\right\} \tag{A.6}$$

Substituting Eq. (A.3) in Eq. (A.6), we get

$$\phi_{kn} = \frac{1}{N}\sum_{s=0}^{N-1}\left\{\frac{1}{M}\sum_{r=0}^{M-1} z\left(r\Delta x, s\Delta y\right)\exp\left(-i\frac{2\pi kr}{M}\right)\right\}\exp\left(-i\frac{2\pi ns}{N}\right) \tag{A.7}$$

$$\phi_{kn} = \frac{1}{NM}\sum_{s=0}^{N-1}\sum_{r=0}^{M-1} z\left(r\Delta x, s\Delta y\right)\exp\left(-i2\pi\left(\frac{kr}{M}+\frac{ns}{N}\right)\right) \tag{A.8}$$

Comparing Eq. (A.8) and Eq. (A.1),

$$\phi_{kn} = Z_{km} \tag{A.9}$$

Thus,

$$E\left\{\left|X_k\left(s\Delta y\right)\right|^2\right\} = \sum_{n=0}^{N-1}\left|Z_{kn}\right|^2 \tag{A.10}$$

and

$$\left|X_k\left(s\Delta y\right)\right|_{rms} = \sqrt{\sum_{n=0}^{N-1}\left|Z_{kn}\right|^2} \tag{A.11}$$

Similarly one could do analysis with $x = r\Delta x$ as the prescribed parameter, which would give

$$\left|Y_k\left(r\Delta x\right)\right|_{rms} = \sqrt{\sum_{p=0}^{M-1}\left|Z_{pk}\right|^2} \tag{A.12}$$

Now let us define the 1D equivalent DFT coefficients as the mean of the rms of the DFT coefficients along *X* and *Y* directions, i.e.

$$\left|Z_k\right| = \frac{1}{2}\left[\left(X_k\right)_{rms} + \left(Y_k\right)_{rms}\right] \tag{A.13}$$

From the properties of FFT coefficients the amplitudes Δ_k are related to the coefficients as [190]:

$$\Delta_0 = \left|Z_0\right| \qquad k = 0 \tag{A.14}$$

$$\Delta_k = 2\left|Z_k\right| \qquad 1 \le k < N/2 \tag{A.15}$$

$$\Delta_{N/2} = \left|Z_{N/2}\right| \qquad k = N/2 \tag{A.16}$$

Note that Δ_0 is ignored in the 1D equivalent amplitude representation.

REFERENCES

[1] Dowson D. History of tribology. London: Longman, 1979.

[2] Blok H. Surface Temperature Measurements on Gear Teeth under Extreme Pressure Lubricating Condition. Proceedings of the Institution of Mechanical Engineers 1937;2:14.

[3] Blok H. Theoretical Study of Temperature Rise at Surfaces of Actual Contact under Oiliness Lubricating Condition. Proceedings of the Institute of Mechanical Engineers General Discussion of Lubrication, vol. 2. London: Institute of Mechanical Engineers, 1937. p.222.

[4] Jaeger JC. Moving Sources of Heat and the Temperature at Sliding Contacts. Journal and Proceedings of the Royal Society of New South Wales 1943;76:203.

[5] Cameron A, Gordon AN, Symm GT. Contact Temperatures in Rolling/Sliding Surfaces. Royal Society - Proceedings Series A 1965;286:45.

[6] Yuen WYD. Heat Conduction in Sliding Solids. International Journal of Heat and Mass Transfer 1988;31:637.

[7] Bos J, Moes H. Frictional Heating of Elliptic Contacts. In: Dowson D, editor. 20th Leeds-Lyon Symposium on Tribology. Lyon, France: Elsevier Science, 1994. p.491.

[8] Bos J, Moes H. Frictional Heating of Tribological Contacts. Journal of Tribology, Transactions of the ASME 1995;117:171.

[9] Symm GT. Surface Temperatures of Two Rubbing Bodies. The Quarterly Journal of Mechanics and Applied Mathematics 1967;20:381.

[10] Kadiric A, Sayles RS, Ioannides E. Thermo-mechanical model for moving layered rough surface contacts. Journal of Tribology 2008;130:011016.

[11] Kuhlmann-Wilsdorf D. Flash temperatures due to friction and Joule heat at asperity contacts. Wear 1985;105:187.

[12] Kuhlmann-Wilsdorf D. Temperatures at Interfacial Contact Spots: Dependence on Velocity and on Role Reversal of Two Materials in Sliding Contact. Journal of Tribology, Transactions of the ASME 1987;109:321.

[13] Kuhlmann-Wilsdorf D. Demystifying flash temperatures I. Analytical expressions based on a simple model. Materials Science and Engineering 1987;93:107.

[14] Holm R. Electric Contacts: Almqvist and Wiksells Akademiska Handbocker, Hugo Gebers Forlag, Stockholm, Sweden, 1946.

[15] Thurmond LE, Barber JP. Electrical Contacts for Pulsed Power Systems. 1989. p.160.

[16] Brown L, Xu D, Ravi-Chandar K, Satapathy S. Coefficient of Friction Measurement in the Presence of High Current Density. IEEE Transactions on Magnetics 2007;43:334.

[17] Holm R. Calculation of Temperature Development in Contact Heated in Contact Surface, and Application to Problem of Temperature Rise in Sliding Contact. Journal of Applied Physics 1948;19:361.

[18] Coffin JLF. Transition Temperature for Surface Damage in Sliding Metallic Contact. Lubrication Engineering 1957;13:399.

[19] Furey MJ. Surface Temperatures in Sliding Contact. American Society of Lubrication Engineers -- Transactions 1964;7:133.

[20] Dayson C. Surface Temperature at Unlubricated Sliding Contacts. A.S.L.E. - Transactions 1967;10:169.

[21] Uetz H, Sommer K. Investigations of the Effect of Surface Temperatures in Sliding Contact. Wear 1977;43:375.

[22] Wang Q, Liu G. A Thermoelastic Asperity Contact Model Considering Steady-State Heat Transfer. Tribology Transactions 1999;42:763

[23] Yang J, Cowan RS, Winer WO. Prediction of failure transitions in sliding contacts by a thermomechanical wear model. Journal of Tribology, Transactions of the ASME 1993;115:432.

[24] Cowan RS, Winer WO. Thermomechanical Wear Modelling. TriboTest 1994;1:111.

[25] Loewen EG, Shaw MC. On Analysis of Cutting-Tool Temperatures. American Society of Mechanical Engineers -- Transactions 1954;76:217.

[26] Liang SY, Su JC. Residual Stress Modeling in Orthogonal Machining. CIRP Annals - Manufacturing Technology 2007;56:65.

[27] Komanduri R, Hou ZB. Thermal Modeling of the Metal Cutting Process - Part II: Temperature Rise Distribution due to Frictional Heat Source at the Tool-Chip Interface. International Journal of Mechanical Sciences 2001;43:57.

[28] Dufrenoy P. Two-Three-Dimensional Hybrid Model of the Thermomechanical Behaviour of Disc Brakes. Proceedings of the Institution of Mechanical Engineers, Part F: Journal of Rail and Rapid Transit 2004;218:17.

[29] Gao CH, Huang JM, Lin XZ, Tang XS. Stress Analysis of Thermal Fatigue Fracture of Brake Disks Based on Thermomechanical Coupling. Journal of Tribology 2007;129:536.

[30] Taburdagitan M, Akkok M. Determination of surface temperature rise with thermo-elastic analysis of spur gears. Wear 2006;261:656.

[31] Hooke CJ, Mao K, Walton D, Breeds AR, Kukureka SN. Measurement and prediction of the surface temperature in polymer gears and its relationship to gear wear. Journal of Tribology, Transactions of the ASME 1993;115:119.

[32] Zhao X, Jin X, Zhai W. Analysis of thermal-elastic stress of wheel-rail in rolling-sliding contact. Chinese Journal of Mechanical Engineering (English Edition) 2007;20:18.

[33] Archard JF. The Temperature of Rubbing Surfaces. Wear 1959;2:438.

[34] Ling FF. A Quasi-Iterative Method for Computing Interface Temperature Distributions. Zeitschrift für Angewandte Mathematik und Physik (ZAMP) 1959;10:461.

[35] Francis HA. Interfacial Temperature Distribution within a Sliding Hertzian Contact. ASLE Transactions 1971;14:41.

[36] Kennedy FE, Jr. Surface Temperatures in Sliding Systems-A Finite Element Analysis. Transactions of the ASME. Journal of Lubrication Technology 1981;103:90.

[37] Floquet A, Play D, Godet M. Surface Temperatures in Distributed Contacts. Application to Bearing Design. ASME Journal of Lubrication Technology 1977;99:277.

[38] Gecim B, Winer WO. Steady Temperature in a Rotating Cylinder Subject to Surface Heating and Convective Cooling. Journal of Tribology, Transactions of the ASME 1984;106:120.

[39] Gecim B, Winer WO. Transient Temperatures in the Vicinity of an Asperity Contact. Journal of Tribology, Transactions of the ASME 1985;107:333.

[40] Lai WT, Cheng HS. Temperature Analysis in Lubricated Simple Sliding Rough Contacts. ASLE Transactions 1985;28:303.

[41] Tian X, Kennedy FE, Jr. Contact Surface Temperature Models for Finite Bodies in Dry and Boundary Lubricated Sliding. Journal of Tribology, Transactions of the ASME 1993;115:411.

[42] Tian X, Kennedy FE. Maximum and Average Flash Temperatures in Sliding Contacts. Journal of Tribology, Transactions of the ASME 1994;116:167.

[43] Qiu L, Cheng HS. Temperature Rise Simulation of Three-Dimensional Rough Surfaces in Mixed Lubricated Contact. London, UK: ASME, New York, NY, USA, 1997. p.9.

[44] Komanduri R, Hou ZB. Analysis of Heat Partition and Temperature Distribution in Sliding Systems. Wear 2001;250-251:925.

[45] Komanduri R, Hou ZB. Tribology in Metal Cutting - Some Thermal Issues. Journal of Tribology 2001;123:799.

[46] Carslaw HS, Jaeger JC. Conduction of Heat in Solids. New York: Oxford University Press, 1959.

[47] Johnson KL. Contact Mechanics. Cambridge, The United Kingdom: Cambridge University Press, 1985.

[48] Hoffman JD. Numerical Methods for Engineers and Scientists. New York: Marcel Dekker, 2001.

[49] Faires JD, Burden R. Numerical Methods: Brooks Cole, CA USA, 2002.

[50] Vernersson T. Temperatures at railway tread braking. Part 1: Modelling. Proceedings of the Institution of Mechanical Engineers, Part F: Journal of Rail and Rapid Transit 2007;221:167.

[51] Kuhlmann-Wilsdorf D. Demystifying flash temperatures II. First-order approximation for plastic contact spots. Materials Science and Engineering 1987;93:119.

[52] Greenwood JA. An Interpolation Formula for Flash temperatures. Wear 1991;150:153.

[53] Bansal DG, Streator JL. A Method for Obtaining the Temperature Distribution at the Interface of Sliding Bodies. Wear 2009;266:721.

[54] Bhushan B. Principles and Application of Tribology. New York: Wiley, 1999.

[55] Barber JR. Distribution of Heat Between Sliding Surfaces. Journal of Mechanical Engineering Science 1967;9:351.

[56] Greenwood JA. Constriction Resistance and the Real Area of Contact. British Journal of Applied Physics 1966;17:1621.

[57] Greenwood JA, Williamson JBP. Electrical Conduction in Solids II. Theory of Temperature-Dependent Conductors. Proceedings of the Royal Society of London. Series A, Mathematical and Physical Sciences 1958;246:13.

[58] Timsit R. Electrical Contact Resistance: Fundamental Principles. In: Slade PG, editor. Electrical Contacts: Principles and Applications. New York: Marcel Dekker, 1999. p.1.

[59] Bansal DG, Streator JL. Design Curves for Temperature Rise in Sliding Elliptical Contacts. Tribology International;In Press, Corrected Proof.

[60] Bhushan B. Surface Roughness Analysis and Measurement Techniques. New York: CRC Press, 2001.

[61] Bowden FP, Williamson JBP. Electrical conduction in solids I. Influence of the passage of current on the contact between solids. Proceedings of the Royal Society of London, Series A (Mathematical and Physical Sciences) 1958;246:1.

[62] Greenwood JA, Williamson JBP. Contact of Nominally Flat Surfaces. Proceedings of the Royal Society of London. Series A, Mathematical and Physical Sciences (1934-1990) 1966;295:300.

[63] Timoshenko S, Goodier JN. Theory of elasticity. New York: McGraw-Hill, 1951.

[64] Abbott EJ, Firestone FA. Specifying Surface Quality - A Method Based on Accurate Measurement and Comparison. Mechanical Engineering 1933;65:569.

[65] Greenwood JA, Tripp JH. The contact of two nominally flat rough surfaces. Proceedings of the Institution of Mechanical Engineers 1970;185:625.

[66] Bush AW, Gibson RD, Thomas TR. The elastic contact of a rough surface. Wear 1975;35:87.

[67] Nayak RP. Random process model of rough surfaces. ASME Journal of Lubrication Technology 1971;93:398.

[68] Whitehouse DJ, Archard JF. The Properties of Random Surfaces of Significance in their Contact. Proceedings of the Royal Society of London. Series A, Mathematical and Physical Sciences 1970;316:97.

[69] McCool JI. Comparison of models for the contact of rough surfaces. Wear 1986;107:37.

[70] Bush AW, Gibson RD, Keogh GP. Stronogly Anisotropic Rough Surfaces. ASME Journal of Lubrication Technology 1979;101:15.

[71] Sayles RS, Thomas TR. Thermal Conductance of a Rough Elastic Contact. Applied Energy 1976;2:249.

[72] Johnson KL, Greenwood JA, Higginson JG. The contact of elastic regular wavy surfaces. International Journal of Mechanical Sciences 1985;27:383.

[73] Westergaard HM. Bearing pressures and cracks. American Society of Mechanical Engineers -- Transactions -- Journal of Applied Mechanics 1939;6:49.

[74] Chang WR, Etsion I, Bogy DB. An Elastic-Plastic Model for the Contact of Rough Surfaces. Transactions of the ASME. Journal of Tribology 1987;109:257.

[75] Zhao Y, Maietta DM, Chang L. An Asperity Microcontact Model Incorporating the Transition From Elastic Deformation to Fully Plastic Flow. Journal of Tribology, Transactions of the ASME 2000;122:86.

[76] Jeng Y-R, Wang P-Y. An Elliptical Microcontact Model Considering Elastic, Elastoplastic, and Plastic Deformation. Journal of Tribology 2003;125:232.

[77] Zhao Y, Chang L. A Model of Asperity Interactions in Elastic-Plastic Contact of Rough Surfaces. Journal of Tribology 2001;123:857.

[78] Love AEH. Stress produced in a semi-infinite solid by pressure on part of the boundary. Philosophical Transactions of the Royal Society of London 1929;228:377.

[79] Kogut L, Etsion I. Elastic-Plastic Contact Analysis of a Sphere and a Rigid Flat. Journal of Applied Mechanics 2002;69:657.

[80] Tabor D. The hardness of metals. Oxford :: Oxford University Press, 1951.

[81] Jackson RL, Green I. A Finite Element Study of Elasto-Plastic Hemispherical Contact Against a Rigid Flat. Journal of Tribology 2005;127:343.

[82] Johnson KL. An Experimental Determination of the Contact Stresses Between Plastically Deformed Cylinders and Spheres. Engineering Plasticity. Cambridge: Cambridge University Press, 1968.

[83] Jackson RL, Green I. A statistical model of elasto-plastic asperity contact between rough surfaces. Tribology International 2006;39:906.

[84] Etsion I, Front I. Model for static sealing performance of end face seals. S T L E Tribology Transactions 1994;37:111.

[85] Polycarpou AA, Etsion I. Analytical approximations in modeling contacting rough surfaces. Journal of Tribology 1999;121:234.

[86] Hess DP, Soom A. Normal and angular motions at rough planar contacts during sliding with friction. Journal of Tribology 1992;114:567.

[87] Hess DP, Soom A. Effects of relative angular motions on friction at rough planar contacts. Journal of Tribology 1993;115:96.

[88] Liu Z, Neville A, Reuben RL. An Analytical Solution for Elastic and Elastic-Plastic Contact Models. Tribology Transactions 2000;43:627.

[89] Green I. A transient dynamic analysis of mechanical seals including asperity contact and face deformation. Tribology Transactions 2002;45:284.

[90] Jackson RL. The wear and thermo-elastohydrodynamic behavior of thrust washer bearings under non-axisymmetric loads, 2004.

[91] Krithivasan V, Jackson RL. An analysis of three-dimensional elasto-plastic sinusoidal contact. Tribology Letters 2007;27:31.

[92] Lee SC, Cheng HS. On the Relation of Load to Average Gap in the Contact Between Surfaces with Longitudinal Roughness. Tribology Transactions 1993;35:523.

[93] Ren N, Lee SC. Contact simulation of three-dimensional rough surfaces using moving grid method. Journal of Tribology 1993;115:597.

[94] Ren N, Lee SC. Effects of surface roughness and topography on the contact behavior of elastic bodies. Journal of Tribology 1994;116:804.

[95] Lee SC, Ren N. Behavior of elastic-plastic rough surface contacts as affected by surface topography, load, and material hardness. Tribology Transactions 1996;39:67.

[96] Ju Y, Farris TN. Spectral analysis of two-dimensional contact problems. Orlando, FL, USA: ASME, 1995. p.10pp.

[97] Liu S, Wang Q, Liu G. A versatile method of discrete convolution and FFT (DC-FFT) for contact analyses. Wear 2000;243:101.

[98] Peng W, Bhushan B. A numerical three-dimensional model for the contact of layered elastic/plastic solids with rough surfaces by a variational principle. Journal of Tribology 2001;123:330.

[99] Majumdar A, Tien CL. Fractal characterization and simulation of rough surfaces. Wear 1990;136:313.

[100] Majumdar A, Bhushan B. Role of fractal geometry in roughness characterization and contact mechanics of surfaces. Transactions of the ASME. Journal of Tribology 1990;112:205.

[101] Majumdar A, Bhushan B. Fractal model of elastic-plastic contact between rough surfaces. Transactions of the ASME. Journal of Tribology 1991;113:1.

[102] Yan W, Komvopoulos K. Contact analysis of elastic-plastic fractal surfaces. Journal of Applied Physics 1998;84:3617.

[103] Komvopoulos K, Ye N. Three-dimensional contact analysis of elastic-plastic layered media with fractal surface topographies. Journal of Tribology 2001;123:632.

[104] Jackson RL, Streator JL. A multi-scale model for contact between rough surfaces. Wear 2006;261:1337.

[105] Archard JF. Elastic Deformation and the Laws of Friction. Proceedings of the Royal Society of London, Series A (Mathematical and Physical Sciences) 1957;243:190.

[106] Boyer L, Noel S, Houze F. Constriction Resistance of a Multispot Contact: An Improved Analytical Expression. IEEE Transactions on Components, Hybrids, and Manufacturing Technology 1991;14:134.

[107] Malucci RD. Multispot model of contacts based on surface features. Electrical Contacts, 1990., Proceedings of the Thirty-Sixth IEEE Holm Conference on ... and the Fifteenth International Conference on Electrical Contacts, 1990. p.625.

[108] Malucci RD. Dynamic model of stationary contacts based on random variations of surface features. IEEE Transactions on Components, Hybrids, and Manufacturing Technology 1992;15:339.

[109] Nakamura M. Constriction resistance of conducting spots in an electric contact surface. 1993:127.

[110] Nakamura M. Computer simulation for the constriction resistance depending on the form of conducting spots. IEEE Transactions on Components, Hybrids, and Manufacturing Technology, Part A 1995;18:382.

[111] Jang YH, Barber JR. Effect of contact statistics on electrical contact resistance. Journal of Applied Physics 2003;94:7215.

[112] Majumdar A, Tien CL. Fractal network model for contact conductance. Journal of Heat Transfer, Transactions ASME 1991;113:516.

[113] Kogut L, Komvopoulos K. Electrical contact resistance theory for conductive rough surfaces. Journal of Applied Physics 2003;94:3153.

[114] Kogut L, Komvopoulos K. Electrical contact resistance theory for conductive rough surfaces separated by a thin insulating film. Journal of Applied Physics 2004;95:576.

[115] Kogut L. Electrical performance of contaminated rough surfaces in contact. Journal of Applied Physics 2005;97:103723.

[116] Braunovic M, Konchits VV, Myshkin NK. Electrical Contacts - Fundamentals, Applications and Technology. Boca Raton, FL: CRC Press, 2007.

[117] Holm R. Electric Contacts: Theory and Application. New York: Springer-Verlag, 1967.

[118] Holm R. Electric Tunnel Effect across Thin Insulator Films in Contacts. Journal of Applied Physics 1951;22:569.

[119] Runde M, Hodne E, Totdal B. Current-induced aging of contact spots. Electrical Contacts, 1989., Proceedings of the Thirty Fifth Meeting of the IEEE Holm Conference on, 1989. p.213.

[120] Runde M. Mass Transport in Stationary Contact Points. Components, Hybrids, and Manufacturing Technology, IEEE Transactions on 1987;10:89.

[121] Runde M. Material transport and related interfacial phenomena in stationary aluminium contacts. Electrical Engineering, vol. Dr.Ing. dissertation. Norway: Universitetet i Trondheim, 1987. p.143.

[122] Aronstein J. Electromigration Failure of Aluminum Contact Junctions. Proceedings of the Forty-First IEEE Holm Conference on Electrical Contacts, 1995., 1995. p.10.

[123] Aronstein J, Hare TK. AC and DC Electromigration Failure of Aluminum Contact Junctions. IEEE Transactions on Components and Packaging Technologies 2005;28:701.

[124] Williamson JBP. Significance of non-destructive tests of compression joints. Proceedings of the Institution of Electrical Engineers 1962;109A:224.

[125] Takano E, Mano K. Theoretical lifetime of static contacts. IEEE Transactions on Parts, Materials and Packaging 1967;PMP-3:184.

[126] Naybour RD, Farrell T. Connectors for Aluminum Cables: A Study of the Degradation Mechanisms and Design Criteria for Reliable Connectors. IEEE Transactions on Parts, Hybrids and Packaging 1973;PHP-9:30.

[127] Timsit RS. Electrical instabilities in stationary contacts: Al/Al and Al/brass junctions. Proceedings of the Thirty Fourth Meeting of the IEEE Holm Conference on Electrical Contacts, 1988., , 1988. p.151.

[128] Timsit RS. Electrical contact resistance: properties of stationary interfaces. Components and Packaging Technologies, IEEE Transactions on 1999;22:85.

[129] Timsit R. Some Fundamental Properties of Aluminum-Aluminum Electrical Contacts. Components, Hybrids, and Manufacturing Technology, IEEE Transactions on 1980;3:71.

[130] Bhushan B, Majumdar A. Elastic-Plastic Contact Model for Bifractal Surfaces. Wear 1992;153:53.

[131] Babu SS, Santella ML, Feng Z, Riemer BW, Cohron JW. Empirical Model of Effects of Pressure and Temperature on Electrical contact Resistance of Metals. Science and Technology of Welding and Joining 2001;6:126.

[132] Tamai T, Tsuchiya K. Direct Observation for the Effect of Electric Current on the Contact Interface. IEEE Transactions on Components Hybrids and Manufacturing Technology 1979;2:76.

[133] Runde M, Kongsjorden H, Kulsetas J, Totdal B. Detection of a-Spots in Aluminum Contacts. IEEE Transactions on Components Hybrids and Manufacturing Technology 1986;9:77.

[134] Runde M, Hodne E, Totdal B. Experimental study of the conducting spots in aluminum contact interfaces. IEEE Transactions on Components, Hybrids, and Manufacturing Technology 1990;13:1068.

[135] Kohlrausch F. The stationary temperature state of an electrical heated conductor. Annalen Der Physik 1900;1:132.

[136] Timsit R. On the Evalutation of Contact Temperature from Potential-Drop Measurements. IEEE Transactions on Components, Hybrids, and Manufacturing Technology 1983;6:115.

[137] Bennett BW. The effect of current on stationary contact behaviour. Proceedings of the Thirty Fourth Meeting of the IEEE Holm Conference on Electrical Contacts. New York, NY, USA: IEEE, 1988. p.267.

[138] Williamson JBP. The Microworld of the Contact Spot. Proceedings of the 36th IEEE Holm Conference on Electrical Contacts, 1981. p.1.

[139] Timsit RS. The `melting' voltage in electrical contacts. IEEE Transactions on Components, Hybrids, and Manufacturing Technology 1991;14:285.

[140] Kuhlmann-Wilsdorf D. Metal Fiber Brushes. In: Slade PG, editor. Electrical Contacts: Principles and Applications. New York: Marcel Dekker, 1999. p.943.

[141] ASM Specialty Handbook: Aluminum and aluminum alloys. Materials Park, OH: ASM International, 1993.

[142] ASM Specialty Handbook: Copper and Copper Alloys. Materials Park, OH: ASM International, 2001.

[143] Guy AG, Hren JJ. Elements of Physical Metallurgy. Reading, MA: Addison-Wesley Publishing Company, 1974.

[144] Merchant HD, Murty GS, Bahadur SN, Dwivedi LT, Mehrotra Y. Hardness-Temperature Relationships in Metals. Journal of Materials Science 1973;8:437.

[145] Savitsky EM. The Influence of Temperature on the Mechanical Properties of Metals and Alloys. Stanford, CA: Stanford University Press, 1961.

[146] Frost HJ, Ashby MF. Deformation-Mechanism Maps: The Plasticity and Creep of Metals and Ceramics. Oxford, UK: Pergamon Press, 1982.

[147] Deryagin AI, Zavalishin VA. Role of Thermoelectric Phenomena in the Electroplastic Effect. Physics of Metals and Metallography 1984;58:142.

[148] Galligan JM. Dislocation Drag Mechanisms in Normal State Metals. Scripta Metallurgica 1984;18:653.

[149] Conrad H, Sprecher AF, Mannan SL. The Electroplastic Effect in Metals. Journal of Metals 1983;35:A62.

[150] Roshchupkin AM, Bataronov IL, Troitskii OA, Moiseenko MM. Electric current effect on metal surface layers. Physica Status Solidi B 1989;151:121.

[151] Livesay BR, Donlin NE, Garrison AK, Harris HM, Hubbard JL. Dislocation based mechanisms in electromigration. San Diego, CA, USA: Publ by IEEE, 1992. p.217.

[152] Antolovich SD, Conrad H. The effects of electric currents and fields on deformation in metals, ceramics, and ionic materials: An interpretive survey. Materials and Manufacturing Processes 2004;19:587.

[153] Varma SK, Cornwell LR. The electroplastic effect in aluminum. Scripta Metallurgica 1979;13:733.

[154] Sprecher AF, Mannan SL, Conrad H. Overview no. 49: On the mechanisms for the electroplastic effect in metals. Acta Metallurgica 1986;34:1145.

[155] Conrad H, Sprecher AF, Cao WD, Lu XP. Electroplasticity. The effect of electricity on the mechanical properties of metals. JOM 1990;42:28.

[156] Kopanev AA. Nature of the electroplastic effect in metals. Strength of materials 1991;23:55.

[157] Roshchupkin AM, Bataronov IL. Physical basis of the electroplastic deformation of metals. Russian Physics Journal 1996;39:230.

[158] Strizhalo VA, Novogrudskii LS. Determination of the energy of electroplastic deformation of metals. Strength of Materials 1997;29:345.

[159] Bond N. Aluminum Contact Surfaces in Electrical Transition Interfaces. IEEE Transactions on Parts, Materials and Packaging 1969;5:104.

[160] Jackson RL. Electrical Performance of Aluminum/Copper Bolted Joints. IEEE Proceedings, Part C: Generation, Transmission and Distribution 1982;129:177.

[161] Braunovic M. Fretting damage in tin-plated aluminum and copper connectors. IEEE Transactions on Components, Hybrids, and Manufacturing Technology 1989;12:215.

[162] Ben Jemaa N, Carvou E. Electrical contact behaviour of power connector during fretting vibration. Electrical contacts - 2006, proceedings of the fifty-second ieee holm conference on, 2006. p.263.

[163] McNab IR. Advances in electrical current collection. Wear 1982;78:1.

[164] Ma XC, He GQ, He DH, Chen CS, Hu ZF. Sliding wear behavior of copper-graphite composite material for use in maglev transportation system. Wear 2008;265:1087.

[165] Reichner P. Metallic Brushes for Extreme High-Current Applications. Components, Hybrids, and Manufacturing Technology, IEEE Transactions on 1980;3:21.

[166] Groth K, Heidenfelder F, Holinski R. Advancements of tribological performance of carbon brushes in electrical motors. Industrial Lubrication and Tribology 2001;53:5.

[167] Bonwitt WF. An experimental investigation of the electrical performance of bolted aluminum-to-copper connections. Transactions of the American Institute of Electrical Engineers 1948;67:1208.

[168] Runde M, Magnusson N, Lenes A. Bolted connectors for stranded aluminum power conductors. IEEE Transactions on Power Delivery 2008;23:523.

[169] Rabinowicz E. The temperature rise at sliding electrical contacts. Wear 1982;78:29.

[170] Lawson DK, Dow TA. Sparking and Wear of High Current Density Electrical Brushes. Wear 1984;102:105.

[171] Barber JP, Bauer DP, Jamison K, Parker JV, Stefani F, Zielinski A. A Survey of Armature Transition Mechanisms. IEEE Transactions on Magnetics 2003;39:47.

[172] Stefani F, Levinson S, Satapathy S, Parker J. Electrodynamic transition in solid armature railguns. IEEE Transactions on Magnetics 2001;37:101.

[173] Young FJ, Hughes WF. Rail and Armature Current Distributions in Electromagnetic Launchers. IEEE Transactions on Magnetics 1982;18:33.

[174] Parks PB. Current Melt-Wave Model for Transitioning Solid Armature. Journal of Applied Physics 1990;67:3511.

[175] Barber JP, McNab IR. Magnetic Blow-Off in Armature Transition. IEEE Transactions on Magnetics 2003;39:42.

[176] Persad C, Yeoh A, Prabhu G, White G, Eliezer Z. On the nature of the armature-rail interface: Liquid metal effects. IEEE Transactions on Magnetics 1997;33:140.

[177] Stefani F, Parker JV. Experiments to Measure Wear in Aluminum Armatures. IEEE Transactions on Magnetics 1999;35:100.

[178] Persad C, Peterson DR. High Energy Rate Modification of Surface Layers of Conductors. IEEE Transactions on Magnetics 1986;MAG-22:1658.

[179] Davidson RF, Cook WA, Rabern DA, Schnurr NM. Predicting Bore Deformations and Launcher Stresses in Railguns. IEEE Transactions on Magnetics 1986;MAG-22:1435.

[180] Bedford A. Rail Damage and Armature Parameters for Different Railgun Rail Materials. IEEE Transactions on Magnetics 1984;20:352.

[181] Persad C, Lund CJ, Eliezer Z, Peterson DR, Hahne J, Zowarka R. Wear of Conductors in Railguns: Metallurgical Aspects. IEEE Transactions on Magnetics 1989;25:433.

[182] Wolfe T, Spiegelberg W, Evangelist M. Exploratory metallurgical evaluation of worn rails from a 90 mm electromagnetic railgun. IEEE Transactions on Magnetics 1995;31:770.

[183] Gee RM, Persad C. The Response of Different Copper Alloys as Rail Contacts at the Breech of an Electromagnetic Launcher. IEEE Transactions on Magnetics 2001;37:263.

[184] Brailsford JR. Influence of Electric Current on the Static Friction of Metal Surfaces in Air. Wear 1973;25:85.

[185] Chen J-C, Vook R. Characterization of sliding Al-Cu Electrical contacts. IEEE Transactions on Components, Hybrids, and Manufacturing Technology 1986;9:17.

[186] Paulmier D, Bouchoucha A, Zaidi H. Influence of the electrical current on wear in a sliding contact copper-chrome steel, and connection with the environment. Vacuum 1990;41:2213.

[187] Cabrera N, Mott NF. Theory of the oxidation of metals. Reports on Progress in Physics 1948;12:163.

[188] Bouchoucha A, Zaidi H, Kadiri EK, Paulmier D. Influence of electric fields on the tribological behaviour of electrodynamical copper/steel contacts. Wear 1997;203-204:434.

[189] Senouci A, Zaidi H, Frene J, Bouchoucha A, Paulmier D. Damage of surfaces in sliding electrical contact copper/steel. Applied Surface Science 1999;144:287.

[190] Newland DE. An introduction to random vibrations and spectral analysis. London: Longman, 1975.